

UNIVERSITÀ DEGLI STUDI DI NAPOLI "FEDERICO II"

SCUOLA POLITECNICA E DELLE SCIENZE DI BASE



DOCTORAL THESIS IN CHEMICAL SCIENCES (XXVIII cycle)
2013-2016

**NOVEL AU(I)-BASED MOLECULAR CATALYSTS:
FROM KNOW HOW TO KNOW WHY**

Ph.D. student

Marina Trinchillo

TUTORS

Prof. V. Busico, Dr. A. D'Amora

SUPERVISOR

Prof. F. Auriemma

COORDINATOR

Prof. L. Paduano

Preface

The work described in the present manuscript has been carried out under the financial support of the MIUR (Rome, Italy) and the FIRB-Futuro-in-Ricerca project RBFR1022UQ [“Novel Au(I)-based molecular catalysts: from know-how to know-why (AuCat)”].

TABLE OF CONTENTS

CHAPTER 1	
HOMOGENEOUS GOLD(I) CATALYSIS: GENERAL INTRODUCTION	4
CHAPTER 2	
SYNTHESIS OF GOLD(I) COMPLEXES	28
CHAPTER 3	
GOLD(I)-CATALYZED METHOXYLATION OF ALKYNES	58
CHAPTER 4	
NUCLEOPHILES AND SUBSTRATES	133
CHAPTER 5	
DETERMINATION OF ACTIVATION PARAMETERS	156
CHAPTER 6	
COMPUTATIONAL STUDY OF COUNTERION EFFECT	169
CHAPTER 7	
GOLD(I) N-HETEROCYCLIC CARBENE COMPLEXES AS ANTICANCER AGENTS: THE OTHER SIDE OF THE COIN	213
CHAPTER 8	
GENERAL CONCLUSIONS	239
APPENDIX A	
ACRONYMS AND ABBREVIATION LIST	243
APPENDIX B	
LIST OF PUBLICATIONS	254

CHAPTER

1

**HOMOGENEOUS GOLD(I) CATALYSIS:
GENERAL INTRODUCTION**

1. Gold, a precious metal

Gold has fascinated, inspired and accompanied humankind from the very early days. Throughout the centuries almost every established culture has used gold to symbolize power, beauty, purity and accomplishment. Due to its golden shine and glitter, its resistance to corrosion and its rarity, gold was always considered a very precious and highly sought after material, as nicely reflected by the Greek myth of king Midas. The desire to possess more and more gold has incited the exploration of the most hostile regions of earth, such as the Spanish exploration of the New World in search of “el Dorado” or the gold rushes in California, Alaska, South Africa and Australia, but also wars, conflicts and even growth in science and chemistry.

Of all the minerals mined from the Earth, none is more useful than gold. Examples of the use of gold in jewelry were found in Ancient Egypt about 3,000 – 5,000 years ago or as a medium of exchange or money, because it is highly valued and in very limited supply. The first known use of gold in transactions dates back over 6000 years.

2. Uses of gold

The merits of gold are unparalleled. Gold is dense, soft, malleable and ductile metal, which is resistant to corrosion, and is a great conductor of electricity.

Nowadays gold is still mostly employed in jewelry. Until recently, jewelry constituted nearly all the demand for gold and stood far and away as the most common use of gold. The last several years have seen a rapid rise in the demand of gold as an investment however and today jewelry represents 58.4% of total yearly demand.¹

The properties of gold – namely being malleable, ductile, noble, rare, and shiny – all help contribute to making gold a preferred metal in the creation and use of jewelry. Pure gold is too soft to stand up to the stresses applied to many jewelry items. Craftsmen learned that alloying gold with other metals such as copper, silver, and platinum would increase its durability. Since then most gold used to make jewelry is an alloy of gold with one or more other metals. The alloys of gold have a lower value per unit of weight than pure gold. A standard of trade known as "karatage" was developed to designate the gold content of these alloys.

The second most popular use of gold is in the form of investment through various tools such as ETFs (Exchange Traded Fund), certificates, accounts, spread betting, derivatives or shares. Related to this, central banks have once again become net buyers of gold and are starting to fill up their coffers with gold bullion to serve as reserves with the US Dollar starting to lose its credibility.

The most important industrial use of gold is in the manufacture of electronics. Solid state electronic devices use very low voltages and currents, which are easily interrupted by corrosion or tarnish at the contact points. Gold is the highly efficient conductor that can carry these tiny currents and remain free of corrosion.

Electronic components made with gold are highly reliable. Gold is used in connectors, switch and relay contacts, soldered joints, connecting wires and connection strips. A

¹ Source of the data: World Gold Council's website. Investing in gold. Demand and supply <http://www.gold.org/supply-and-demand/gold-demand-trends/back-issues/gold-demand-trends-q2-2015>

small amount of gold is used in almost every sophisticated electronic device, including cell phones, calculators, personal digital assistants, global positioning system units and other small electronic devices.

Gold is also used in the standard desktop or laptop computer. The rapid and accurate transmission of digital information through the computer and from one component to another requires an efficient and reliable conductor. Gold meets these requirements better than any other metal.

The aerospace industry uses gold in a variety of ways. Because gold is a precious metal, you wouldn't think mankind would send it into space, but because of some of the unique qualities of gold, it's extremely valuable in the space program, too. For instance, it's used in space suits: a thin layer of gold is applied to the suits astronauts wear in outer space in order to protect them from radiation and reflect and deflect the burning heat of the sun. In addition, many parts of every space vehicle are fitted with gold-coated polyester film, which reflects infrared radiation and helps stabilize the temperature of the spacecraft, because without this coating, dark colored parts of the spacecraft would absorb significant amounts of heat.

Gold is also used as a lubricant between mechanical parts: in the vacuum of space, organic lubricants would volatilize and they would be broken down by the intense radiation beyond Earth's atmosphere. Gold has very low shear strength and thin films of gold between critical moving parts serves as a lubricant (the gold molecules slip past one another under the forces of friction and that provides a lubricant action).

In dentistry, gold is a very popular substance, because it is chemically inert, non-allergenic and easy for the dentist to work. The earliest found records of gold being used in dentistry stretches back to 700 B.C. with Etruscan dentists using gold wires to place replacement teeth into the patient's mouth. Modern uses of gold in dentistry is usually in the form of white gold or gold alloys and include areas such as bridges, fillings, crowns, and orthodontic appliances.

High quality pure metallic gold is used in food, in the form of leafs, flakes or dust, and has the E number 175.² It is tasteless and acts as decorative ingredient in some gourmet foods and drinks, because metallic gold is inert to all body chemistry and provides no nutrition.

The Figure 1 shows the gold demand in the 2014.¹

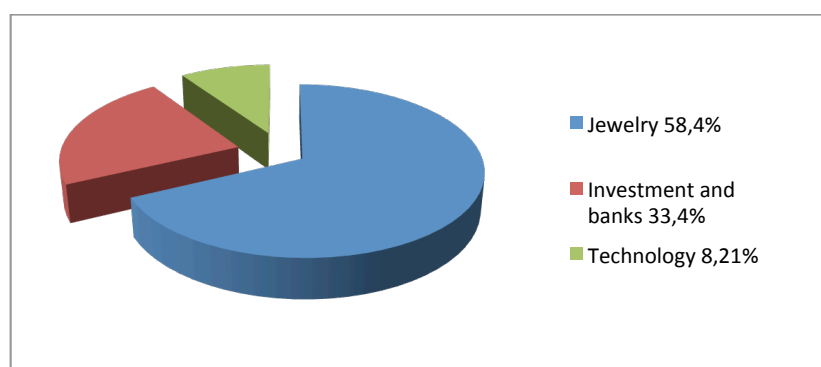


Figure 1. Gold demand in 2014

Moreover, gold and its compounds have a long history of medical application.

The German physician and microbiologist Robert Koch (Nobel laureate in Medicine, 1905), who can be considered the pioneer of the modern use of gold in medicine, reported in 1890 antibacterial effects of gold cyanide, $K[Au(CN)_2]$, against tubercle bacilli.³ Gold therapy for tuberculosis was subsequently introduced in the 1920s, and in 1929 the use of gold therapy was extended to the rheumatoid arthritis following the indication that the tubercle bacillus was a causative agent for this disease. Gold therapy soon resulted ineffective for tuberculosis, but after World War II, the Empire Rheumatism Council in the UK initiated a clinical study, which confirmed that gold drugs might provide an effective treatment for many patients suffering from rheumatoid arthritis.

In spite of these favorable findings, there have been no major changes in this field since the introduction of auranofin for the treatment of rheumatoid arthritis in 1985.

² http://www.capitalco.com.au/Portals/0/Docs/Minerals_Energy/Gold.pdf

³ Kean, W.F. and Kean, I.R.L. *Clinical pharmacology of gold* **2008**

Since that time, research has continued to include not only the prolonged use of gold complexes to treat rheumatoid arthritis, but has also expanded to investigate its possible utility as antitumor, anti-HIV agents, and so on. Nowadays, the *Chrysotherapy* (from the Greek word for gold, *chrysos*), the treatment with gold based-drugs, is an accepted part of modern medicine.

Finally, the gold-198 isotope is also widely used in medicine and it has two major uses: ^{198}Au has a diagnostic use for liver imaging, in the form of a gold colloid, and a therapeutic use in some cancer treatment, in the form of radioactive gold nanoparticles, as a radiation source.

3. Gold in chemistry

The “noble” character of gold was at the origin of the late development of its chemistry, compared to its neighbors in the periodic table, and several misconceptions because of its chemical inertness, rarity and preciousness, which have led to the assumption of gold as a useful element rather than a catalyst in chemical transformations. For this reason the role of gold in organic/organometallic chemistry had long been confined to its stoichiometric usage and the potential of gold in catalysis was left largely unexplored, until mid-1900s with gold applications in heterogeneous catalysis. Conversely, the homogeneous catalysis using gold is more recent, starting to blossom in the last few decades.

It must be taken into account that gold is not the only rare and precious metal, but several metals like platinum, palladium, ruthenium, rhodium, osmium and iridium are widely used in organic chemistry. Furthermore, it is not even the more expensive among them (for example, the prices of platinum and rhodium are higher than gold). In fact, gold supply is higher than these other metals and no less than 2,500 tons of gold are mined each year, leading to a higher stability of the price, which can positively affect the feasibility of a possible industrial usage.

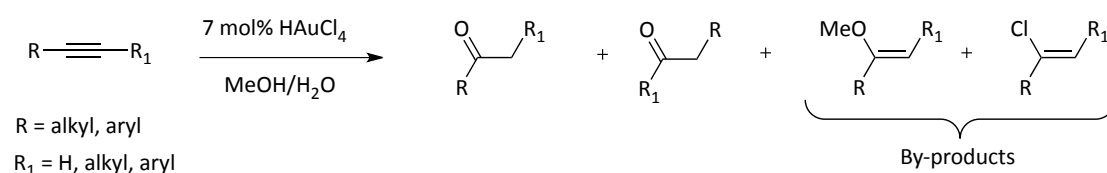
In addition, it is noteworthy that gold can be easily recycled and it is not active in catalysis in its elemental state, but in the form of complex, obtained from gold (I) and gold (III) salts, which are less expensive than the pure metal, and we should keep in mind that usually the price of a organometallic complex is determined by the ligand rather than the metal.

The rearrangement of strained small ring hydrocarbons can be considered the very first report of a gold-catalyzed organic transformation,⁴ but the major breakthrough in the field of homogeneous gold catalysis was made in 1976, with the first example of alkynes activated by gold(III) salts reported by the group of Thomas (Scheme 1).⁵

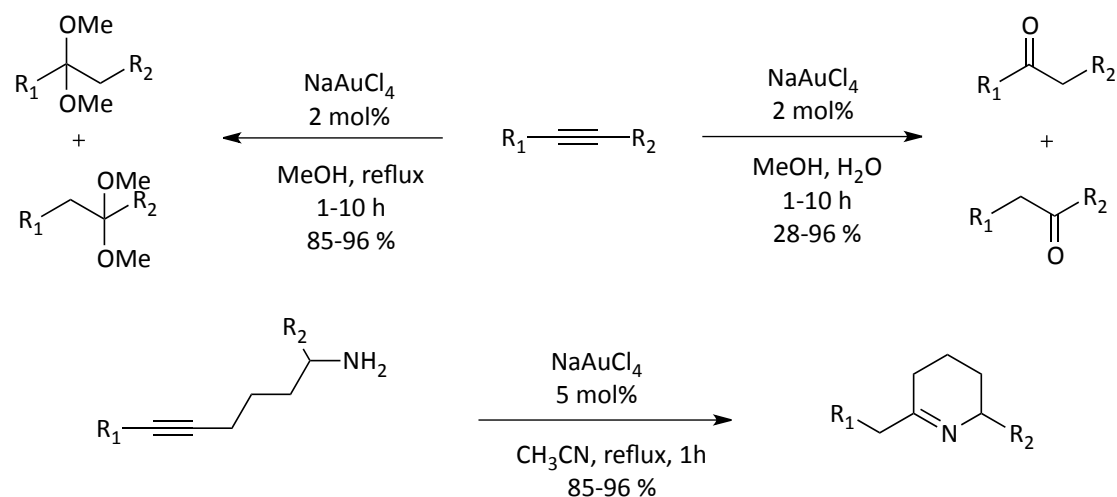
⁴ (a) P. G. Gassman, G. R. Meyer, F. J. Williams, *J. Am. Chem. Soc.* **1972**, *94*, 7741-7748; (b) L.-U. Meyer, A. de Meijere, *Tetrahedron Lett.* **1976**, *17*, 497-500

⁵ R. O. C. Nomran, W. J. E. Parr, C. B. Thomas, *J. Chem. Soc., Perkin Trans. 1* **1976**, 1983-1987

Later on, in 1991, Fukuda and Utimoto⁶ demonstrated that alkynes are susceptible to the addition of nucleophiles such as water, alcohols, and amines in the presence of a gold(III) salt giving ketones, ketals, and cyclic imines, respectively (Scheme 2).



Scheme 1. Gold catalyzed nucleophilic addition to alkynes



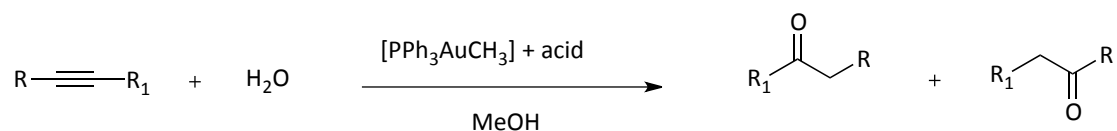
Scheme 2. Addition of nucleophiles to alkynes in presence of gold(III) salts

A few years later (1998), Teles and coworkers⁷ reported the first application of phosphine-gold complexes in homogeneous catalysis; in particular, they used cationic gold(I) complexes bearing an arsine, a phosphine or a phosphite ligand as excellent catalysts in the hydration of alkynes (Scheme 3), generated in situ from the gold precursor and the methanesulfonic acid, which leads to a more efficiently and selectively bis-hydroalkoxylation of alkynes. The extended version was published in

⁶ Y. Fukuda, K. Utimoto, *J. Org. Chem.* **1991**, *56*, 3729-3731

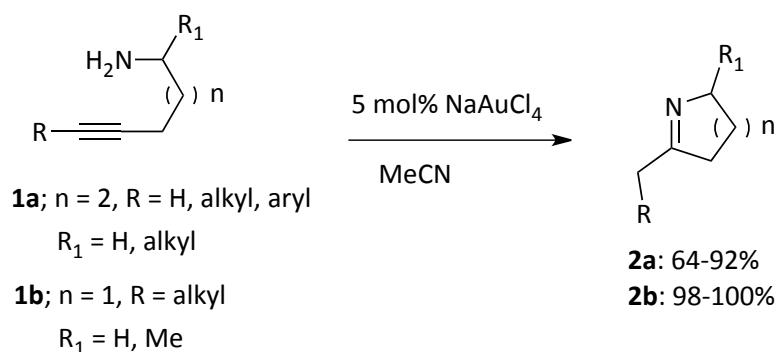
⁷ J. H. Teles, S. Brode, M. Chabanas, *Angew. Chem. Int. Ed.* **1998**, *37*, 1415-1418

2002 by Hayashi and Tanaka, using $[(\text{PPh}_3)\text{AuCH}_3]$ in combination with an acid as the catalytic system.⁸



Scheme 3. First example of the use of a cationic gold(I) complex as catalyst

Furthermore, in 1987 Utimono et al.⁹ described a convenient methodology for the intramolecular hydroamination of alkynes using sodium tetrachloroaurate as catalyst in terms of higher selectivity and milder conditions, as alternative to the existed palladium catalyzed synthesis of N-hydroheterocycles (Scheme 4).



Scheme 4. Gold catalyzed hydroamination of alkynes

⁸ E. Mizushima, K. Sato, T. Hayashi, M. Tanaka, *Angew. Chem. Int. Ed.* **2002**, *41*, 4563- 4565

⁹ a) Y. Fukuda, K. Utimono, H. Nozaki, *Heterocycles.* **1987**, *25*, 297; (b) Y. Fukuda, K. Utimono, *Synthesis.* **1991**, 975

4. Gold rush

On the basis of these initial results, the interest in homogenous gold catalysis and in the potential of gold in organic synthesis has grown exponentially,¹⁰ leading to an exponential raise in activity in this area, the so-called "Gold Rush". The impressive number of organic reactions catalyzed by gold salts reported attest that homogeneous gold catalysis is presently a hot topic in organic synthesis. Most of these reactions have clear advantages over alternative approaches, including milder conditions and compatibility with a wide range of functional groups. In some cases gold species can catalyze a variety of transformations that cannot be performed by other transition metals, thanks to their peculiar reactivity and tolerance to oxygen. This makes gold the star of the metal catalysis.

As Stephen Hashmi wrote in his review, "A change in paradigm has taken place. While the ancient alchemists investigated the question of how to make gold, now the question is what to make with gold".¹¹

¹⁰ A. S. K. Hashmi, *Gold Bull.* **2004**, *37*, 51-65

¹¹ A. S. K. Hashmi, *Chem. Rev.* **2007**, *107*, 3180

5. Gold: a special Lewis acid

Gold has the electronic configuration [Xe] 4f¹⁴ 5d¹⁰ 6s¹. Its oxidation states can vary from -1 to +5, but the most common ones are by far +1 and +3.

The unique properties of gold species arise from the special nature of the metal center.

Gold physical and chemical properties, like the resistance to oxidation and the superior Lewis acidity, are consequences of strong relativistic effects, as noted by Pfitzer¹² and Pyykkö¹³ in 1979.

The term 'relativistic effects' refers to any phenomenon resulting from the need to consider velocity as significant relative to the speed of light.

Relativistic effects become apparent when the velocity of the electron is arbitrarily close to the speed of light.

As atomic nuclear charge (Z) increases throughout the periodic table, electrons move in a field of a very high nuclear charge and their average velocity increases, approaching the speed of light. This is especially true for electrons that penetrate to the nucleus (in the *s* orbitals and, to a smaller extent, in the *p* orbitals); therefore, they need to be treated according to Einstein's theories of relativity. As a result, their mass increases and this increase in mass corresponds to a decrease in Bohr radius, which is inversely proportional to the mass of the electron orbiting a nucleus. This relativistic contraction of the 1s orbital also applies to all other *s* and *p* orbitals, and it is only significant for elements where the 4*f* and 5*d* orbitals are filled. This effect is most pronounced for gold, which explains the unique position of gold among all the elements (Figure 2).¹⁴

¹² K. Pitzer, *Accnts. Chem. Res.*, **1979**, *12*, 271

¹³ P. Pyykkö and J-P. Desclaux, *Accnts. Chem. Res.*, **1979**, *12*, 276

¹⁴ D. J. Gorin, F. D. Toste, *Nature* **2007**, *446*, 395

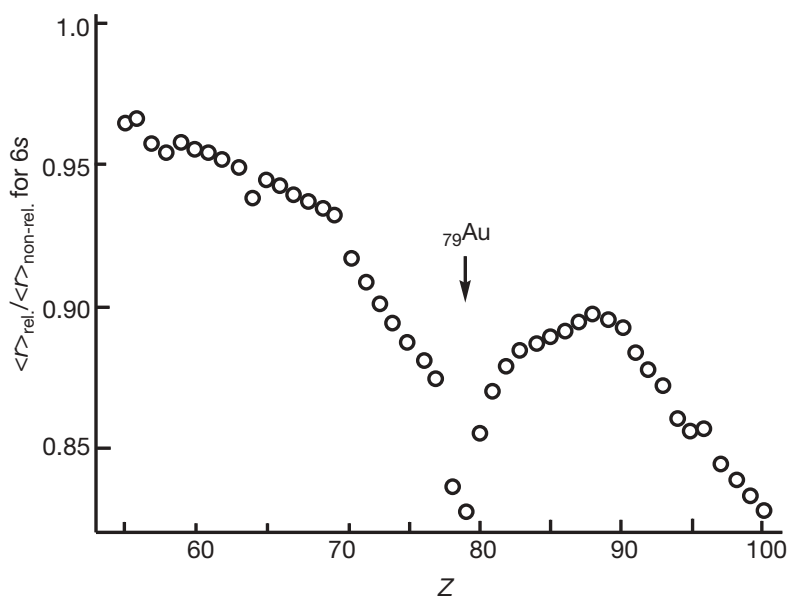


Figure 2. Calculated relativistic contraction of the 6s orbital. Reproduced from ref. 14

In the heavier elements, the *s* electrons are in smaller orbitals and are more strongly bound and shield the other electrons (especially *d* and *f*) from the nuclear charge more effectively than if the relativistic effects were absent. The *d* and *f* electrons see a weaker nuclear attraction and occupy larger orbitals. These effects scale roughly with Z^2 and become important for elements heavier than the lanthanides.¹⁵

Relativistic effects are crucial to explain the electronic structure and some properties of gold: for example, highest electrochemical potential and the highest electronegativity of gold among all the metals, but also the charming golden color, due to excitation of the 5*d* electrons to the Fermi level, which occurs with a bandgap of 2,38 eV, therefore blue visible light is absorbed. For another element of the group 11, silver, the transition 4*d* – 5*s* has a gap of 3,7 eV and the absorption is in the ultraviolet region, leading to the metallic shine of silver (Figure 3). The “non-relativistic band structures” of silver and gold are very similar, so if relativistic effects did not exist gold would look like silver.¹⁶

¹⁵ P. Pyykkö, *Chem. Rev.*, **1988**, *88*, 563

¹⁶ S. A. Cotton, *Chemistry of Precious Metals*, Blackie & Son Ltd., London, **1997**



Figure 3. Metallic silver and gold

The electronic configuration of Au^0 ($5d^{10}6s^1$) suggests that the metallic form of gold should be reactive, because of the single 6s electron, whereas it is predominant. This is probably due to the 6s orbital contracted toward the nucleus, whose electron does not react easily. For the same reason, gold has also high electron affinity.

Relativistic effects are also responsible of the enhanced dispersion forces in gold chemistry, which are relevant for the strong intermetallic affinity, so-called "Aurophilicity". In Au(I) complexes the expansion of the $5d^{10}$ orbital results in the delocalization of its electrons and in the interaction with other elements or with other gold atoms in molecules or clusters. In fact, in the 1980s, sub van der Waals distances Au-Au in range 2,8 - 3,5 Å were found between linear two-coordinated centers in complexes of the formula L-Au-X ,¹⁷ with the lower and the upper limits are shorter than the interatomic distance in metallic gold (2,89 Å) and the estimated sum of two van der Waals radii of a gold atom (3,65 Å), respectively. This cannot be explained in terms of classical bonding.

Gold cations act as "soft π -acids" coordinating multiple bonds and depleting their electron density, which can result in the activation of the ligand towards a nucleophilic attack. But gold is not the only late transition metal able of mediating reactions by functioning as Lewis acid, therefore it was investigated the reason why cationic gold species are superior Lewis acids. Intuitively, the relativistic contraction

¹⁷ Jones, P. G. *Gold Bull.* **1981**, *14*, 102

of the valence *s* and *p* orbitals of gold could be responsible, leading to a low-lying lowest unoccupied molecular orbital (LUMO) and to a strong Lewis acidity.

In addition, intriguing computational calculations, performed by Irikura & Goddard,¹⁸ suggested a different coordinating mode than simple Lewis acid-base interaction, finding out higher bond energy in the Au-CH₂⁺ fragment, compared to other late transition metal. According to them, the fragment features a multiple bond character, due to the σ -complexation of singlet CH₂ and backbonding from Au to the carbon atom. Later on, it was hypothesized a triple-bond character for the species AuC⁺ by Barysz & Pyykkö,¹⁹ and mass spectroscopy evidences for such a species has been collected.²⁰

These findings about significant back-donation from Au into the empty *p* orbitals are in contrast with the presumed absence of backbonding in Au-carbonyl and Au-alkyne/alkene complexes. Au^I carbonyls have been characterized spectroscopically,²¹ showing a blueshift of the CO stretching frequency,²² suggesting a σ -only complexation and lack of back donation from Au into the CO π^* orbital.²³ In the case of Au^I-alkyne or Au^I-alkene, experimental evidences are only indirect and not sufficiently unambiguous, principally because a weakening of the coordinated C-C bond results from both donation and back-donation; therefore information about the C-C bond length or the stretching frequency, obtained by Raman or IR spectroscopy, are not particularly helpful and a deep theoretical interpretation of the electronic structure is needed.

The most popular understanding of metal coordination bond is in terms of the Dewar-Chatt-Duncanson model of ligand-to-metal donation and metal-to-ligand back-donation, which govern gold catalysis. This kind of analysis is still limited and without

¹⁸ Irikura, K.K., Goddard, W.A., *J. Am. Chem. Soc.* **1994**, *116*, 8733–8740

¹⁹ Barysz, M., Pyykkö, P. *Chem. Phys. Lett.* **1998**, *285*, 398–403

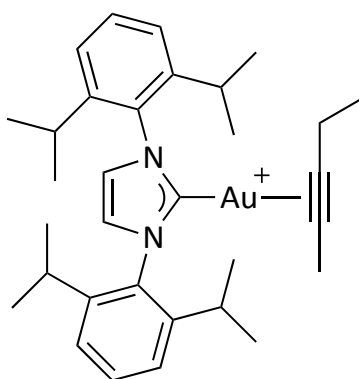
²⁰ Aguirre, F., Husband, J., Thompson, C.J., Metz, R.B. *Chem. Phys. Lett.* **2000**, *318*, 466–470

²¹ Xu, Q., Imamura, Y., Fujiwara, M., Souma, Y. *J. Org. Chem.* **1997**, *62*, 1594–1598

²² I. Antes, S. Dapprich, G. Frenking, P. Schwerdtfeger, *Inorg. Chem.* **1996**, *35*, 2089 – 2096

²³ D. J. Gorin, F. D. Toste, *Nature* **2007**, *446*, 395 – 403; *Modern Supramolecular Gold Chemistry: Gold-Metal Interactions and Applications* (Ed.: A. Laguna), Wiley, New York, 2008; J. Velasquez, B. Njagic, M. S. Gordon, M. A. Duncan, *J. Phys. Chem. A* **2008**, *112*, 1907–1913

predictive ability,²⁴ but in recent years a novel approach was developed, combining relativistic quantum chemical calculations and a detailed analysis of the change in electron density due to the metal-carbon bond formation, called Charge Displacement (CD) Analysis.²⁵ It permits an unambiguous measure of the donation and back-donation components, which are at the heart of the Dewar-Chatt-Duncanson model, providing a clear picture of the electron density redistribution after the gold-carbon bond formation. The key idea is expressed by the CD function, which defines at each point z along a chosen axis the amount of the electronic charge: a positive (or negative) value corresponds to electrons flowing in the direction of decreasing (or increasing) z . As reported by Zuccaccia *et al.*,²⁶ the species L-Au-(2-hexyne), where L is NHC [1,3-bis(diisopropylphenyl)imidazol-2-ylidene] (Scheme 5), presents a 3D contour plot of the electron density difference between complex and its no-interacting fragments (Figure 4), showing that the charge significantly rearranges at both gold and alkyne sites upon coordination. A charge accumulation (blue) takes place in the bonding region and the electron density (red) decreases at the outer part of the triple bond, which becomes suitable for a nucleophilic attack.



Scheme 5. [(NHC)Au-(2-hexyne)]⁺

²⁴ Benitez, D., Shapiro, N. D., Tkatchouk, E., Wang, Y., Goddard, W. A., Toste, F. D., *Nat. Chem.* **2009**, *1*, 482

²⁵ Belpassi, L., Infante, I., Tarantelli, F., Visscher, L. *J. Am. Chem. Soc.* **2008**, *130*, 1048

²⁶ Zuccaccia, D., Belpassi, L., Macchioni, A., Tarantelli, F. *Eur. J. Inorg. Chem.* **2013**, *24*, 4121-4135

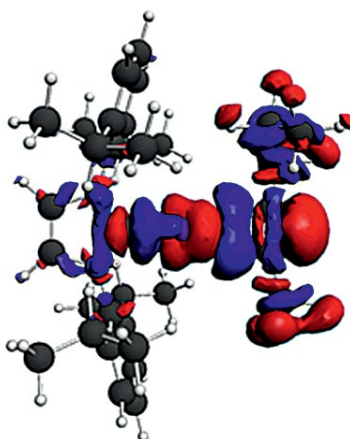


Figure 4. Three-dimensional plot of electron density difference for NHC-Au-(2-hexyne)

The CD function is separated into two irreducible representations, A' and A'' , providing a rigorous definition of the components of the DCD bond model. The CD curve for NHC-Au-ethyne (Figure 5) relative to A' symmetry is positive and describes a net flux of electronic charge from the alkyne to the metal, whereas the CD curve for the A'' symmetry is negative in the Au-ethyne bond region and indicates a reverse flux from metal to alkyne. The figure shows a pronounced negative peak in the bonding region, meaning that the back-donation constitutes a large component of the gold-carbon interaction. The total CD curve results from the sum of both curves and represent the net acidity, arising from the delicate balance of the opposite donation and back-donation. These components can be quantified through the charge transfer between the alkyne and the L-Au moiety. Ultimately, the back-donation was found to be a large and important component in the gold-substrate bond, even larger than for the other coinage metals, silver and copper. Furthermore, the view that the peculiar catalytic activity of gold in activating multiple C-C bonds may originate from a small, or even negligible, back-donation must be abandoned. In view of these results, also the observation of gold(I) carbonyls as “non classical”, because of the blue-shifted CO stretching frequency, could be confuted, considering that this blueshift is mainly due to the polarization of the C-O bond, which strengthens the CO covalent interaction.

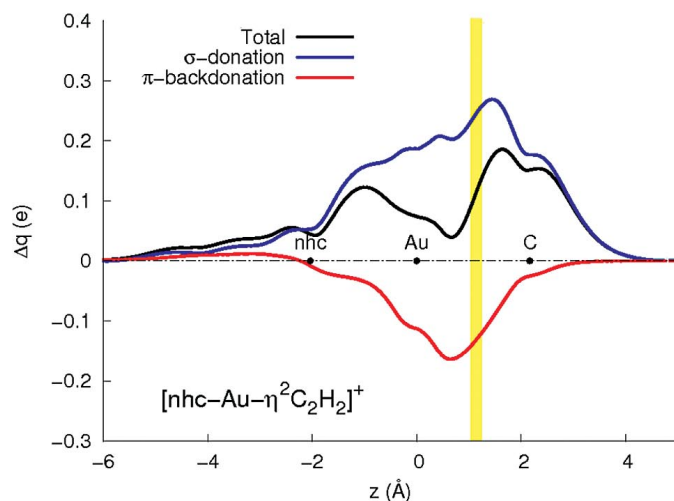


Figure 5. CD curves for the complex NHC-Au-ethyne. The black dots represent the z coordinate of the atoms. The yellow vertical band identifies a suitable boundary between the L-Au and ethyne fragments. Reproduced from ref. 27

These observations are relevant to explain the remarkable catalytic properties of gold in activating multiple C-C bonds: the back-donation is seen to penetrate the external side of the coordinated substrate where the nucleophilic attack takes place.

CD analysis is also helpful to rationalize the notably higher “alkynophilicity” over the “alkenophilicity” of gold(I) complexes.²⁷ Au^I catalysts selectively activate alkynes in presence of alkenes or other functional groups,^{11,28,29} and the origin is kinetic rather than thermodynamic.²⁸ Indeed, computed structural and spectroscopic parameters show a ≈ 10 kcal mol⁻¹ greater stabilization of Au^I-ethylene complex over the one with ethyne, indicating a no preferred bonding to the alkyne, but the discrimination by the nucleophile in attacking the Au(I)-activated electrophiles might be the reason of the observed reactivity.

²⁷ Tarantelli, F., Salvi, N., Belpassi, L. *Chem. Eur. J.* **2010**, *16*, 7231-7240

²⁸ M. García-Mota, N. Cabello, F. Maseras, A.M. Echavarren, J. Pérez-Ramírez, N. Lopez, *ChemPhysChem* **2008**, *9*, 1624 – 1629

²⁹ A. Leyva, X. Zhang, A. Corma, *Chem. Commun.* **2009**, 4947 – 4949

6. Homogeneous gold catalysis

The peculiar reactivity reveals the relevance of gold(I) in organic synthesis and represents a versatile synthetic tool for the formation of carbon-carbon and carbon-heteroatom bonds.

The activation of the π -system towards the nucleophilic attack represents the first step of the general accepted reaction mechanism (Scheme 6), through the coordination of the substrate (becoming more electrophilic) by the gold metal fragment (Scheme 6, Intermediate I). Hereafter the substrate undergoes the nucleophilic attack, with the formation of an organogold intermediate (Scheme 6, intermediate II). In the final step the gold-carbon bond is cleaved by an electrophile, usually a proton (protodeauration), with the regeneration of active species and the formation of the desired product (Scheme 6).³⁰ Additionally, in almost all gold-catalyzed reactions, decay or deactivation of the gold catalyst takes place,³¹ leading to the formation of the inactive species $[L_2Au]^+$, which can undergo the reduction to gold (0).

Among the gold-catalyzed reactions, the intermolecular alkoxylation of alkynes and similar reaction (hydration and hydrophenoxylation) are the oldest applications of cationic gold (I) catalyst: we can affirm that the “gold rush” started with the discovery that gold can catalyze the addition of nucleophiles, like water or alcohol, to alkynes.

Initially Hg(II) salts are used as catalyst³² under strongly acidic conditions, but, due to the quick reduction of Hg(II) catalyst to metallic mercury, which is catalytically inactive, and environmental concerns, alternative catalysts were investigated, such as Au(III)³³ and Pt(II)³⁴ catalysts, resulting unfortunately in less efficiencies. For example,

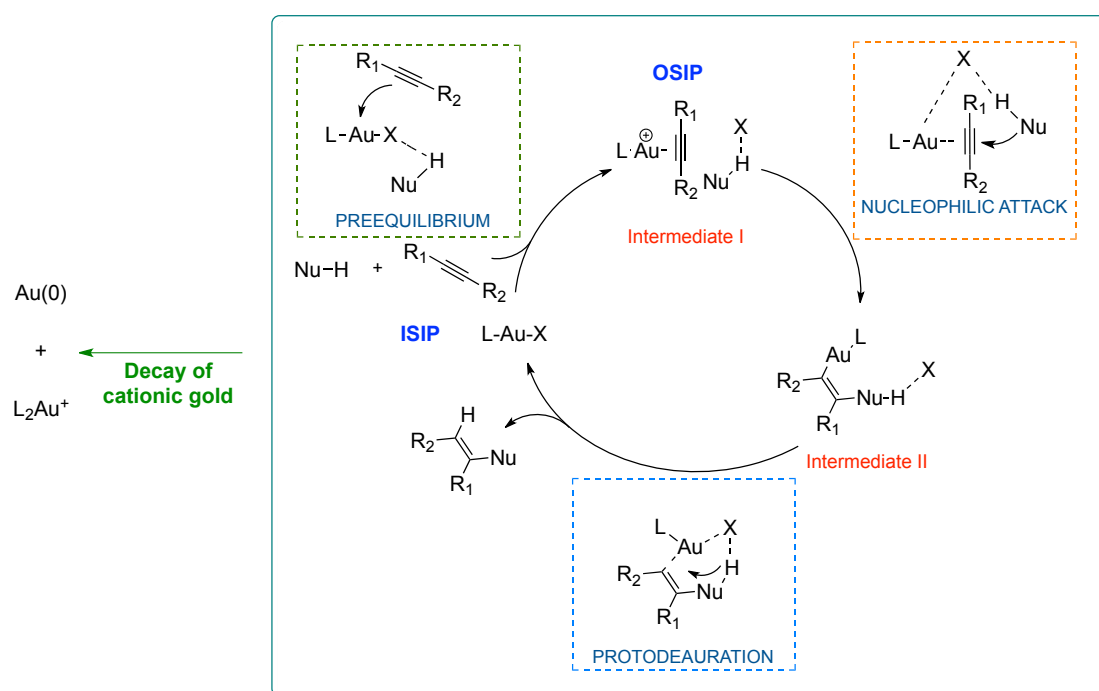
³⁰ a) A. Arcadi, *Chem. Rev.* **2008**, *108*, 3266; b) N. Bongers, N. Krause, *Angew. Chem.* **2008**, *120*, 2208; *Angew. Chem. Int. Ed.* **2008**, *47*, 2178

³¹ Kumar, M., Jasinski, J., Hammond, G.B., Xu, B. *Chem. Eur. J.* **2014**, *20*, 3113

³² Reichert, J. S., Bailey, J. H., Niewland, J. A. *J. Am. Chem. Soc.* **1923**, *45*, 1553

³³ Fukuda, Y., Utimono, K. *J. Org. Chem.* **1991**, *56*, 3729; Fukuda, Y., Utimono, K. *Bull. Chem. Soc. Jpn.*, **1991**, *64*, 2013

³⁴ Hartman, J. W., Hiscox, W. C., Jennings, P. W. *J. Org. Chem.*, **1993**, *58*, 7613; Hartman, J. W., Sperry, L. *Tetrahedron*, **2004**, *45*, 3787

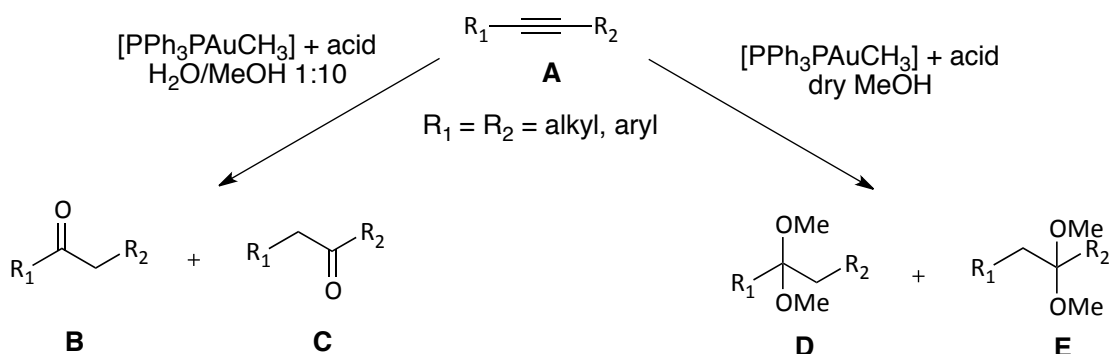


Scheme 6. General accepted reaction mechanism for nucleophilic addition to unsaturated substrate

the alkoxylation or the hydration of non-activated alkynes catalyzed by NaAuCl_4 showed the fast reduction to gold (0) and the need of a higher catalyst loading.

As mentioned above, Teles⁷ and Tanaka⁸ reported the first example of addition of water or alcohol to alkynes catalyzed by air stable gold(I) species $[\text{LAu}]^+$, where L is a phosphine, a phosphite or an arsine, under mild conditions (Scheme 7). When dry methanol is used, the reaction leads to the formation of only the acetals **D** and **E**, whereas in presence of water the ketones **B** and **C** are the only products (Scheme 7). These catalysts achieved turnover numbers up to 10^5 moles of product per mole of catalyst, compared to 100 and 50 moles of product per mole of catalyst of $\text{Hg}(\text{II})$ and $\text{Au}(\text{III})$ salts, respectively.

From the seminal work of Teles, this class of reactions has been deeply studied in order to find highly active catalysts and to shed more light on the reaction mechanism, making nowadays alkoxylation an industrially important process,



Scheme 7. Hydration and alkoxylation of alkynes catalyzed by [(PPh₃)Au]⁺

together with the hydration of alkynes, for the synthesis of carbonyl compounds.³⁵

In general, in the transition metal catalysts the ligands play a major role in the tuning of the activities, as demonstrated by the Buchwald's palladium-catalyzed amination,³⁶ fluorination³⁷ and trifluoromethylation³⁸ of aryl halides or triflates using custom-made dialkylbiphenyl phosphine ligands.

Also in gold catalysis, the activity is crucially influenced by the nature and the properties of the ancillary ligand, but there are no conclusive experimental data on how the ligand affects the kinetic of each stage in the catalytic cycle and, moreover, the same ligand can influence differently, depending on the reaction. Generally, in most of the gold-catalyzed reactions, the electron-deficient phosphine ligands perform better than the electron-rich ones, but in the specific case of the gold-catalyzed hydroamination of allen³⁹ and ring expansion of propargyl cyclopropanols,⁴⁰ reported by Toste and co-workers, the reactions are accelerated by electron deficient phosphine ligands, such as (*p*-CF₃C₆H₄)₃P, whereas with electron-rich phosphine

³⁵ Dorel, R.; Echevarren, A. M. *Chem. Rev.* **2015**, *115*, 9028-9072

³⁶ Fors, B. P.; Watson, D. A.; Biscoe, M. R.; Buchwald, S. L. *J. Am. Chem. Soc.* **2008**, *130*, 13552

³⁷ Watson, D. A.; Su, M.; Teverovskiy, G.; Zhang, Y.; Garcia-Fortanet, J.; Kinzel, T.; Buchwald, S. L. *Science* **2009**, *325*, 1661

³⁸ Cho, E. J.; Senecal, T. D.; Kinzel, T.; Zhang, Y.; Watson, D. A.; Buchwald, S. L. *Science* **2010**, *328*, 1679

³⁹ Wang, Z. J.; Benitez, D.; Tkatchouk, E.; Goddard, W. A. III; Toste, F. D. *J. Am. Chem. Soc.* **2010**, *132*, 13064

⁴⁰ Markham, J. P.; Staben, S. T.; Toste, F. D. *J. Am. Chem. Soc.* **2005**, *127*, 9708

ligands the rate slows down. This example clearly shows the complexity of gold catalysis.

The catalytic performances of gold complexes are affected by the ligand because the electronic structure of the ligand, and in particular its overall electron-donating ability, modulates the acidic character of the metal fragment and affects the stability of the intermediates in the catalytic cycle.

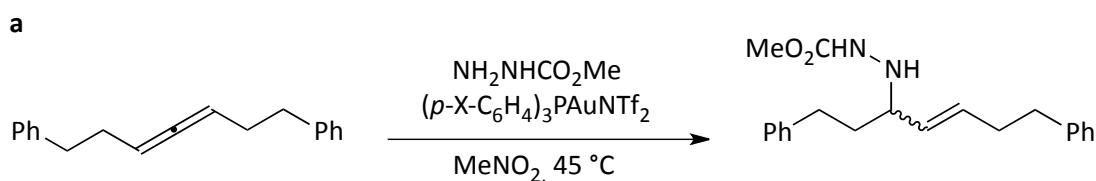
Hammond and Xu⁴¹ found that electron-poor ligands accelerate the nucleophilic attack: they make the gold center more electron-poor itself, which compensates this depletion in electron density pulling the alkyne/alkene electron density and generating a more electrophilic substrate. On the other hand, electron rich ligands accelerate the protodeauration step, supplying electron density to the gold center and promoting the reaction of the organogold intermediate (Scheme 6, Intermediate II) with the electrophile (e.g., H⁺).

In the light of this, we should design of the catalyst, choosing the appropriate ligand, depending on which is the turnover-limiting step of the considered reaction. Usually it is the nucleophilic addition, when the nucleophile is relatively weak (electron-poor amines or amides) or the substrate is a less reactive allene or alkene (type I). A typical example is the hydroamination of allenes, shown in Scheme 8a. Otherwise, when the nucleophile is relatively strong and the substrate is a reactive alkyne, as in case of the cyclization of propargyl amide (Scheme 8b), the turnover-limiting step is the protodeauration (type II).

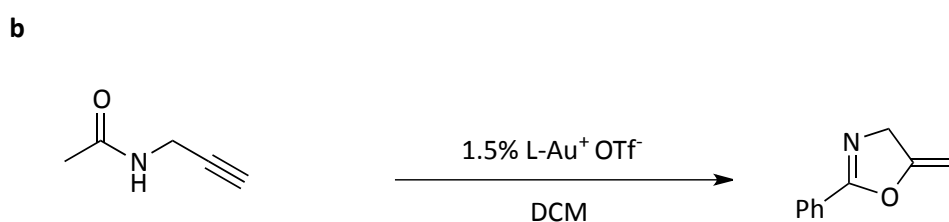
In addition, because for many reactions the decay of cationic gold (Scheme 6) is significant, we also should add special steric handles to the ligands, to enhances the [LAu]⁺ stability and minimize the catalyst deactivation, which reduces the turnover of product formation. An ideal steric handle should be able to embed or surround the cationic gold center, which may slow down catalyst decay.⁴²

⁴¹ Wang, W., Hammond, G.B., Xu, B. *J. Am. Chem. Soc.* **2012**, *134*, 5697

⁴² Kumar, M., Jasinski, J., Hammond, G.B., Xu, B. *Chem Eur J* **2014**, *20*, 3113



rate: $(p\text{-CF}_3\text{-C}_6\text{H}_4)_3\text{P} > (p\text{-Cl-C}_6\text{H}_4)_3\text{P} > (p\text{-H-C}_6\text{H}_4)_3\text{P} > (p\text{-Me-C}_6\text{H}_4)_3\text{P}$



rate: $\text{Cy}_3\text{P} > (p\text{-Me-C}_6\text{H}_4)_3\text{P} > (p\text{-H-C}_6\text{H}_4)_3\text{P} > (p\text{-CF}_3\text{-C}_6\text{H}_4)_3\text{P}$

Scheme 8. Typical type I and type II gold-catalyzed reactions

A further important factor affecting the catalytic performances of the species $[\text{L-Au-S}]^+\text{X}^-$ (L = ligand, S = substrate, X = anion) is the role, played by the anion, which can influence both Intermediate I and Intermediate II of the catalytic cycle (Scheme 6). It is known from the literature that the anion can influence the catalytic activity,⁴³ the regioselectivity⁴⁴ and even the stereoselectivity⁴⁵ of the process. Brouwer and He⁴⁶ reported a strong dependence of the efficiency on the counterion in the hydroamination of 1,3-dienes, using $[\text{PPh}_3\text{AuCl}]$ as pre-catalyst, activated by a silver salt. Another impressive example reported by Toste and co-workers⁴⁵ showed that in the asymmetric hydroalkoxylation of allenes high enantiomeric excess might be obtained with a suitable chiral anion, which can be kept close to the catalytic site modulating the polarity of the solvent.

⁴³ a) Brouwer, C., He, C. *Angew. Chem. Int. Ed.* **2006**, *45*, 1744; *Angew. Chem.* **2006**, *118*, 11, 1776-1779;
 b) Weber, D., Jones, T. D., Adduci, L., Gagné, M. R. *Angew. Chem.* **2012**, *124*, 2502-2506; *Angew. Chem. Int. Ed.* **2012**, *51*, 10, 2452-2456

⁴⁴ Xia, Y., Dudnik, A. S., Gevorgyan, V., Li, Y. *J. Am. Chem. Soc.* **2008**, *130*, 6940

⁴⁵ Hamilton, G. L., Kang, E. J., Mba, M., Toste, F. D. *Science* **2007**, *317*, 496.

⁴⁶ Brouwer, C., He, C. *Angew. Chem.* **2006**, *118*, 1776; *Angew. Chem. Int. Ed.* **2006**, *45*, 1744

The ion pair is crucial in determining the catalytic performances, because it affects the structure and the reactivity of ionic transition metal, therefore a detailed description of the anion-cation structure is essential to understand how the anion actually influences the reaction mechanism.

In recent years, Macchioni and co-workers have extensively used NOE and pulsed field gradient spin-echo NMR spectroscopic techniques to disclose the structure of ion pair in solution,⁴⁷ and they applied the method to several classes of ionic transition metal complexes, differing in metal, ligands and geometry, as in case of organometallic catalysts for alkene polymerization⁴⁸ and alkene/CO copolymerization,⁴⁹ finding a correlation between the ion-pair structure and the reactivity.

More recently, they applied the same method to study the gold ion pairs, in particular the species $[L-Au-S]^+X^-$ (L is the ancillary ligand, S is the unsaturated substrate and X is the counterion), combining advanced NOE NMR spectroscopy measurements with computational studies of the potential energy surfaces and Coulomb potential of the ions, which helps identify the locus of positive charge and thus explains the location of the counterion. In their review⁵⁰ they showed that the ligand crucially influences the role of the ion pair in solution, as well as the nature of the gold-substrate bond, and highlighted the ability to use ligand structure to tune the distribution of cationic charge in gold(I) π -complexes.

Considering a series of triarylphosphine and NHC gold alkene and alkyne complexes, they were able to rationalize the ligand effects on the ion-pair interactions.

⁴⁷ Macchioni, A. *Eur. J. Inorg. Chem.* **2003**, 195 and references therein

⁴⁸ a) C. Zuccaccia, N. G. Stahl, A. Macchioni, M. C. Chen, J. A. Roberts, T. J. Marks, *J. Am. Chem. Soc.* **2004**, *126*, 1448; b) G. Ciancaleoni, N. Fraldi, P. H. M. Budzelaar, V. Busico, A. Macchioni, *Dalton Trans.* **2009**, 8824; c) L. Rocchigiani, G. Bellachioma, G. Ciancaleoni, A. Macchioni, D. Zuccaccia, C. Zuccaccia, *Organometallics* **2011**, *30*, 100; d) L. Rocchigiani, G. Ciancaleoni, C. Zuccaccia, A. Macchioni, *Angew. Chem.* **2011**, *123*, 11956; *Angew. Chem. Int. Ed.* **2011**, *50*, 11752; e) G. Ciancaleoni, N. Fraldi, P. H. M. Budzelaar, V. Busico, A. Macchioni, *Organometallics* **2011**, *30*, 3096

⁴⁹ B. Binotti, G. Bellachioma, G. Cardaci, C. Carfagna, C. Zuccaccia, A. Macchioni, *Chem. Eur. J.* **2007**, *13*, 1570 and references therein

⁵⁰ Zuccaccia, D., Belpassi, L., Macchioni, A., Tarantelli, F. *Eur. J. Inorg. Chem.* **2013**, *2013*, 4121–4135

Three main relative ion-pair orientations were identified for a linear cationic fragment (Figure 6): in the orientations A and C the anion is located near the ligand or the substrate, respectively, and in orientation B the anion is close to the gold atom.

When L is a poorly donating ligand such as triphenylphosphine, the counterion approaches mainly opposite gold, on the side of the alkene/alkyne as in C (Figure 7), that reflects the great electron-withdrawing power of the ligand and leads to an enhanced π -acidity that localizes positive charge on the coordinated π -system.

In contrast, use of the NHC ligand results in the anion-cation orientation A (B is not probable because the aryl moiety with the hindered *ortho*-substituents introduce steric encumbrance above and below the metal center), as shown in Figure 7. This orientation is favored by the excellent electron-donating properties of NHC, which decrease the Lewis acidity of the NHC-Au⁺ moiety, resulting in a not greatly depleted substrate electron density.

The pictures are confirmed by the inspection of the map of the Coulomb potential for the isolated cation (Figure 8), where the blue regions are the most attractive and by theoretical calculations.

They concluded that electronic and steric properties of the ligand finely modulate the exact position of the anion.

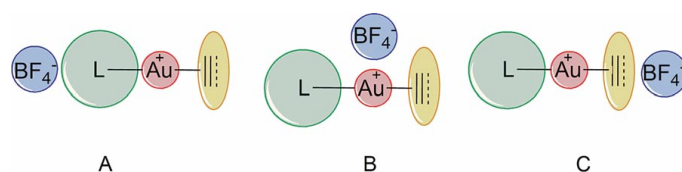


Figure 6. Three orientations, A, B and C, of the counterion in [(L-Au-S)]BF₄ complexes

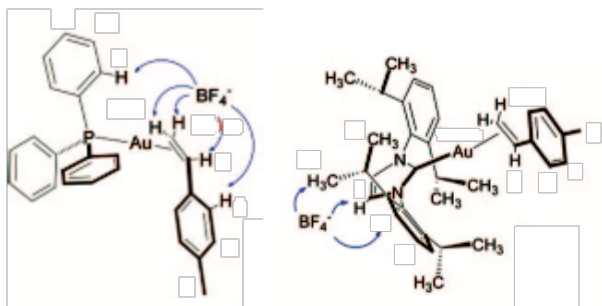


Figure 7. $[(PPh_3)Au(4-Me-styrene)]BF_4$ (left) and $[(NHC)Au(4-Me-styrene)]BF_4$ (right)

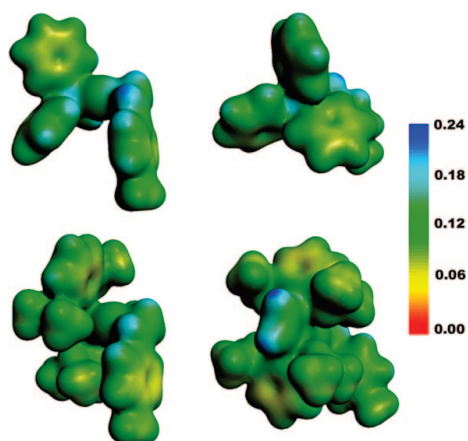


Figure 8. Lateral (left) and back (right) views of the Coulomb potential of $[(PPh_3)Au(4-Me-styrene)]BF_4$ (up) and $[(NHC)Au(4-Me-styrene)]BF_4$ (down), mapped on an electronic isodensity surface

CHAPTER

2

SYNTHESIS OF GOLD(I) COMPLEXES

This chapter describes the synthesis and the properties of gold(I) complexes, whose applications in homogeneous catalysis and in medicinal chemistry will be discussed in detail in the following chapters.

The remarkable advantage of gold(I) compounds are their stability (tolerance to the oxygen, air and water), the easy preparation, storage and handling (both on small and large scale, being crystalline), their solubility in a wide range of solvents, and, finally, their noteworthy activity.

In this thesis, three different class of complexes have been investigated:

- **[(NHC)-Au-X]** type (**1X**), where NHC is 1,3-bis(2,6-di-isopropylphenyl)-imidazol-2-ylidene (**L1**), and X is OTs⁻ (*p*-toluenesulfonate), OMs⁻ (methanesulfonate), NO₃⁻, ClO₄⁻, OTf⁻ (trifluoromethanesulfonate), TFA⁻ (trifluoroacetate), OAc⁻ (acetate), BF₄⁻ (tetrafluoroborate), BAr^{F-} (tetrakis(3,5-bis(trifluoromethyl)phenyl)borate), ptm⁻ (phthalimide), NTf₂⁻ (bis(trifluoromethylsulfonyl)imide) and PFHp⁻ (2,2,3,3,4,4,5,5,6,6,7,7,7-tridecafluoroheptanoate), as depicted in Figure 1;
- **[(PR₃)-Au-X]** type, where PR₃ is PPh₃ (triphenyl phosphine, **L2**), P(^tBu)₃ (*t*-butyl phosphine, **L3**), PAr^F (tris(3,5-bis(trifluoromethyl)phenyl)phosphine, **L4**), phos (tris(2,4-di-*tert*-butylphenyl)phosphite, **L5**), JohnPhos (2(di-*tert*-

- butylphosphino)biphenyl, **L6**) and X is OTs^- (*p*-toluenesulfonate), OTf^- (trifluoromethanesulfonate) and TFA^- (trifluoroacetate), as shown in Figure 2;
- (magi)AuX (**7X**) and [(magi)AuR]BF₄ (**[7R]BF₄**) type, where magi is 1-methyl-3-(2,3,4,6-tetra-*O*-acetyl- β -D-glucopyranosyl)imidazolyldiene (**L7**), X is chloride or 2-mercaptopyrimidine, and R is PPh₃ or magi, as illustrated in Figure 3.

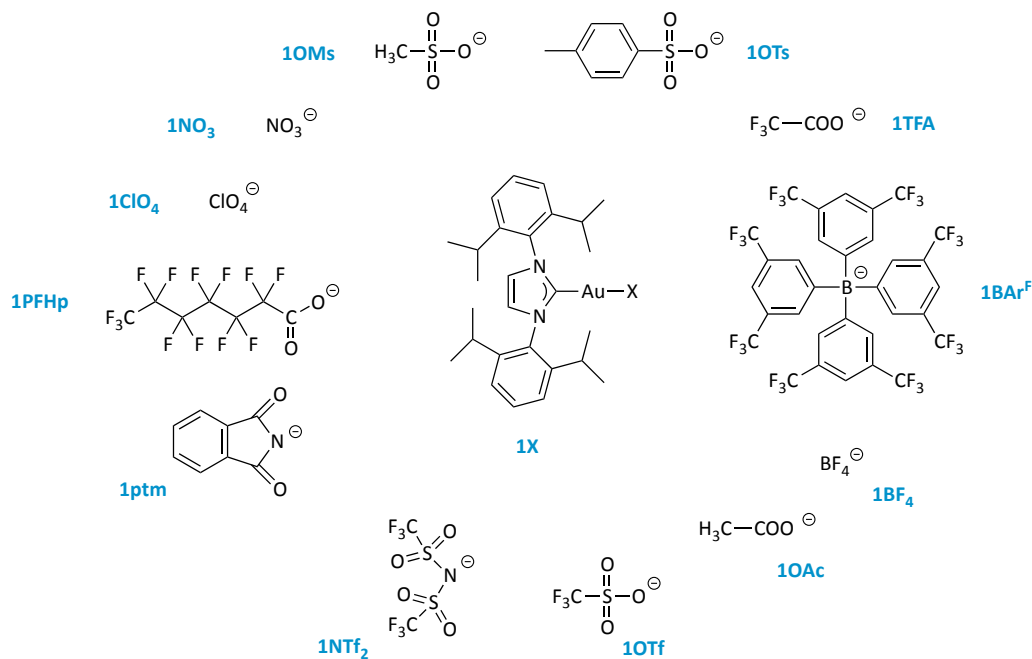
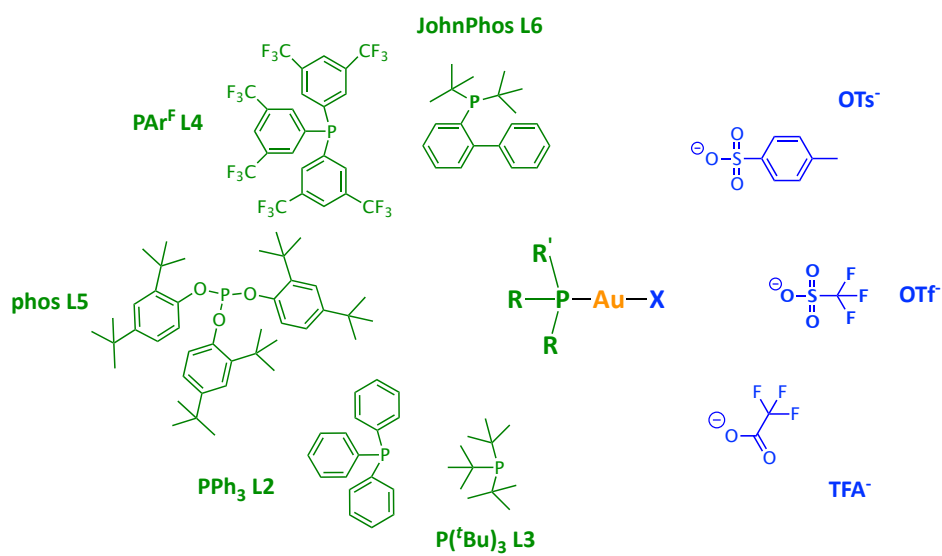


Figure 1. [(NHC)AuX] (**1X**) complexes

Figure 2. [(PR₃)AuX] complexes

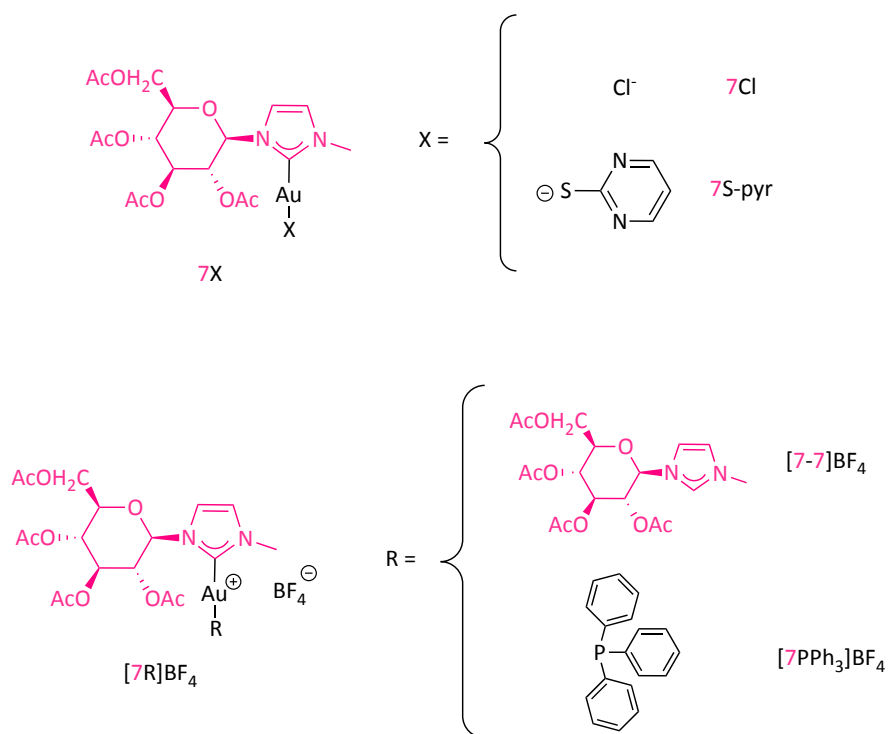
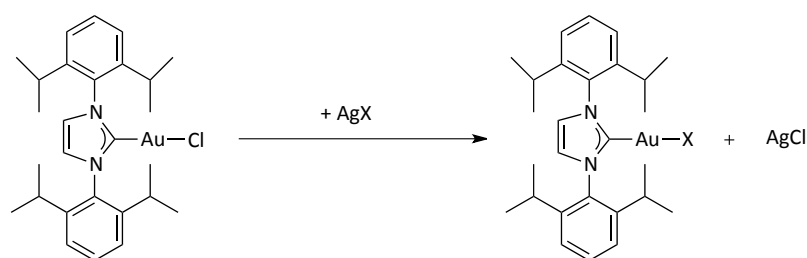


Figure 3. $[(magi)AuX]$ ($7X$) and $[(magi)AuR]BF_4$ ($[7R]BF_4$) complexes

1. [(NHC)AuX] complexes

Gold compounds were synthesized according to literature procedure (see **Experimental Section**). As described by Gagosz,¹ the complex [(NHC)-Au-Cl] (**1Cl**) was reacted at room temperature in an organic solvent with a slight excess of the appropriate silver salt as halide abstractor (Scheme 1).



Scheme 1. Synthesis of [(NHC)AuX] complexes

The complexes **1OTs**, **1TFA**, **1BAR^F**, **1OMs**, **1NO₃**, **1ClO₄**, and **1PFHp** (Figure 1) have been synthesized for the very first time, whereas **1NTf₂**,¹ **1OAc**,² **1OTf**,³ and **1BF₄**⁴ (Figure 1) have been prepared according to the literature. In particular, in order to prepare **1PFHp**, also the corresponding silver salt has been synthesized, following a different procedure from that reported in literature (see **Experimental Section**).

In case of BF₄⁻ and BAR^{F-} anions, the [(NHC)AuX] complexes are not stable enough and [(NHC)Au(η²-3-hexyne)]X complexes have been used as catalysts. Finally, **1ptm** (Figure 1) was prepared by the exchange reaction between the parent [(NHC)Au(η²-3-hexyne)]BF₄ (**1BF₄**) and phthalimide potassium salt in CH₂Cl₂, differently from the procedure reported in the literature.⁵

¹ Ricard, L.; Gagosz, F. *Organometallics* **2007**, *26*, 4704–4707

² Iglesias, A. Muniz, K. *Chem. Eur. J.* **2009**, *15*, 10563–10569

³ Tsui, E.Y.; Müller, P.; Sadighi, J. P. *Angew. Chem.* **2008**, *120*, 9069–9072; *Angew. Chem., Int. Ed.* **2008**, *47*, 8937–8940

⁴ Ciancaleoni, G. Biasolo, L. Bistoni, G. Macchioni, A. Tarantelli, F. Belpassi, L. Zuccaccia, D. *Organometallics* **2013**, *32*, 4444–4447

⁵ Han, J.; Shimizu, N.; Lu, Z.; Hammond, G. B.; Xu, B. *Org. Lett.* **2014**, *16*, 3500–3503

All complexes, isolated as microcrystalline compounds in good yield (above 85%), were proven to be stable toward air and moisture and were fully characterized (see **Experimental Section**). All the proton and carbon resonances belonging to the different fragments were assigned through ^1H and ^{13}C NMR spectroscopy (see **Experimental Section**).

The occurred formation of the final complex is confirmed by ^{13}C NMR spectra, displaying the characteristic signals of the carbene carbon bound to a cationic gold(I) with values falling in the range between 159.4 and 178.60 ppm, shifted with respect to that of [(NHC)-Au-Cl].⁶ As an example, the ^{13}C NMR spectra for the complex **10Ts** and its precursor **1Cl** are reported below (Figure 4).

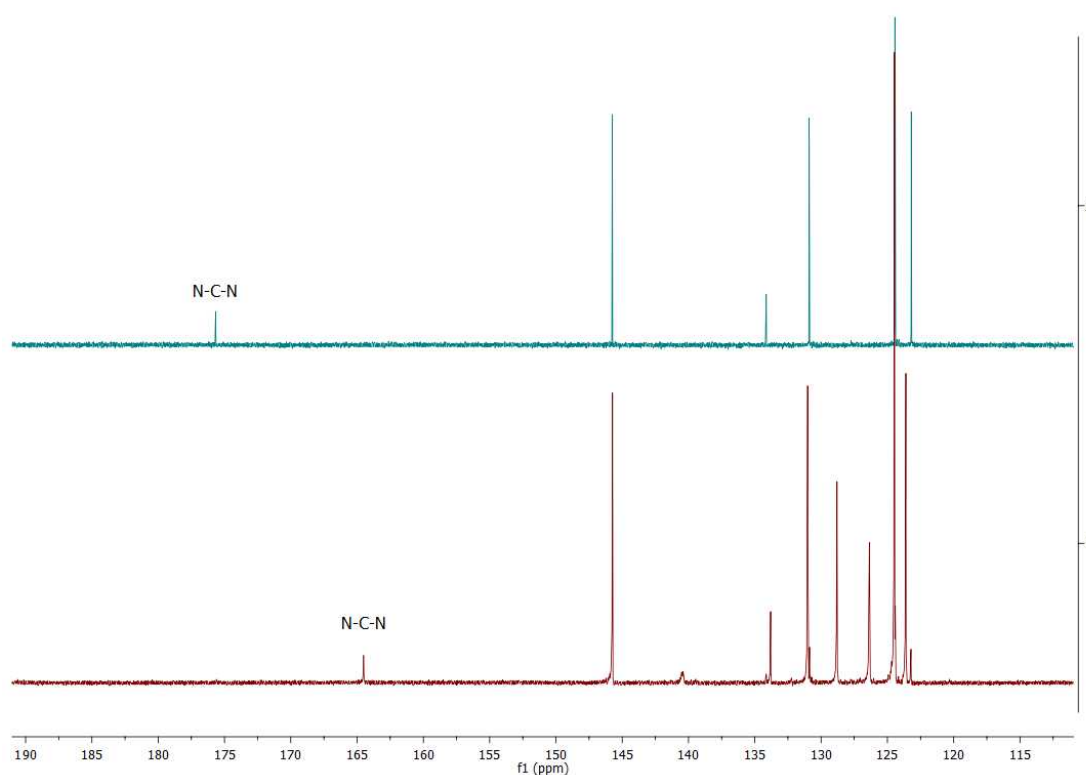


Figure 4. ^{13}C NMR stacked spectra of **1Cl** (up) and **10Ts** (down)

Furthermore, ^{19}F NMR spectra were collected for all F-containing complexes.

⁶ de Fremont, P.; Scott, N. M.; Stevens, E. D.; Nolan, S. P. *Organometallics* **2005**, *24*, 2411–2418

Suitable crystals for X-ray structure determination were grown from complexes **1OTs** and **1PFHp** by slow evaporation of $\text{CH}_2\text{Cl}_2/n$ -hexane and their solid-state structures were solved (see **Experimental Section**). The structures confirm their identity as coordinated NHC-Au(I) complexes (Figure 5 – 6). A linear environment of Au atom is found, with the C-Au-O bond angle very close to 180° . In the N-heterocyclic carbene ligand of both the complexes, the encumbered aryl groups are almost perpendicular with respect to the plane of the imidazole group in order to have good isopropyl $\text{CH}\cdots\text{Au}$ intramolecular interactions. In **1OTs** the intramolecular isopropyl $\text{CH}\cdots\text{Au}$ distances are longer than in **1PFHp**, probably due to the participation of tosyl oxygen atoms in weak intramolecular $\text{CH}\cdots\text{O}$ interactions.

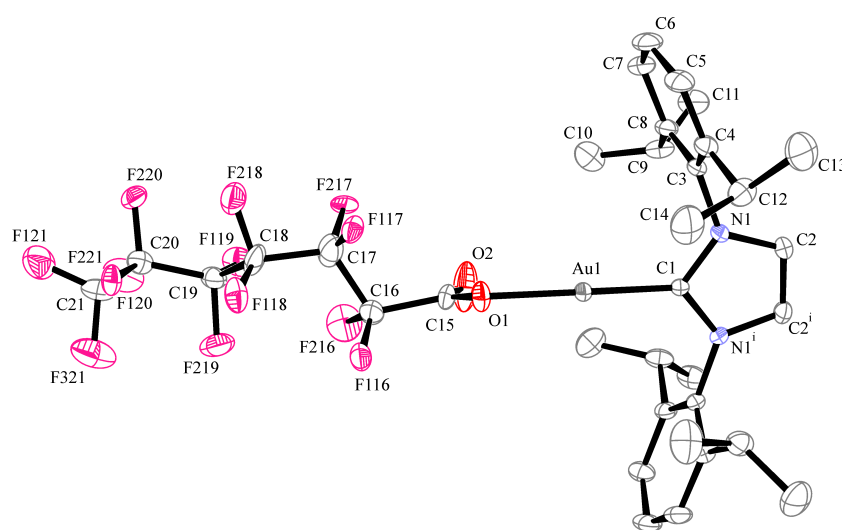


Figure 5. Ortep view of the molecular complex **1PFHp**

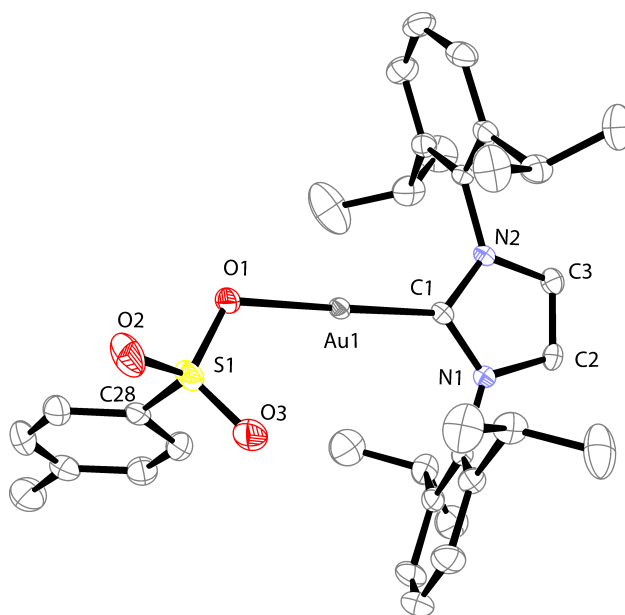


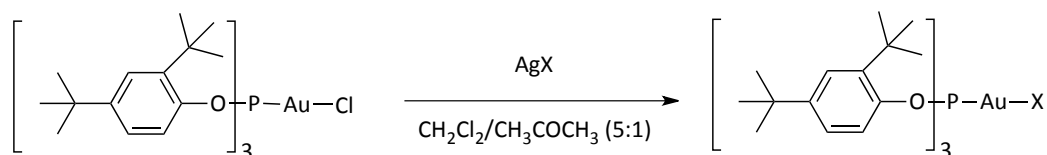
Figure 6. Ortep view of the molecular complex 10Ts

2. [(PR₃)AuX] complexes

Among the [(PR₃)AuX] complexes, [(phos)AuOTs] (**5OTs**) and [(phos)AuTFA] (**5TFA**) have been isolated in good yields, whereas the remaining complexes (**2-4OTs**, **2-4TFA**, **6OTs** and **6TFA**) were generated *in situ*, due to their limited stability in ordinary conditions.

All the complexes have been synthesized through a metathesis reaction between the chloride precursor and a slightly excess (1.5 eq) of the appropriate silver salt.

The isolated catalysts, **5OTs** and **5TFA**, have been prepared according to a published method for phosphine gold(I) complexes,⁷ as shown in Scheme 2.



Scheme 2. Synthesis of [(PR₃)AuX] complexes

In particular, **5OTs** complex was prepared for the very first time, and both catalysts have been fully characterized by homo- and hetero-nuclear NMR spectroscopy. The occurred formation of the desired products has been confirmed by the presence of the signals relative to tosylate anion in the ¹H NMR spectrum, in addition to a significant shift observed for the phosphorus resonance, moving from 100.8 ppm, for the chloride precursor, to 85.9 ppm and 88.9 ppm for the final complexes, **5OTs** and **5TFA**, respectively. In case of **5TFA**, the appearance of a signal at -73.8 ppm in the ¹⁹F NMR spectrum, relative to CF₃CO₂⁻ moiety, further corroborated the formation of the product. For an illustrative purpose, a section of ¹H NMR spectrum for **5OTs** is shown below (Figure 7).

⁷ Biasiolo, L.; Del Zotto, A.; Zuccaccia, D. *Organometallics* **2015**, *34*, 1759–1765

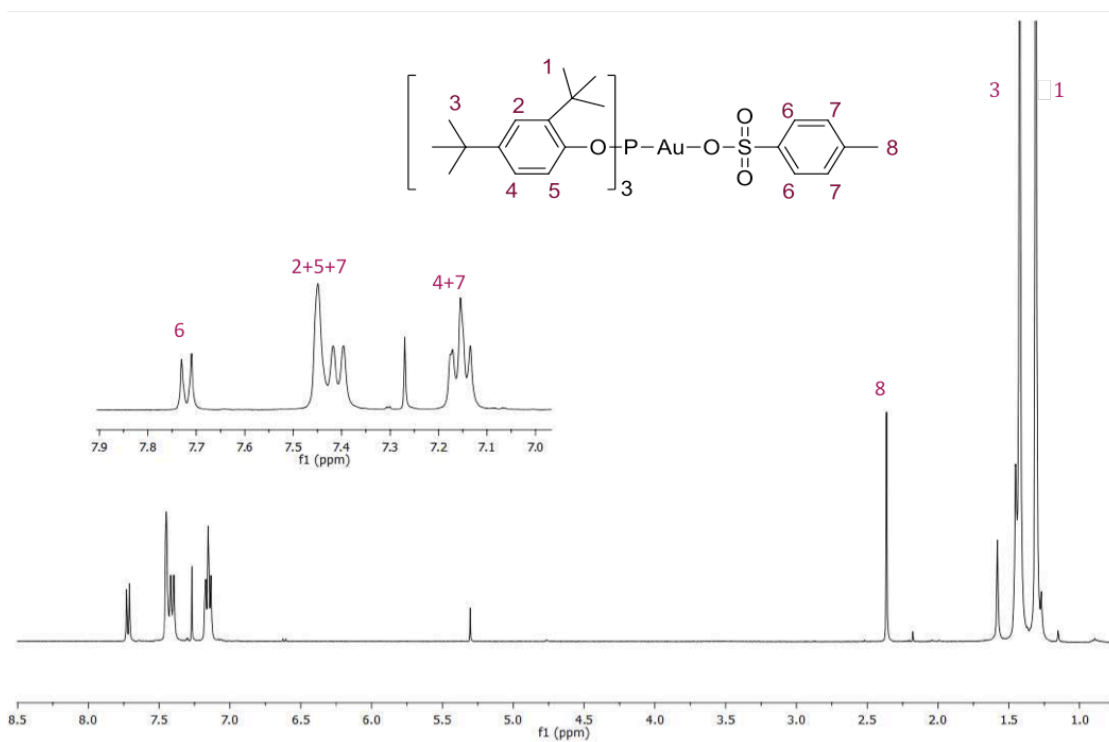


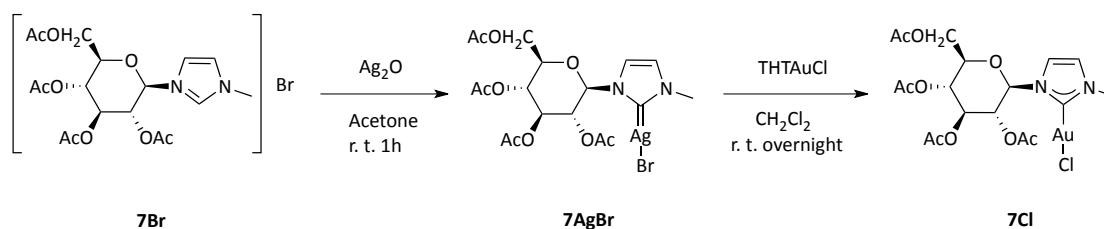
Figure 7. ¹H NMR spectrum section for 5OTs

The catalysts **2-4OTs**, **6OTs** and **2-6OTf** have been generated *in situ* in a NMR tube, by mixing equimolar amounts of precursor **2-4Cl** or **6Cl** with the appropriate silver salt.

3. (magi)AuX and [(magi)AuR]BF₄ complexes

Magi gold(I) complexes have been synthesized for the very first time, according to the following steps. First of all, a glucopyranoside-incorporated NHC precursor, 1-methyl-3-(2,3,4,6-tetra-O-acetyl-β-D-glucopyranosyl)imidazolium bromide (**7Br**), was synthesized by the reaction of 2,3,4,6-tetra-O-acetyl-R-D-glucopyranosyl bromide and 1-methylimidazole in acetonitrile, as reported in literature.⁸

In the second step the corresponding Ag-complex (**7AgBr**) was prepared from Ag₂O, to act as starting materials for transmetalation⁸ (Scheme 3).



Scheme 3. Synthesis of carbene gold(I) complex, 7Cl

The formation of the silver complex (**7AgBr**) has been confirmed by the disappearance of the signal for the proton at the 2-position in the imidazole ring. Later on, by adapting the synthetic procedure reported by Kinoshita *at al.* on iridium (III) complexes,⁸ the reaction of **7AgBr** with gold(I) precursor, THTAuCl (THT = tetrahydrothiophene), in dichloromethane at room temperature overnight, (Scheme 3) led to transmetalation to gold and afforded to the formation of the carbene gold(I) complex, **7Cl**, which was assessed by ¹H and ¹³C NMR spectroscopy. The singlet corresponding to the imidazole proton in 2-position disappeared, and a significant shift in the signal of the C2 carbon atom from $\delta = 138.4$ ppm in the imidazolium salt to $\delta = 172.4$ ppm in the complex was observed, as shown in Figure 8.

⁸ Nishioka, T., Shibata, T., Kinoshita, I., *Organometallics* **2007**, *26*, 1126-1128

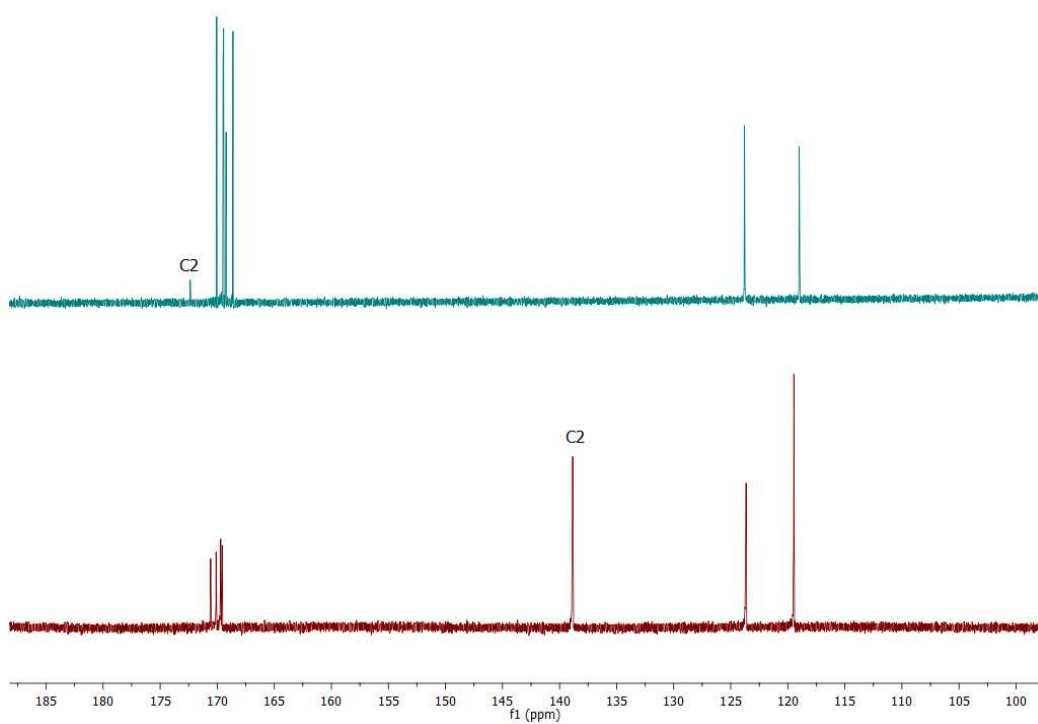
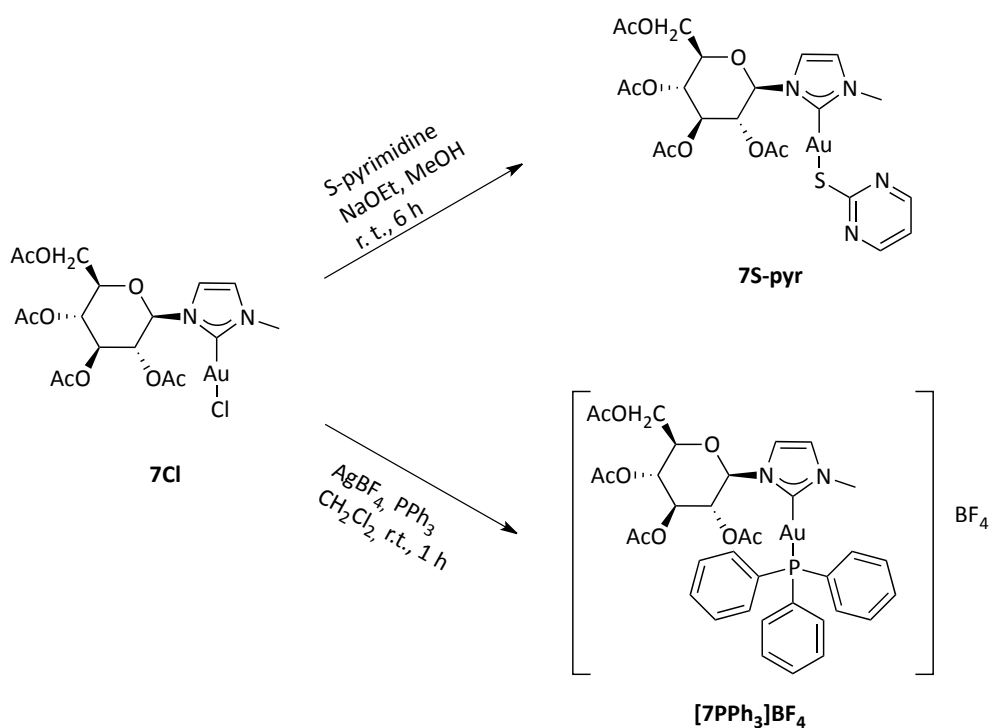


Figure 8. ¹³C NMR stacked spectra of 7Cl (up) and 7Br (down)

Starting from **7Cl**, the gold derivatives, **7S-pyr** and **[7PPh₃]BF₄** were isolated in pure form in yields of 80 – 90% (Scheme 4), by modifying literature procedures.^{9,10}

⁹ Bertrand, B., Bodio, E., Richard, P., Picquet, M., Le Gendre, P., Casini, A., *J. Organom. Chem.* **2015**, 775, 124-129

¹⁰ Shuh, E., Plugger, C., Citta, A., Folda, A., Rigobello, M. P., Bindoli, A., Casini, A., Mohr, F., *J. Med. Chem.* **2012**, 55, 5518-5528



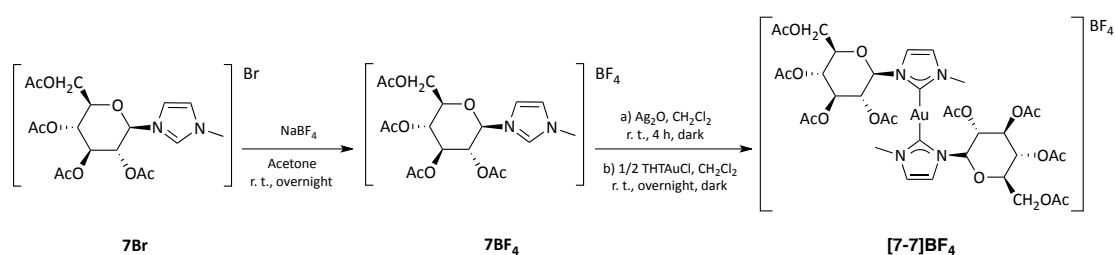
Scheme 4. Synthesis of carbene gold(I) derivatives, 7S-pyr and [7PPh₃]BF₄

The thiolato complex **7S-pyr** was prepared by the reaction of the glucopyranoside-incorporated NHC gold chloro complex (**7Cl**) with the sodium salt of 2-mercaptopyrimidine, *in situ* generated (Scheme 4).¹⁰

The resulting Au(I) complex **7S-pyr** was characterized by ¹H NMR spectroscopy and elemental analysis, confirming its identity.

The unsymmetrical cationic carbene/phosphine complex, **[7PPh₃]BF₄** was also synthesized in good yield, by reacting **7Cl** with triphenylphosphine, in the presence of silver tetrafluoroborate, as a chloride abstractor (Scheme 4).⁹ The coordination of triphenylphosphine ligand was assessed by ¹H NMR, with appearance of the PPh₃ signals in the aromatic region. Additionally, in ¹³C{¹H} NMR the signal corresponding to the carbene was shifted from 172.4 ppm to 185.1 ppm, as expected for coordination to a cationic Au(I) center.

In order to obtain the cationic bis-carbene metal derivative, a classical method¹¹ was used, starting from salts containing a non-halide anion, which is then reacted with silver oxide yielding the silver bis-carbene complex, acting as a halide abstractor and ligand transfer agent. **7Br** was thus reacted quantitatively with an excess of sodium tetrafluoroborate, leading to the formation of the tetrafluoroborate analogue, **7BF₄**. The latter was reacted with silver(I) oxide and half an equivalent of THTAuCl to afford the cationic bis-carbene complex, **[7-7]BF₄**, in 60% yield (Scheme 5). Its formation was confirmed by ¹³C NMR spectroscopy, where the carbene gave a signal at 182.95 ppm, characteristic of this type of cationic Au(I) complexes.¹²



Scheme 5. Synthesis of bis-carbene gold(I) derivative, [7-7]BF₄

¹¹ Lin, I.J.B., Vasam, C.S. *Can. J. Chem.* **2005**, *83*, 812-825

¹² W. Liu, K. Bendsdorf, M. Proetto, A. Hagenbach, U. Abram, R. Gust, *J. Med. Chem.* **2012**, *55*, 3713-3724

4. Experimental section

4.1. General procedures and materials

All reagents and solvents were obtained from commercial sources and were used without any further purification. The products were characterized by ^1H , ^{19}F , ^{31}P and ^{13}C NMR spectroscopies. The spectra were recorded with a Bruker AVANCE Ultra ShieldTM 400 spectrometer. Referencing is relative to TMS (^1H and ^{13}C), CCl_3F (^{19}F) and H_3PO_4 (^{31}P). The elemental analyses were carried out with a Carlo Erba 1106 elemental analyzer.

4.2. Synthesis of complexes

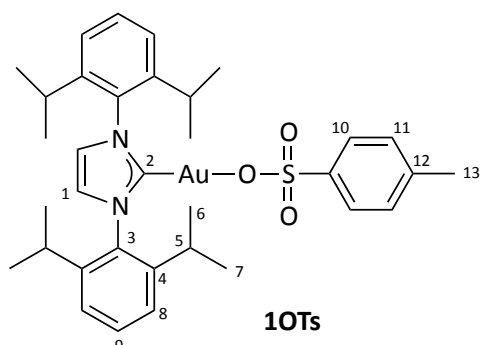
HAuCl_4 , tetrahydrothiophene (THT) and 3-hexyne, silver *p*-toluenesulfonate (AgOTs), silver trifluoroacetate (AgTFA), sodium tetrakis[3,5-bis(trifluoromethyl)phenyl]borate (NaBAR^{F}), silver methanesulfonate (AgOMs), silver nitrate (AgNO_3), silver perchlorate (AgClO_4), silver tetrafluoroborate (AgBF_4), phthalimide potassium salt (Kptm) and 2-mercaptopyrimidine were purchased from Ricci Chimica and Sigma-Aldrich. 1,3-bis(diisopropylphenyl)imidazolium chloride (NHC),¹³ (THT)AuCl¹⁴, **1Cl**¹⁵, **5Cl**,¹⁶ **7Br**,⁸ **7AgBr**,⁸ **1NTf₂**¹, **1OAc**,² **1OTf**³ and **1BF₄**⁴ were synthesized according to the literature.

¹³ Hintermann L., *Beilstein Journal of Organic Chemistry* **2007**, 3, No. 22, 1-5

¹⁴ Uson, R. Laguna, A. Laguna M., *Inorg. Syn.* **1989**, 26, 85

¹⁵ Collado, A. Gómez-Suárez, A. Martín, A. R.. Slawin, A. M. Z Nolan, S. P. *Chem. Commun.* **2013**, 49, 5541-5543

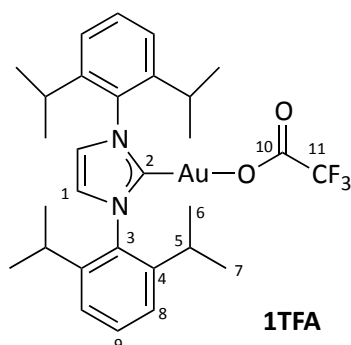
¹⁶ Wang, M.Z.; Wong, M.K.; Che, C.M. *Chem. Eur. J.* **2008**, 14, 8353 – 8364



1OTs. (NHC)AuCl (100 mg, 0.161 mmol) was dissolved in the minimal amount of CH₂Cl₂. Subsequently, 1.1 eq (0.177 mmol) of AgOTs was added, leading to the precipitation of AgCl. After 1 h at room temperature, the reaction mixture was filtered on Celite® pad, washed with 3x1 mL of CH₂Cl₂, concentrated under vacuum and then n-hexane (4mL) was added, resulting in the formation of precipitate. The resulting solid was filtered off and washed with 3x2 mL of n-hexane. Then dried under vacuum to afford the product as a white powder (yield 93%). Anal. Calcd. for C₃₄H₄₄AuN₂O₃S (757.76): C, 53.89; H, 5.85; Au, 25.99; N, 3.70; O, 6.33; S, 4.23. Found: C, 53.91; H, 5.84; N, 3.6.

¹H NMR (400 MHz, CDCl₃, 298 K): δ (ppm) 7.55 (t, 2H, $J_3^{\text{HH}} = 7.8$, H9), 7.39 (d, 2H, $J_3^{\text{HH}} = 7.3$, H10), 7.31 (d, 4H, d, 2H, $J_3^{\text{HH}} = 7.9$, H8), 7.21 (s, 2H, H1), 6.98 (d, 2H, $J_3^{\text{HH}} = 7.4$, H11), 2.47 (sept, 4H, $J_3^{\text{HH}} = 6.8$, H5), 2.32 (s, 3H, H13), 1.29 (d, 12H, $J_3^{\text{HH}} = 6.8$, H6), 1.21 (d, 12H, $J_3^{\text{HH}} = 6.8$, H7).

¹³C{¹H}-NMR (400 MHz, CDCl₃, 298 K): δ (ppm) 164.56 (s, C2), 145.69 (s, C4), 133.86 (s, C9), 131.12 (s, C3), 128.87 (s, C_{Ar}-OTs), 126.42 (s, C_{Ar}-OTs), 124.57 (s, C1), 123.59 (s, C8), 123.20 (s, C_{Ar}-OTs) 29.05 (s, C5), 24.32 (d, C6-7), 21.58 (s, CH₃-OTs).

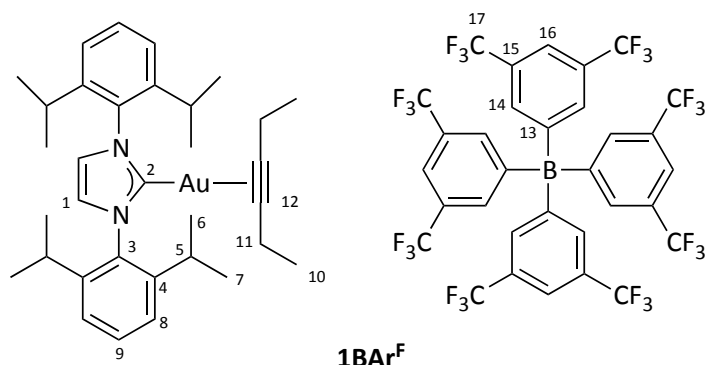


1TFA. (NHC)AuCl (100 mg, 0.161 mmol) was dissolved in the minimal amount of CH₂Cl₂. Subsequently, 1.1 eq (0.177 mmol) of AgOTs was added, leading to the precipitation of AgCl. After 1 h at room temperature, the reaction mixture was filtered on Celite® pad, washed with 3x1 mL of CH₂Cl₂, concentrated under vacuum and then n-hexane (4mL) was added, resulting in the formation of precipitate. The resulting solid was filtered off and washed with 3x2 mL of n-hexane. Then dried under vacuum to afford the product as a white powder (yield 87%). Anal. Calcd. for C₂₉H₃₇AuF₃N₂O₂ (699.58) C, 49.79; H, 5.33; Au, 28.16; F, 8.15; N, 4.00; O, 4.57. Found: C, 49.82; H, 5.84; N, 3.86.

¹H NMR (400 MHz, CD₂Cl₂, 298 K): δ (ppm) 7.58 (t, 2H, $J_3^{\text{HH}} = 7.8$, H9), 7.37 (d, 4H, $J_3^{\text{HH}} = 7.7$, H8), 7.28 (s, 2H, H1), 2.56 (sept, 4H, $J_3^{\text{HH}} = 6.9$, H5), 1.35 (d, 12H, $J_3^{\text{HH}} = 6.8$, H6), 1.24 (d, 12H, $J_3^{\text{HH}} = 6.8$, H7).

¹³C{¹H}-NMR (400 MHz, CD₂Cl₂, 298 K): δ (ppm) 166.01 (s, C2), 162.11 (bs, C15), 146.46 (s, C4), 134.44 (s, C9), 131.27 (s, C3), 124.85 (s, C1), 124.37 (s, C8), 116.50 (s, C14), 29.49 (s, C5), 24.52 (d, C6-7).

¹⁹F NMR (400 MHz, CD₂Cl₂, 298 K): δ (ppm) -73.89 (s, CF₃).

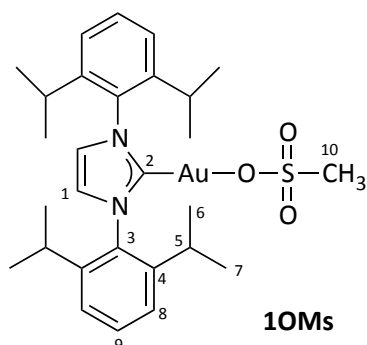


1BAr^F. (NHC)AuCl (49.7 mg, 0.08 mmol) and 3-hexyne (14 μ L, 0.12 mmol) were added in a Schlenk tube in 1 mL of CH₂Cl₂. Subsequently AgBF₄ (23 mg, 0.12 mmol) was added. The reaction mixture was stirred at room temperature for 15 min observing the precipitation of AgCl. The reaction mixture was filtered on Celite[®] pad, washed with 3x1 mL of CH₂Cl₂, concentrated under vacuum and then NaBAr^F (77.8 mg, 0.09 mmol) was added, resulting in the formation of a thin new precipitate. The reaction mixture was filtered again on Celite[®] pad, washed with 3x1 mL of CH₂Cl₂, concentrated under vacuum and then n-pentane (4mL) was added, resulting in the formation of precipitate. The resulting solid was filtered off and washed with 3x2 mL of n-pentane. Then dried under vacuum to afford the product as a mild-yellow powder (yield 85%). Anal. Calcd. for C₆₅H₅₈AuBF₂₄N₂₂ (1530.91): C, 51.00; H, 3.82; Au, 12.87; B, 0.71; F, 29.78; N, 1.83. Found: C, 51.02; H, 3.84; N, 1.82.

¹H NMR (CD₂Cl₂, 400 MHz, 298 K): δ (ppm) 7.72 (bs, 8H, H14), 7.57 (t, $J_3^{\text{HH}} = 7.8$ Hz, 2H, H9), 7.56 (bs, 4H, H16), 7.43 (s, 2H, H1), 7.37 (d, $J_3^{\text{HH}} = 7.6$ Hz, 4H, H8), 2.51 (sept, $J_3^{\text{HH}} = 6.8$ Hz, 4H, H5), 2.30 – 2.07 (m, $J_3^{\text{HH}} = 7.3$ Hz, 4H, H11), 1.29 (d, $J_3^{\text{HH}} = 6.8$ Hz, 12H, H6 or H7), 1.26 (d, $J_3^{\text{HH}} = 6.8$ Hz, 12H, H6 or H7), 0.61 (t, $J_3^{\text{HH}} = 7.4$ Hz, 6H, H10).

¹³C{¹H}-NMR (400 MHz, CD₂Cl₂, 298 K): δ (ppm) 178.60 (s, C2), 162.5 (m, C13), 146.49 (s, C4), 135.50 (s, C14), 133.61 (s, C3), 132.22 (s, C9), 129.44 (m, C15), 126.65 (s, C17), 125.33 (bs, C1 and C8), 118.15 (s, C16), 87.92 (s, C12), 29.58 (s, C5), 24.98 (d, C6-7), 24.36 (d, C6-7), 15.34 (s, C11), 13.65 (s, C10).

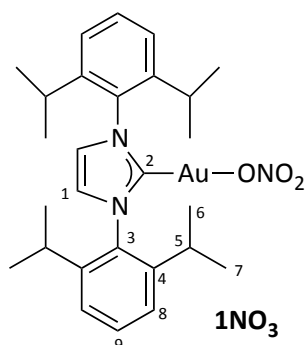
¹⁹F NMR (400 MHz, CD₂Cl₂, 298 K): δ (ppm) -62.84 (s, CF₃).



1OMs. [(NHC)-Au-Cl] (100 mg, 0.161 mmol) was dissolved in the minimal amount of acetone and AgOMs (1.2 eq, 0.322 mmol) was added, leading to the precipitation of AgCl. After stirring 1 h at room temperature, the reaction mixture was filtered on Celite® pad and dried under vacuum to afford an oil. The latter was dissolved in the minimal amount of CH₂Cl₂, and then *n*-hexane (4mL) was added, resulting in the formation of a precipitate. The solid was filtered off, washed with 3x2 mL of *n*-hexane, and then dried under vacuum to afford the product as a white powder (yield 93%). Anal. Calcd. for C₂₈H₃₉AuN₂O₃S (680.65): C, 49.41; H, 5.78; Au, 28.94; N, 4.12; O, 7.05; S, 4.71. Found: C, 49.45; H, 5.81; N, 4.15.

¹H NMR (400 MHz, CD₂Cl₂, 298 K): δ (ppm) 7.57 (t, 2H, ³J_{HH} = 7.8 Hz, H9), 7.36 (d, 4H, ³J_{HH} = 7.8 Hz, H8), 7.29 (s, 2H, H1), 2.52 (sept, 4H, ³J_{HH} = 6.9 Hz, H5), 2.38 (s, 3H, H10) 1.35 (d, 12H, ³J_{HH} = 6.9 Hz, H6), 1.23 (d, 12H, ³J_{HH} = 6.9 Hz, H7).

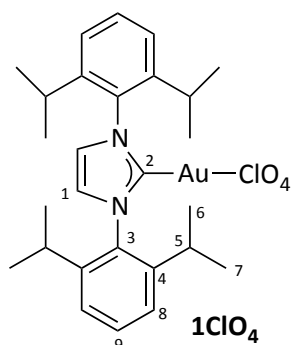
¹³C{¹H}-NMR (100 MHz, CD₂Cl₂, 298 K): δ (ppm) 164.26 (s, C2), 146.16 (s, C4), 134.15 (s, C9), 131.24 (s, C3), 124.71 (s, C1), 124.18 (s, C8), 39.45 (s, CH₃-OMs), 29.24 (s, C5), 24.45 (d, C6), 24.21 (d, C7).



1NO₃. A solution of AgNO₃ (1.2 eq, 0.193 mmol) in H₂O (2 mL) was added to a solution of [(NHC)-Au-Cl] (100 mg, 0.161 mmol) in CH₂Cl₂ (4 mL) leading to the precipitation of AgCl. After stirring 1 h at room temperature, the organic phase was recovered, washed with water (3x2 mL), dried with Na₂SO₄, filtered on Celite® pad and, finally, concentrated under vacuum. Addition of *n*-hexane (4mL) resulted in the formation of a precipitate, which was filtered off, washed with *n*-hexane (3x2 mL), and then dried under vacuum to afford the product as a white powder (yield 93%). Anal. Calcd. for C₂₇H₃₆AuN₃O₃ (647.56): C, 50.08; H, 5.60; Au, 30.42; N, 6.49; O, 7.41. Found: C, 50.04; H, 5.58; N, 6.51.

¹H NMR (400 MHz, CD₂Cl₂, 298 K): δ (ppm) 7.57 (t, 2H, ³J_{HH} = 7.6 Hz, H9), 7.36 (d, 4H, d 2H, ³J_{HH} = 7.6 Hz, H8), 7.29 (s, 2H, H1), 2.55 (sept, 4H, ³J_{HH} = 6.8 Hz, H5), 1.35 (d, 12H, ³J_{HH} = 6.8 Hz, H6), 1.23 (d, 12H, ³J_{HH} = 6.8 Hz, H7).

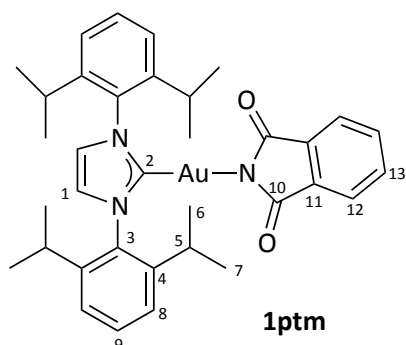
¹³C{¹H}-NMR (100 MHz, CD₂Cl₂, 298 K): δ (ppm) 164.92(s, C2), 146.39 (s, C4), 134.39 (s, C9), 131.44 (s, C3), 124.85 (s, C1), 124.41 (s, C8), 29.28 (s, C5), 24.78 (d, C6), 24.62 (d, C7)



1ClO₄. AgClO₄ (42 mg, 0.2 mmol) was poured into a Schlenk tube containing CH₂Cl₂ (2 mL) and CH₃OH (0.1 mL), then was added [(NHC)-Au-Cl] (62 mg, 0.10 mmol). The reaction mixture was stirred at room temperature for 30 minutes, then it was brought to dryness under vacuum and CH₂Cl₂ (0.5 mL) was added. The mixture was filtered on Celite® pad, dried under vacuum and the resulting solid was dissolved in the minimum amount of CH₂Cl₂. The addition of *n*-pentane (4 mL) resulted in the formation of a precipitate. The solid was filtered off, washed with *n*-pentane (3x2 mL), and then dried under vacuum to afford the product as a white powder (yield 76%). Anal. Calcd. for C₂₇H₃₆AuClN₂O₄ (684.20): C, 47.34; H, 5.30; Au, 28.75; Cl, 5.18; N, 4.09; O, 9.34. Found: C, 47.45; H, 5.70; N, 4.20.

¹H NMR (200 MHz, CD₂Cl₂, 298 K): δ (ppm) 7.59 (t, 2H, *J*_{3^{HH}} = 8.1, H9), 7.38 (s, 2H, H1), 7.33 (d, 3H, *J*_{3^{HH}} = 8.1, H8), 2.50 (set, 4H, *J*_{3^{HH}} = 7.0, H5), 1.33 (d, 12H, *J*_{3^{HH}} = 6.9, H6), 1.23 (d, 12H, *J*_{3^{HH}} = 6.8, H7).

¹³C{¹H}-NMR (50 MHz, CD₂Cl₂, 298 K): δ (ppm) 159.41 (s, C2), 145.78 (s, C4), 133.49 (s, C3), 131.15 (s, C9), 124.50 (s, C8), 124.36 (s, C1) 28.91 (s, C5), 24.18 (s, C6 or C7), 23.84 (s, C6 or C7).



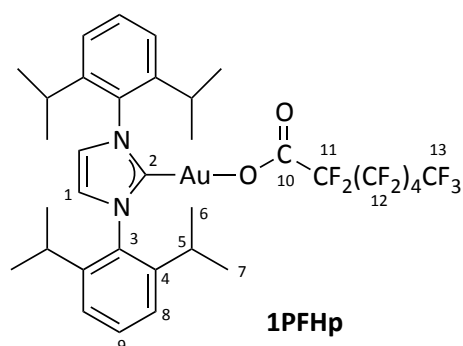
1ptm. [(NHC)-Au-Cl] (50 mg, 0.08 mmol) and 3-hexyne (14 μ L, 0.12 mmol) were poured into a Schlenk tube containing CH_2Cl_2 (1 mL). Then, AgBF_4 (23 mg, 0.12 mmol) was added. The reaction mixture was stirred at room temperature for 15 min, then it was filtered on Celite[®] pad, washed with CH_2Cl_2 (3x1 mL) and concentrated under vacuum. Addition of phthalimide potassium salt (16,6 mg, 0.09 mmol) resulted in the formation of a thin precipitate. The mixture was filtered on Celite[®] pad, washed with CH_2Cl_2 (3x1 mL), and concentrated under vacuum. Addition of *n*-hexane (4mL) resulted in the formation of a precipitate, which was filtered off, washed with *n*-hexane (3x2 mL), and then dried under vacuum to afford the product as a mild-yellow powder (yield 85%). Anal. Calcd. for $\text{C}_{35}\text{H}_{40}\text{AuN}_3\text{O}_2$ (731.68): C, 57.45; H, 5.51; Au, 26.92; N, 5.74; O, 4.37. Found: C, 57.50; H, 5.53; N, 5.72.

^1H NMR (400 MHz, CD_2Cl_2 , 298 K): δ (ppm) 7.49 (t, 2H, $^3J_{\text{HH}} = 7.6$ Hz, H9), 7.41-7.39 (m, 4H, H12-H13), 7.31 (d, 4H, d 2H, $^3J_{\text{HH}} = 7.6$ Hz, H8), 7.21 (s, 2H, H1), 2.61 (sept, $^3J_{\text{HH}} = 7.2$ Hz, 4H, H5), 1.43 (d, $^3J_{\text{HH}} = 6.8$ Hz, 12H, H6 or H7), 1.24 (d, $^3J_{\text{HH}} = 6.8$ Hz, 12H, H6 or H7).

$^{13}\text{C}\{^1\text{H}\}$ -NMR (100 MHz, CD_2Cl_2 , 298 K): δ (ppm) 178.20 (s, C10), 177.34 (s, C2), 146.49 (s, C4), 136.75 (s, C11), 134.85 (s, C3), 132.38 (s, C13), 131.16 (s, C9), 124.61 (s, C8), 123.91 (s, C1), 121.79 (s, C12), 29.64 (s, C5), 24.85 (d, C6-7), 24.34 (d, C6-7).

Silver (I) 2,2,3,3,4,4,5,5,6,6,7,7,7-tridecafluoroheptanoate. Perfluoroheptanoic acid (80 mg, 0.21 mmol) was dissolved in methanol (2 mL). To the solution was added silver oxide (25 mg, 0.107 mmol) and the suspension was stirred for 1 h at room

temperature. The mixture was filtered over Celite® pad and the elimination of the solvent under vacuum afforded the silver salt PFHp⁻Ag⁺ as a white solid. The product was re-crystallized from a mixture of ethyl ether and *n*-hexane (yield 90%). Anal. Calcd. for C₇AgF₁₃O₂ (470.92): C, 17.85; Ag, 22.91; F, 52.95; O, 6.79. Found: C, 17.76. ¹⁹F NMR (376 MHz, CD₃OD, 298 K): - δ (ppm) 81.70 - 81.82 (m, 3F, CF₃), 116.56 - 116.77 (m, 2F, CF₂COO), 121.92 - 122.22 (m, 2F, CF₂), 122.74 - 122.96 (m, 2F, CF₂), 123.03 - 123.32 (m, 2F, CF₂), 126.50 - 126.74 (m, 2F, CF₂CF₃).

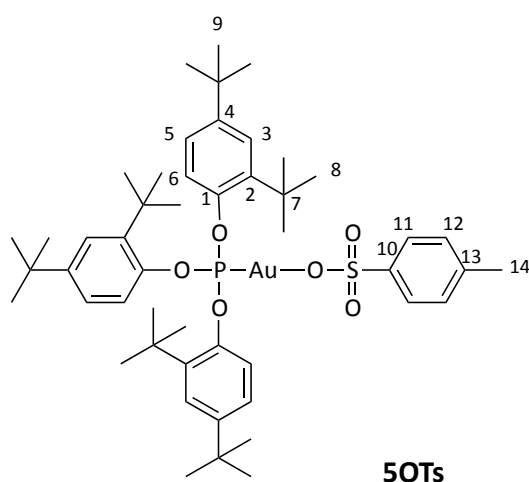


1PFHp. [(NHC)-Au-Cl] (100 mg, 0.161 mmol) was dissolved in the minimal amount of CH₂Cl₂. AgPFHp (1.2 eq, 0.193 mmol) was added leading to the precipitation of AgCl. After stirring 1 h at room temperature, the reaction mixture was filtered on Celite® pad, washed with CH₂Cl₂ (3x1 mL), and concentrated under vacuum. Addition of *n*-hexane (4 mL) resulted in the formation of a precipitate, which was filtered off, washed with *n*-hexane (3x2 mL), and then dried under vacuum to afford the product as a white powder (yield 87%). Anal. Calcd. for C₃₄H₃₆AuF₁₃N₂O₂ (948.61) C, 43.05; H, 3.83; Au, 20.76; F, 26.04; N, 2.95; O, 3.37. Found: C, 43.10; H, 3.86; N, 3.01.

¹H NMR (400 MHz, CD₂Cl₂, 298 K): δ (ppm) 7.58 (t, 2H, ³J_{HH} = 8.0 Hz, H9), 7.36 (d, 4H, ³J_{HH} = 7.6 Hz, H8), 7.28 (s, 2H, H1), 2.55 (sept, 4H, ³J_{HH} = 6.8 Hz, H5), 1.34 (d, 12H, ³J_{HH} = 6.8 Hz, H6), 1.24 (d, 12H, ³J_{HH} = 6.8 Hz, H7).

¹³C{¹H}-NMR (100 MHz, CD₂Cl₂, 298 K, signals for the C11-16 of PFHp anion were not observed): δ (ppm) 166.20 (s, C2), 161.12 (bs, C10), 146.23 (s, C4), 134.29 (s, C9), 131.22 (s, C3), 124.72 (s, C1), 124.16 (s, C8), 29.31 (s, C5), 24.37 (d, C6-7).

^{19}F NMR (376 MHz, CD_2Cl_2 , 298 K): - δ (ppm) 83.96 – 84.05 (m, 3F, CF_3), 119.76 – 119.88 (m, 2F, $\text{CF}_2(11)$), 124.94 – 125.19 (m, 2F, CF_2), 125.85 – 126.28 (m, 4F, CF_2), 129.20 – 129.39 (m, 2F, CF_2).

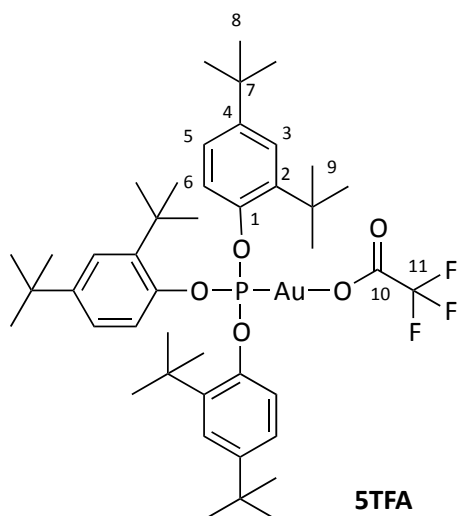


5OTs. 30mg (0.034 mmol) of [(phos)AuCl] were dissolved in 1.5 mL of CH_2Cl_2 /acetone (5:1 = v/v). Subsequently, 1.5 eq of AgOTs (14.2 mg; 0.051 mmol) were added, leading to the precipitation of AgCl. The reaction mixture was stirred overnight. Then the mixture was filtered on Celite® pad, washed with 3x1 mL of CH_2Cl_2 , dried under vacuum, to afford as a white powder (yield 83%). Anal. Calcd. for $\text{C}_{49}\text{H}_{70}\text{AuO}_6\text{PS}$ (1015,08) C, 57.98; H, 6.95; Au, 19.40; O, 9.46; P, 3.05; S, 3.16. Found: C, 57.94; H, 6.90; Au, 19.37; O, 9.41; P, 3.02; S, 3.10.

^1H NMR (400 MHz, CDCl_3 , 298 K): δ (ppm) 7.71 (d, 2H, $^3J_{\text{HH}} = 8.0$ Hz, H11), 7.48-7.35 (m, 6H), 7.21-7.09 (m, 5H), 2.36 (s, 3H, H14), 1.42 (s, 27H, H8), 1.30 (s, 27H, H9).

$^{13}\text{C}\{^1\text{H}\}$ -NMR (100 MHz, CDCl_3 , 298 K): δ (ppm) 148.30 (3C), 147.42 (3C), 139.28 (3C), 128.87 ($\text{C}_{\text{ar}}\text{-OTs}$), 126.42 ($\text{C}_{\text{ar}}\text{-OTs}$), 125.54 (3C), 124.34 (3C), 123.20 ($\text{C}_{\text{ar}}\text{-OTs}$), 119.35 (3C), 35.27 (3C), 34.84 (3C), 31.56 (9C), 30.72 (9C), 21.58 ($\text{CH}_3\text{-OTs}$).

$^{31}\text{P}\{^1\text{H}\}$ -NMR (162 MHz, CDCl_3 , 298 K): δ (ppm) 85.9.



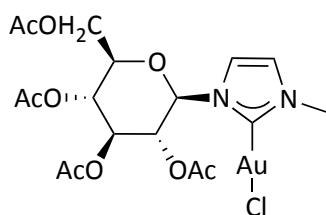
5TFA. 30mg (0.034 mmol) of [(phos)AuCl] were dissolved in 1.5 mL of CH₂Cl₂/acetone (5:1 = v/v). Subsequently, 1.5 eq of AgTFA (11.2 mg; 0.051 mmol) were added, leading to the precipitation of AgCl. The reaction mixture was stirred overnight. Then the mixture was filtered on Celite® pad, washed with 3x1 mL of CH₂Cl₂, dried under vacuum, to afford as a white powder (yield 80%). Anal. Calcd. for C₄₄H₆₃AuF₃O₅P (956,90) C, 55.23; H, 6.64; Au, 20.58; F, 5.96; O, 8.36; P, 3.24. Found: C, 55.20; H, 6.59; Au, 20.31; F, 5.88; O, 8.27; P, 3,18.

¹H NMR (400 MHz, CDCl₃, 298 K): δ (ppm) 7.46-7.39 (m, 6H), 7.16-7.10 (dd, 3H, ¹J = 4Hz, ²J = 8Hz, H5), 1.44 (s, 27H, H9), 1.29 (s, 27H, H8).

¹³C{¹H}-NMR (100 MHz, CDCl₃, 298 K, signals for anion TFA were not observed): δ (ppm) 148.5 (3C), 147.2 (3C), 139.2 (3C), 125.5 (3C), 124.3 (3C), 119.2 (3C), 35.1 (3C), 34.7 (3C), 31.4 (9C), 30.5 (9C).

³¹P{¹H}-NMR (162 MHz, CDCl₃, 298 K): δ (ppm) 88.9.

¹⁹F NMR (376 MHz, CD₂Cl₂, 298 K): - δ (ppm) 73.8 (3F).

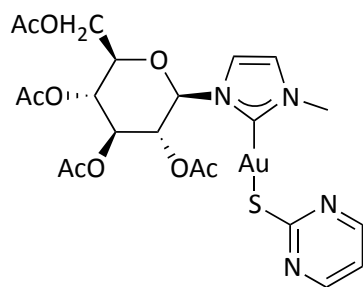
**7Cl**

1-methyl-3-(2,3,4,6-tetra-*O*-acetyl- β -D-glucopyranosyl)imidazol-2-yl)gold(I)chloride

(7Cl): a solution of THTAuCl (213 mg, 0.666 mmol) in CH_2Cl_2 (4mL) was added to a solution of 1-methyl-3-(2,3,4,6-tetra-*O*-acetyl- β -D-glucopyranosyl)imidazol-2-yl)silver(I) bromide [(magi)AgBr] (400 mg, 0.666 mmol) in CH_2Cl_2 (4mL) and the mixture was stirred at room temperature overnight. After removal of the insoluble solids by filtration using Celite, the solution was concentrated and *n*-hexane was added to afford a white solid (yield 83%). Anal. Calcd. for $\text{C}_{18}\text{H}_{24}\text{AuClN}_2\text{O}_9$ (644.81) C, 33.53; H, 3.75; Au, 30.55; Cl, 5.50; N, 4.34; O, 22.33. Found: C, 33.50; H, 3.73; Au, 30.51; Cl, 5.45; N, 4.31; O, 22.29.

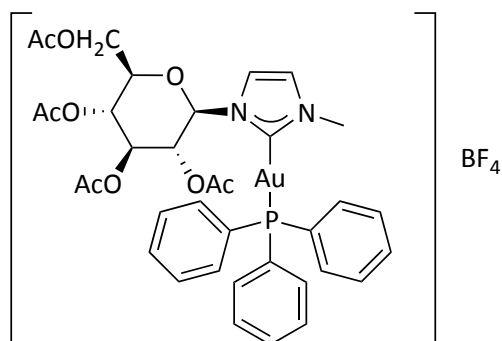
^1H NMR (400 MHz, $(\text{CD}_3)_2\text{SO}$, 298 K): δ (ppm) 7.80 (d, 1H, 4-imidazolium, $^3J_{\text{HH}} = 2$), 7.51 (d, 1H, 5-imidazolium, $^3J_{\text{HH}} = 2$), 6.22 (d, 1H, 1- glucose, $^3J_{\text{HH}} = 8.8$), 5.67 (t, 1H, 3-glucose, $^3J_{\text{HH}} = 9.6$), 5.46 (t, 1H, 2-glucose, $^3J_{\text{HH}} = 9.6$), 5.24 (t, 1H, 4-glucose, $^3J_{\text{HH}} = 9.6$), 4.37 (m, 1H, 5-glucose), 4.32 (m, 2H, 6- glucose), 4.17 (s, 3H, CH_3N), 2.10 (s, 3H, AcO), 2.08 (s, 3H, AcO), 2.06 (s, 3H, AcO), 2.01 (s, 3H, AcO).

$^{13}\text{C}\{^1\text{H}\}$ -NMR (100 MHz, $(\text{CD}_3)_2\text{SO}$, 298 K): δ (ppm) 172.4 (2-imidazolium), 170.1 (C=O), 169.5 (C=O), 169.4 (C=O), 169.22 (C=O), 123.8 (4-imidazolium), 119.0 (5-imidazolium), 84.86 (1-glucose), 72.89 (5-glucose), 71.62 (3-glucose), 70.94 (2-glucose), 67.50 (4- glucose), 61.90 (6-glucose), 37.95 ($\text{CH}_3\text{-N}$), 20.51 ($\text{CH}_3\text{-AcO}$), 20.40 ($\text{CH}_3\text{-AcO}$), 20.21 ($\text{CH}_3\text{-AcO}$), 20.412 ($\text{CH}_3\text{-AcO}$).

**7S-pyr**

1-methyl-3-(2,3,4,6-tetra-*O*-acetyl- β -D-glucopyranosyl)imidazol-2-yl)gold(I)pyrimidine-2-thiolate (**7S-pyr**): Mercaptopyrimidine (20 mg, 0.174 mmol) and NaOEt (16 mg, 0.232 mmol) was dissolved in MeOH (30 mL) and stirred for 10 min. **7Cl** (75 mg, 0.116 mmol) was added, and the mixture was stirred at room temperature for 6 h. The solvent was concentrated in vacuum, and hexane was added until appearance of a precipitate. The white solid was isolated by filtration and washed with 0.2 M KOH in MeOH and water and subsequently dried under vacuum (yield 80%). Anal. Calcd. for $C_{22}H_{27}AuN_4O_9S$ (720.50) C, 36.67; H, 3.78; Au, 27.34; N, 7.78; O, 19.99; S, 4.45. Found: C, 36.62; H, 3.75; Au, 27.28; N, 7.69; O, 19.94; S, 4.37.

1H NMR (500 MHz, $CDCl_3$, 298 K): δ (ppm) 8.37 (d, 2H, m-CH, $^3J_{HH} = 5$), 7.22 (d, 1H, 4-imidazolium, $^3J_{HH} = 2$), 6.99 (d, 1H, 5-imidazolium, $^3J_{HH} = 2$), 6.82 (t, p-CH, $^3J_{HH} = 5$), 6.21 (d, 1H, 1- glucose, $^3J_{HH} = 9$), 5.43 (t, 1H, 3-glucose, $^3J_{HH} = 9.5$), 5.25 (t, 1H, 2-glucose, $^3J_{HH} = 9$), 5.20 (t, 1H, 4-glucose, $^3J_{HH} = 10$), 4.29 (dd, H5, $^3J_{HH} = 5$), 4.15 (dd, H6, $^3J_{HH} = 2$), 4.04 (m, H6'), 3.90 (s, 3H, CH_3N), 2.09 (s, 3H, AcO), 2.07 (s, 3H, AcO), 2.02 (s, 3H, AcO), 1.99 (s, 3H, AcO).



[7PPh₃]BF₄

1-methyl-3-(2,3,4,6-tetra-*O*-acetyl- β -D-glucopyranosyl)imidazol-2-yl(triphenylphosphine) gold(I) tetrafluoroborate (**[7PPh₃]BF₄**):

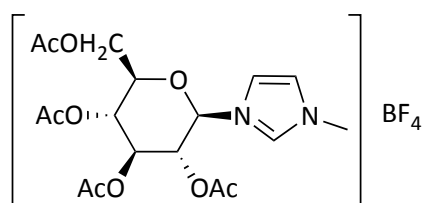
a Schlenk tube was filled with 70 mg of **7Cl** (0.108 mmol) and 31 mg of PPh₃ (0.119 mmol) which were dissolved into 5 mL of distilled dichloromethane. AgBF₄ in solution in methanol was added dropwise at room temperature. The reaction was maintained for one hour during which a white precipitate appeared and became grey after some minutes. After a filtration over celite, the volatiles were removed under vacuum to afford a colorless oil which gave rise to a white precipitate after being washed with Et₂O. The white precipitate was washed with Et₂O to give the pure product (90% yield). Anal. Calcd. for C₃₆H₃₉AuBF₄N₂O₉P (958.45) C, 45.11; H, 4.10; Au, 20.55; B, 1.13; F, 7.93; N, 2.92; O, 15.02; P, 3.23. Found: C, 44.97; H, 3.98; Au, 20.47; B, 1.10; F, 7.87; N, 2.88; O, 14.95.

¹H NMR (500 MHz, CDCl₃, 298 K): δ (ppm) 7.69 – 7.28 (m, 17H), 5.86 (d, 1H, 1-glucose, ³J_{HH} = 9.5), 5.54 (t, 1H, 3-glucose, ³J_{HH} = 9.5), 5.40 (t, 1H, 2-glucose, ³J_{HH} = 9.5), 5.10 (t, 1H, 4-glucose, ³J_{HH} = 9.5), 4.19 (m, 1H, 5-glucose), 4.08 (m, 2H, 6- glucose), 4.02 (s, 3H, CH₃N), 2.04 (s, 3H, AcO), 1.99 (s, 3H, AcO), 1.91 (s, 3H, AcO), 1.84 (s, 3H, AcO).

¹⁹F{¹H}-NMR (376 MHz, CD₂Cl₂, 298 K): - δ (ppm) 152.67, 152.72

¹³C{¹H}-NMR (100 MHz, (CD₃)₂SO, 298 K): δ (ppm) 185.1 (2-imidazolium), 170.6 (C=O), 169.8 (C=O), 169.5 (C=O), 169.2 (C=O), 134.3 (C_{ortho}PPh₃), 134.2 (C_{meta}PPh₃), 130.0 (C_{para}PPh₃), 129.9 (C_{ipso}PPh₃), 124.1 (4-imidazolium), 121.0 (5-imidazolium), 86.44 (1-

glucose), 75.24 (5-glucose), 72.98 (3-glucose), 71.77 (2-glucose), 67.92 (4- glucose), 61.83 (6-glucose), 39.43 (CH₃-N), 20.82 (CH₃-AcO), 20.70 (CH₃-AcO), 20.49 (CH₃-AcO), 20.41 (CH₃-AcO).

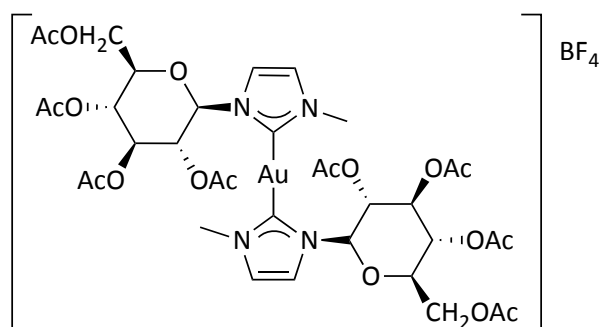


1-methyl- 3-(2,3,4,6-tetra-*O*-acetyl- β -D-glucopyranosyl)imidazolium tetrafluoroborate (**7BF₄**): A round-bottom flask was filled with 108 mg of 1-methyl- 3-(2,3,4,6-tetra-*O*-acetyl- β -D-glucopyranosyl)imidazolium bromide (0.219 mmol) and 72 mg of NaBF₄ (0.657 mmol) in 20 mL of acetone. The reaction was maintained at room temperature overnight. After removing of acetone under vacuum, the obtained white solid was partially dissolved in 30 mL of dichloromethane, and filtrated through paper to give a colorless solution. Dichloromethane was then evaporated under vacuum to lead to the pure product (98% yield). Anal. Calcd. for C₁₉H₂₈BF₄N₂O₉ (515.24) C, 44.29; H, 5.48; B, 2.10; F, 14.75; N, 5.44; O, 27.95. Found: C, 44.25; H, 5.44; B, 2.05; F, 14.71; N, 5.39; O, 27.88.

¹H NMR (400 MHz, CDCl₃, 298 K): δ (ppm) 9.55 (s, 1H, 2-imidazolium), 7.60 (bt, 1H, 4-imidazolium), 7.52 (bt, 1H, 5-imidazolium), 6.15 (d, 1H, 1- glucose, ³J_{HH} = 9.2), 5.43 (t, 1H, 3-glucose, ³J_{HH} = 9.6), 5.30 (t, 1H, 2-glucose, ³J_{HH} = 9.2), 5.23 (t, 1H, 4-glucose, ³J_{HH} = 9.6), 4.21 (m, 3H), 4.03 (s, 3H, CH₃N), 2.05 (s, 3H, AcO), 2.02 (s, 3H, AcO), 1.98 (s, 3H, AcO), 1.97 (s, 3H, AcO).

¹³C{¹H}-NMR (100 MHz, CDCl₃, 298 K): δ (ppm) 170.8 (C=O), 170.0 (C=O), 169.9 (C=O), 169.68 (C=O), 137.3 (2-imidazolium), 124.5 (4-imidazolium), 120.0 (5-imidazolium), 84.29 (1-glucose), 75.03 (5-glucose), 72.47 (3-glucose), 70.63 (2-glucose), 67.464 (4-glucose), 61.58 (6-glucose), 37.11 (CH₃-N), 20.83 (CH₃-AcO), 20.67 (CH₃-AcO), 20.59 (CH₃-AcO), 20.44 (CH₃-AcO).

¹⁹F{¹H}-NMR (376 MHz, CD₂Cl₂, 298 K): - δ (ppm) 150.57, 150.63



[7-7]BF₄

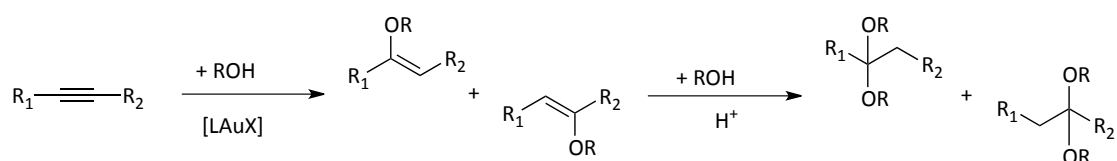
Bis(1-methyl-3-(2,3,4,6-tetra-*O*-acetyl- β -D-glucopyranosyl)imidazol-2-yl)gold(I) tetrafluoroborate (**[7-7]BF₄**): a round-bottom flask was filled with 101 mg of **7BF₄** (0.202 mmol), 37 mg of Ag₂O (0.16 mmol), and molecular sieves 4 Å (MS 4 Å) (100 mg) in 12 mL of dichloromethane. The mixture was reacted for 4 h at room temperature in the dark. Then 32 mg of THTAuCl (0.101 mmol) dissolved into 3.4 mL of dichloromethane were added dropwise to the previous mixture and reacted overnight at room temperature in the dark. After a filtration over celite, the volatiles were removed under vacuum to give the product as a white solid. (60% yield). Anal. Calcd. for C₃₆H₄₈AuBF₄N₄O₁₈ (1108.55) C, 39.00; H, 4.36; Au, 17.77; B, 0.98; F, 6.86; N, 5.05; O, 25.98. Found: C, 38.96; H, 4.32; Au, 17.67; B, 0.95; F, 6.79; N, 4.98; O, 25.92. ¹H NMR (400 MHz, (CD₃)₂SO, 298 K): δ (ppm) 7.87 (d, 1H, 4-imidazolium, ³J_{HH} = 1.6), 7.62 (d, 1H, 5-imidazolium, ³J_{HH} = 1.6), 6.29 (d, 1H, 1- glucose, ³J_{HH} = 8.4), 5.62 (t, 1H, 3-glucose, ³J_{HH} = 9.6), 5.57 (t, 1H, 2-glucose, ³J_{HH} = 9.6), 5.25 (t, 1H, 4-glucose, ³J_{HH} = 9.2), 4.37 (m, 1H, 5-glucose), 4.32 (m, 2H, 6- glucose), 3.95 (s, 3H, CH₃N), 2.05 (s, 3H, AcO), 2.01 (s, 3H, AcO), 1.99 (s, 3H, AcO), 1.92 (s, 3H, AcO). ¹³C{¹H}-NMR (100 MHz, (CD₃)₂SO, 298 K): δ (ppm) 182.95 (2-imidazolium), 170.04 (C=O), 169.55 (C=O), 169.42 (C=O), 168.74 (C=O), 124.45 (4-imidazolium), 119.59 (5-imidazolium), 84.94 (1-glucose), 73.22 (5-glucose), 71.83 (3-glucose), 70.57 (2-glucose), 67.60 (4- glucose), 61.86 (6-glucose), 37.93 (CH₃-N), 20.48 (CH₃-AcO), 20.39 (CH₃-AcO), 20.23 (CH₃-AcO). ¹⁹F{¹H}-NMR (376 MHz, (CD₃)₂SO₂, 298 K): - δ (ppm) 148.23, 148.28

CHAPTER

3

GOLD(I)-CATALYZED METHOXYLATION
OF ALKYNES

This chapter describes the alkoxylation reaction of alkynes, catalyzed by gold(I) complexes (Scheme 1).



Scheme 1. Gold(I) catalyzed alkoxylation of alkynes

Among the gold-catalyzed reactions, the intermolecular alkoxylation of alkynes and similar reaction (hydration and hydrophenoxylation) are the oldest applications of cationic gold(I) catalyst. Over the years, this class of reactions has been deeply studied in order to find highly active catalysts and shed more light on the reaction mechanism, making nowadays alkoxylation an industrially important process, together with the hydration of alkynes, for the synthesis of carbonyl compounds.¹

The catalytic performances of gold complexes are affected by the ligand, which modulates the acidic character of the metal fragment, but also by the anion, which is

¹ Dorel, R., Echevarren, A. M. *Chem. Rev.* **2015**, *115*, 9028-9072

known to influence also the regioselectivity² and even the stereoselectivity³ of the process.

Thus, the role of the anion has been analyzed in different step of the catalytic cycle in the alkoxylation of alkynes and, although both the nature of the ligand⁴ and counterion effect is considered important factor in gold catalysis, a rational understanding of their synergy/antagonism is still lacking.

Furthermore, the relative orientation of the anion/cation in solution is crucial in determining the catalytic performances, because it affects the structure and the reactivity of ionic transition metal, therefore a detailed description of the ion pair structure is essential to understand how the anion actually affects the reaction mechanism.

In the following paragraphs, the extensive study on the gold(I) catalyzed methoxylation reaction of 3-hexyne will be discussed from different point of view: the anion effect, the influence of the ligand/anion combination, and the effect of the ion pair on the catalysis.

The results have been previously published in:

- Biasiolo, L.; Trinchillo, M.; Belanzoni, P.; Belpassi, L.; Busico, V.; Ciancaleoni, G.; D'Amora, A.; Macchioni, A.; Tarantelli, F.; Zuccaccia, D. *Chem. - Eur. J.* **2014**, *20*, 14594–14598;
- Marina Trinchillo, Paola Belanzoni, Leonardo Belpassi, Luca Biasiolo, Vincenzo Busico, Angela D'Amora, Lorenzo D'Amore, Alessandro Del Zotto, Francesco Tarantelli, Angela Tuzi, and Daniele Zuccaccia *Organometallics*, **2016**, *35*, 641–654

² Xia, Y., Dudnik, A. S., Gevorgyan, V., Li, Y. *J. Am. Chem. Soc.* **2008**, *130*, 6940

³ Hamilton, G. L., Kang, E. J., Mba, M., Toste, F. D. *Science* **2007**, *317*, 496

⁴ Gorin, D. J.; Sherry, B. D.; Toste, F. D. *Chem. Rev.* **2008**, *108*, 3351–3378; Marion, N.; Nolan, S. *Chem. Soc. Rev.* **2008**, *37*, 1776–1782

1. Introduction

In recent years, homogeneous gold catalysis has received significant consideration and is representing a fast emergent area.⁵ In-depth kinetic and mechanistic studies on gold(I)-catalyzed nucleophilic addition to a carbon–carbon unsaturated bond have been appearing in the literature,⁶ with the purpose to understand the ligand effects in the different steps of the catalytic cycle.^{7, 8, 9, 10, 11, 12, 13} On the other hand, also the anion plays an important role in gold catalysis influencing the catalytic activity,¹⁴ the regioselectivity,² and even the stereoselectivity³ of the process.

Furthermore, it has been observed that the anion can influence the structure of the catalyst¹⁵ and of the intermediates in the catalytic cycle.¹⁶ Even if several

⁵ (a) Hashmi, A. S. K. *Chem. Rev.* **2007**, *107*, 3180–3211. (b) Bandini, M. *Chem. Soc. Rev.* **2011**, *40*, 1358–1367. (c) Boorman, T. C.; Larrosa, I. *Chem. Soc. Rev.* **2011**, *40*, 1910–1925. (d) Corma, A.; Leyva-Pérez, A.; Sabater, M. J. *Chem. Rev.* **2011**, *111*, 1657–1712. (e) Leyva-Pérez, A.; Corma, A. *Angew. Chem., Int. Ed.* **2012**, *51*, 614–635. (f) Hashmi, A. S. K.; Rudolph, M. *Chem. Soc. Rev.* **2012**, *41*, 2448–2462

⁶ Wang, W.; Hammond, G. B.; Xu, B. J. *Am. Chem. Soc.* **2012**, *134*, 5697–5705

⁷ (a) Benitez, D.; Tkatchouk, E.; Gonzalez, A. Z.; Goddard, W. A., III; Toste, F. D. *Org. Lett.* **2009**, *11*, 4798–4801. (b) Clavier, H.; Nolan, S. P. *Chem. Commun.* **2010**, *46*, 841–861. (c) Klahn, P.; Kirsch, S. F. *ChemCatChem* **2011**, *3*, 649–652. (d) Rüttinger, R.; Leutzow, J.; Wilsdorf, M.; Wilckens, K.; Czekelius, C. *Org. Lett.* **2011**, *13*, 224–227. (e) Xu, X.; Kim S. H.; Zhang X.; Das A. K.; Hirao H.; Hong S. H. *Organometallics* **2013**, *32*, 164–171

⁸ (a) Hashmi, A. S. K. *Angew. Chem., Int. Ed.* **2010**, *49*, 5232–5241; (b) Obradors, C.; Echavarren A. M. *Chem. Commun.* **2014**, *50*, 16–28

⁹ (a) Schmidbaur, H.; Schier A. *Organometallics* **2010**, *29*, 2–23 and reference therein. (b) Brooner, R. E. M.; Widenhoefer, R. *Angew. Chem. Int. Ed.* **2013**, *52*, 11714–11724. (c) Liu, L.; Hammond, G. B. *Chem. Soc. Rev.* **2012**, *41*, 3129–3139

¹⁰ Zuccaccia, D.; Belpassi, L.; Tarantelli, F.; Macchioni, A. *Eur. J. Inorg. Chem.* **2013**, *24*, 4121–4135

¹¹ (a) Hashmi, A. S. K.; Schuster, A. M.; Rominger, F. *Angew. Chem., Int. Ed.* **2009**, *48*, 8247–8249. (b) Shi, Y.; Ramgren, S. D.; Blum, S. A. *Organometallics* **2009**, *28*, 1275–1277; (c) Mohr, F.; Falvello, L. R.; Laguna, M. *Eur. J. Inorg. Chem.* **2006**, 833–838, and references therein. (d) Weber, D.; Tarselli, M. A.; Gagné, M. R. *Angew. Chem. Int. Ed.* **2009**, *48*, 5733–5736

¹² Fürstner, A.; Alcarazo, M.; Goddard, R.; Lehmann, C. W. *Angew. Chem., Int. Ed.* **2008**, *47*, 3210–3214

¹³ (a) Xi, Y.; Su, Y.; Yu, Z.; Dong, B.; McClain, E. J.; Lan, Y.; Shi, X. *Angew. Chem., Int. Ed.* **2014**, *53*, 9817–9821. (b) Yu, Z.; Ma, B.; Chen, M.; Wu, H. H.; Liu, L.; Zhang, J. *J. Am. Chem. Soc.* **2014**, *136*, 6904–6907. (c) Brooner, R. E. M.; Brown, T. J.; Widenhoefer, R. A. *Angew. Chem., Int. Ed.* **2013**, *52*, 6259–6261. (d) Seidel, G.; Fürstner, A. *Angew. Chem., Int. Ed.* **2014**, *53*, 4807–4811

¹⁴ (a) Brouwer, C.; He, C. *Angew. Chem., Int. Ed.* **2006**, *45*, 1744–1747. (b) Gramage-Doria, R.; Bellini, R.; Rintjema, J.; Reek, J. N. H. *ChemCatChem* **2013**, *5*, 1084–1087. (c) Homs, A.; Obradors, C.; Lebœuf, D.; Echavarren, A. M. *Adv. Synth. Catal.* **2014**, *356*, 221–228

¹⁵ K. Aikawa, M. Kojima, K. Mikami, *Angew. Chem.* **2009**, *121*, 33, 6189–6193; *Angew. Chem. Int. Ed.* **2009**, *48*, 6073–6077

¹⁶ D. Weber, T. D. Jones, L. Adduci, M. R. Gagné, *Angew. Chem.* **2012**, *124*, 10, 2502–2506; *Angew. Chem. Int. Ed.* **2012**, *51*, 2452–2456

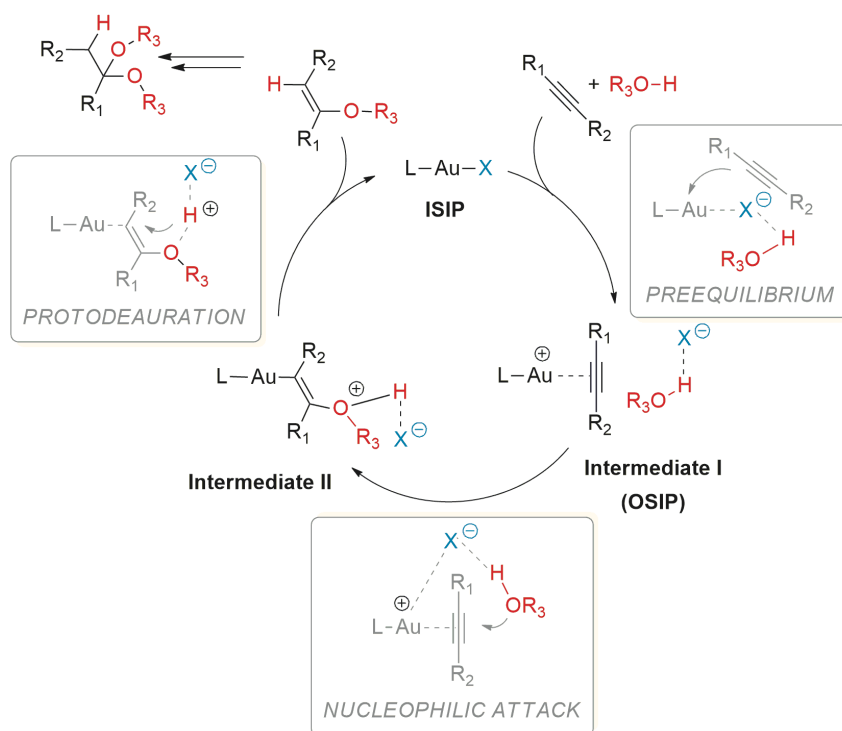
experimental data pointed out a significant 'effect of the counterion' in gold catalysis,¹⁷ its mechanistic explanation is still far from being fully achieved.

Among the gold-catalyzed processes, the alkoxylation of alkynes is still the most investigated one.¹⁸ Its accepted mechanism consists of a pre-equilibrium step, with the L-Au-X species (L = ancillary ligand, X = counterion, ISIP = inner-sphere ion pair), that coordinates the alkyne acting as a Lewis acid (Scheme 2, Intermediate I, OSIP = outer sphere ion pair) and activating it towards the nucleophilic attack by alcohol, forming the vinyl gold intermediate (Scheme 2, Intermediate II). Then, the reaction is completed by the anion- or solvent- proton transfer from the alcohol OH group to the other carbon atom (protodeauration), with cleavage of gold-carbon bond, formation of the vinyl ether intermediate and regeneration of the catalyst. Subsequent reaction of the vinyl ether with a second alcohol molecule leads to the formation of the acetal final product and it is considered a classical proton-catalyzed process.¹⁹

¹⁷ Jia, M.; Bandini, M. *ACS Catal.* **2015**, *5*, 1638-1652, and reference therein

¹⁸ (a) Li, Z.; Brouwer, C.; He, C. *Chem. Rev.* **2008**, *108*, 3239–3265 and references therein; (b) Jiménez-Nuñez, E.; Echavarren, A. M. *Chem. Rev.* **2008**, *108*, 3326–3350. and references therein; (c) Hashmi, A. S. K. *Chem. Rev.* **2007**, *107*, 3180–3211; (d) Krause, N.; Winter, C. *Chem. Rev.* **2011**, *111*, 1994–2009

¹⁹ Zhdanko, A.; Maier, M. M. *Chem. Eur. J.* **2014**, *20*, 1918-1930



Scheme 2. Proposed gold alkoxylation catalytic cycle

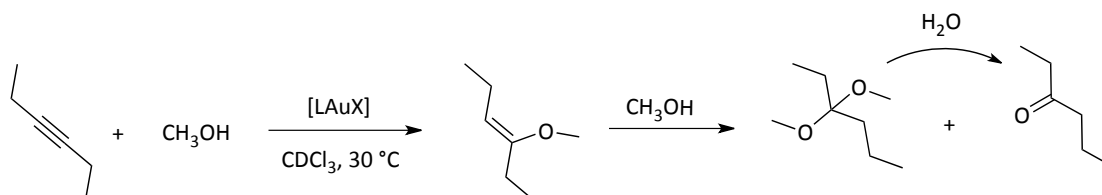
The acetal product is converted in the corresponding ketone, in presence of water traces, through a hydrolysis reaction.¹⁹

2. Results and discussion

2.1. Counterion effect

Despite the amount of work on the alcohol addition to alkynes, systematic experimental studies aimed at understanding the role of the anion are only very recent and the mechanistic explanation of the “effect of the counterion” is still far from being fully achieved. Recent studies^{20,21,22} about the Au-catalyzed intermolecular alkoxylation^{23,24} of alkynes showed that the nucleophilic attack of methanol has to be assisted by the anion through the formation of a hydrogen bond. Thus, the anion is not only a ‘proton shuttle’, as proposed in a previous work,²⁵ but can play a more complex role in the catalytic cycle.

In this thesis the role of the anion in different steps of the catalytic cycle has been analyzed in detail, using the methoxylation of 3-hexyne as a model reaction (Scheme 3).



Scheme 3. NHC-gold(I) catalyzed methoxylation of 3-hexyne

[(NHC)AuX] complexes were chosen as catalysts, in order to largely simplify the mechanistic framework. Indeed, the application of a very bulky ligand, such as NHC, can totally eliminate under the catalytic conditions the formation of *gem*-diaurated species [(NHC-Au)₂S]X, which is a drawback for the whole catalytic cycle.¹⁹

²⁰ Biasiolo, L.; Trinchillo, M.; Belanzoni, P.; Belpassi, L.; Busico, V.; Ciancaleoni, G.; D’Amora, A.; Macchioni, A.; Tarantelli, F.; Zuccaccia, D. *Chem. Eur. J.* **2014**, *20*, 14594-14598

²¹ Ciancaleoni, G.; Belpassi, L.; Zuccaccia, D.; Tarantelli, F.; Belanzoni, P. *ACS Catal.* **2015**, *5*, 803-814

²² Zhdanko, A.; Maier, M. E. *ACS Catal.* **2014**, *4*, 2770–2775

²³ Teles, J. H.; Brode, S.; Chabanas, M. *Angew. Chem., Int. Ed.* **1998**, *37*, 1415-1417

²⁴ Teles, J. H. in “Modern Gold catalyzed synthesis” Edited by Hashmi, A. S. K.; Toste, F. D. Eds; Wiley-VHC Verlag GmbH & Co. KGaA: Weinheim, **2012**

²⁵ Kovács, G.; Ujaque, G.; Lledós, A. *J. Am. Chem. Soc.*, **2008**, *130*, 853-864

Nowadays, N-heterocyclic carbenes rank among the most powerful tool in modern chemistry and, in particular, their attractive features make them suitable ligands for transition metals.²⁶ One property is the inherent σ -donor ability, with a formal sp^2 -hybridized lone pair available for donation into a σ -accepting orbital of the metal, but, although the σ -donation is the most important component of metal-ligand bonding, the contribution of both π -back-bonding into the carbene p -orbital and π -donation from the carbene p -orbital may be not negligible (Figure 1). The coordination to the metal is generally depicted as a single rather than a double bond, while the π -contributions are involved in the delocalization within the NHC ring, often represented as a curved line between the heteroatoms.²⁶

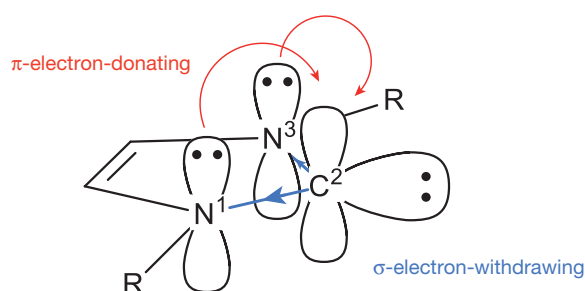


Figure 1. Ground state electronic structure of imidazole-2-ylidenes. Reproduced by ref. 26

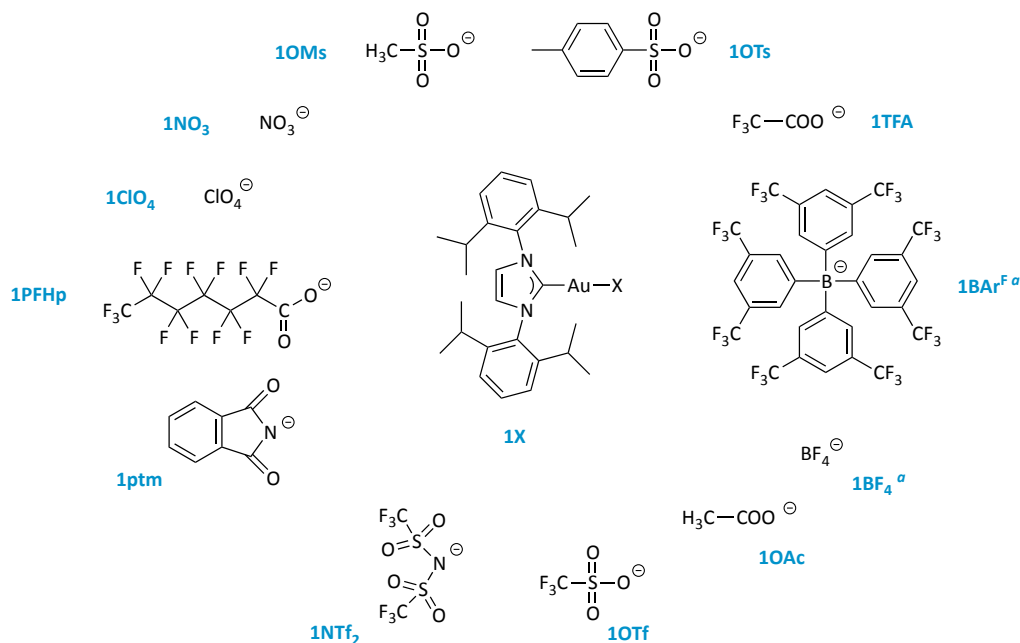
Compared to phosphines, NHCs are more electron-donating ligands, leading to thermodynamically stronger metal-ligand bonds, greater bond dissociation energies and shorter metal-ligand bond lengths. Furthermore, whereas phosphines have a cone-shaped spatial arrangement of the steric bulk, NHCs can be described as fan- or umbrella-shape, with the substituents on the nitrogen atoms oriented towards the metal. As a consequence, these steric and electronic properties contribute to increase the catalyst stability and to improve the catalytic activity.²⁶

Based on these considerations, a set of [(NHC)AuX] complexes (NHC = 1,3-bis(2,6-diisopropylphenyl)-imidazol-2-ylidene **L1**), differing for the counterion X^- (Scheme 4),

²⁶ Hopkinson, M. N., Richter, C., Schedler, M., Glorius, F. *Nature* **2014**, *510*, 485-486

has been synthesized and characterized through NMR spectroscopy and X-ray techniques, most of them for the very first time in this work (for more details see Chapter 2).

A series of anions with different coordinating ability and basicity properties has been chosen: tosylate (OTs⁻), triflate (OTf⁻), tetrafluoroborate (BF₄⁻), trifluoroacetate (TFA⁻), acetate (OAc⁻), tetrakis(3,5-bis(trifluoro-methyl)phenyl)-borate (BAR^{F-}), mesylate (OMs⁻), nitrate (NO₃⁻), perchlorate (ClO₄⁻), phthalimide (ptm⁻), bis(trifluoromethanesulfonyl)imide (NTf₂⁻) and 2,2,3,3,4,4,5,5,6,6,7,7,7-tridecafluoroheptanoate (PFHp⁻).



Scheme 4. Complete set of gold(I) catalysts. ^a [(NHC)Au(η²-3-hexyne)]X species have been used as catalysts

The novel gold complexes **1OTs**, **1OMs**, **1NO₃**, **1ClO₄**, **1PFHp**, **1BAR^{F-}**, **1TFA**, together with the already known **1OTf**, **1BF₄**, **1OAc**, **1NTf₂** and **1ptm** were tested in the methoxylation of 3-hexyne at 30 °C, followed by NMR spectroscopy.

The experimental results, shown in Figure 2, demonstrate that the anion plays an active role in the reaction mechanism. The most active complexes are **1OTs** and

1OMs, followed by **1OTf**, **1NTf₂**, **1BF₄**, **1BAR^F**, **1ClO₄**, **1PFHp** and **1TFA**. The complexes **1OAc**, **1NO₃** and **1ptm** do not show any catalytic activity.

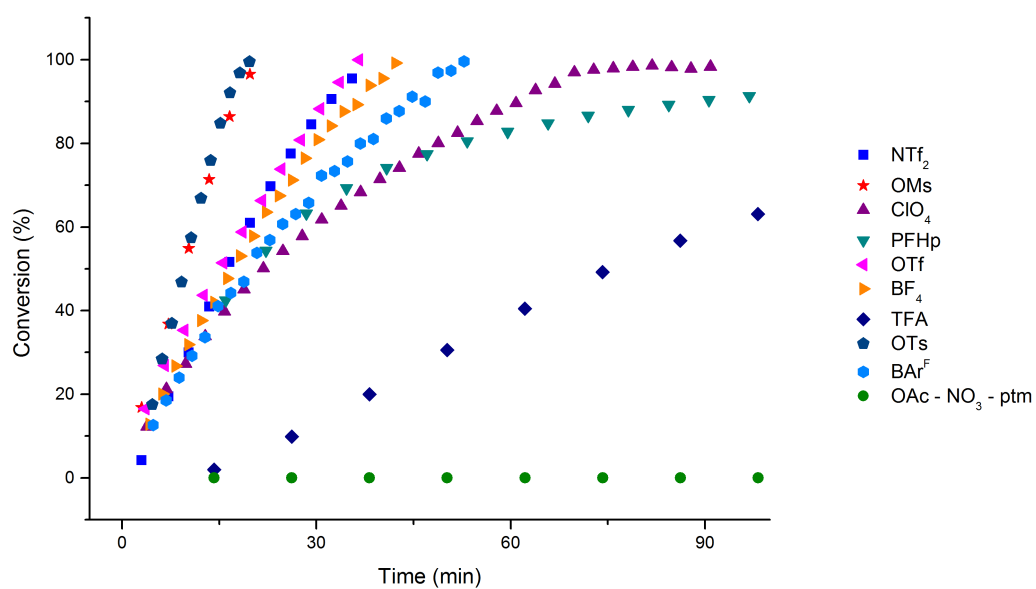


Figure 2. Rate of methoxylation of 3-hexyne catalyzed by gold(I) complexes

Table 1. Gold(I) catalyzed methoxylation of 3-hexyne^a

entry	catalyst	conversion ^b (%)	time ^c (min)	TOF ^d (h ⁻¹)
1	1OMs	99	19	294
2	1NTf₂	98	35	185
3	1NO₃	0	-	-
4	1ClO₄	95	59	140
5	1ptm	0	-	-
6	1PFHp	98	132	135
7	1OTs	99	17	309
8	1OTf	99	33	196
9	1BF₄	99	40	178
10	1BAr^F	99	48	153
11	1TFA	96	266	40
12	1OAc	0	-	-
13 ^e	1OTs	98	65	200
14 ^e	1OTf	98	55	261
15 ^f	1OTs	99	20	297
16 ^g	1OTs	99	22	263
17 ^h	1OTs	99	18	292
18 ^h	1OTf	99	47	120
19 ^h	1BF₄	99	64	178
20 ^h	1BAr^F	99	89	153

^a Catalysis conditions: 30 °C, 3-hexyne (0.88 mmol, 100 μL), CH₃OH (3.52 mmol, 143 μL), 1 mol% catalyst, CDCl₃ (400 μL). ^b Determined by ¹H NMR; averaged value of three measurements. ^c Time necessary to reach a 95% conversion. ^d TOF = (n_{product} / n_{catalyst})/t(h) at 50% of conversion. ^e Reaction performed with 0.5 mol % catalyst in CD₃NO₂ at 50 °C. ^f With 5% of NBu₄OTs as additive. ^g With 15% of *p*TsOH as additive. ^h 30 °C, 3-hexyne (0.88 mmol, 100 μL), CH₃OD (3.52 mmol, 143 μL), 1 mol% catalyst, CDCl₃ (400 μL).

Very surprisingly, the trend of the TOF values does not reflect the coordinating power²⁷ of the anions. Usually, when the first catalytic step involves the competition between the substrate and the anion on the metal coordination vacancy, strong coordinating anions reduce the catalytic activity.²⁸ Indeed, from the mechanism depicted in Scheme 2, we may expect that non-coordinating anions should maximize the catalytic rate. On the other hand, the trend of TOF does not reflect the basicity of the anions²⁹ towards the abstraction of the alcoholic proton of the methanol before or after the nucleophilic attack, neither.

The anions containing a R-SO₃ moiety (*e.g.* OMs⁻, OTs⁻) show the optimal balance between coordinating and proton-acceptor abilities, that enhances the nucleophilicity of the attacking methanol via a hydrogen bond and holds the reactive methanol molecule in an ideal spatial arrangement. On the other hand, the total lack of activity shown by **1OAc**, **1NO₃** and **1ptm** may be attributed to the high coordination affinity of these counterions toward the NHC-Au⁺ fragment, which inhibits the reaction by preventing the alkyne coordination (Scheme 2, pre-equilibrium step).

As regards the other counterions, the poorer catalytic activities of **1ClO₄** and **1BF₄** can be explained by their lower basicity and the reduced coordination attitude, due to their spherical symmetry. The last aspect results prevalent in case of the non-coordinating anion BAr^{F-}, which does not enter into the reaction mechanism.

In addition, **1NTf₂** and **1OTf** show an intermediate level of nucleophilicity and proton acceptor ability and exhibits a catalytic efficiency, which is intermediate between that of ClO₄⁻/BF₄⁻ and OMs⁻/OTs⁻ (Table 1, entries 2 and 8 vs entries 4, 9, 1, and 7).

In order to get a deeper insight into these intriguing results, we analyzed the effect of the anion in the ISIP/OSIP pre-equilibrium step (Scheme 2). The equilibrium (NHC)AuX + 3-hexyne \leftrightarrow [(NHC)Au(η^2 -3-hexyne)]X between the ISIP and the OSIP (Scheme 2) is

²⁷ Macchioni, A. *Chem. Rev.* **2005**, *105*, 1917-2722

²⁸ Kündig, E. P. Saudan, C. M. Bernardinelli, G. *Angew. Chem.* **1999**, *111*, 1298; *Angew. Chem., Int. Ed.* **1999**, *38*, 1220

²⁹ Kütt, A. Rodima, T. Saame, J. Raamat, E. Memets, V. Kaljurand, I. Koppel, I. A. Garlyauskayte, R. Y. Yagupolskii, Y. L. Yagupolskii, L. M. Bernhardt, E. Willner, H. Leito, I. *J. Org. Chem.* **2011**, *76*, 391-395

completely shifted to the right when weakly and non-coordinating BF_4^- and $\text{BAR}^{\text{F}-}$ anions are considered.³⁰ This means that the concentration of ISIP is constant during the reaction, leading to a linear profile of the conversion against time (Figure 2).

Differently, for **1TFA** (Figure 2) the reaction rate is not constant, but it lowers when the time is around 90 minutes. Recording the ^{19}F NMR spectrum at different reaction times, we observed the disappearance of the broad resonance at -74.8 ppm and simultaneously the formation of a sharp new resonance at -76.2 ppm (assigned to the trifluoroacetic acid TFAH, Figure 3). Dissolving **1TFA** in CDCl_3 with 400 eq. of methanol (Figure 4), the same phenomenon is observed, with the total disappearance of the NMR signal relative to **1TFA** within one hour. If 3-hexyne is added to the solution after three hours (at complete formation of TFAH), no catalytic activity was observed. These experimental results can be explained by assuming an acid-base reaction between TFA^- and MeOH , giving TFAH and MeO^- , which, in turn, probably poisons the catalyst forming the catalytically inert $[(\text{NHC})\text{Au}(\text{OMe})]$ species.³¹

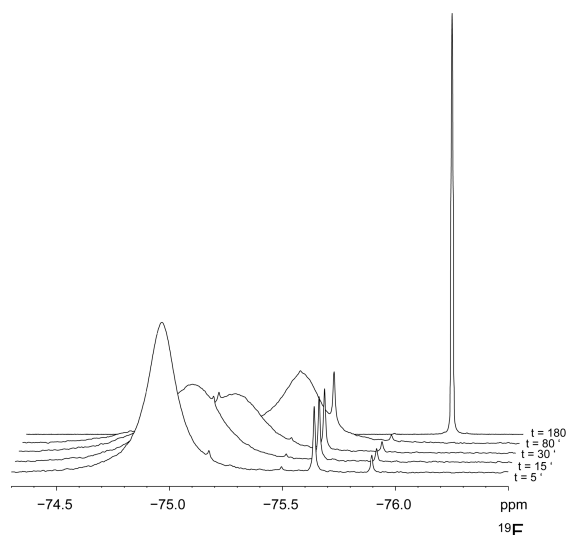


Figure 3. ^{19}F NMR spectra of **1TFA** in catalytic condition, recorded at different times

³⁰ G. Ciancaleoni, L. Biasiolo, G. Bistoni, A. Macchioni, F. Tarantelli, D. Zuccaccia, L. Belpassi, *Organometallics*, **2013**, *32*, 4444-4447

³¹ a) J. Roithová, Š. Janková, L. Jašiková, J. Váňa, S. Hybelbauerová, *Angew. Chem.* **2012**, *124*, 33, 8503-8507; *Angew. Chem. Int. Ed.* **2012**, *51*, 8378-8382; b) Y. Oonishi, A. Gómez-Suárez, A. R. Martin, S. P. Nolan, *Angew. Chem.* **2013**, *125*, 37, 9949-9953; *Angew. Chem. Int. Ed.* **2013**, *52*, 9767-9771

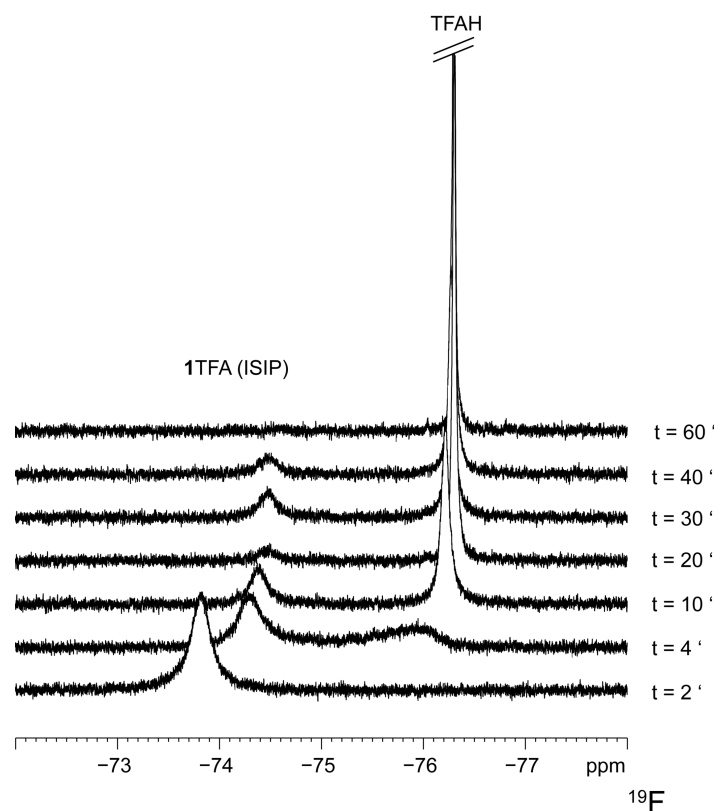


Figure 4. ^{19}F NMR spectra of 1TFA (CDCl_3 , 1mM) in presence of 400 eq of methanol recorded at different times

For **10Ac**, which shows no catalytic activity (Figure 2), the reaction with the excess of MeOH is very slow, giving less than 30% of acetic acid in 48 hours and methoxide, which coordinates to the gold center. In this case the ISIP is predominant in solution due to the strong coordinating ability of the anion. Indeed, treating a 1 mM solution of **10Ac** in CDCl_3 with 100, 200, 300 and 400 equivalents of methanol, the sharp ^1H NMR signal relative to the coordinated OAc^- at 1.78 ppm becomes broader and shifts to lower frequencies. At the same time, a different sharp signal rises at 2.18 ppm (Figure 5). The latter was assigned to trifluoroacetic acid by comparison with pure sample.

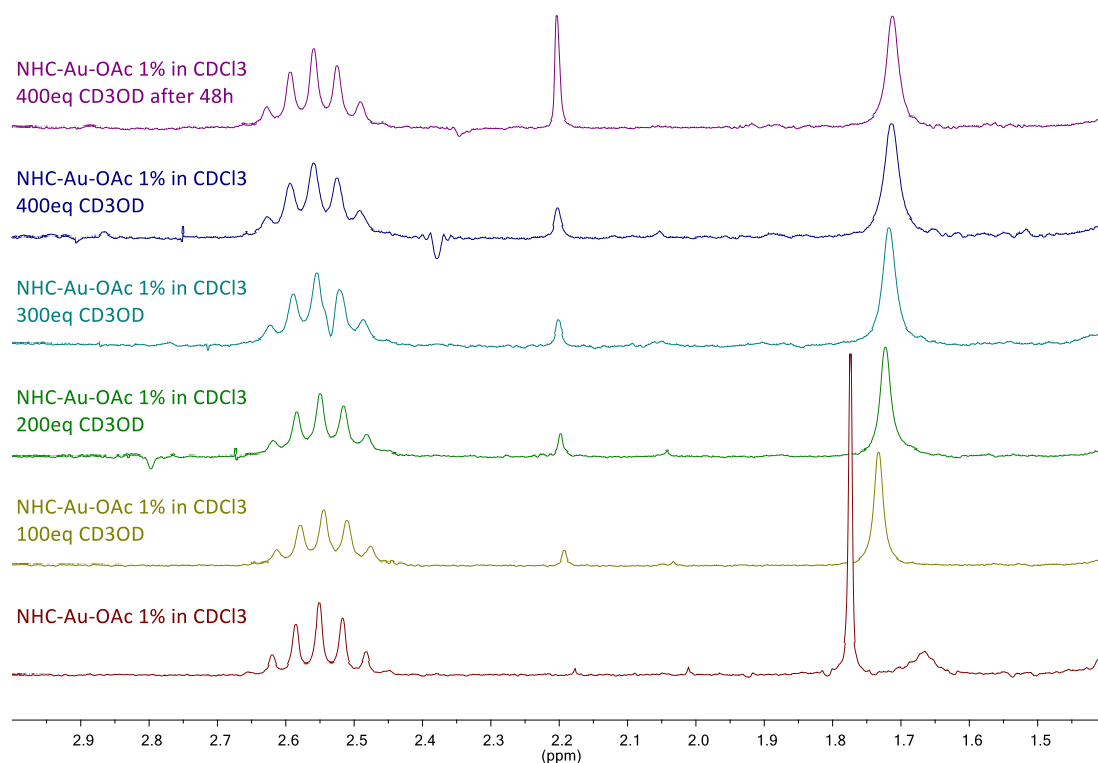


Figure 5. ^1H NMR spectra of 10Ac (CDCl_3 , 1 mM) in presence of an increasing concentration of methanol and after 48 hours (last spectrum)

Finally for **1OTs**, the treatment of a 1 mM solution of **1OTs** in CDCl_3 with 3.3, 9, 18 and 100 equivalents of 3-hexyne did not cause any variation in the ^1H NMR spectra of the cation, whereas the NMR signal of the anion (Figure 6) become progressively broader and slightly shifted to higher frequencies. Such broadening indicates that the anion and the 3-hexyne are involved in a dynamic equilibrium, which likely is the substitution of the anion by the 3-hexyne (ISIP/OSIP equilibrium). The fact that the frequency of the tosylate anion is only slightly influenced by the excess of 3-hexyne demonstrates that the OSIP is thermodynamically less favored than the ISIP, but kinetically accessible.

Analyzing the aromatic region of the NMR spectra recorded during the addition of MeOH to 3-hexyne catalyzed by **1OTs**, it is evident that the anion resonances changes during the course of the catalysis. In particular, the doublet due to the *ortho*-protons of the tosylate shifts from 7.14 ppm at $t = 6$ minutes to 7.08 ppm at $t = 18$ minutes

(Figure 7). The NMR signal of a non-coordinated tosylate anion can be estimated by the NMR shift of the salt NBu_4OTs , which is 7.17 ppm in $\text{CDCl}_3/\text{CD}_3\text{OD}$ (same concentration of methanol as in the catalytic conditions) and 7.05 in pure CDCl_3 . Since the pre-equilibrium is completely shifted toward the ISIP in absence of methanol, we can surmise that methanol may help the de-coordination of the anion, probably through the formation of a hydrogen bond.³² The importance of the pre-equilibrium step is demonstrated by the fact that the addition of an external salt as NBu_4OTs (5%) reduces the TOF to 297 h^{-1} , likely because of the shift of the ISIP/OSIP equilibrium toward the ISIP.

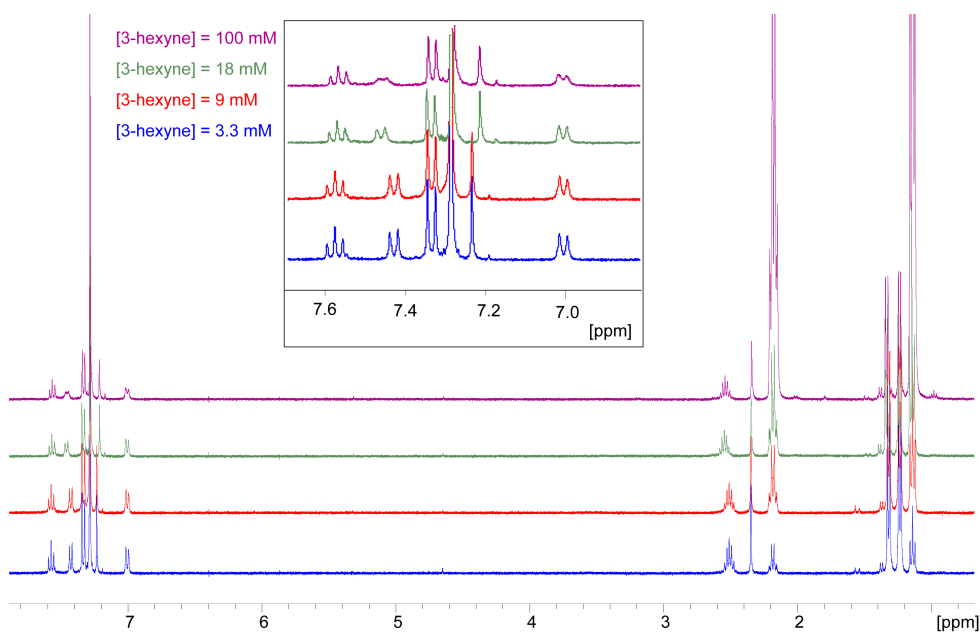


Figure 6. ^1H NMR spectra of 1OTs (CDCl_3 , 1 mM) in presence of an increasing concentration of 3-hexyne

³² M. Raducan, M. Moreno, C. Bour, A. M. Echavarren, *Chem. Commun.* **2012**, 48, 52-54

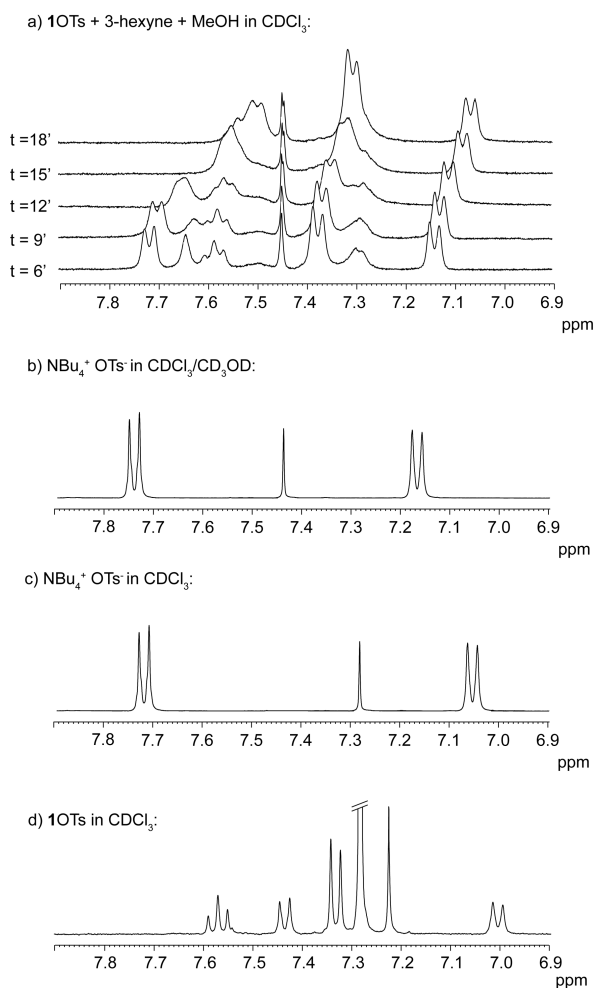


Figure 7. a) Aromatic region of ^1H NMR spectra recorded at different reaction times (indicated at the side of the spectra, in minutes) during the alkoxylation of 3-hexyne catalysed by 1OTs; b) ^1H NMR spectrum of NBu_4OTs in $\text{CDCl}_3/\text{CD}_3\text{OD}$; c) ^1H NMR spectrum of NBu_4OTs in CDCl_3 ; d) ^1H NMR spectrum of 1OTs in CDCl_3

Also in case of **1TFA**, the anion substitution by 3-hexyne is unfavored, but kinetically accessible. The treatment of a 1 mM solution of **1TFA** in CDCl_3 with 0.6, 1.6, 4 and 43 equivalents of 3-hexyne did not cause any variation in the ^1H NMR spectra and a small variation on the broad NMR signal of the anion (Figure 8). In particular, when the concentration ratio between the gold complex and the 3-hexyne is larger than 40, the NMR signal of the anion becomes broader and shifts to lower frequencies.

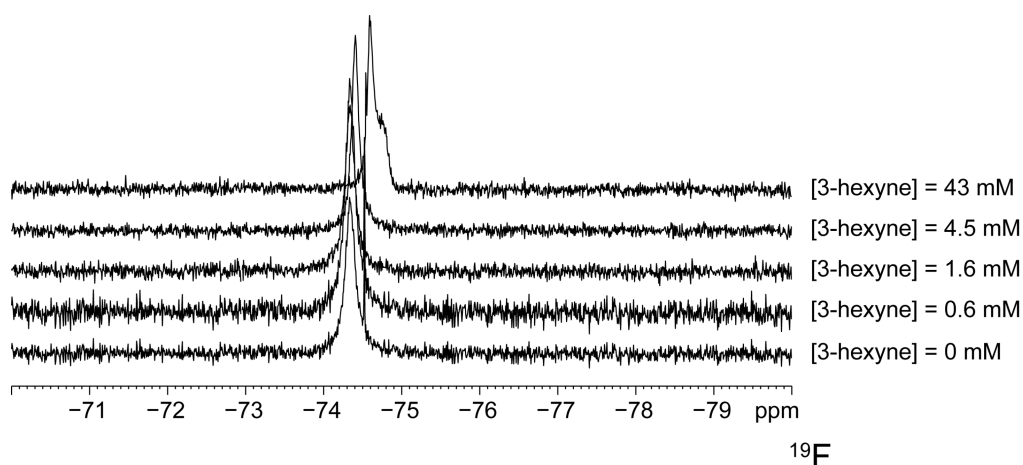


Figure 8. ^{19}F NMR spectra of **1TFA** (CDCl_3 , 1 mM) in presence of an increasing concentration of **3-hexyne**

Concerning **1PFHp**, the catalytic results (Table 1, entry 6) appear somewhat unexpected: the coordination/basicity properties of the PFHp^- anion should resemble those of the outperforming anions (OTs^- and OMs^-) while, when it behaves as counterion in **1PFHp**, the resulting catalytic activity is very poor (even lower than that shown by **1BAr^F**). Figure 2 clearly shows that its conversion profile is not well represented by a straight line but rather presents a bend at about 20 min. This pattern is consistent with one or more deactivation processes of the catalyst, which involve the anion. Two possible deactivation paths can be suggested: i) the PFHp^- anion can accept the alcoholic proton inducing formation of free MeO^- in solution, which poisons the catalyst (as previously observed for **1TFA**) and/or ii) it can form an unreactive tricoordinated species.³³ The treatment of a 1 mM solution of **1PFHp** in CDCl_3 with 400 eq of methanol did not cause any variation in the ^{19}F NMR spectra (Figure 9) and the formation of the corresponding acid, H-PFHp, was not observed, even in the catalytic conditions (Figure 10),³⁴ thus supporting that the formation of the unreactive tricoordinate species may be a reasonable explanation for the reduced activity of **1PFHp**.

³³ Ciancaleoni, G.; Belpassi, L.; Zuccaccia, D.; Tarantelli, F.; Belanzoni, P. *ACS Catal.* **2015**, *5*, 803-814

³⁴ Rocchigiani, L.; Jia, M.; Bandini, M.; Macchioni, A. *ACS Catal.* **2015**, *5*, 3911-3915

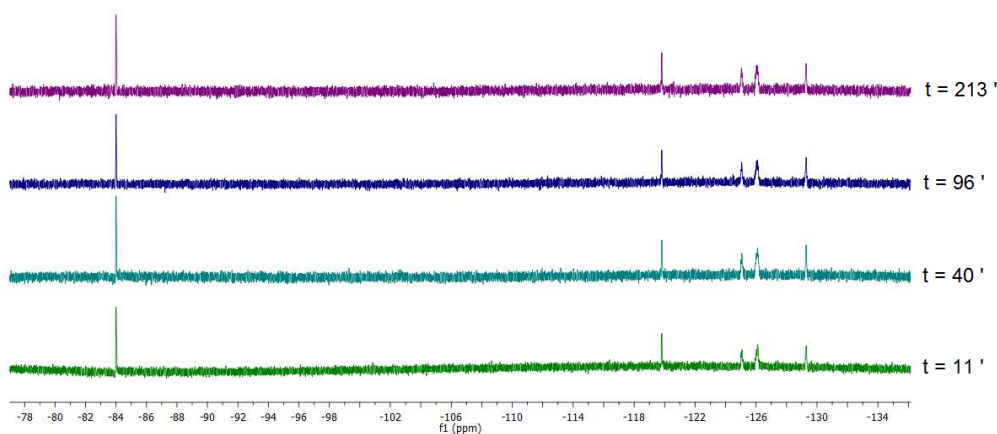


Figure 9. ^9F NMR spectra of 1PFHp (CDCl_3 , 1mM) in presence of 400 eq of methanol, recorded at different times

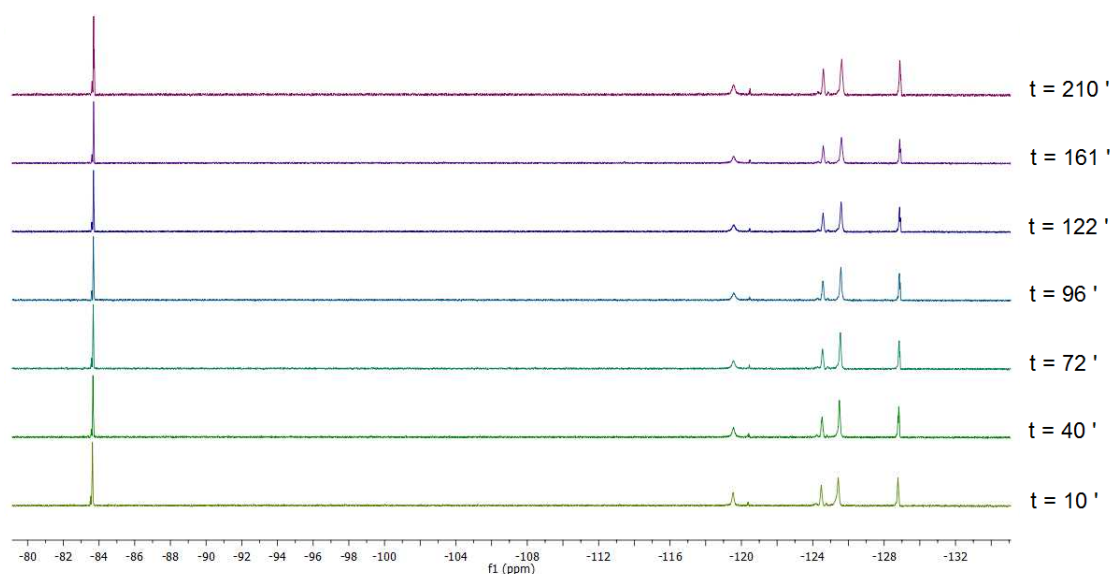


Figure 10. ^9F NMR spectra of 1PFHp in catalytic condition, recorded at different times

In order to highlight the pivotal importance of the anion in the catalytic performances of the complexes, a few catalytic trials were run in nitromethane- d_3 at 50 °C. In these experimental conditions (which are known to prevent the ion pairing phenomenon),³⁵ the complexes **1OTs** and **1OTf** exhibit a similar catalytic efficiency (Table 1, entries 13 and 14, Figure 11), regardless the nature of the anion.

³⁵ Zuccaccia, D.; Macchioni, A. *Organometallics* **2005**, *24*, 3476-3486

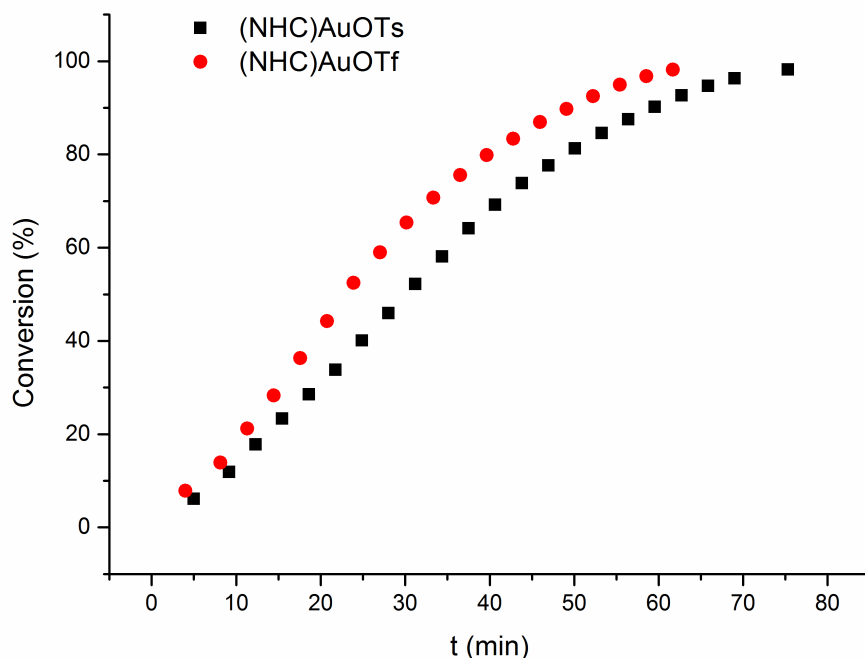


Figure 11. Rate of alkoxylation of 3-hexyne catalyzed by 1OTs and 1OTf in CD_3NO_2

The order of reaction with respect to **1OTs** was determined, which resulted to be 1 (see **Experimental Section**). Note that the same order has been measured in the case of non-coordinating anions.⁶

Consequently, only one gold atom is involved in the rate-determining step of the reaction. However, the latter can be either the nucleophilic attack or the protodeauration (Scheme 2). Different catalytic conditions have been tested. In order to prove that protodeauration was the rate-determining step, the reaction was carried out in presence of HOTs (15%), observing a deceleration with TOF values changing from 309 to 263 h^{-1} (entries 7 and 16, Table 1). In addition, using CH_3OD instead of CH_3OH , we observe a slight reduction of the TOF, which shifts from 309 to 292 h^{-1} (compare entries 7 and 17, Table 1), giving a Kinetic Isotopic Effect (KIE)³⁶

³⁶ M. Gómez-Gallego M. A. Sierra *Chem. Rev.* **2011**, *111*, 4857-4963

equal to 1.1. For **1BF₄** and **1BAr^F**, the KIE resulted equal to 1.7 and 1.9 respectively (entries 9-19, 10-20, Table 1). These values of KIE point out that, under our conditions, the turnover-limiting step is the nucleophilic attack of the methanol.³⁷ However, the small increase of the KIE going from more coordinating anion (OTs⁻) to non-coordinating one (BAr^{F-}), may indicate that the importance of protodeauration step in the mechanism increases from OTs⁻ to BF₄⁻ and from BF₄⁻ to BAr^{F-}. In agreement with our findings, Zhdanko and Maier showed clearly that the reaction rate of the hydroalkoxylation of 3-hexyne by methanol (in methanol), is independent from the amount of acid, excluding the protodeauration as the rate-limiting step.⁶ We also note that the turnover-limiting step strongly depends on the reaction conditions and on the reactants. In a recent paper by Straub and co-workers³⁸ a KIE of 3-5 is observed for the hydration of terminal alkyne conducted in methanol, while the group of Gagné and Widenhoefer reported a KIE of 5.3 for the gold-catalyzed intramolecular hydroalkoxylation of 2,2-diphenyl-4,5-hexadien-1-ol to a 2-vinyltetrahydrofuran derivative.³⁹ These authors suggest that protonolysis of the gold-carbon bond was the turnover-limiting step in both cases.

³⁷ E. M. Simmons J. F. Hartwig, *Angew. Chem.* **2012**, *124*, 13, 3120-3126; *Angew. Chem. Int. Ed.* **2012**, *51*, 3066-3072

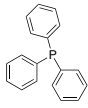
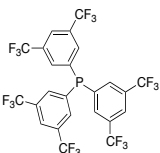
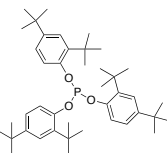
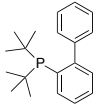
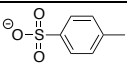
³⁸ S. G. Weber, D. Zahner, F. Rominger, B. F. Straub *ChemCatChem* **2013**, *5*, 2330-2335

³⁹ T. J. Brown, D. Weber, M. R. Gagné, R. A. Widenhoefer, *J. Am. Chem. Soc.* **2012**, *134*, 9134-9137

2.2. Nature of the ligand and anion effect interaction

A rational understanding about the effect of ligand and the anion on the catalytic performances was obtained in the methoxylation of 3-hexyne (Scheme 3).

With this aim, a set of 10 gold complexes (Scheme 5) were generated *in situ*, combining five P-ligands, differing in the electron withdrawing ability, in order to modulate the acid character of the $L-Au^+$ fragment, with two anions OTs^- and OTf^- , which have different coordinating ability and basicity.

L					
X⁻	L2 PPh ₃	L3 (tBu) ₃ P	L4 PAr ^F	L5 phos	L6 JohnPhos
	2OTs	3OTs	4OTs	5OTs	6OTs
	2OTf	3OTf	4OTf	5OTf	6OTf

Scheme 5. Complete set of phosphine gold catalysts, generated *in situ*

In general, phosphines are usually strong σ -donor ligands and weak π -acceptors, and this effect can be increased with electron-donating groups in the R substituents, while electron withdrawing groups favor the π -acceptor backbonding.

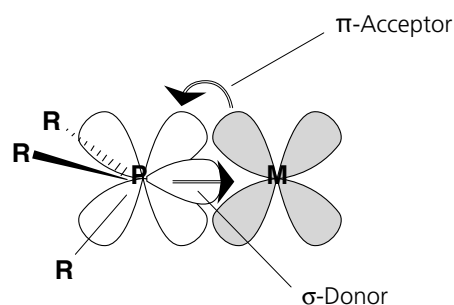


Figure 12. Electronic structure of phosphine ligands

The size and the steric demand of phosphine ligands are approximately described by the Tolman's cone angle,⁴⁰ θ .

Among the aryl-type, PPh_3 , **L2**, is the most commonly used in catalysis, because of its higher stability and easier handling. Starting from the triphenylphosphine, the electronic properties can be modulated through the substituents on the aromatic rings, as in case of PAR^{F} ligand, **L4**, whose $-\text{CF}_3$ groups enhance the acidity of the metallic fragment.

In the case of the asymmetric phosphine JohnPhos, **L6**, the value of the cone angle is very large due to the protruding phenyl ring. On the other hand, the electron-donating properties can be described by Tolman's electronic parameter, which is the C=O infrared absorption of the compound $\text{R}_3\text{P-Ni}(\text{CO})_3$. Tolman's electronic parameter is not available for ligands **L6** and **L5**, but one can easily guess that the latter is the least electron-donating ligand, among the considered ones, because of its small donation (due to the electron-withdrawing oxygen atoms) and large ability to accept back-donation (due to the low σ^* orbital) typical of phosphites.⁴¹

The electronic feature of phosphine **L6** is less obvious: having two *tert*-butyl groups and an aromatic one, we could expect that it is less electron-donating than **L3**. On the other hand, it was shown that the protruding phenyl of **L6** has the possibility to interact with the gold atom,⁴² this could increase its electron density donation to the metal.⁴³

A typical catalytic run was performed by mixing 3-hexyne and methanol in the presence of the catalyst precursor **2-6Cl** and the appropriate silver salt ($\text{X}^- = \text{OTs}^-$ and OTf^-), at 30 °C in CDCl_3 .

⁴⁰ Tolman, C. A. *Chem. Rev.*, **1976**, 77, 313-348

⁴¹ Crabtree R. H. *Carbonyls, Phosphine Complexes, and Ligand Substitution Reaction*, in *The Organometallic Chemistry of the Transition Metals*, Fourth Edition, John Wiley & Sons, Inc., Hoboken, NJ, **2005**, USA

⁴² Touil, M. Bechem, B. Hashmi, A. S. K. Engels, B. Omary M. A. and Rabaâ, H. *Mol. Struct. J. THEOCHEM*, **2010**, 957, 21-25

⁴³ Ciancaleoni, G., Belpassi, L., Tarantelli, F., Zuccaccia, D., Macchioni, A. *DaltonTrans.*, **2013**,42, 4122-4131

The “silver effects” are negligible under our catalytic conditions, as demonstrated by Zuccaccia *et al.*,⁴⁴ who obtained similar reactivity with the isolated complex [(PPh₃)AuOTf] and the *in situ* generated catalyst [(PPh₃)AuCl]/AgOTf.

The progress of the reaction was monitored by NMR spectroscopy, until 30% of conversion was reached; the linear reaction profiles ensure that the catalyst deactivation can be neglected. It is noteworthy that gold catalyst decay involves the formation of the catalytically inactive species [L-Au-L], which subsequently undergoes the reduction to gold(0), and is a ubiquitous phenomenon, particularly pronounced with phosphines.⁴⁵

The catalytic results are reported in Table 2 and Figure 13. For useful comparison, the already obtained results concerning complexes **1X** (**L1** = NHC, 1,3-bis(2,6-diisopropylphenyl)imidazol-2-ylidene; **X** = OTs⁻, OTf⁻) have been added.

⁴⁴ Biasolo, L., Del Zotto, A., Zuccaccia, D. *Organometallics*, **2015**, *34*, 1759–1765

⁴⁵ Wang, W., Hammond, G. B., Xu, B. *J. Am. Chem. Soc.* **2012**, *134*, 5697-5705

Table 2: TOF values for gold(I) catalyzed methoxylation of 3-hexyne

Catalyst	TOF (h ⁻¹) ^a
1OTs	309
2OTs	52.2
3OTs	90
4OTs	204
5OTs	426
6OTs	240
1OTf	196
2OTf	96
3OTf	510
4OTf	102
5OTf	504
6OTf	330

^a TOF determined by ¹H NMR spectroscopy; TOF = $(n_{\text{product}} / n_{\text{catalyst}}) / \text{time}$ at 30% of conversion

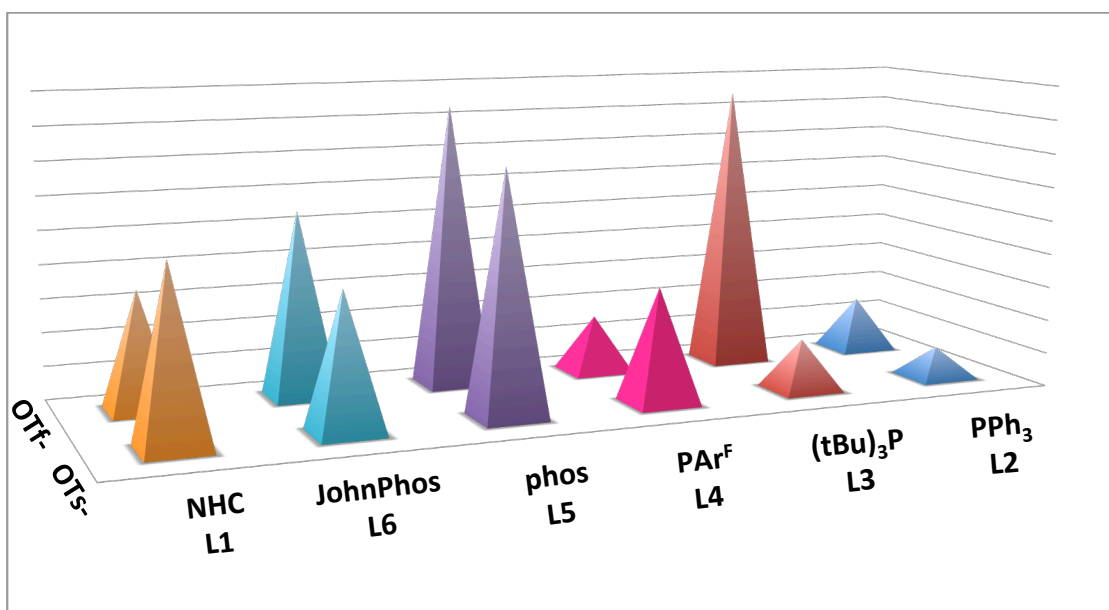


Figure 13. TOF, Turnover Frequencies (h⁻¹), values for the reaction promoted by 1-6X, determined at 30% of conversion

When the anion is OTs⁻, the higher catalytic activity is observed with the ligand **L5**, (tris(2,4-di-*tert*-butylphenyl)phosphite, **phos**), followed by **L6** (2-biphenyl)di-*tert*-butylphosphane, **JohnPhos**), **L4** (tris(3,5-bis-trifluoromethylphenyl)phosphane, **PAr^F**), **L3** (tri-*tert*-butylphosphane, **(tBu)₃P**), and, finally, **L2** (triphenylphosphane, **PPh₃**), with TOF values of 426, 240, 204, 90 e 52.2 h⁻¹ respectively.

On the other hand, with OTf as anion, **L3** and **L5** showed high and similar activities (TOF = 510 and 504 h⁻¹), **L6** an intermediate activity (TOF = 330 h⁻¹), and, finally, **L4** and **L2** the poorest activities (TOF = 102 and 96 h⁻¹).

For P-ligands, OTf seems to be the most suitable anion, except for **L4**, which presents TOF values higher with OTs⁻ than with OTf. The reduced catalytic activity of **4OTf** can be explained considering its strong catalyst deactivation, as confirmed by the ³¹P NMR spectra (Figure 14).

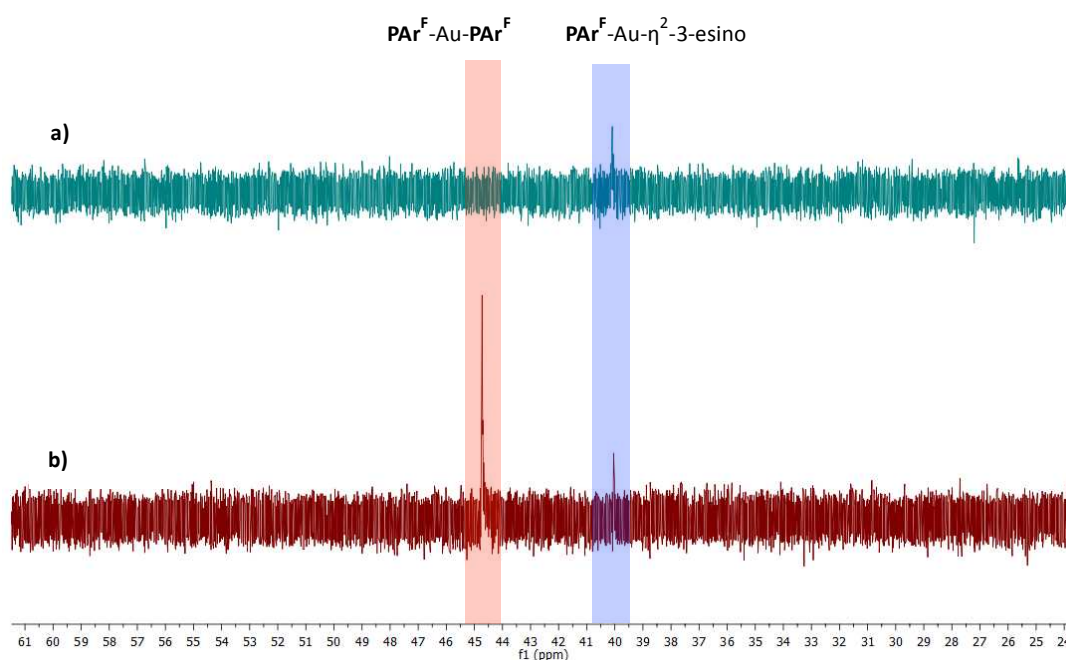


Figure 14. Section of ^{31}P NMR spectra for methoxylation of 3-hexyne promoted by a) 4OTs and b) 4OTf

The opposite trend is observed with NHC-containing catalysts, with TOF values of 309 h^{-1} for **1OTs** and 196 h^{-1} for **1OTf**. We can ascribe the worse catalytic behavior when phosphanes are bound to gold, rather than NHC, to the higher coordination power of OTs^- , but it is also possible that OTs^- shows a different ability to hold the methanol for the outer sphere attack, as a hydrogen bond acceptor, when NHC are replaced with the other phosphanes.

The counterion role becomes significant when **L3** is considered. In particular, the latter combined with OTs^- showed a poor catalytic activity (90 h^{-1}), whereas the presence of OTf^- , less coordinating and basic, leads to the highest activity registered in the considered series (510 h^{-1}).

2.3. Role of the ion pair

The counterion plays a crucial role in deciding the coordination mode of the ligand to the metal center. A key point is the comprehension of the structure and activity of the ion pair and therefore of the postulated intermediates (Scheme 2), strongly depending on the solvent and on the properties of the anion.

Ion pairs are defined as pairs of oppositely charged ions, with a common solvation shell, held together prevalently by Coulombic forces.⁴⁶ We can distinguish three different types of transition metal ion pairs (Figure 15): an ion pair in which no solvent molecule interposes between the two ions is called a *contact (or intimate or tight) ion pair* (A3 or D3), whereas when one solvent shell separates the two ions it is called *solvent-shared ion pair* (B3), otherwise *solvent-separated ion pair* (C3) if every ion has its own solvation shell.

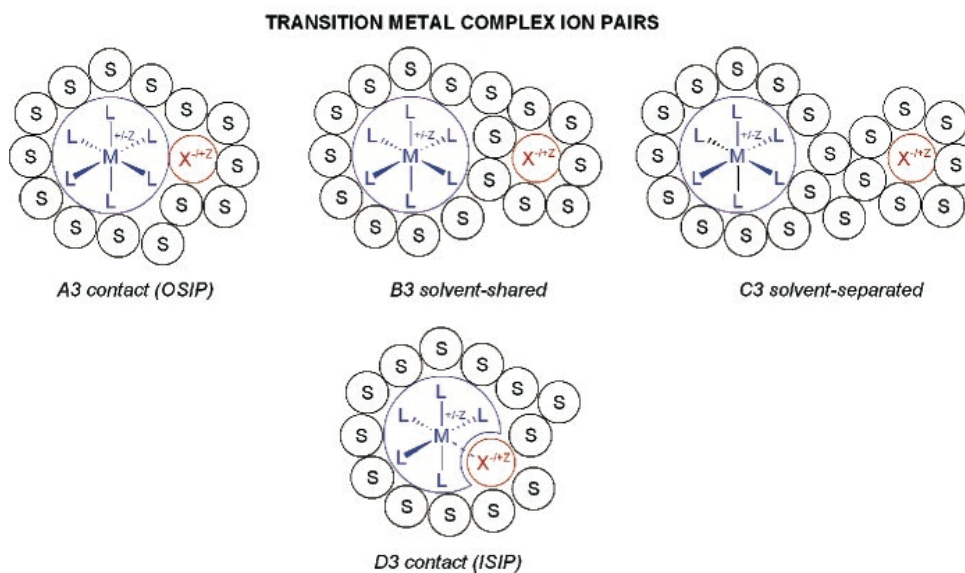


Figure 15. Transition metal complex ion pairs. Reproduced from ref. 42

⁴⁶Macchioni, A. *Chem. Rev.* **2005**, 105, 2039–2073

Assuming that the anion-cation interactions are always of an electrostatic nature, we can define the two contact ion pairs as outer-sphere ion pairs (OSIPs) and inner-sphere ion pairs (ISIPs) (A3 and D3 in Figure 15, respectively).

The tendency to form ion pairs normally decreases when the relative permittivity of the solvent increases. However, the presence of transition-metal organometallic ion pairs is not only limited to low-polarity solvents ($\epsilon_r < 10$) but also significant in solvents with moderate ($10 < \epsilon_r < 20$) to high relative permittivity ($\epsilon_r > 30$). It is not easy to predict the tendency of transition-metal organometallic ion pairs to form in solvents of different nature, even if they have the same relative permittivity.

In order to investigate the relative orientation anion - cation, the methoxylation of 3-hexyne were carried out in four different solvents, with increasing polarity, such as benzene ($\epsilon_r = 2.284$),⁴⁷ chloroform ($\epsilon_r = 4.806$),²³ nitromethane ($\epsilon_r = 35.87$)²³ and propylene carbonate ($\epsilon_r = 66$).⁴⁸

All the reactions were promoted by Au(I)-complexes, **5OTs** and **5TFA**, bearing phosphite ligand and OTs⁻ or TFA⁻ as counterions. In particular, [(phos)AuOTs] was synthesized in our laboratory for the very first time (see **Chapter 2, Experimental Section**).

All the results are shown in Table 3 and Figure 16.

⁴⁷Maryott, A. A.; Smith, R. E. *Table of Dielectric Constants of Pure Liquids*, United States Department of Commerce, National Bureau of Standards Circular 514, **1951**.

⁴⁸Simeral, L.; Amey, R. L. *The Journal of Physical Chemistry* **1970**, *74*, 1443-1446

Table 3. TOF values for methoxylation of 3-hexyne in different solvents

Solvent	5OTs ^a (h ⁻¹)	5TFA ^a (h ⁻¹)
Benzene	228	6.6
Chloroform	414	19.2
Nitromethane	234	22.8
Propylene Carbonate	90	17.4

^a TOF determined by ¹H NMR spectroscopy; TOF = ($n_{\text{prodotti}} / n_{\text{catalyst}}$) / time at 30% of conversion

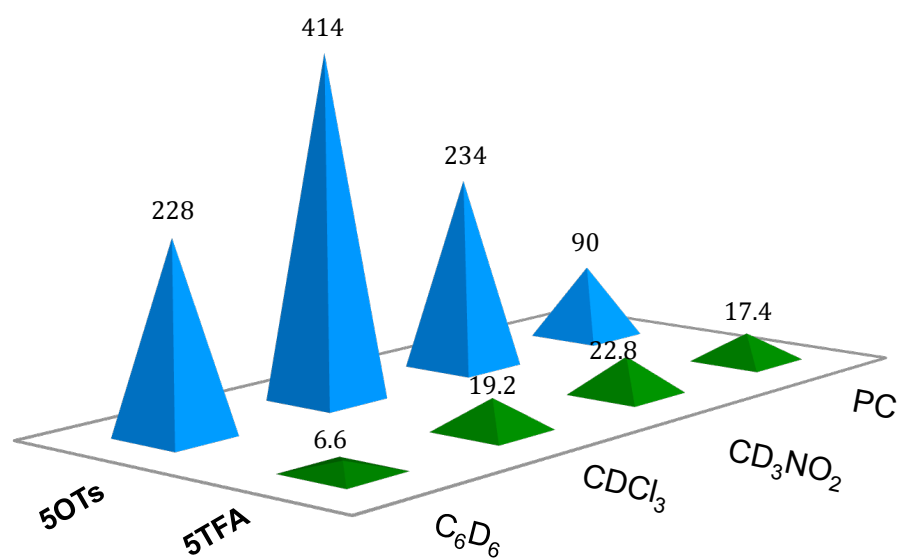


Figure 16. TOF values for the methoxylation of 3-hexyne promoted by 5OTs and 5TFA in different solvents

The results clearly show an effect of the solvent on the structure of the ion-pair. In particular, the best catalytic performances were registered using OTs⁻ anion in chloroform: in this solvent, with a moderate permittivity, the anion holds the reactive methanol molecule in the right position, helping the nucleophilic attack.

Whereas, the lower activity registered in the others solvents is probably due to: in benzene, the low permittivity leads to the shift to the ISIP species in the pre-equilibrium step (Scheme 2), preventing the substrate coordination and, therefore, the reaction; in the nitromethane and in PC, the anion is moved apart from the cation because of the high permittivity of the solvents, becoming just a spectator.

On the other hand, **5TFA** showed an overall worsening in the TOF values. The more coordinating TFA⁻ leads to a higher ISIP concentration than OTs⁻ and this explains the lower catalytic activity. A light enhancement in TOF value takes place in chloroform, but, a reduced activity compared to **5OTs**, it is a consequence of the catalyst poisoning, as already described for **1TFA** (see **Section 2.2**).

However, no raise in the catalytic activity is registered increasing solvent polarity, (from chloroform to nitromethane and PC). We can imagine a competition between the substrate and OMe⁻ for the cationic [L-Au]⁺ species. In fact, monitoring the reaction in CD₃NO₂, ³¹P NMR spectra showed a signal at 122 ppm for both **5OTs** and **5TFA**, relative to [(phos)Au(η²-3-hexyne)]⁺, whereas, just in case of **5TFA**, the presence of another resonance at 136 ppm suggests the formation of a different species, which could be either [(phos)AuOMe] or [L₂Au]⁺ (Figure 17). Unfortunately, to the best of our knowledge, there are no literature data to confirm this hypothesis.

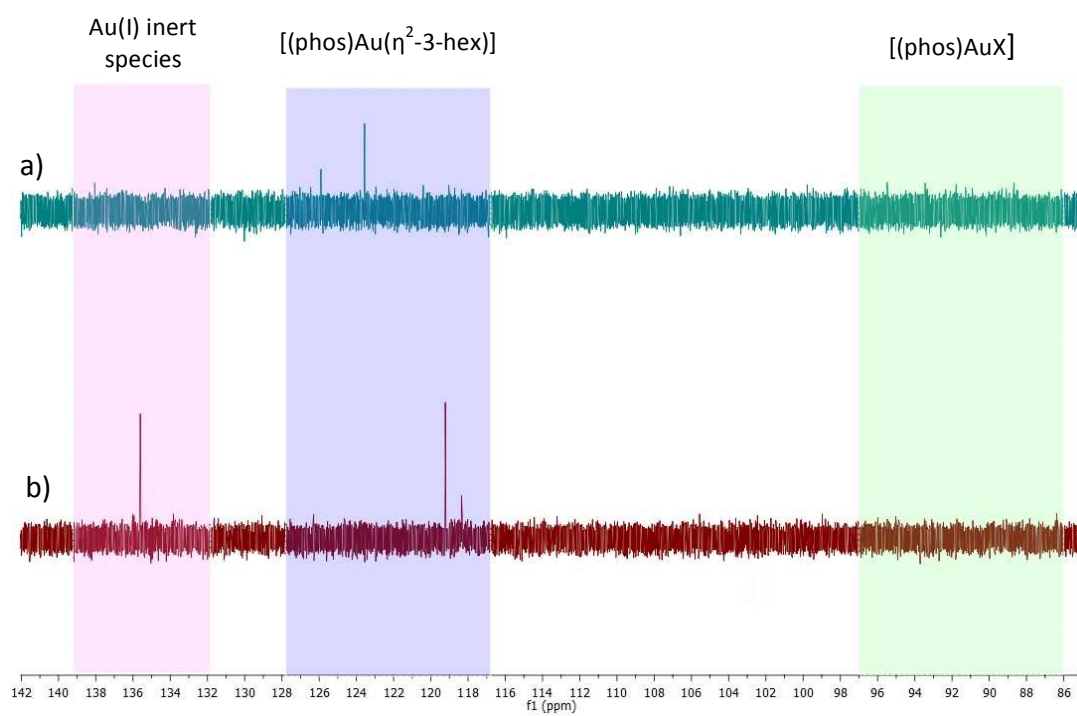


Figure 17. Section of ^{31}P NMR spectra for methoxylation of 3-hexyne promoted by a) 5OTs and b) 5TFA

3. Experimental section

3.1. General procedures and materials

All reagents and solvents were obtained from commercial sources and were used without any further purification. The products were characterized by ^1H , ^{19}F and ^{31}P NMR spectroscopies. The spectra were recorded with a Bruker AVANCE Ultra ShieldTM 400 spectrometer. Referencing is relative to TMS (^1H), H_3PO_4 (^{31}P) and CCl_3F (^{19}F).

3.2. Alkoxylation procedure

All experiments were followed by *in situ* ^1H NMR. 3-hexyne (100 μL , 0.88 mmol), TMS (20 μL) and the appropriate solvent (400 μL) were added in a screw-cap NMR tube containing the proper catalyst loading (see **Table S1**). In case of **2-4OTs**, **6OTs** and **2-6OTf**, the catalyst has been activated *in situ*, mixing the appropriate precursor with corresponding silver salt. Then, CH_3OH or CH_3OD (143 μL , 3.52 mmol) was added by syringe. The tube was briefly shaken for a moment and the time count was started. The reaction mixture was further monitored by NMR at 30 $^\circ\text{C}$ (50 $^\circ\text{C}$ using CD_3NO_2 only with **1OTf** and **1OTs** 0.5 mol%). In case of propylene carbonate as solvent the reactions were carried out in our laboratory, taking 50 μL aliquots every 30 min (for **5TFA**) and 15 min (for **5OTs**), cooled at -30 $^\circ\text{C}$ and, then, the product characterization was obtained by NMR spectroscopy in CDCl_3 .

Conversion was calculated from the integral intensities of the corresponding signals (conversion [%] = $(n_{\text{acetal}} + n_{\text{vinylether}} + n_{\text{ketone}}) / (n_{\text{alkyne}}) \times 100$).

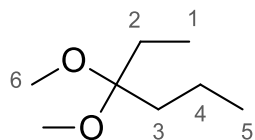
Table S1. Catalytic conditions

solvent	nucleophile	catalyst	Catalyst loading (%)
CDCl ₃	MeOH (3.52 mmol, 143 μL)	1TFA, 1OTf, 1OAc, 1BF₄, 1BAR^F, 1OMs, 1NTf₂, 1NO₃, 1ptm, 1ClO₄, 1PFHp, 1OTs	1
CDCl ₃	MeOH (3.52 mmol, 143 μL)	2OTs,^a 2OTf,^a 3OTs,^a 3OTf,^a 4OTs,^a 4OTf,^a 5OTs, 5OTf,^a 5TFA, 6OTs,^a 6OTf^a	0.5
CDCl ₃	MeOH (3.52 mmol, 143 μL)	1OTs^b	1
CDCl ₃	MeOH (3.52 mmol, 143 μL)	1OTs	0.5, 1.5, 2
CDCl ₃	CH ₃ OD (3.52 mmol, 143 μL)	1OTs, 1BF₄, 1BAR^F	1
CD ₃ NO ₂	MeOH (3.52 mmol, 143 μL)	1OTs, 1OTf, 5OTs, 5TFA	0.5
benzene	MeOH (3.52 mmol, 143 μL)	5OTs, 5TFA	0.5
Propylene carbonate	MeOH (3.52 mmol, 143 μL)	5OTs, 5TFA	0.5

^a generated *in situ*; ^b with 5% N(Bu)₄OTs or 15% *p*TsOH

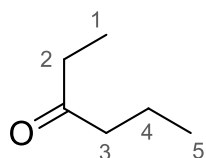
All experiments were performed starting from the same concentration of [3-hexyne]₀ at initial time (t = 0) (within the experimental error as evaluated by NMR), and a conversion up to 99% in acetal was achieved. In the presence of **1OTs** the catalysis was carried out by changing the catalyst loading (entries 1-4, Table S1) from 0.5 to 2 mol% observing a pseudo-linear correlation between the average rate [3-hexyne]₀/t versus [**1OTs**]. This trend suggests a 1st order dependence on catalyst as recently reported in the literature¹⁹ for non-coordinating anions.

3.3 Product characterization



3,3-dimethoxyhexane - ^1H NMR (CDCl_3 , 400 MHz, 298 K): δ (ppm) 3.15 (s, 6H, H6), 1.54 (m, 4H, H2 and H3), 1.25 (m, 2H, H4), 0.92 (t, $J_3^{\text{HH}} = 7.3$ Hz, 3H, H1), 0.82 (t, $J_3^{\text{HH}} = 7.4$ Hz, 3H, H5).

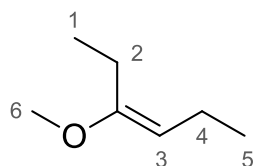
3,3-dimethoxyhexane D2 - ^1H NMR (CDCl_3 , 400 MHz, 298 K): δ (ppm) 3.15 (s, 6H, H6), 1.59 (q, $J_3^{\text{HH}} = 7.6$ Hz, 2H, H2), 1.33 – 1.15 (m, 2H, H4), 0.93 (t, $J_3^{\text{HH}} = 7.3$ Hz, 3H, H1), 0.82 (t, $J_3^{\text{HH}} = 7.5$ Hz, 3H, H5).



3-hexanone - ^1H NMR (CDCl_3 , 400 MHz, 298 K): δ (ppm) 2.36 – 2.39 (t - q, $J_3^{\text{HH}} = 7.4$ Hz, $J_3^{\text{HH}} = 7.3$ Hz, 4H, H2 and H3), 1.58 (m, 2H, H4), 1.03 (t, $J_3^{\text{HH}} = 7.4$ Hz, 3H, H1), 0.89 (t, $J_3^{\text{HH}} = 7.4$ Hz, 3H, H5).

3-hexanone D2 - ^1H NMR (CDCl_3 , 400 MHz, 298 K): δ (ppm) 2.37 (q, $J_3^{\text{HH}} = 7.5$ Hz, 2H), 1.61-1.57 (m, 2H, H4), 1.04 (t, $J_3^{\text{HH}} = 7.4$ Hz, 3H, H1), 0.87 (t, $J_3^{\text{HH}} = 7.3$ Hz, 3H, H5).

3-methoxy-3-hexene - ^1H NMR (CDCl_3 , 400 MHz, 298 K): δ (ppm) 4.35 (t, $J_3^{\text{HH}} = 7.3$, 1H, H3), 3.53 (s, 3H, H6), 2.00 (m, 4H, H2 and H4), 1.06 (t, $J_3^{\text{HH}} = 7.2$, 6H, H1 and H5).



3-methoxy-3-hexene D1 - ^1H NMR (CDCl_3 , 400 MHz, 298 K): δ (ppm) 3.52 (s, 3H, H6), 2.05-2.01 (m, 4H, H2 and H4), 1.09 (t, $J_3^{\text{HH}} = 7.4$ Hz, 6H, H1 and H5).

Table S2. 1OTs 0.5 mol%

t [min]	Conversion [%]
5.9	12.04
8.9	21.40
11.9	28.91
14.9	37.84
17.9	47.18
20.9	56.35
23.9	65.92
26.9	76.24
29.9	84.45
32.9	94.83
35.9	97.31

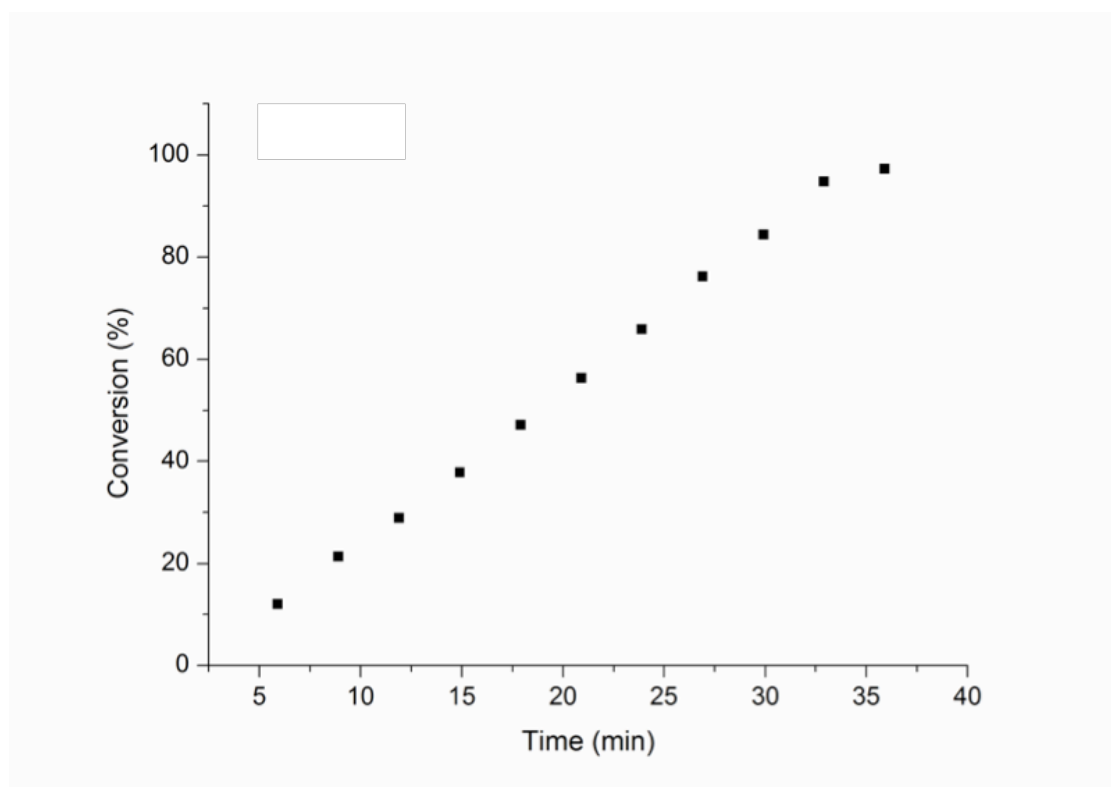


Figure S1. Plot of conversion (%) vs time (min)

Table S3. 1OTs 1 mol%

t [min]	Conversion [%]
4.67	17.53
6.17	28.46
7.67	36.95
9.17	46.86
10.67	57.43
12.17	66.90
13.67	75.88
15.17	84.82
16.67	92.12
18.17	96.87
19.67	99.54

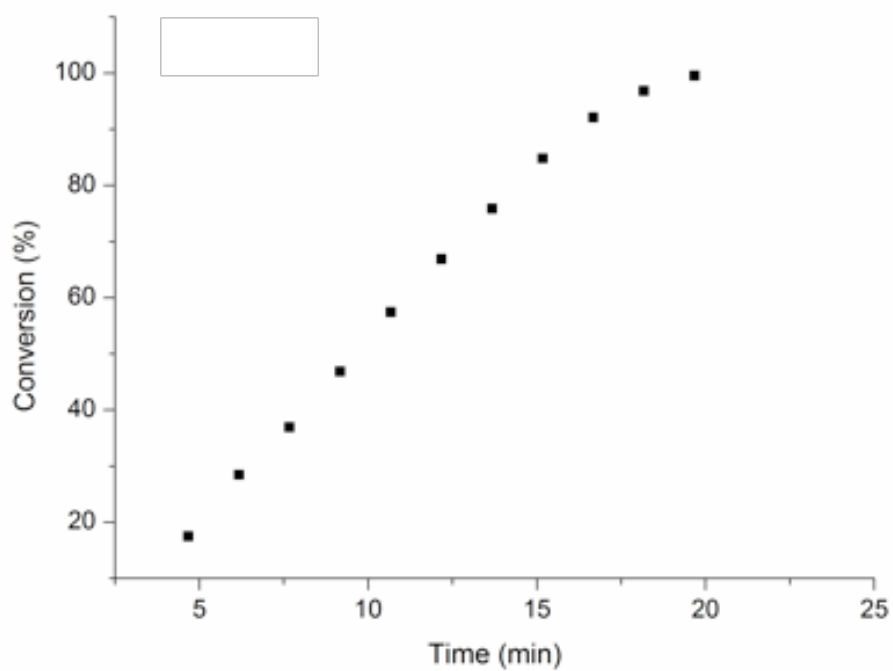


Figure S2. Plot of conversion (%) vs time (min)

Table S4. 1OTs 1.5 mol%

t [min]	Conversion [%]
3.5	21.58
6.5	52.34
9.5	87.39
12.5	98.32

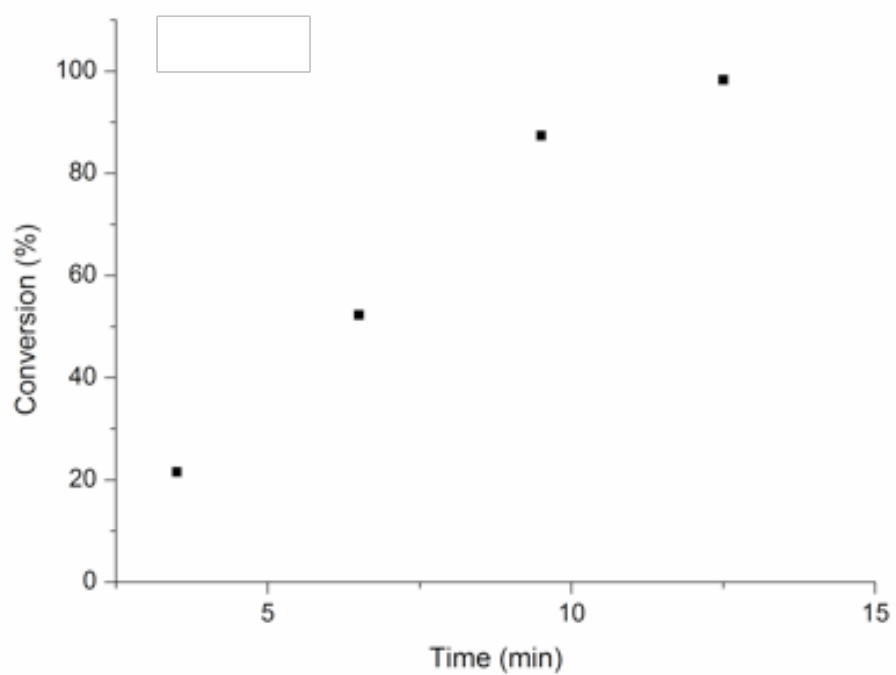


Figure S3. Plot of conversion (%) vs time (min)

Table S5. 1OTs 2 mol%

t [min]	Conversion [%]
3.8	44.62
6.8	94.61
9.8	99.04

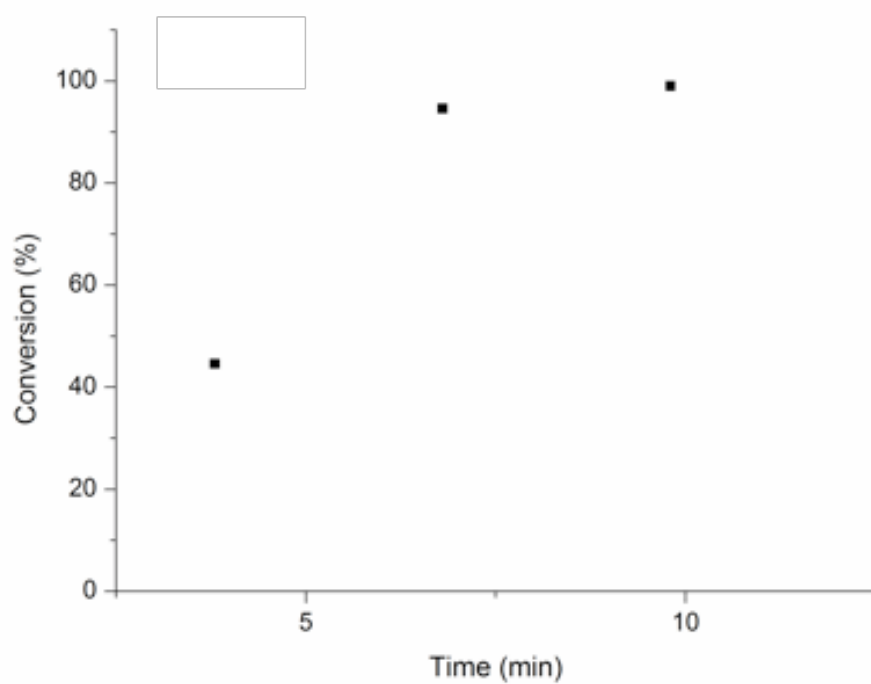


Figure S4. Plot of conversion (%) vs time (min)

Table S6. $1BF_4$

t [min]	Conversion [%]
4,2	12,83
6,2	20,04
8,2	26,75
10,2	31,87
12,2	37,61
14,2	41,97
16,2	47,71
18,2	53,08
20,2	57,83
22,2	63,55
24,2	67,46
26,2	71,22
28,2	76,46
30,2	80,87
32,2	84,18
34,2	87,6
36,2	89,25
38,2	93,87
40,2	95,53
42,2	99,21

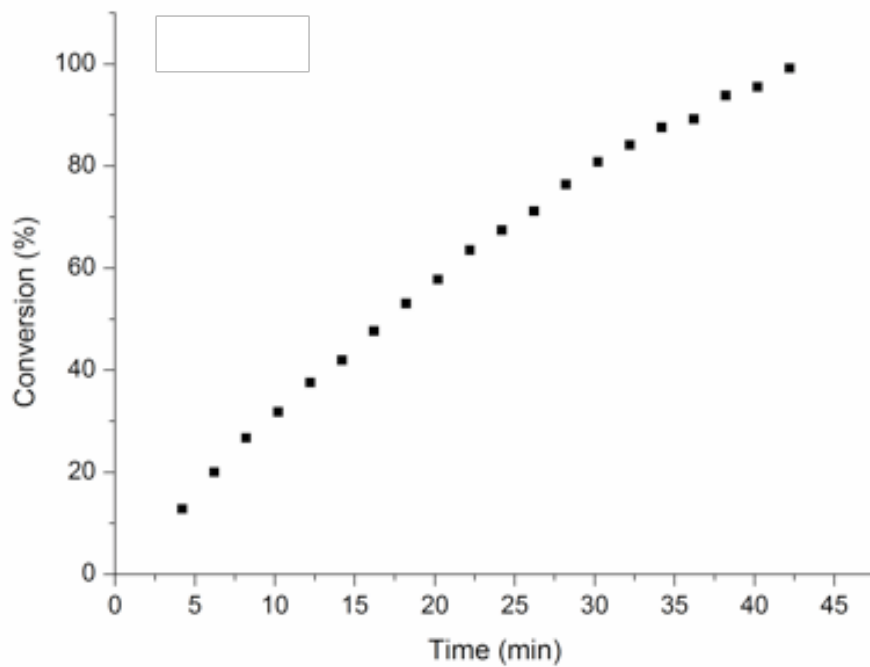


Figure S5. Plot of conversion (%) vs time (min)

Table S7. 1BAr^F

t [min]	Conversion [%]
4.8	12.67
6.8	18.50
8.8	24.00
10.8	29.20
12.8	33.63
14.8	41.07
16.8	44.25
18.8	46.90
20.8	53.81
22.8	56.89
24.8	60.71
26.8	63.11
28.8	65.79
30.8	72.32
32.8	73.36
34.8	75.65
36.8	80.00
38.8	81.03
40.8	85.96
42.8	87.72
44.8	91.15
46.8	90.04
48.8	96.92
50.8	97.37
52.8	99.56

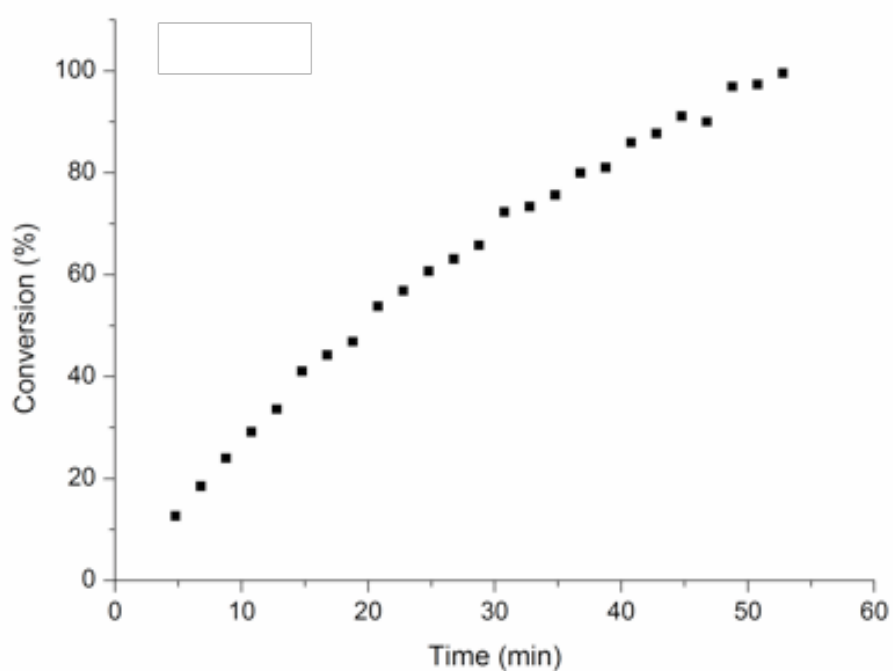


Figure S6. Plot of conversion (%) vs time (min)

Table S8. 1TFA

t [min]	Conversion [%]
14.2	1.96
26.2	9.91
38.2	20.00
50.2	30.56
62.2	40.48
74.2	49.24
86.2	56.71
98.2	63.10
110.2	68.25
122.2	72.79
134.2	76.50
146.2	79.53
158.2	81.82
170.2	84.04
182.2	86.15
194.2	88.83
206.2	90.26
218.2	92.97
236.2	93.75
266.2	95.73
272.2	96.04

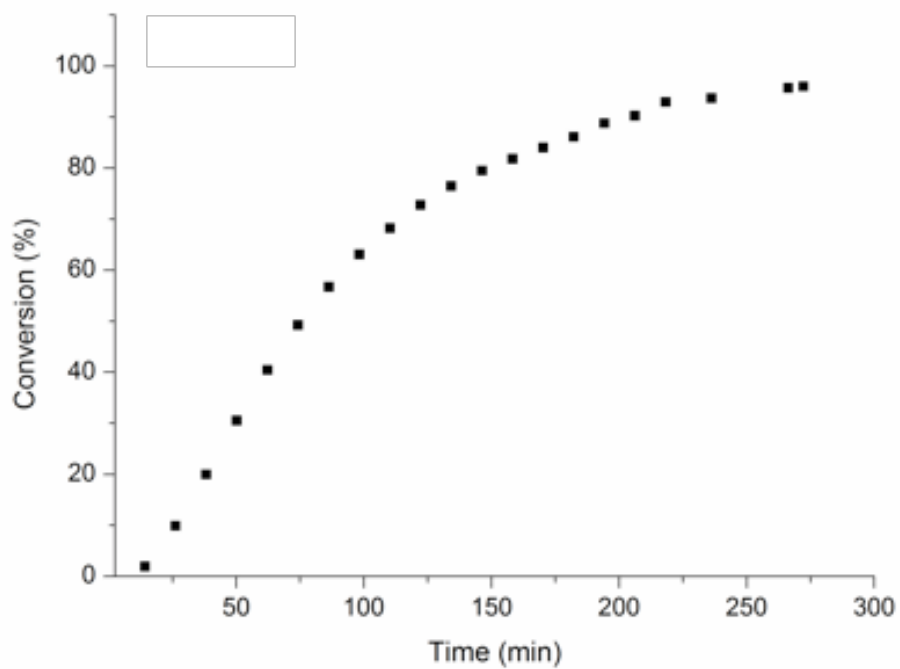


Figure S7. Plot of conversion (%) vs time (min)

Table S9. 1OTs + CD₃OD

t [min]	Conversion [%]
3.5	25.91
5.5	37.75
7.5	48.86
9.5	58.90
11.5	70.16
13.5	79.61
15.5	87.74
17.5	94.84
19.5	100.00

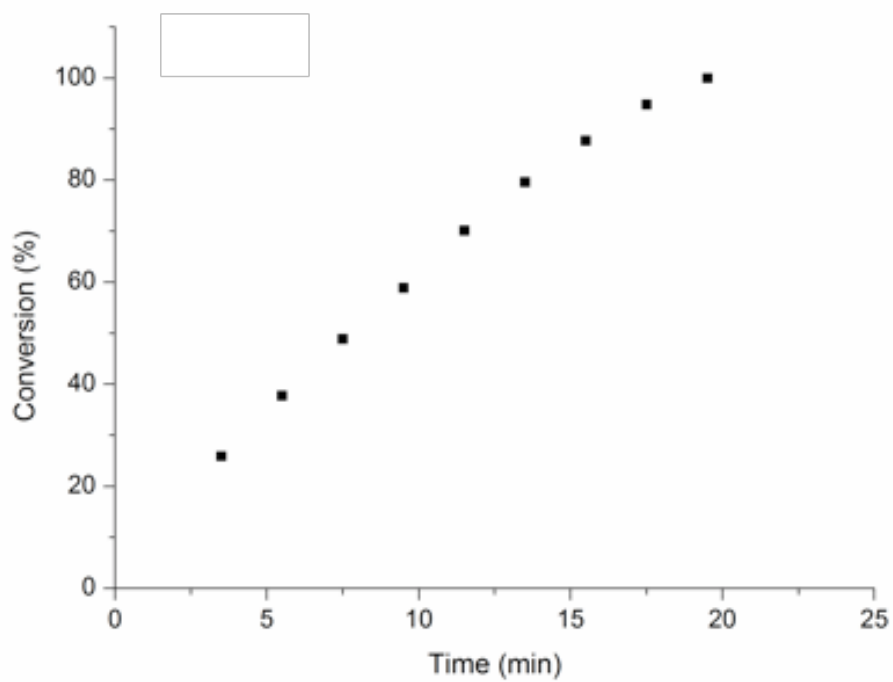


Figure S8. Plot of conversion (%) vs time (min)

Table S10. $1\text{BF}_4 + \text{CD}_3\text{OD}$

t [min]	Conversion [%]
4,93	10,38
7,93	18,40
10,93	24,57
13,93	29,31
16,93	35,76
19,93	40,48
22,93	45,17
25,93	50,69
28,93	54,51
31,93	58,08
34,93	62,85
37,93	65,74
40,93	69,44
43,93	73,61
46,93	76,29
49,93	80,00
52,93	85,02
55,93	85,22
58,93	90,28
61,93	93,10
64,93	95,86
67,93	98,97
70,93	98,97

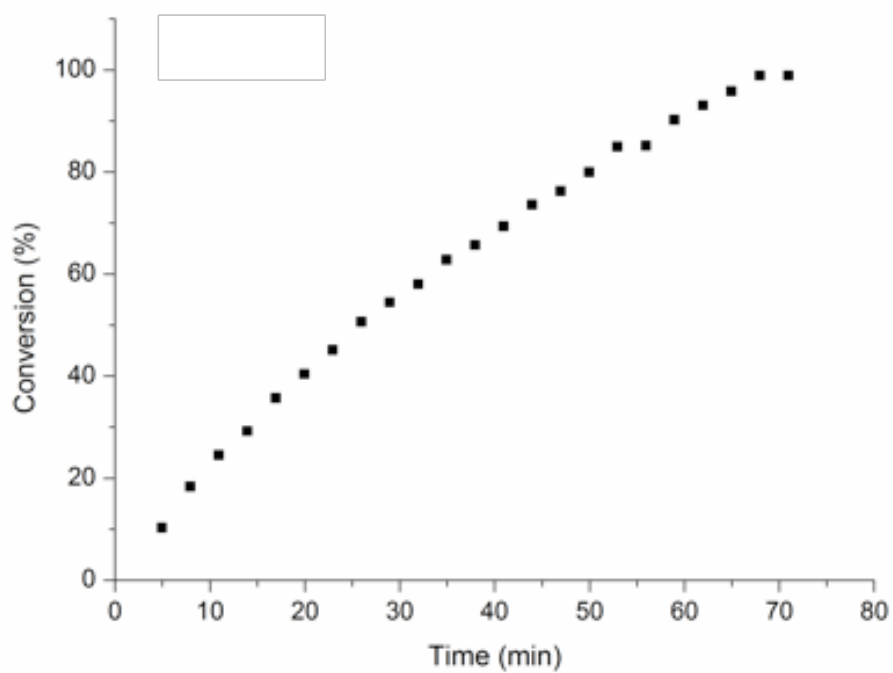


Figure S9. Plot of conversion (%) vs time (min)

Table S11. 1BAr^F + CD₃OD

t [min]	Conversion [%]		
5.05	11.21	53.05	66.20
8.05	15.21	56.05	67.31
11.05	20.33	59.05	71.05
14.05	23.86	62.05	72.76
17.05	28.81	65.05	74.86
20.05	32.79	68.05	78.01
23.05	35.96	71.05	80.19
26.05	40.44	74.05	82.22
29.05	44.14	77.05	84.49
32.05	47.48	80.05	86.88
35.05	50.29	83.05	89.59
38.05	52.64	86.05	91.64
41.05	55.65	89.05	95.24
44.05	60.31	92.05	96.92
47.05	60.31	95.05	98.08
50.05	64.04	98.05	99.59

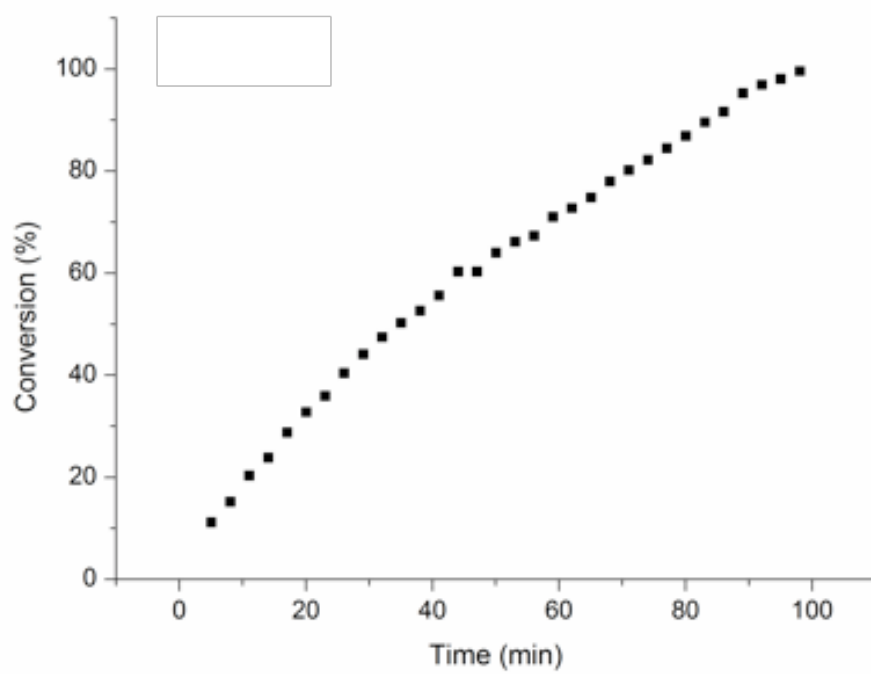


Figure S10. Plot of conversion (%) vs time (min)

Table S12. 1NTf₂

t [min]	Conversion [%]
3.0	4.2
7.2	19.5
10.3	30.0
13.5	40.9
16.6	51.6
19.8	61.0
22.9	69.7
26.1	77.6
29.2	84.6
32.4	90.6
35.5	95.5

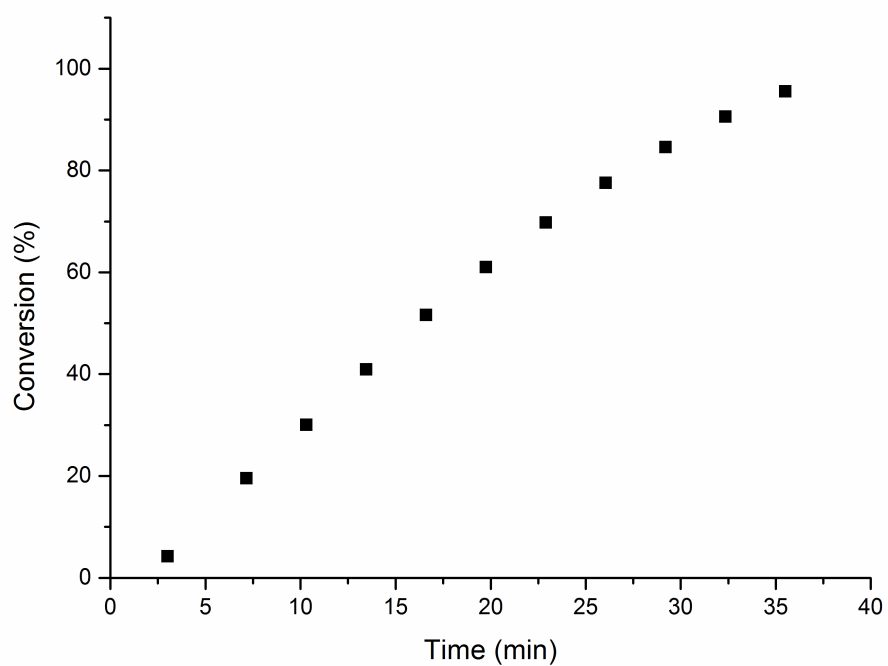


Figure S11. Plot of conversion (%) vs time (min)

Table S13. 1OMs

t [min]	Conversion [%]
3.0	16.8
7.2	36.8
11.3	54.9
13.5	71.4
16.6	86.4
19.8	96.5

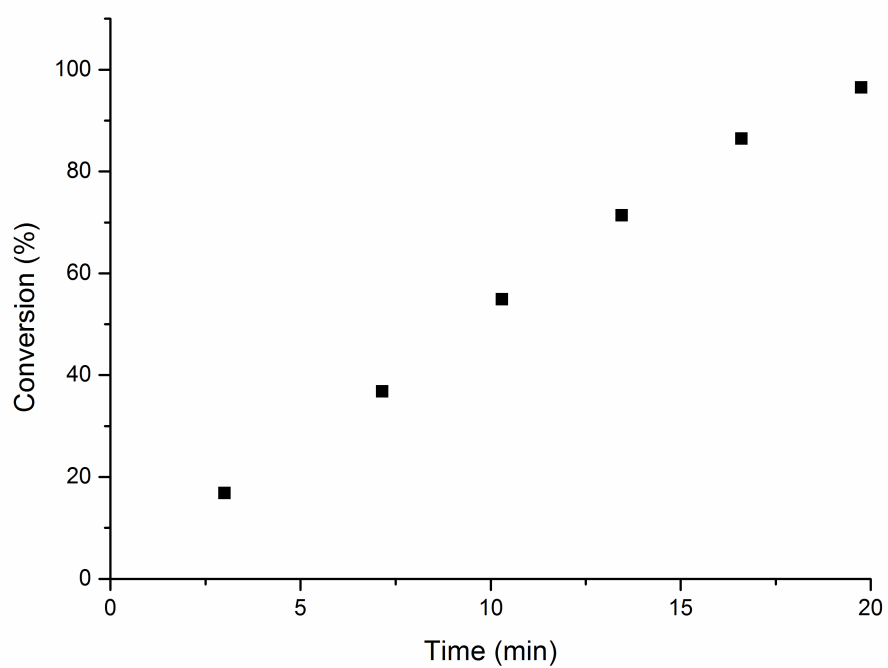


Figure S12. Plot of conversion (%) vs time (min)

Table S14. 1ClO_4

t [min]	Conversion [%]
3.82	12.3
6.82	21.2
9.82	27.3
12.82	33.8
15.82	39.8
18.82	45.0
21.82	50.1
24.82	54.3
27.82	57.8
30.82	61.8
33.82	65.0
36.82	68.3
39.82	71.5
42.82	74.2
45.82	77.5
48.82	80.1
51.82	82.5
54.82	85.3
57.82	87.8
60.82	89.6
63.82	92.7
66.82	94.2
69.82	96.9
72.82	97.6
75.82	97.9
78.82	98.3
81.82	98.6
84.82	98.2
87.82	97.8
90.82	98.3

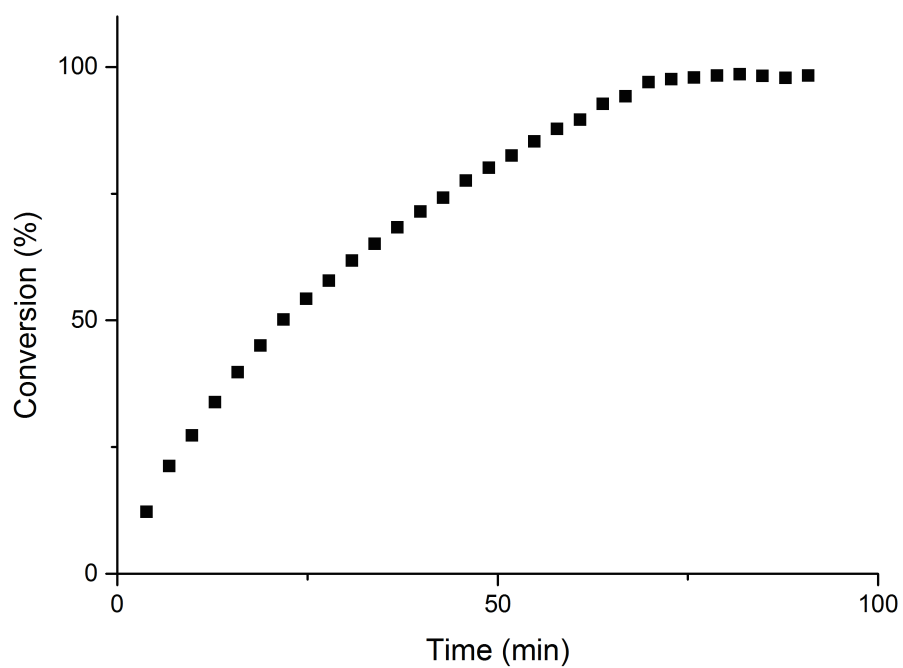


Figure S13. Plot of conversion (%) vs time (min)

Table S15. 1PFHp

t [min]	Conversion [%]		
16.0	42.5	109.3	92.9
22.2	54.4	115.5	93.5
28.4	63.3	121.7	94.1
34.7	69.3	127.9	94.6
40.9	74.1	134.1	95.1
47.1	77.5	140.3	95.4
53.3	80.5	146.6	95.8
59.5	82.8	152.8	96.1
65.7	84.8	159.0	96.5
72.0	86.6	165.2	96.7
78.2	87.9	171.4	96.9
84.4	89.2	177.6	97.2
90.6	90.4	183.9	97.4
96.8	91.3	190.1	97.5
103.0	92.2	196.3	97.6
		202.5	97.7

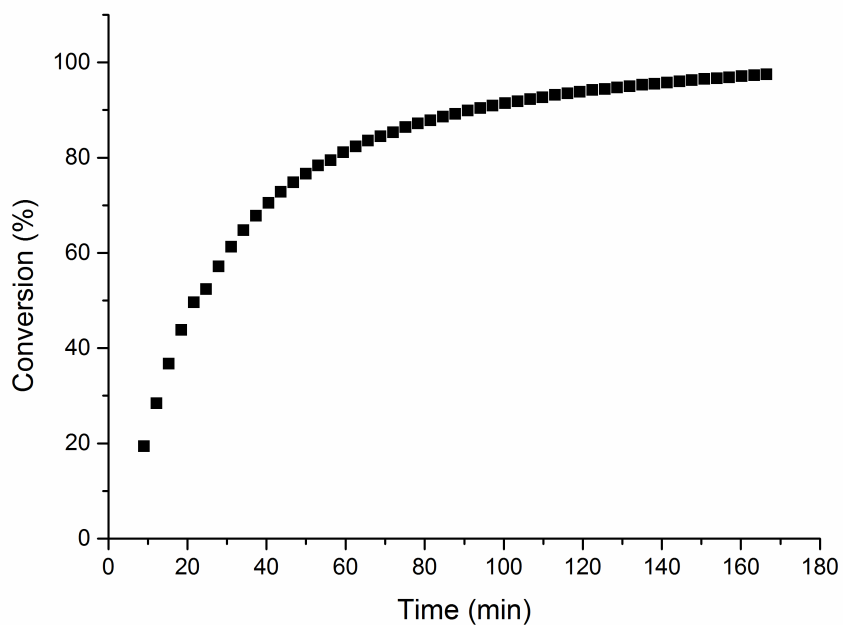


Figure S14. Plot of conversion (%) vs time (min)

Table S16. 1OTs + CD₃NO₂

t [min]	Conversion [%]
5.0	6.1
9.2	11.9
12.3	17.8
15.5	23.4
18.6	28.5
21.8	33.8
24.9	40.1
28.1	46.0
31.2	52.2
34.4	58.1
37.5	64.2
40.7	69.2
43.8	73.8
47.0	77.6
50.1	81.3
53.3	84.6
56.4	87.5
59.6	90.2
62.7	92.7
65.9	94.7
69.0	96.4
75.3	98.2

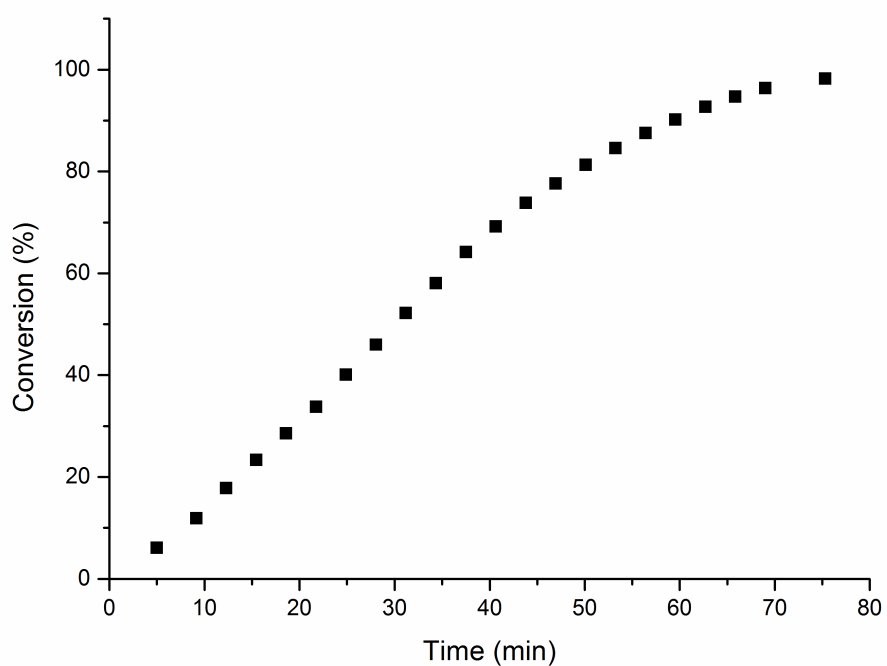


Figure S15. Plot of conversion (%) vs time (min)

Table S17. 1OTf + CD₃NO₂

t [min]	Conversion [%]
4.0	7.8
8.2	13.9
11.3	21.2
14.5	28.3
17.6	36.3
20.8	44.2
23.9	52.5
27.1	58.9
30.2	65.4
33.4	70.7
36.5	75.5
39.7	79.8
42.8	83.4
46.0	86.9
49.1	89.7
52.3	92.5
55.4	94.9
58.6	96.8
61.7	98.2

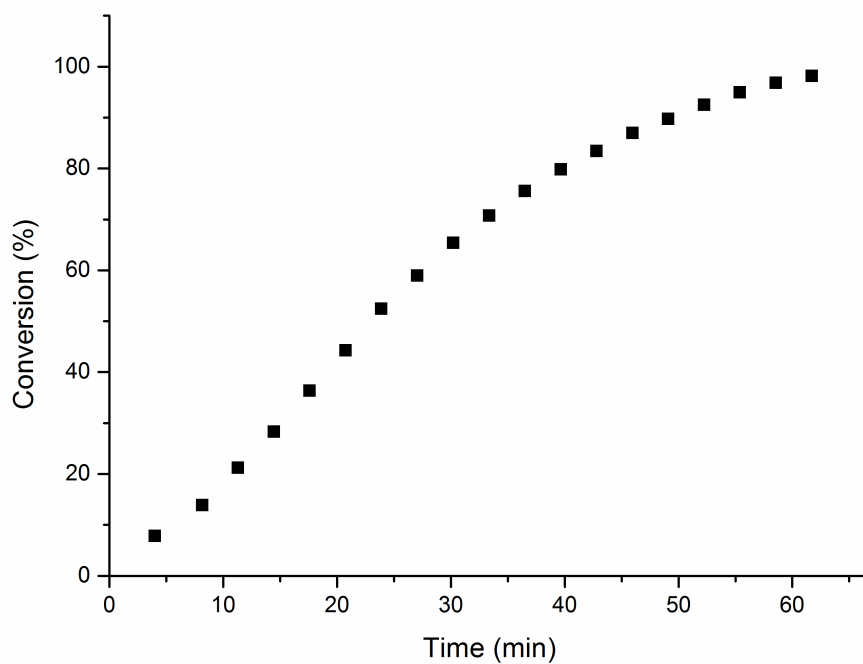


Figure S16. Plot of conversion (%) vs time (min)

Table S18. 1OTs + pTsOH

t [min]	Conversion [%]
3.7	12.40
6.2	24.70
8.7	36.20
11.2	49.20
13.7	60.80
16.2	72.10
18.7	82.50
21.2	92.50
23.7	100.00

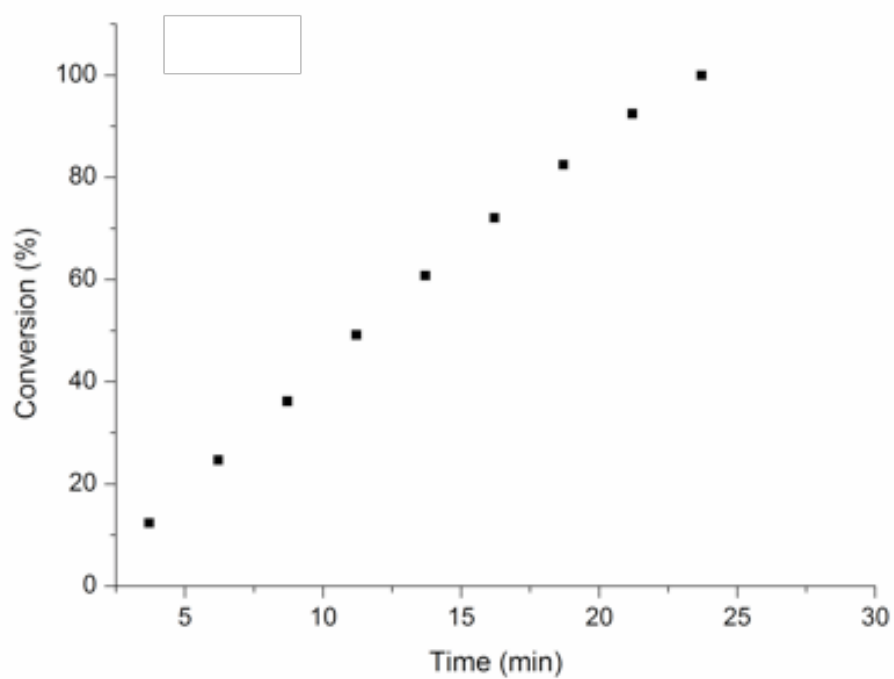


Figure S17. Plot of conversion (%) vs time (min)

Table S19. 1OTs + NBu₄OTs

t [min]	Conversion [%]
4.1	13.38
6.6	30.34
9.1	44.60
11.6	58.37
14.1	69.58
16.6	79.70
19.1	89.89
21.6	97.10
24.1	99.11
26.6	99.96

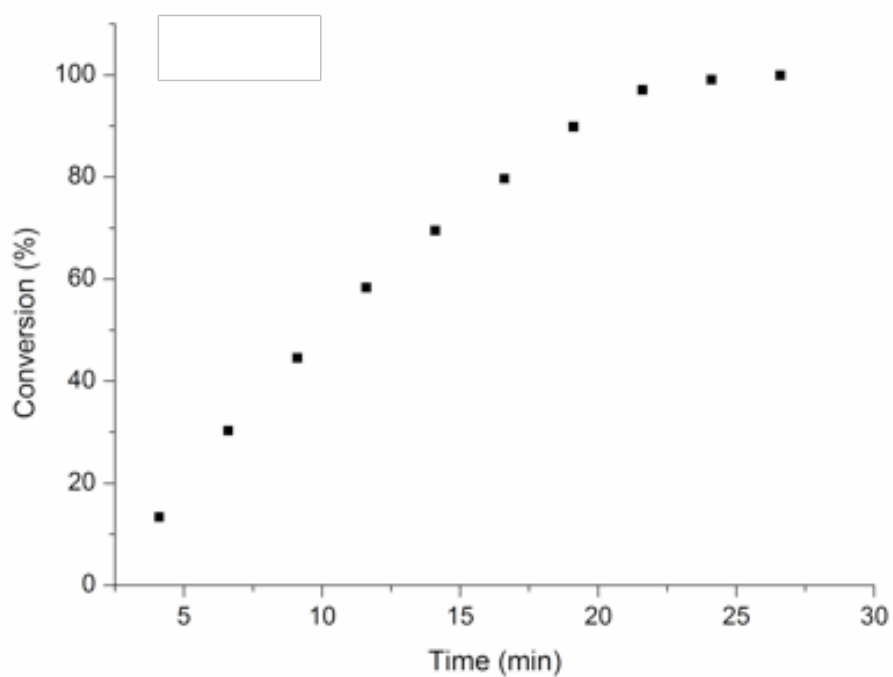


Figure S18. Plot of conversion (%) vs time (min)

Table S20. 2OTs

t [min]	Conversion [%]
5	1.80
10	3.43
13	4.40
49	18.64
72	31.58
77	34.13
83	37.08
87	39.49
91	41.09
96	41.76
100	43.59
111	47.73
120	51.40
134	58.16
143	58.96
157	63.16

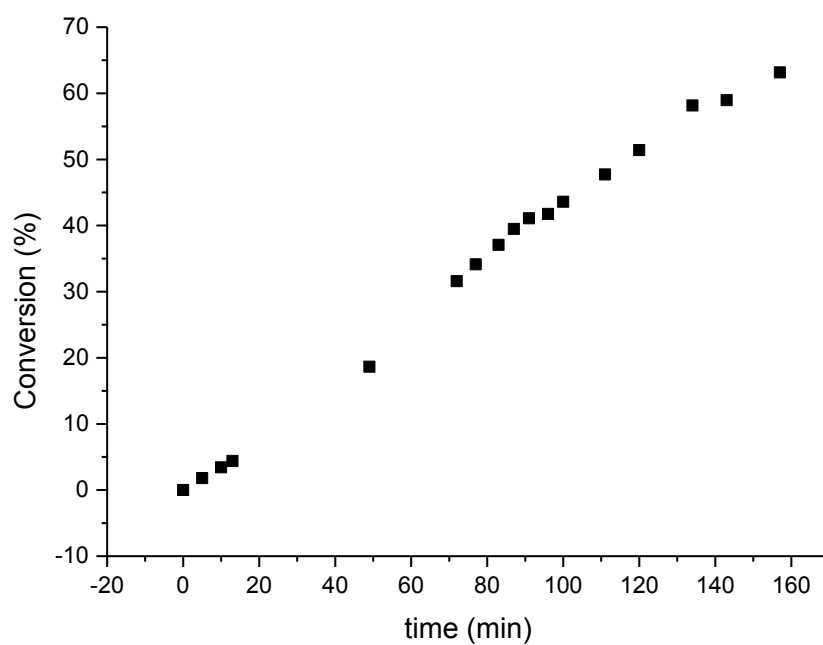


Figure S19. Plot of conversion (%) vs time (min)

Table S21. 3OTs

t [min]	Conversion [%]
6	7.28
13	12.63
16	14.55
20	17.37
26	21.44
38	28.06
62	39.67
72	44.28
80	49.02
139	67.68
187	78.17
224	84.17

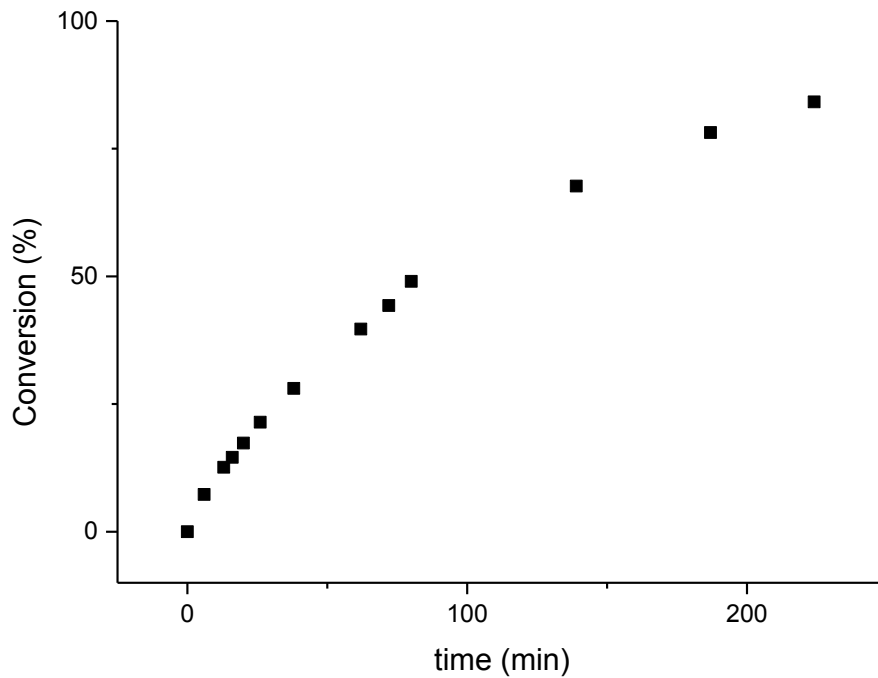


Figure S20. Plot of conversion (%) vs time (min)

Table S22. 4OTs

t [min]	Conversion [%]
5	4.08
11.9	16.85
17.8	31.09
23.7	45.16
29.5	56.36
35.4	64.98
41.3	71.67
47.2	76.95
53.1	81.22
59.0	84.69
64.8	87.47
70.7	89.81
76.6	91.75
82.5	93.30
88.4	94.29
94.3	95.32
100.1	96.25
106.0	97.01
111.9	97.60
117.8	98.01
123.7	98.41

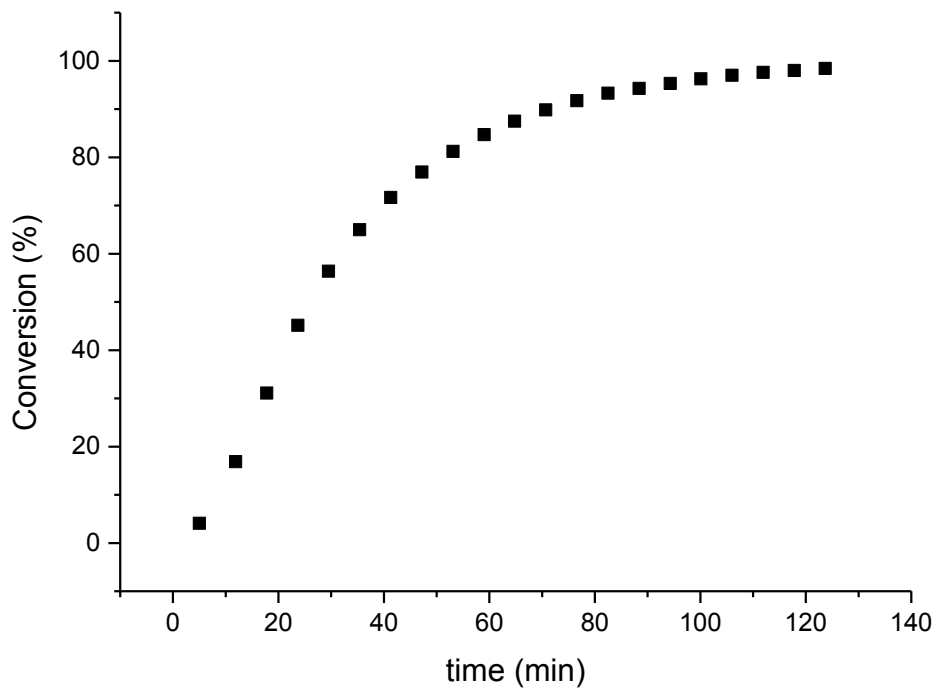


Figure S21. Plot of conversion (%) vs time (min)

Table S23. 50Ts

t [min]	Conversion [%]
6	20.50
11	39.93
17	57.26
22	66.45
27	73.02
31	78.56
37	83.43
43	89.09
47	91.07
52	93.54
59	95.73
64	96.90
68	97.70

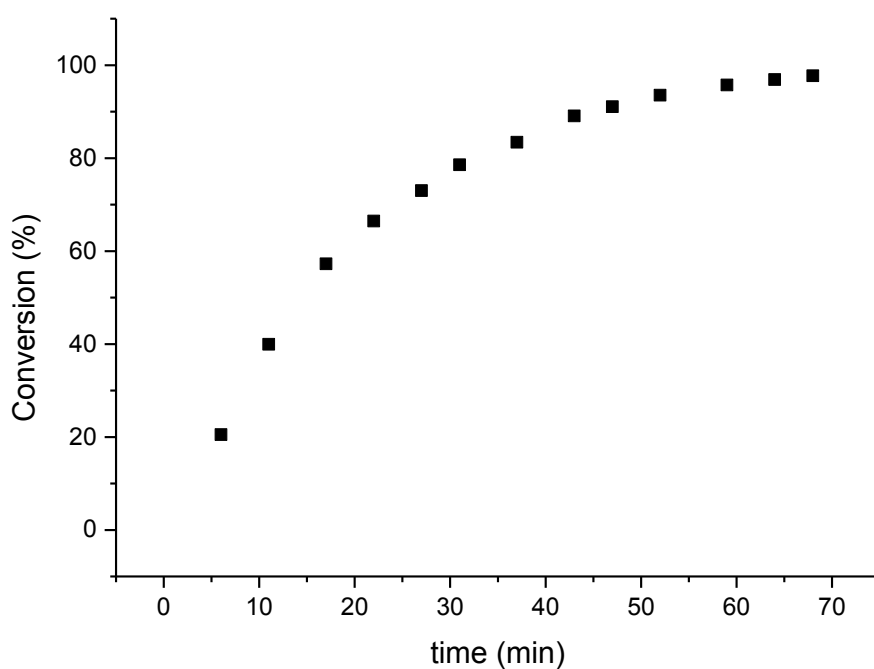


Figure S22. Plot of conversion (%) vs time (min)

Table S24. 6OTs

t [min]	Conversion [%]		
4.0	5.14	54.3	69.89
10.2	22.21	57.4	71.70
13.3	27.64	60.6	73.26
16.5	32.55	63.7	74.76
19.6	37.20	66.9	76.29
22.8	41.50	70.0	77.44
25.9	45.50	73.2	78.76
29.1	49.18	76.3	79.88
32.2	52.55	79.5	80.99
35.4	55.72	82.6	81.96
38.5	58.57	85.8	82.89
41.7	61.24	88.9	83.75
44.8	63.64	92.1	84.59
48.0	65.89	95.2	85.40
51.1	67.97	98.4	86.04
		101.5	86.60

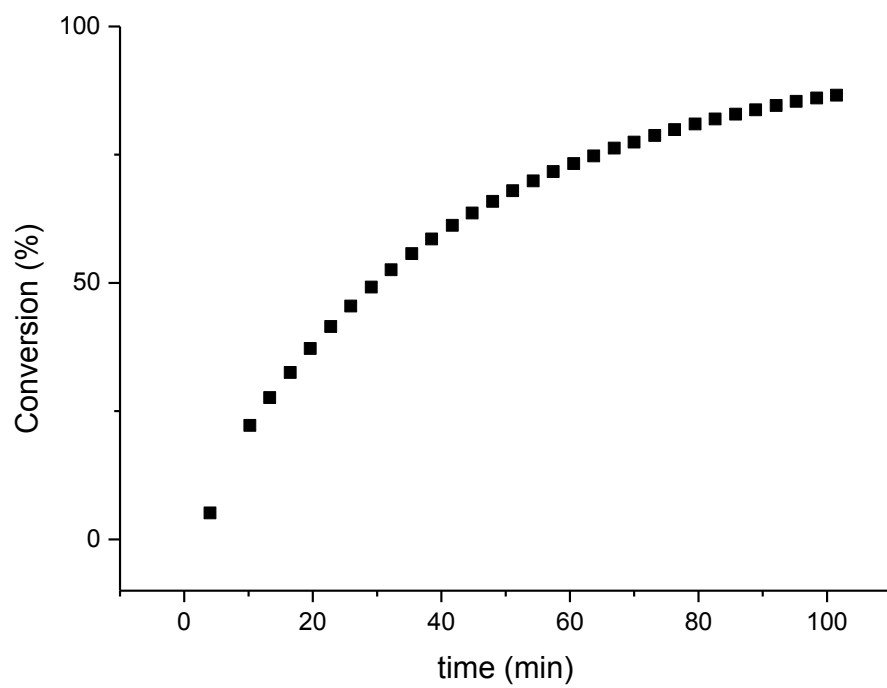


Figure S23. Plot of conversion (%) vs time (min)

Table S25. 2OTf

t [min]	Conversion [%]
6	3.04
8	4.02
12	6.82
17	9.79
21	14.66
31	25.44
36	29.60
40	33.56
44	37.73
48	40.64
52	44.77
83	57.20
98	63.57
113	74.77
129	78.88
147	85.46
173	93.00

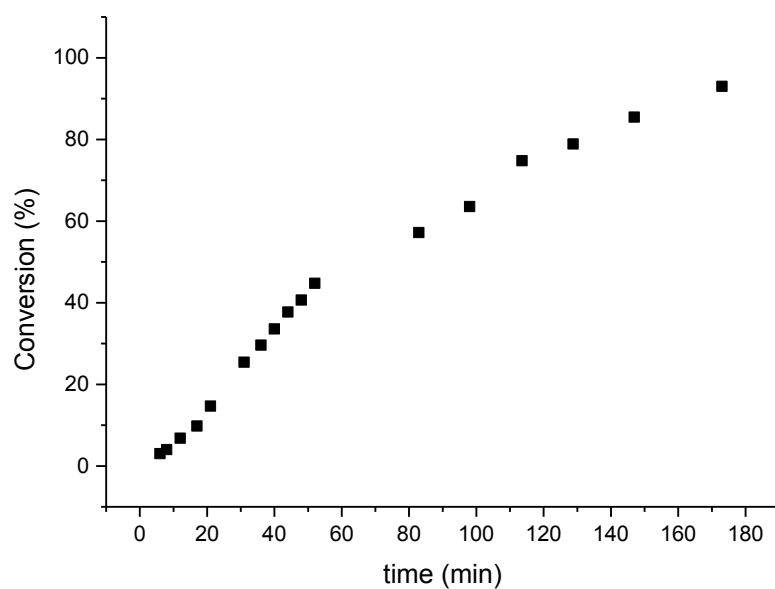


Figure S24. Plot of conversion (%) vs time (min)

Table S26. 3OTf

t [min]	Conversion [%]
6	26.73
18	66.08
26	75.26
33	80.04
40	83.56
47	86.48
53	88.49
60	90.58
67	92.18
74	93.72

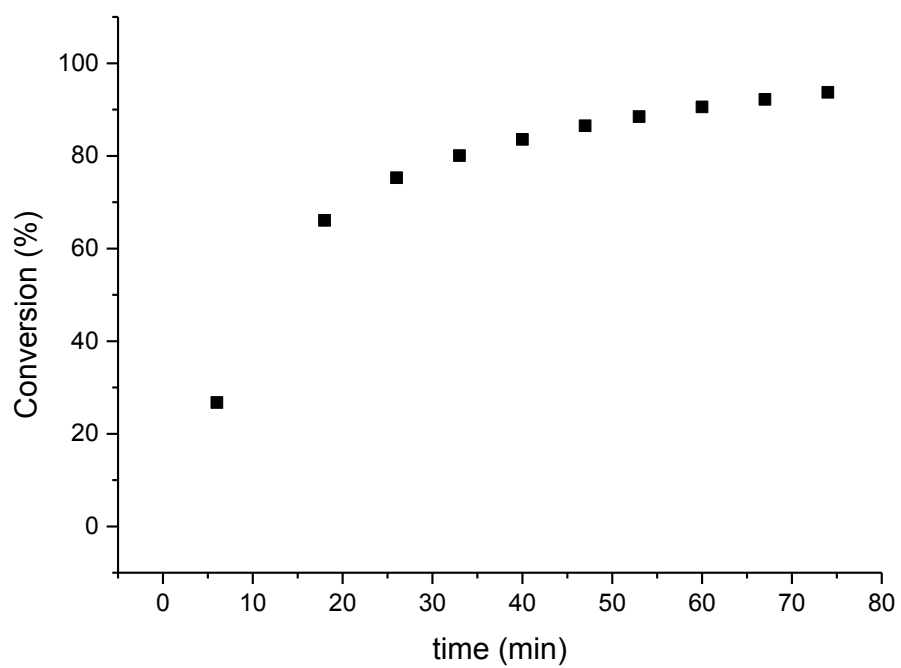


Figure S25. Plot of conversion (%) vs time (min)

Table S27. 4OTf

t [min]	Conversion [%]
4	2.65
11	7.44
21	14.91
28	23.53
32	28.39
37	32.74
42	37.65
47	41.41
56	47.00
59	49.20
63	51.28
66	53.23
69	55.21
72	57.00
75	58.70
79	60.34
82	61.91
85	63.46
88	64.91
91	66.27
95	67.62
98	68.90
101	70.12
157	85.94
168	87.12
171	87.64
174	88.34
178	88.71
181	89.32
184	89.73
187	90.39
190	90.79
193	91.08
196	91.42
255	97.16

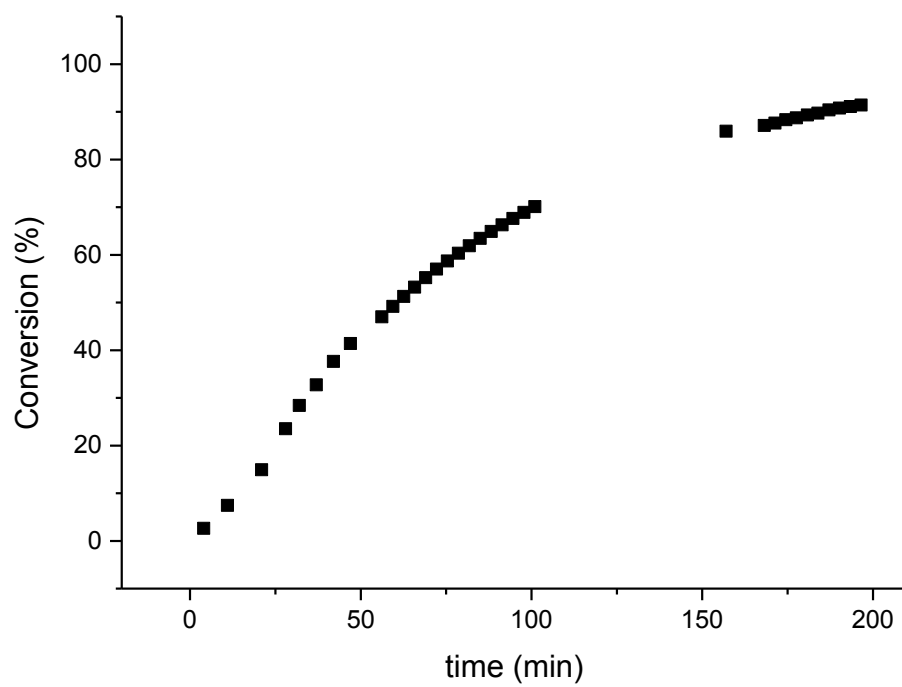


Figure S26. Plot of conversion (%) vs time (min)

Table S28. 5OTf

t [min]	Conversion [%]
5	16.31
9	41.12
13	51.44
17	59.41
20	66.33
24	71.96
27	77.52
30	82.37
34	86.22
37	89.30
41	92.06

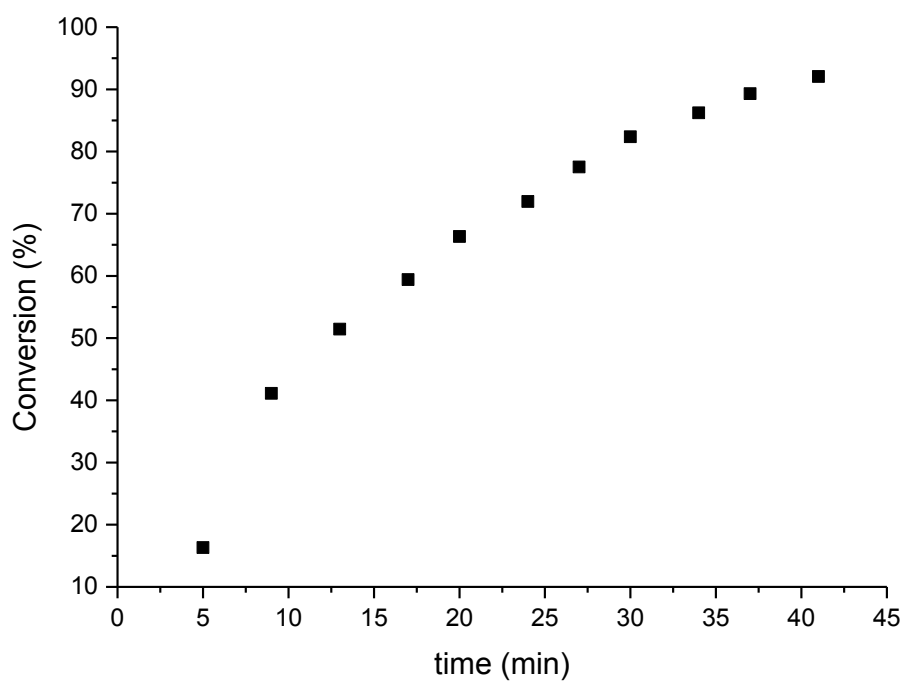


Figure S27. Plot of conversion (%) vs time (min)

Table S29. 6OTf

t [min]	Conversion [%]
5	9.82
9	23.80
13	36.78
17	47.46
21	58.63
25	69.14
29	76.42
35	86.07
39	91.75

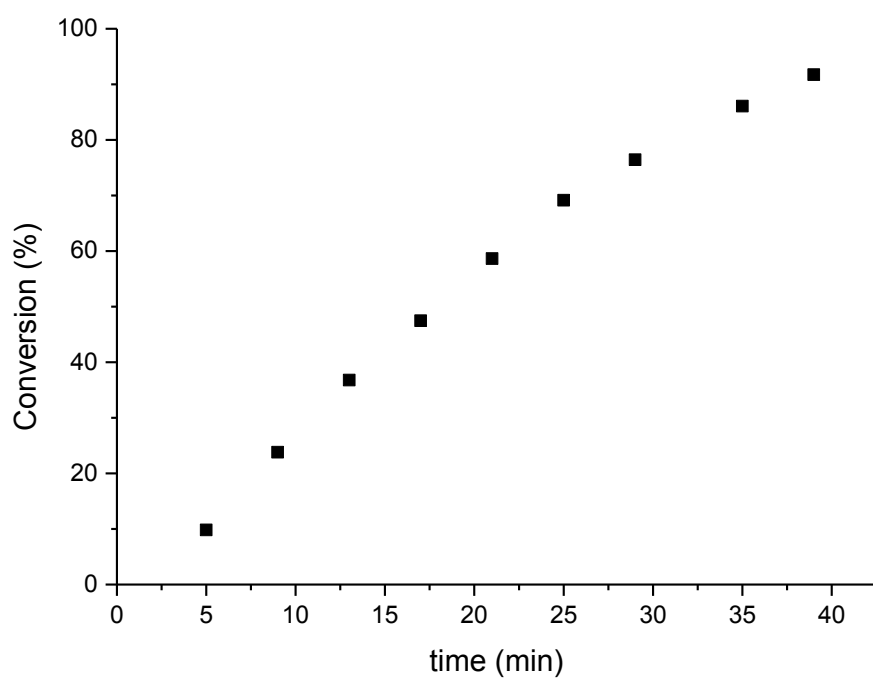


Figure S28. Plot of conversion (%) vs time (min)

Table S30. 5TFA in CDCl_3

t [min]	Conversion [%]
4	0.45
12	2.20
19	3.52
29	5.46
37	6.91
47	8.86
54	9.94
88	15.67
142	23.76
182	29.26
249	37.37
286	41.45

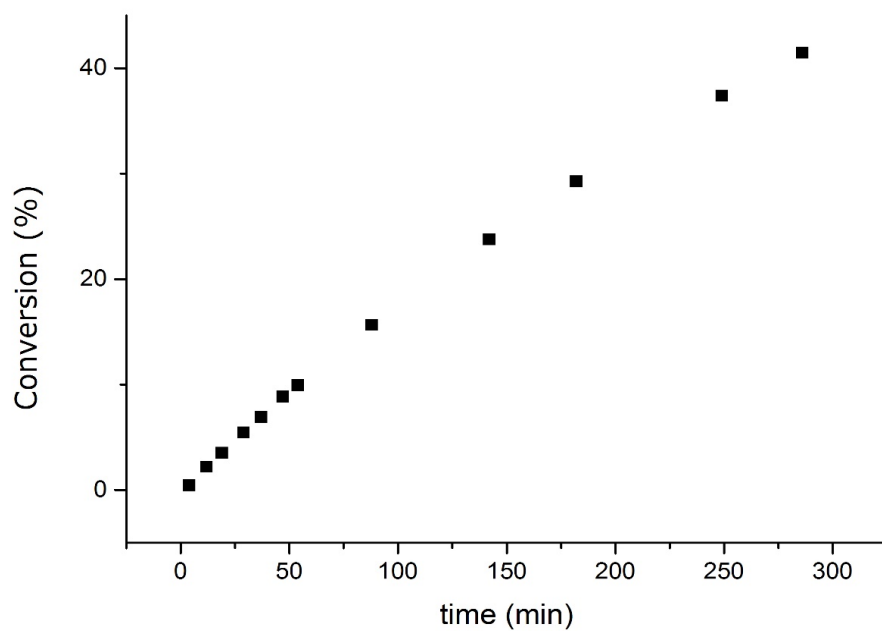


Figure S29. Plot of conversion (%) vs time (min)

Table S31. 5TFA in CD_3NO_2

t [min]	Conversion [%]
5	6.37
41	11.57
64	15.86
93	20.83
171	32.32
179	34.75
194	36.66
225	42.73

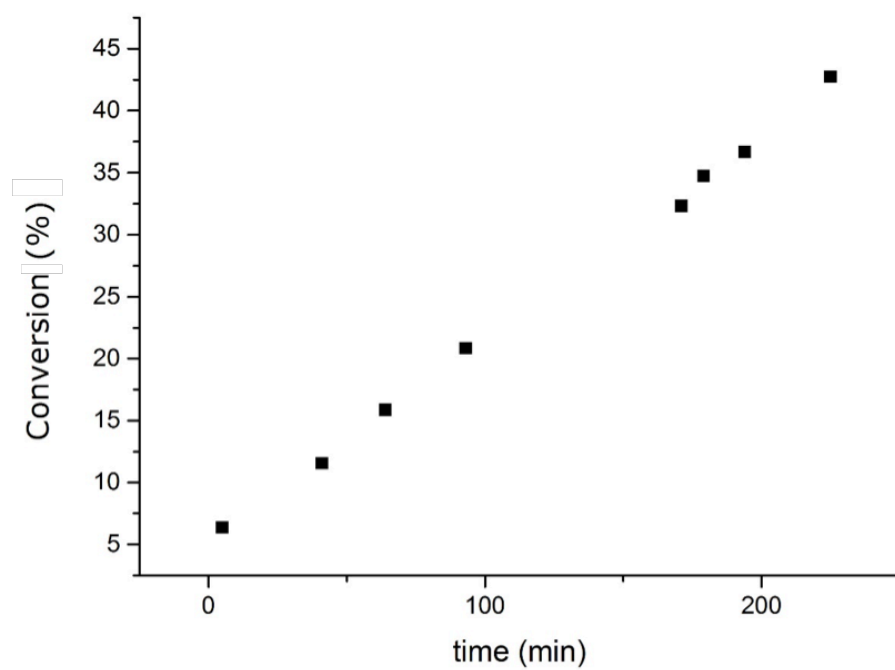


Figure S30. Plot of conversion (%) vs time (min)

Table S32. 5TFA in C₆D₆

t [min]	Conversion [%]		
8.0	0.24	482.1	27.27
19.0	1.13	512.8	28.53
27.0	1.72	543.5	29.78
59.0	4.24	574.2	30.92
113.7	7.79	604.9	32.02
144.4	9.79	635.6	33.15
175.1	11.60	666.3	34.11
205.8	13.27	697.0	35.15
236.5	14.99	727.7	36.07
267.2	16.65	758.4	36.99
297.9	18.26	789.1	37.91
328.6	19.81	819.8	38.78
359.3	21.36	850.5	39.66
390.0	22.98	881.2	40.49
420.7	24.62	911.9	41.34
451.4	25.90	942.6	42.15
		973.3	42.92
		1004.0	43.68

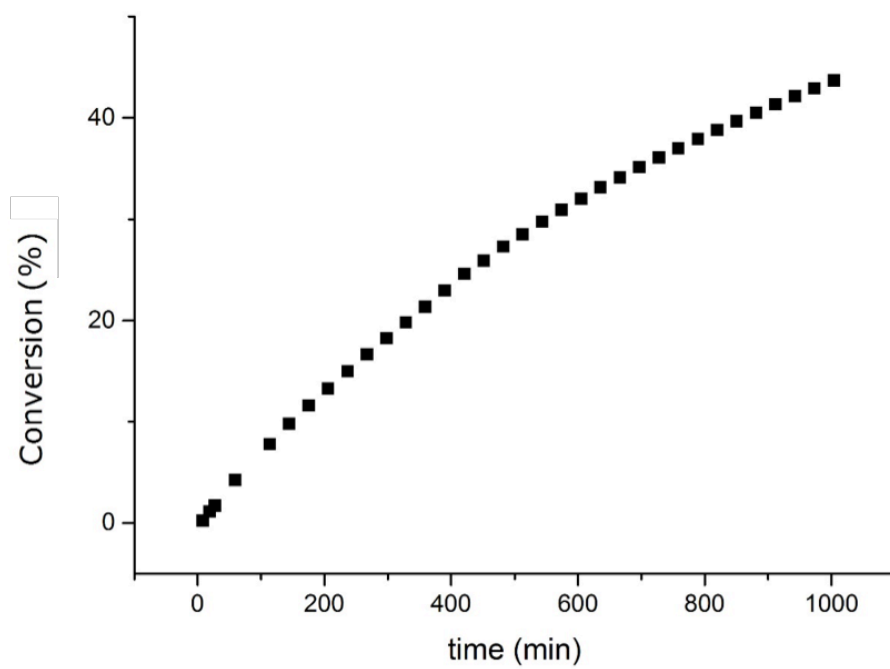


Figure S31. Plot of conversion (%) vs time (min)

Table S33. 5TFA in PC

t [min]	Conversion [%]
62	5.22
90	7.76
121	12.04
151	14.82
220	25.37
250	29.41
280	32.51
310	36.71
340	40.36
370	43.60

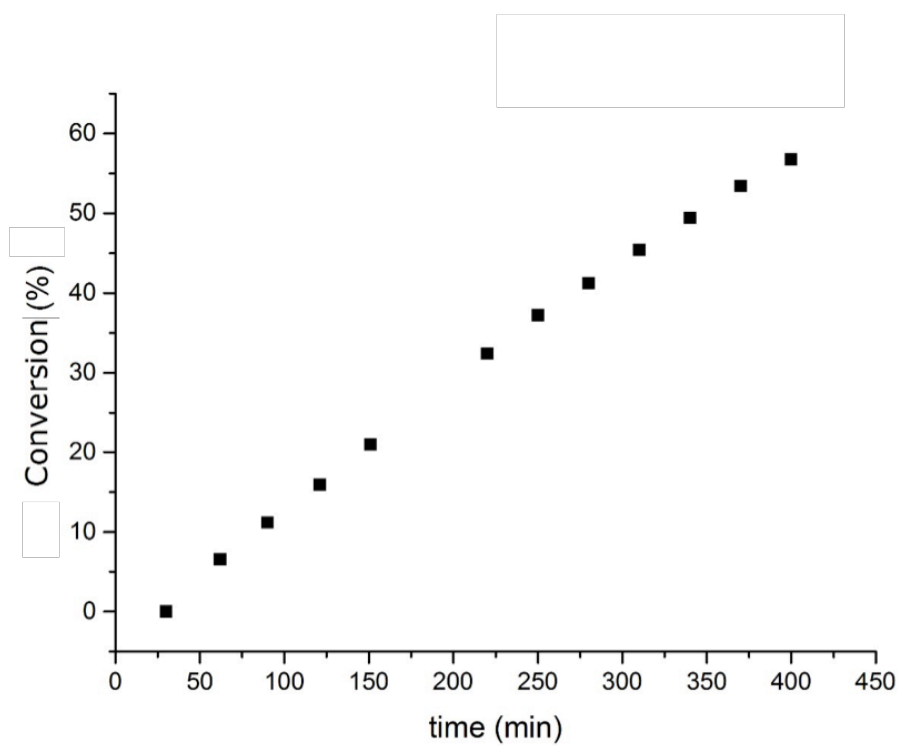


Figure S32. Plot of conversion (%) vs time (min)

Table S34. 5OTs in CDCl_3

t [min]	Conversion [%]
4	11.29
7	24.63
10	35.13
14	43.60
17	51.02
20	57.61
23	63.35
26	68.49
29	73.09
32	77.04
36	80.59
39	83.60
42	86.32
45	88.67
48	90.71
51	92.42
54	93.93
58	95.12
61	96.16
64	97.17
67	97.80
80	99.80

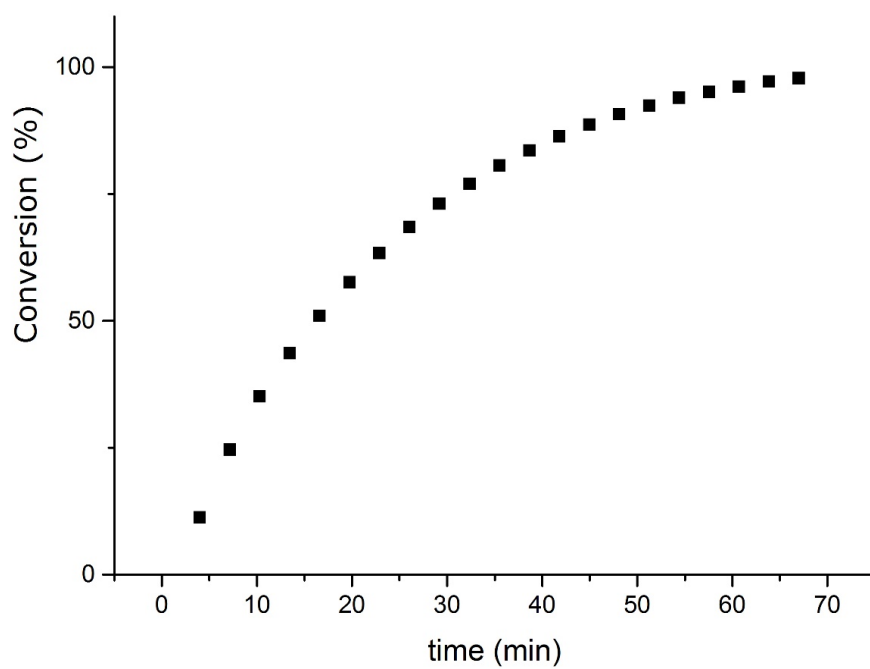


Figure S33. Plot of conversion (%) vs time (min)

Table S35. 50Ts in CD₃NO₂

t [min]	Conversion [%]
4	10.19
9	18.42
13	25.91
17	32.91
26	44.69
30	49.12
34	53.87
41	60.78
46	63.28
51	65.10
59	71.10
62	72.86
66	74.49
69	76.06
72	77.53
75	78.87
78	80.16
82	81.37
85	82.58
88.2	83.67
91.4	84.68
94.6	85.67
97.8	86.00
101.0	87.44
104.3	88.29
124.0	93.14

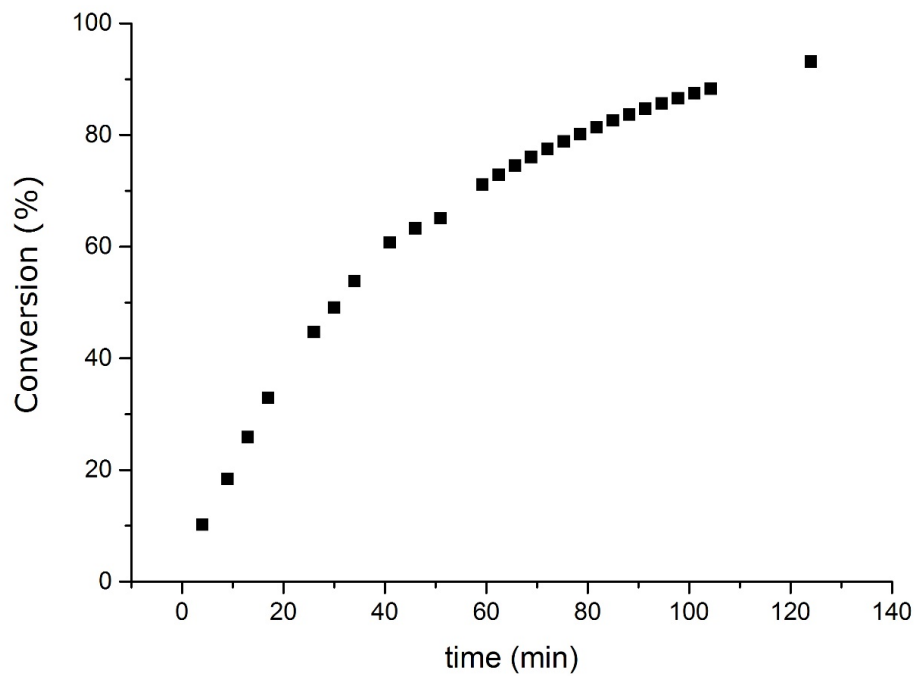


Figure S34. Plot of conversion (%) vs time (min)

Table S36. 5TFA in C₆D₆

t [min]	Conversion [%]
5.0	5.04
20.6	41.28
34.1	62.08
47.7	74.86
61.3	82.59
74.8	87.23
88.4	90.07
102.0	91.81
115.5	92.86
129.1	93.48
142.7	93.91
156.2	94.15

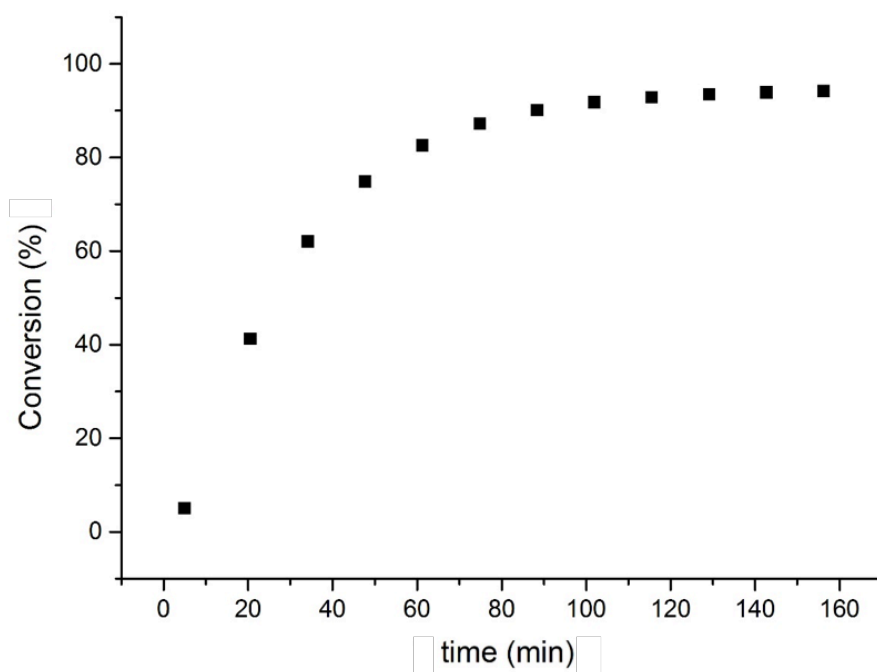


Figure S35. Plot of conversion (%) vs time (min)

Table S37. 50Ts in PC

t [min]	Conversion [%]
15	14.19
30	23.82
45	33.92
60	43.49
75	46.44
90	51.52
105	55.50
120	59.51
135	62.84
150	66.38
240	80.33
255	82.60
285	85.14
315	88.36
345	90.68
380	92.71

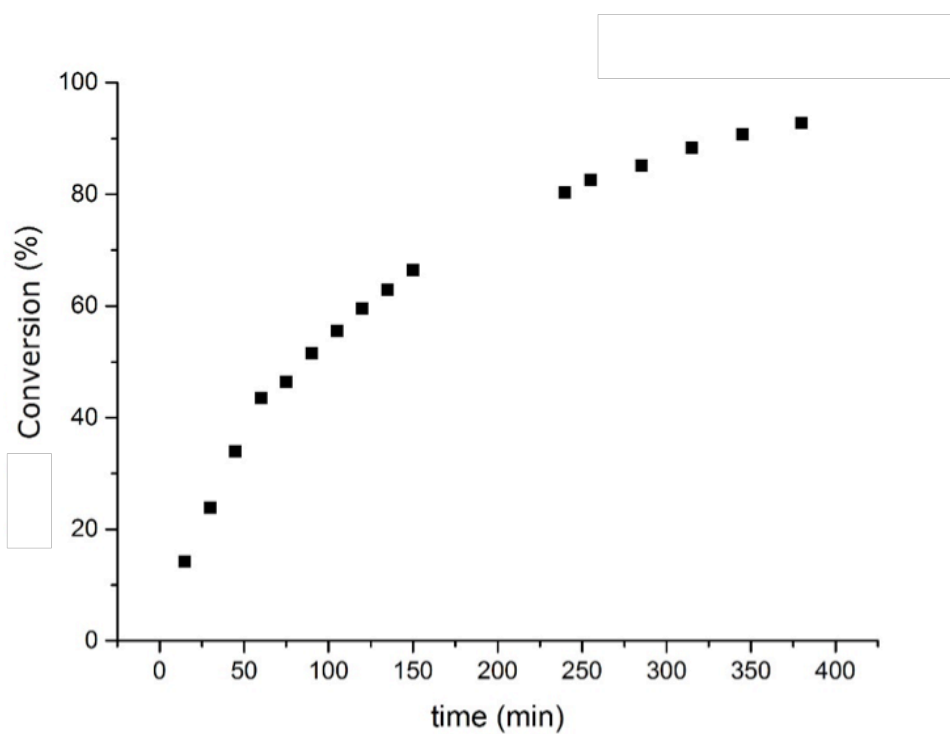
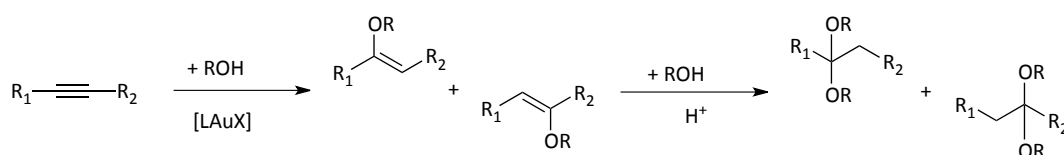


Figure S36. Plot of conversion (%) vs time (min)

CHAPTER 4

NUCLEOPHILES AND SUBSTRATES

In this chapter a systematic experimental study of the role of the anion in connection with the nature of the nucleophile and the substrate is described in the alkoxylation reaction of alkynes, catalyzed by gold(I) complexes (Scheme 1).



Scheme 1. Gold(I) catalyzed alkoxylation of alkynes

The results have been previously published in:

- Trinchillo, M., Belanzoni, P., Belpassi, L., Biasiolo, L., Busico, V., D'Amora, A., D'Amore, L., Del Zotto, A., Tarantelli, F., Tuzi, A., and Zuccaccia, D. *Organometallics*, **2016**, 35, 641–654;

1. Introduction

The addition of oxygen nucleophiles to alkynes is a classic research area that has revealed itself highly useful for organic synthesis.

Recently, several experimental studies have been performed to gain insight into the mechanism of this transformation¹ as well as to determine the effect of a silver salt² and its counterion³ when employed in gold-catalyzed additions to alkynes.

Although this research field has been greatly advanced in recent times, there is significant room for improvement, particularly in the area of the hydroalkoxylation of internal alkynes. Furthermore, the role of the anion in connection with the nature of the nucleophile has never been studied.

In general, terminal alkynes undergo addition at the internal carbon to give the corresponding enol ether **1** or ketal **2** products (Scheme 2). In contrast, internal alkynes can potentially lead to the formation the two possible enol ether products. Depending on which carbon atom of the triple bond of the alkyne is attacked by the nucleophile, **1a** and **1b**, in addition to the corresponding ketals **2a** and **2b**, could all be formed (Scheme 3).

Several factors can determine the selectivity of these reactions, including steric and electronic features, and the identity of the nucleophile.

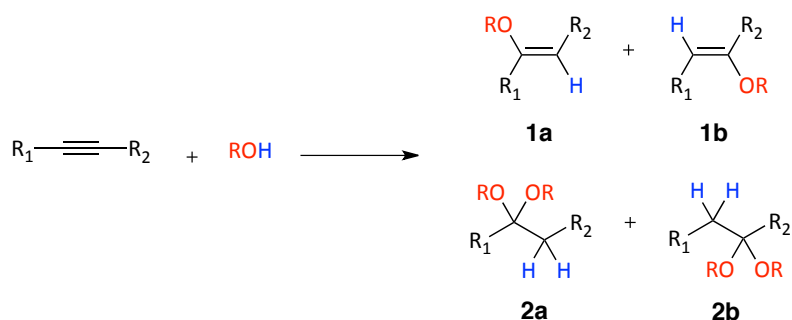


Scheme 2. Nucleophilic addition to terminal alkynes

¹ a) A. Zhdanko and M. E. Maier, *Chem. - Eur. J.*, **2014**, *20*, 1918; b) C. Obradors and A. M. Echavarren, *Chem. Commun.*, **2013**, *50*, 16

² Wang, D. Cai, R. Sharma, S. Jirak, J. Thummanapelli, S. K. Akhmedov, N. G. Zhang, H. Liu, X. Petersen J. L. and Shi, X. *J. Am. Chem. Soc.*, **2012**, *134*, 9012

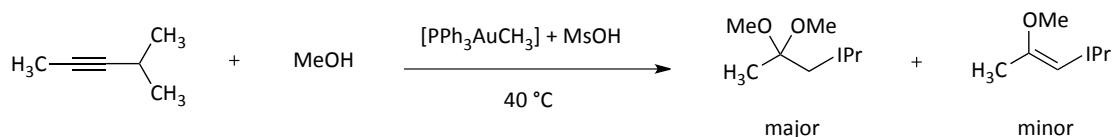
³ (a) L. Biasiolo, M. Trinchillo, P. Belanzoni, L. Belpassi, V. Busico, G. Ciancaleoni, A. D'Amora, A. Macchioni, F. Tarantelli and D. Zuccaccia, *Chem. - Eur. J.*, **2014**, *20*, 14594; (b) A. Zhdanko and M. E. Maier, *ACS Catal.*, **2014**, *4*, 2770



Scheme 3. Nucleophilic addition to internal alkynes

The gold-catalyzed intermolecular hydroalkoxylation of alkynes is extremely challenging from a regioselectivity standpoint; however, as expected, terminal alkynes have been shown to exhibit very high selectivity. In contrast, internal alkynes can generally be attacked by the nucleophile at both positions. The substituents on the alkyne as well as the identity of the nucleophile play a large role in the regioselectivity.⁴

The oldest example of regioselective addition to internal alkyne has been reported by Teles and coworkers,⁵ the selective addition of methanol to the 4-methyl-2-pentyne (Scheme 4) to the methyl substituted position, to give the dimethyl ketal as major product and a small amount of the enol ether. The selectivity arises from the steric nature of the substituents, with the attack favored at the least sterically hindered position.



Scheme 4. Steric effect on regioselective hydroalkoxylation

⁴ Goodwin, J. A., Aponick, A., *Chem. Comm.* **2015**, 51, 8730-8741

⁵ J. H. Teles, S. Brode and M. Chabanas, *Angew. Chem., Int. Ed.*, **1998**, 37, 1415

2. Results and discussion

2.1. Interplay between the nucleophile and the anion

1OTs and **1BAr^F** (as models of catalysts in which the anion plays an active role or, *viceversa*, does not enter into the reaction mechanism, respectively) have been analyzed in the alkoxylation of 3-hexyne, in which different nucleophiles were screened. Among them, ethanol and triethylene glycol monomethyl ether (Gly-OMe) are better nucleophiles than methanol and are expected to have an enhanced capacity to polarize the attack (or the proton shuttle). On the contrary, 2,2,2-trifluoroethanol (TFE), benzyl alcohol, and 2,6-dimethoxyphenol were chosen as poorer nucleophiles than methanol.

By using ethanol, the **1OTs** catalyst provided a complete conversion of 3-hexyne in 15 min slightly faster than methanol (Table 1, entry 1 vs Table 1, entry 7, Chapter 3). When the reaction is run in the presence of TFE, both complexes **1OTs** and **1BAr^F** do not promote any reaction (Table 1, entry 2).

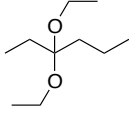
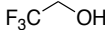
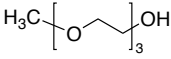
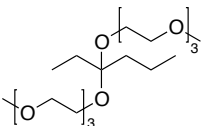
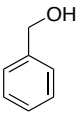
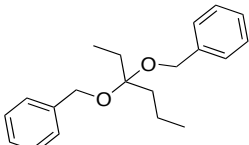
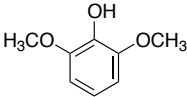
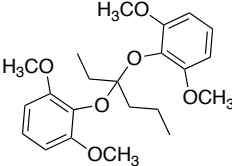
When the alkoxylation of 3-hexyne is performed with a functionalized alcohol such as Gly-OMe, the overall reaction is strongly slowed down, and complexes **1OTs** and **1BAr^F** promote full conversion in similar reaction time (Table 1, entries 3 and 4) while in the case of methoxylation the reaction times were different (17 and 48 min for **1OTs** and **1BAr^F** respectively). On the other hand, the hydroalkoxylation of 3-hexyne with benzyl alcohol proceeded efficiently using **1OTs**, whereas in the case of **1BAr^F** the almost complete formation of the final product was achieved after a much higher reaction time (Table 1, entries 5 and 6). Finally, using **1OTs** an incomplete and slow conversion of substrate was observed upon addition of 2,6-dimethoxyphenol (the poorest nucleophile here employed), while the reaction failed completely in the presence of **1BAr^F** (Table 1, entries 7 and 8).

Taken all together, these experimental evidences reveal that the character of the nucleophile significantly modifies the impact of the anion effect in the catalytic reaction.

With functionalized nucleophiles (*e.g.*, Gly-OMe) the O-H bond may be polarized *via* specific intramolecular interactions, suppressing the anion effect. The role of the anion is crucial in presence of soft nucleophiles (as compared to methanol, *e.g.*, benzyl alcohol and 2,6-dimethoxyphenol), which are less able to attack the coordinated substrate and need to be activated.

The use of TFE as nucleophile even inhibits the reaction, most probably due to the presence of the strongly electron withdrawing CF₃ group, that may in principle either decrease the nucleophilic character of the –OH group or favor the formation of CF₃CH₂O[−] in solution, leading to catalyst deactivation (see **Chapter 6**, for DFT details on this issue).

Table 1. Alkoxylation of 3-hexyne^a

entry	nucleophile	catalyst	product	Conversion ^b (%)	T ^c (min)	TOF ^d (h ⁻¹)
1 ^e		1OTs		97	15	620
2 ^f		1OTs, 1BAr^F	/	0	-	-
3 ^g		1OTs		98	345	34
4 ^g		1BAr^F		98	476	10
5 ^h		1OTs		99	78	158
6 ^h		1BAr^F		99	1619	4
7 ⁱ		1OTs		18	5430	0.03
8 ⁱ		1BAr^F		0	-	-

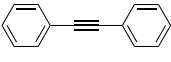
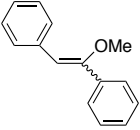
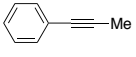
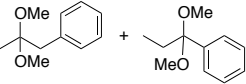
^aCatalysis conditions: 30 °C, 3-hexyne (0.88 mmol, 100 μL), 1 mol% catalyst in CDCl₃ (400 μL).

^bDetermined by ¹H NMR using TMS as internal standard; averaged values of three runs. ^cTime for 95% of conversion or at the highest conversion registered. ^dTOF = (n_{product} / n_{catalyst})/t(h) at 50% of conversion. ^eEthanol (3.52 mmol, 205 μL). ^f2,2,2-trifluoroethanol (3.52 mmol, 256 μL). ^gTriethylene glycol monomethyl ether (1.16 mmol, 186 μL), 3-hexyne (0.29 mmol, 33 μL). ^hBenzyl alcohol (1.16 mmol, 120 μL), 3-hexyne (0.29 mmol, 33 μL). ⁱ2,6-dimethoxyphenol (0.88 mmol, 136 mg), 3-hexyne (0.22 mmol, 25 μL).

2.2. Regioselectivity in methoxylation of alkynes

The catalytic activity of the complex **1OTs** has been tested in the methoxylation of two different internal alkynes.

Table 2. Methoxylation of alkynes^a with **1OTs**

entry	substrate	product	conversn ^d (%)	t ^e (min)	TOF ^f (h ⁻¹)
1 ^b	 S2	 S2a (<i>E</i> : <i>Z</i> = 98:2)	97	64	90
2 ^c	 S3	 S3a (80%) S3b (20%)	99	36	156

^aCatalysis conditions: 30 °C, methanol (3.52 mmol, 143 μL), 1 mol % **1OTs** in CDCl₃ (400 μL).

^bdiphenylacetylene (0.22 mmol, 39.2 mg). ^c1-phenyl-1-propyne (0.88 mmol, 100 mg).

^dDetermined by ¹H NMR using TMS as internal standard; averaged values of three runs. ^eTime for 95% of conversn. ^fTOF = (n_{product} / n_{catalyst})/t(min) at 95% of conversn.

In the case of symmetrical alkyne such as diphenylacetylene **S2**, the main product formed was the corresponding enol-ether **S2a** (entry 1, Table 2), with the formation of the *E* regioisomer as major product (*E*/*Z* = 98:2). With unsymmetrical substrate such as 1-phenyl-1-propyne **S3**, the selective addition of methanol to **S3** afforded the corresponding acetal products **S3a** and **S3b** (entry 2, Table 2) in a 80:20 ratio. According to the literature, the steric nature of substituents induces the selectivity of the reaction, with the attack being favored at the least sterically hindered position.⁶ Under similar experimental conditions, both alkynes **S2** and **S3** are overall less reactive than 3-hexyne (entries 1 and 2, Table 2 vs entry 7, Table 1, Chapter 3). Nevertheless, it has to be noted that these results are among the best reported to date, at least for diphenylacetylene and at room temperature.⁷

⁶ Goodwin, J. A.; Aponick, A. *Chem. Commun.*, **2015**, 51, 8730-8741 and references therein

⁷ Leyva, A.; Corma, A. *J. Org. Chem.* **2009**, 74, 2067-2074

3. Experimental section

3.1. General procedures and materials

All reagents and solvents were obtained from commercial sources and were used without any further purification. The products were characterized by ^1H NMR spectroscopies. The spectra were recorded with a Bruker AVANCE Ultra ShieldTM 400 spectrometer. Referencing is relative to TMS (^1H).

3.2. Alkoxylation procedure

All experiments were followed by *in situ* ^1H NMR. The substrate (see Table S1), TMS (20 μL) and the CDCl_3 (400 μL) were added in a screw-cap NMR tube containing the catalyst (see Table S1). Then, the nucleophile (see Table S1) was added by syringe. The tube was briefly shaken for a moment and the time count was started. The reaction mixture was further monitored by NMR at 30 $^\circ\text{C}$.

Conversion was calculated from the integral intensities of the corresponding signals (conversion [%] = $(n_{\text{acetal}} + n_{\text{vinylether}} + n_{\text{ketone}}) / (n_{\text{alkyne}}) \times 100$).

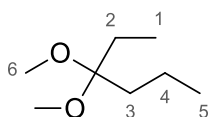
Table S1. Catalytic conditions

substrate	nucleophile	Catalyst (1 mol%)
3-hexyne (0.88 mmol, 100 μL)	ethanol (EtOH) (3.52 mmol, 205 μL)	1OTs
	2,2,2-trifluoroethanol (TFE) (3.52 mmol, 256 μL)	1OTs, 1BAr^F
	triethylene glycol monomethyl ether (Gly-OMe) ^[a] (1.16 mmol, 186 μL)	1OTs, 1BAr^F
	benzyl alcohol (BnOH) ^[a] (1.16 mmol, 120 μL)	1OTs, 1BAr^F
	2,6-dimethoxyphenol (2,6-DMP) ^[b] (0.88 mmol, 136 mg)	1OTs, 1BAr^F
1-phenyl-1- propyne (0.88 mmol, 110 μL)	ethanol (EtOH) (3.52 mmol, 205 μL)	1OTs
	2,2,2-trifluoroethanol (TFE) (3.52 mmol, 256 μL)	1OTs, 1BAr^F
diphenylacetylene (0.11 mmol, 20 mg)	methanol (3.52 mmol, 143 μL)	1OTs
	methanol (0.44mmol, 18 μL)	1OTs, 1BAr^{F[c]}

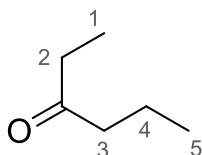
[a] 3-hexyne 0.29 mmol, 33 μL; [b] 3-hexyne 0.22 mmol, 25 μL;

[c] catalyst loading: 4 mol%

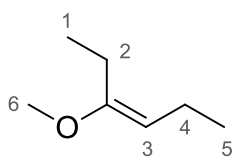
3.3 Product characterization



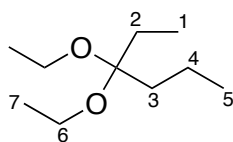
3,3-dimethoxyhexane - ^1H NMR (400 MHz, CDCl_3 , 298 K): δ (ppm) 3.15 (s, 6H, H6), 1.54 (m, 4H, H2 and H3), 1.25 (m, 2H, H4), 0.92 (t, 3H, $^3J_{\text{HH}} = 7.3$ Hz, H1), 0.82 (t, 3H, $^3J_{\text{HH}} = 7.4$ Hz, H5).



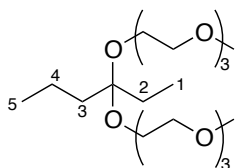
3-hexanone - ^1H NMR (400 MHz, CDCl_3 , 298 K): δ (ppm) 2.36–2.39 (tq, 4H, $^3J_{\text{HH}} = 7.4$ Hz, $^3J_{\text{HH}} = 7.3$ Hz, H2 and H3), 1.58 (m, 2H, H4), 1.03 (t, 3H, $^3J_{\text{HH}} = 7.4$ Hz, H1), 0.89 (t, 3H, $^3J_{\text{HH}} = 7.4$ Hz, H5).



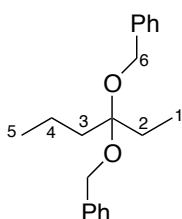
3-methoxy-3-hexene - ^1H NMR (400 MHz, CDCl_3 , 298 K): δ (ppm) 4.35 (t, 1H, $^3J_{\text{HH}} = 7.3$ Hz, H3), 3.53 (s, 3H, H6), 2.00 (m, 4H, H2 and H4), 1.06 (t, 6H, $^3J_{\text{HH}} = 7.2$ Hz, H1 and H5).



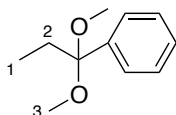
3,3-diethoxyhexane - ^1H NMR (400 MHz, CDCl_3 , 298 K): δ (ppm) 3.39 (q, 4H, $^3J_{\text{HH}} = 6.8$ Hz, H6), 1.54 (m, 4H, H2-3), 1.24 (m, 2H, H4), 1.13 (t, 6H, $^3J_{\text{HH}} = 7.2$ Hz, H7), 0.90 (t, 3H, $^3J_{\text{HH}} = 7.6$ Hz, H1), 0.80 (t, 3H, $^3J_{\text{HH}} = 7.2$ Hz, H5).



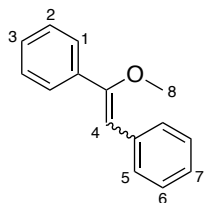
12-ethyl-12-propyl-2,5,8,11,16,19,22-heptaooxatricosane - ^1H NMR (400 MHz, CDCl_3 , 298 K): δ (ppm) 3.78 - 3.26 (m, 30H, Gly-OMe), 1.58 (m, 4H, H2 and H3), 1.27 (m, 2H, H4), 0.91 (t, 3H, $^3J_{\text{HH}} = 7.2$ Hz, H1), 0.82 (t, 3H, $^3J_{\text{HH}} = 7.6$ Hz, H5).



((hexane-3,3-diylbis(oxy))bis(methylene))dibenzene - ^1H NMR (400 MHz, CDCl_3 , 298 K): δ (ppm) 7.35-7.15 (m, 10H, Ar), 4.48 (s, 4H, H6), 1.76 (m, 4H, H2 and H3), 1.35 (m, 2H, H4), 0.92 (t, 3H, $^3J_{\text{HH}} = 7.2$ Hz, H1), 0.85 (t, 3H, $^3J_{\text{HH}} = 7.2$ Hz, H5).



(1,1-dimethoxypropyl)benzene - ^1H NMR (400 MHz, CDCl_3 , 298 K): δ (ppm) 7.49-7.13 (m, 5H, Ar), 3.25 (s, 6H, H2), 2.90 (s, 2H, H3), 1.12 (s, 3H, H1).



(E,Z)-1-(1-methoxyethene-1,2-diyl)dibenzene - ^1H NMR (400 MHz, CDCl_3 , 298 K): δ (ppm) 7.99 (d, 2H, $^3J_{\text{HH}} = 7.6$ Hz, E-H1), 7.69 (d, 2H, $^3J_{\text{HH}} = 7.6$ Hz, Z-H1), 7.55 (d, 2H, $^3J_{\text{HH}} = 7.6$ Hz, Z-H5), 7.43-7.28 (m, 3H, Z,E-H2, H3 and H6), 7.20 (t, 1H, $^3J_{\text{HH}} = 7.6$ Hz, Z-H7), 6.10 (s, 1H, Z-H4), 4.27 (s, 3H, E-H8), 3.62 (s, 3H, Z-H8).

Table S2. 1OTs + EtOH

t [min]	Conversion [%]
3.0	31.5
6.0	61.5
10.2	80.0
13.3	92.1
16.5	97.1

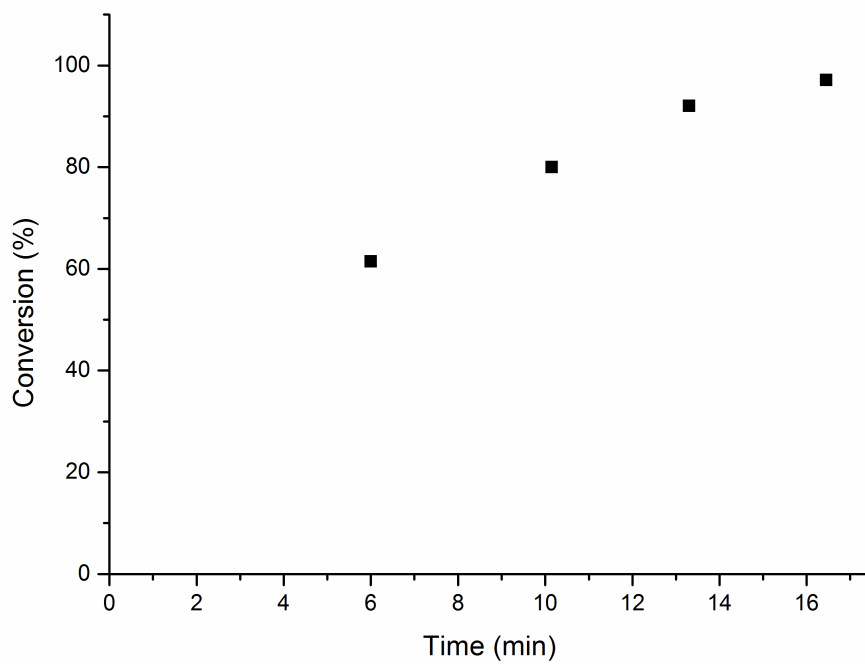


Figure S1. Plot of conversion (%) vs time (min)

Table S3. 1OTs + Gly-OMe

t [min]	Conversion [%]
30.2	16.3
36.4	20.6
42.7	25.4
48.9	29.7
55.1	33.7
61.3	37.4
67.5	40.8
73.7	44.0
80.0	47.0
86.2	49.7
92.4	52.4
98.6	54.8
104.8	57.1
111.0	59.2
117.3	61.2
123.5	63.0
129.7	64.9
135.9	67.2
142.1	68.4
148.3	69.96
154.6	71.6
160.8	73.0
167.0	73.9
173.2	75.3
179.4	76.4
185.6	77.7
191.9	78.8
198.1	79.9
204.3	80.7
210.5	81.8
216.7	82.8
222.9	83.6
229.2	84.4
235.4	85.3
241.6	85.7
247.8	86.7
254.0	87.1
260.2	87.8
266.5	88.3
272.7	89.1
278.9	89.8
285.1	90.6
291.3	91.3
297.5	91.3
303.8	91.9
310.0	92.8
316.2	93.0
322.4	93.4
328.6	94.1
334.8	94.5
341.1	94.7
347.3	95.1
353.5	95.6
359.7	96.0
365.9	96.3
372.1	96.8
378.4	97.2
384.6	97.4
390.8	97.5
397.0	97.9

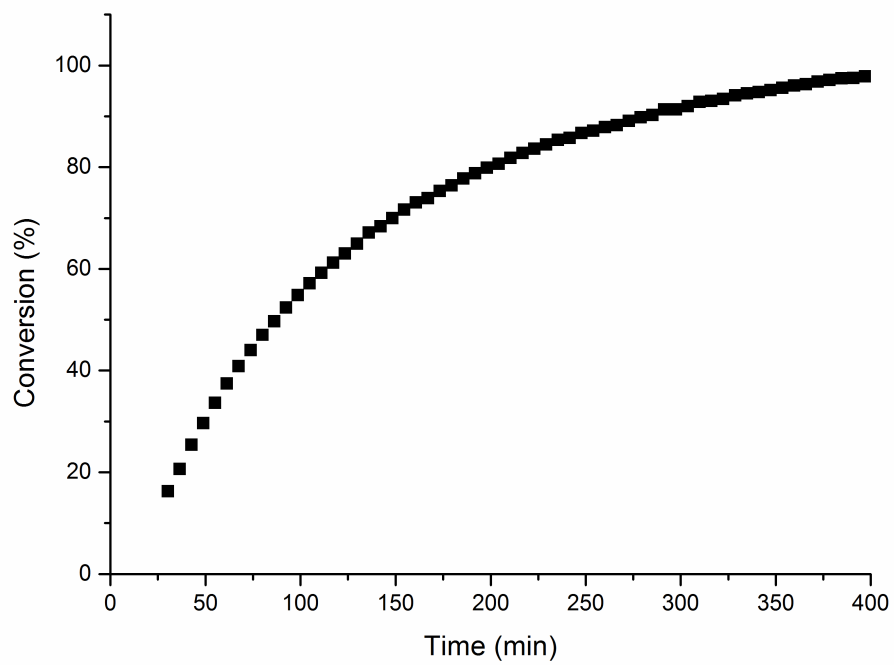


Figure S2. Plot of conversion (%) vs time (min)

Table S4. 1BAr^F + Gly-OMe

t [min]	Conversion [%]
48.5	3.0
54.7	5.4
61.0	8.6
67.2	11.9
73.4	14.6
79.6	17.2
85.8	19.6
92.0	21.7
98.3	23.8
104.5	25.8
110.7	27.3
116.9	29.1
123.1	30.9
129.3	32.5
135.6	34.2
141.8	35.8
148.0	37.4
154.2	38.9
160.4	40.5
166.6	42.0
172.9	43.5
179.1	45.0
185.3	46.5
191.5	47.8
197.7	49.3
203.9	50.7
210.2	52.0
216.4	53.4
222.6	54.7
228.8	55.8
235.0	57.3
241.2	58.6
247.5	59.8
253.7	61.0
259.9	63.4
266.1	65.8
272.3	66.7
278.5	68.0
284.8	68.9
291.0	69.9
297.2	71.1
303.4	72.1
309.6	73.3
315.8	74.1
322.1	75.4
328.3	76.2
334.5	76.5
340.7	78.3
346.9	79.1
353.1	80.0
359.4	81.2
365.6	81.7
371.8	82.9
378.0	83.6
384.2	84.4
390.4	85.4
396.7	86.3
402.9	86.8
409.1	87.6
415.3	88.4
421.5	89.4
427.7	89.8
434.0	90.6
440.2	91.9
446.4	92.5
452.6	93.2
458.8	93.1
465.0	94.0

471.3	94.4	496.1	96.5
477.5	95.1	502.3	97.6
483.7	95.8	508.6	98.1
489.9	95.9		

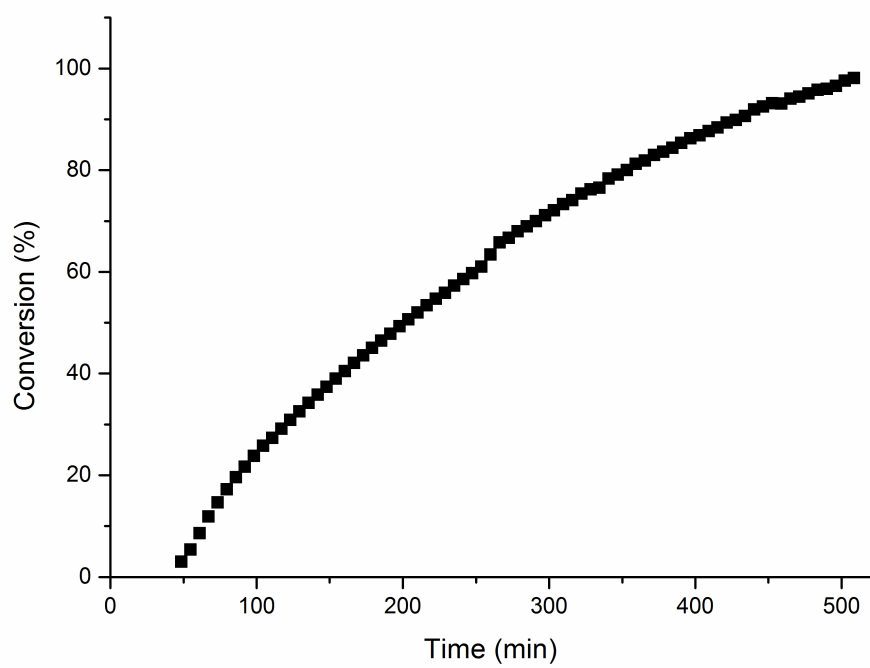


Figure S3. Plot of conversion (%) vs time (min)

Table S5. 1OTs + BnOH

t [min]	Conversion [%]
4.0	13.0
7.2	20.2
10.3	29.4
13.5	37.1
16.6	44.3
19.8	51.1
22.9	56.9
26.1	62.1
29.2	66.5
32.4	70.3
35.5	73.6
38.7	76.7
41.8	79.3
45.0	81.5
48.1	83.6
51.3	85.6
54.4	87.2
57.6	88.8

60.7	90.1
63.9	91.2
67.0	92.3
70.2	93.2
73.3	94.0
76.5	94.7
79.6	95.4
82.8	96.1
85.9	96.6
89.1	97.0
92.2	97.5
95.4	97.9
98.5	98.3
101.7	98.5
104.8	98.8
108.0	99.1
111.1	99.3
114.3	99.5

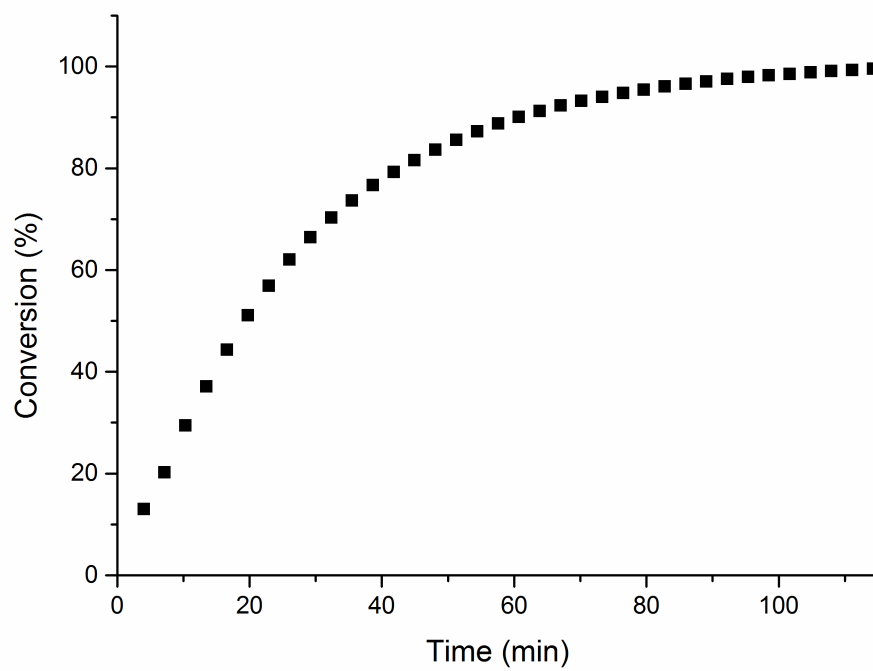


Figure S4. Plot of conversion (%) vs time (min)

Table S6. 1BAr^F + BnOH

t [min]	Conversion [%]
149	5.6
329	13.7
509	24.6
689	38.1
869	53.1
1049	64.8
1289	76.5
1379	81.7
1439	84.6
1499	86.1
1619	92.1
1819	98.7

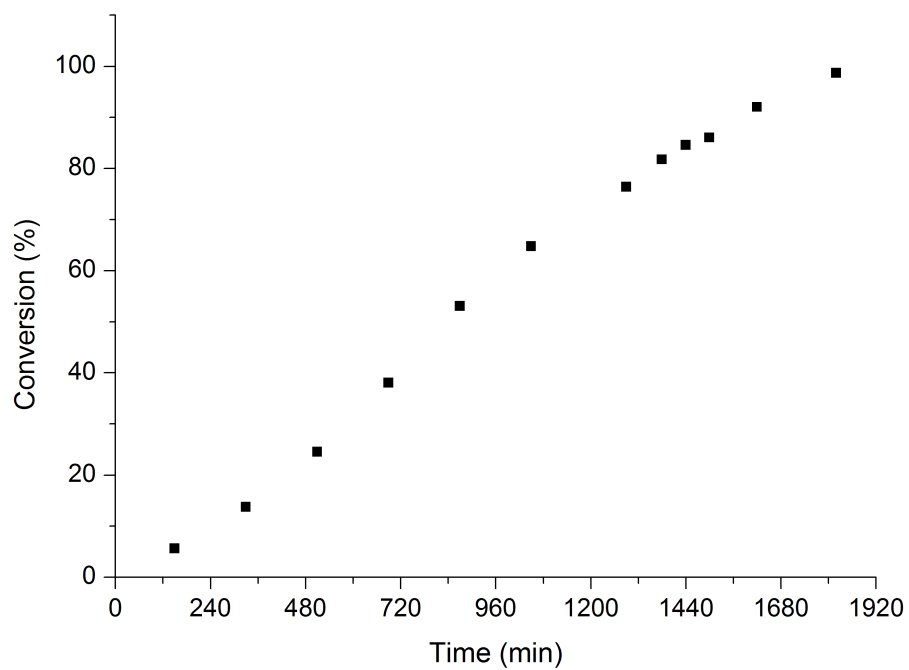


Figure S5. Plot of conversion (%) vs time (min)

Table S7. 1OTs + 2,6-DMP

t [min]	Conversion [%]
190.5	4.3
252.7	4.7
314.8	6.1
1110	9.5
1977	11.5
3326	15.3
4458	17.6
5430	18.4

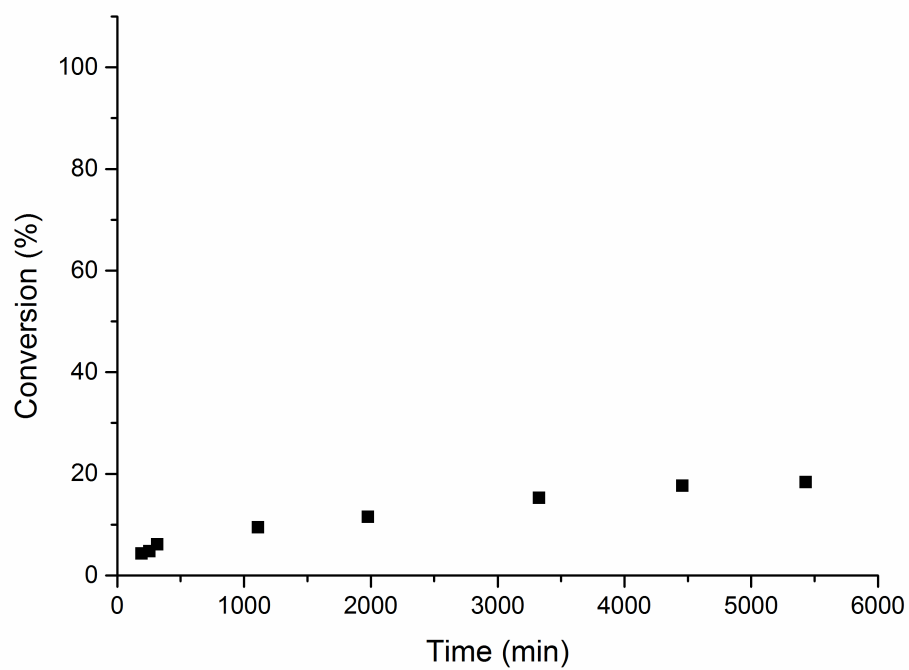


Figure S6. Plot of conversion (%) vs time (min)

Table S8. 1OTs + diphenylacetylene

t [min]	Conversion [%]
10.2	0.35
16.4	0.66
22.7	0.96
28.9	1.25
35.1	1.58
41.3	1.98
47.5	2.23
53.7	2.43
60.0	2.77
66.2	3.24
72.4	3.47
78.6	3.71
84.8	4.05
91.0	4.40
97.3	4.65
103.5	5.02
109.7	5.33
115.9	5.58
122.1	5.88
128.3	6.21
134.6	6.43
140.8	6.70
147.0	7.08
153.2	7.34
159.4	7.52
165.6	7.82
171.9	8.24
178.1	8.56
184.3	8.81
190.5	9.01
196.7	9.36
202.9	9.61
209.2	9.75
215.4	10.05
221.6	10.32
227.8	10.64
234.0	10.90
240.2	11.07
246.5	11.43
252.7	11.69
258.9	11.80
265.1	12.10
271.3	12.35
277.5	12.49
283.8	12.72
290.0	13.07
296.2	13.29
302.4	13.48
308.6	13.68
314.8	13.86
321.1	14.20
327.3	14.35
333.5	14.61
339.7	14.77
345.9	15.11
352.1	15.20
358.4	15.44
364.6	15.71
370.8	15.92
377.0	16.12

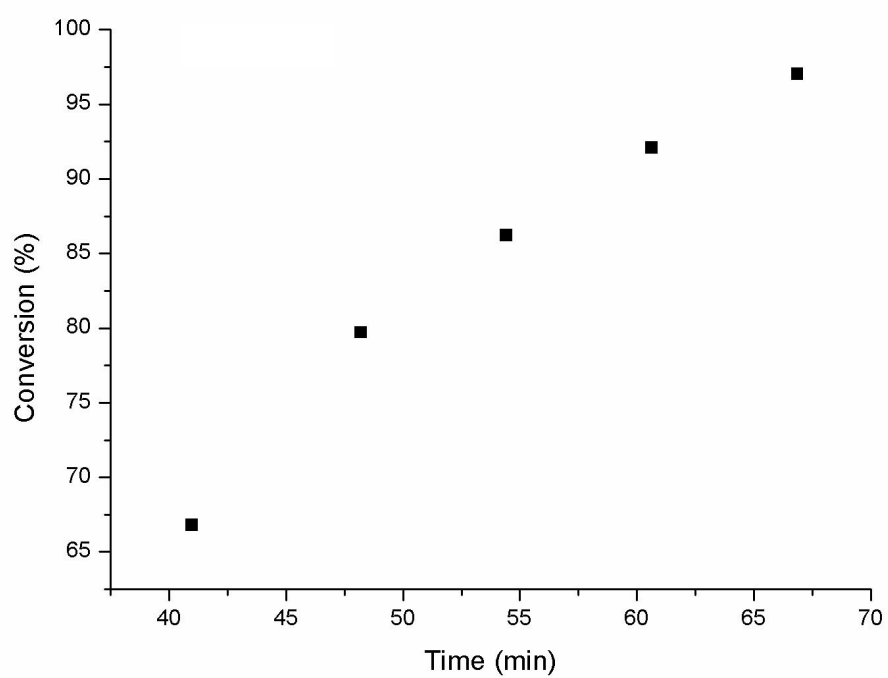


Figure S7. Plot of conversion (%) vs time (min)

Table S9. 1OTs + 1-phenyl-1-propyne

t [min]	Conversion [%]
4.0	3.23
7.2	24.30
10.3	46.55
13.5	61.47
16.6	71.45
19.8	78.75
22.9	84.17
26.1	88.15
29.2	90.97
32.4	93.16
35.5	94.84
38.7	96.06
41.8	97.00
45.0	97.69
48.1	98.23
51.3	98.65

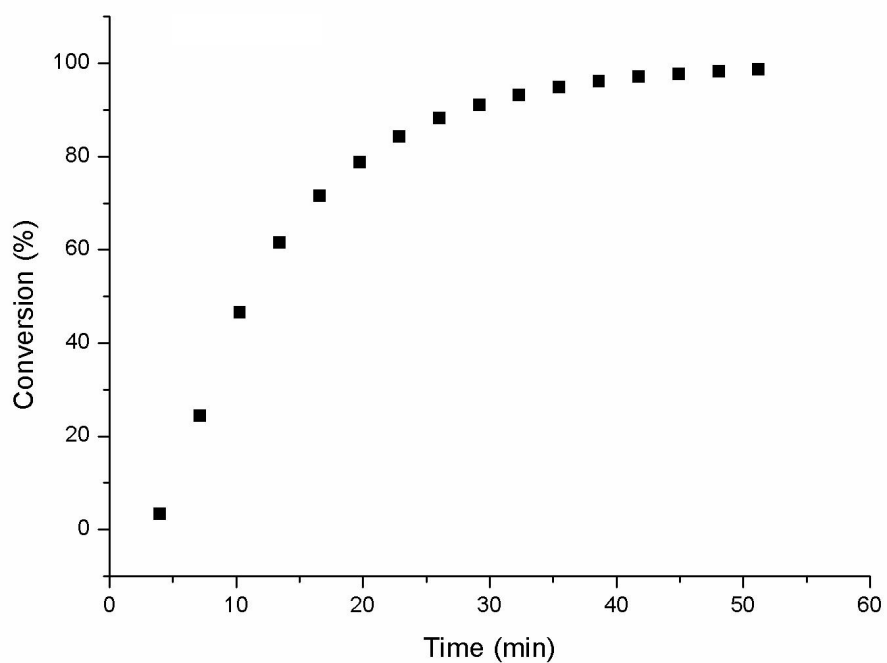


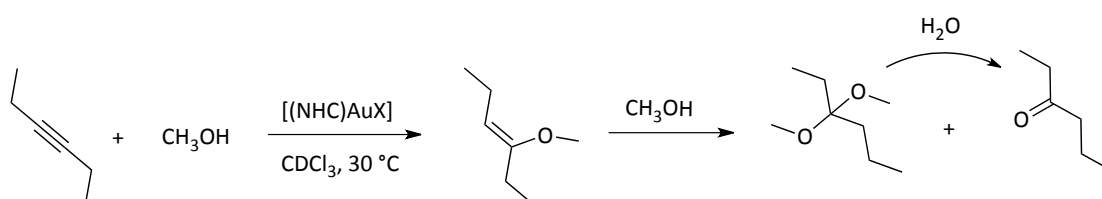
Figure S8. Plot of conversion (%) vs time (min)

CHAPTER

5

DETERMINATION OF
ACTIVATION PARAMETERS

This chapter describes the determination of the activation parameters for the addition of methanol to 3-hexyne for different anions (Scheme 1).



Scheme 1. Gold(I) catalyzed methoxylation of 3-hexyne

The obtained values are the first obtained in gold catalysis as a function of the nature of the counterion.

The results have been previously published in:

- Trinchillo, M., Belanzoni, P., Belpassi, L., Biasiolo, L., Busico, V., D'Amora, A., D'amore, L., Del Zotto, A., Tarantelli, F., Tuzi, A., and Zuccaccia, D. *Organometallics*, **2016**, 35, 641–654;

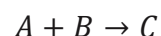
1. Introduction¹

The temperature dependence of reaction rate is described by both Arrhenius and Eyring equations. The Arrhenius equation can be applied only to kinetics of gas reaction, whereas the Eyring equation is also used in the study of reaction in solution and mixed phase reactions, where the simple collision model is not very helpful.

The Eyring's formulation of the transition state theory,² in 1935, has been applied with considerable success to a wide variety of rate processes.

In comparison with the other treatment of rates, one of the advantages is its relative ease of application. Attempts to use improved treatments require much more labor and a larger amount of time.³

Considering the bimolecular reaction:



The reaction rate is:

$$v = \frac{d[C]}{dt} = k[A][B]$$

As the reaction proceeds, A and B come into contact, distort, and begin to exchange or discard atoms. The reaction coordinate is the collection of motions, such as changes in interatomic distances and bond angles, that are directly involved in the transformation of reactants in products. The cluster of atoms corresponding to the region close to the maximum of the reaction profile is called the activated complex (Figure 1). After the maximum, the potential energy falls as the atoms rearrange in the cluster and reaches a value characteristic of the products. The peak of the potential energy corresponds to the activation energy, E_a (Figure 1), where two reactant molecules have come to such a degree of closeness and distortion that a small further distortion will send them in the direction of products. This crucial configuration is called the "transition state of the reaction". Although some molecules

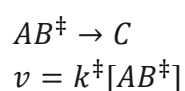
¹ Atkins, P., de Paula, J. *Atkins Physical Chemistry* Eighth edition, W. H. Freeman and Company, 2006, USA

² H. Eyring, *J. Chem. Phys.* **1935**, *3*, 107

³ Laidler, K. J., King, M. C., *J. Phys. Chem.* **1983**, *87*, 2657-2664

entering the transition state might return to reactants, if they pass through this configuration, then it is inevitable that products will emerge from the encounter.

The transition state theory permits the detailed calculation of rate constants using the concept of the statistical thermodynamics. According this theory, the reactants, A and B, are in a rapid pre-equilibrium with the activated complex, which can form the products passing through the transition state.



If its vibration-like motion along the reaction coordinate occurs with a frequency ν , then the frequency with which the cluster of atoms forming the complex approaches the transition state is also ν .

However, it is possible that not every oscillation along the reaction coordinate takes the complex through the transition state. Therefore, we suppose that the rate of passage of the complex through the transition state is proportional to the vibrational frequency along the reaction coordinate:

$$k^\ddagger = \kappa \nu$$

where κ is the *transmission coefficient*. In the absence of information to the contrary, κ is assumed to be about 1.

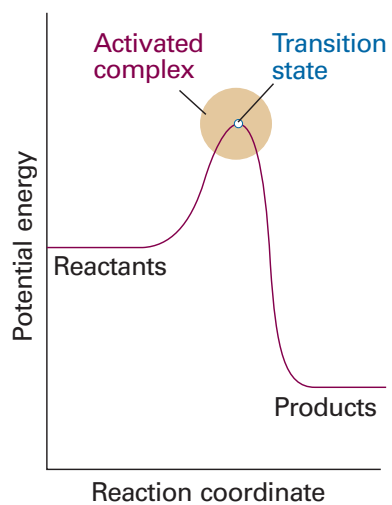


Figure 1. Reaction profile. The horizontal axis is the reaction coordinate, and the vertical axis is potential energy. The activated complex is the region near the potential maximum, and the transition state corresponds to the maximum itself. Reproduced from ref. 1

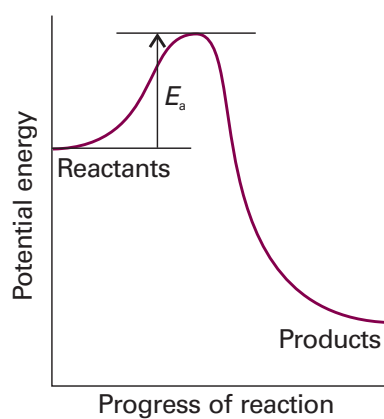


Figure 2. Potential energy profile for an exothermic reaction. The height of the barrier between the reactants and products is the activation energy of the reaction. Reproduced from ref. 1

We have already assumed that a vibration of the activated complex AB^\ddagger tips it through the transition state. The partition function for this vibration is:

$$q = \frac{1}{1 - e^{-h\nu/k_B T}}$$

where ν is its frequency (the same frequency that determines k^\ddagger). This frequency is much lower than for an ordinary molecular vibration because the oscillation corresponds to the complex falling apart, so the force constant is very low.

Therefore, provided that $h\nu/k_B T \ll 1$, the exponential may be expanded and the partition function reduces to

$$q = \frac{1}{1 - (1 - \frac{h\nu}{k_B T} + \dots)} \approx \frac{k_B T}{h\nu}$$

We can therefore write:

$$q_{AB^\ddagger} \approx \frac{k_B T}{h\nu} \bar{q}_{AB^\ddagger}$$

where \bar{q} denotes the partition function for all the other modes of the complex. The constant K^\ddagger is therefore:

$$K^\ddagger = \frac{k_B T}{h\nu} \bar{K}^\ddagger \quad \bar{K}^\ddagger = \frac{N_A \bar{q}_{AB^\ddagger}^\ominus}{q_A^\ominus q_B^\ominus} e^{-\Delta E_0/RT}$$

where \bar{K}^\ddagger is a kind of equilibrium constant, but with one vibrational mode of AB^\ddagger discarded.

Combining all the parts of the calculation into:

$$k = k^\ddagger \frac{RT}{p^\ominus} K^\ddagger = \kappa \nu \frac{k_B T}{h \nu} \frac{RT}{p^\ominus} \bar{K}^\ddagger$$

The unknown frequencies ν cancel, and after writing $\bar{K}_{AB}^\ddagger = (RT/p^\ominus) \bar{K}^\ddagger$, we obtain the *Eyring equation*:

$$k = \kappa \frac{k_B T}{h} \bar{K}_{AB}^\ddagger$$

The factor \bar{K}_{AB}^\ddagger is given the definition $\bar{K}_{AB}^\ddagger = (RT/p^\ominus) \bar{K}^\ddagger$ in terms of the partition functions of A, B, and AB^\ddagger , so in principle we now have an explicit expression for calculating the second-order rate constant for a bimolecular reaction in terms of the molecular parameters for the reactants and the activated complex and the quantity κ .

If we accept that \bar{K}^\ddagger is an equilibrium constant (despite one mode of AB^\ddagger having been discarded), we can express it in terms of a *Gibbs energy of activation*, ΔG^\ddagger , through the definition

$$\Delta G^\ddagger = -RT \ln \bar{K}^\ddagger$$

Then, the rate constant becomes

$$k = \kappa \frac{k_B T}{h} \frac{RT}{p^\ominus} e^{-\Delta G^\ddagger/RT}$$

Because $G = H - TS$, the Gibbs energy of activation can be divided into an entropy of activation, ΔS^\ddagger , and an enthalpy of activation, ΔH^\ddagger , by writing

$$\Delta G^\ddagger = \Delta H^\ddagger - T\Delta S^\ddagger$$

ΔG^\ddagger is always positive, because there is always a barrier (sometimes small) to reaction.

ΔG^\ddagger is calculated directly from k and Eyring equation:

$$\Delta G^\ddagger = RT \ln \left(\frac{k_B T}{h} \right) - RT \ln k$$

By arranging the Eyring equation and taking the logarithms

$$\ln \left(\frac{k}{T} \right) = \ln \left(\frac{k_B}{h} \right) + \frac{\Delta S^\ddagger}{R} - \frac{\Delta H^\ddagger}{R} \left(\frac{1}{T} \right)$$

we obtain a strictly linear relationship which can be plotted.

Plotting $\ln k/T$ vs $1/T$, the slope of the straight line is $-\Delta H^\ddagger/R$ and hence $\Delta H^\ddagger = -(\text{slope})R$.

From the same plot, the intercept is:

$$\text{intercept} = \ln \left(\frac{k_B}{h} \right) + \frac{\Delta S^\ddagger}{R}$$

Thus, ΔS^\ddagger is readily calculated from:

$$\Delta S^\ddagger = R(\text{intercept} - \ln(k_B/h))$$

The drawback of the Eyring Plot is that the Y-intercept (used to determine ΔS^\ddagger) is normally a large extrapolation from the experimental data. Therefore, if the linear fit of $\ln(k/T)$ vs $1/T$ is not extremely good, the error in ΔS^\ddagger can be quite large.

Eyring equation

$$\ln\left(\frac{k}{T}\right) = \ln\left(\frac{k_B}{h}\right) + \frac{\Delta S^\ddagger}{R} - \frac{\Delta H^\ddagger}{R} \left(\frac{1}{T}\right)$$

k_B : Boltzmann constant

h : Plank constant

R : Gas constant

2. Results and discussion

Even if the alkoxylation of alkynes has been deeply studied in the past, its activation parameters (ΔH^\ddagger and ΔS^\ddagger) have not been experimentally evaluated yet. The measurement of the activation parameters for the methoxylation of 3-hexyne, catalyzed by both **1BF₄** and **1OTs**, was obtained by means of kinetic studies, conducted over a 288-313 K temperature range, and by monitoring the reaction through *in situ* ¹H NMR spectroscopy. The results are displayed in Figure 3. The rate of disappearance of the substrate in each case is constant and indicates a pseudo-zero order⁴ rate dependence on substrate concentration over the given temperature range (see **Experimental Section**, Figure S1).

On the basis of the Eyring equation: $\ln(k/T) = \Delta S^\ddagger/R - \ln(h/k_B) - \Delta H^\ddagger/RT$, the activation enthalpy (ΔH^\ddagger) and entropy (ΔS^\ddagger) were obtained respectively from the slope and intercept of the plot of $\ln(k/T)$ against $1/T$ (Figure 3). The activation enthalpy was determined to be 18.1(1.5) and 16.7(1.9) kcal mol⁻¹ for **1BF₄** and **1OTs**, respectively. Activation entropy was determined to be -6.5(0.6) cal K⁻¹ mol⁻¹ for **1BF₄** and -9.4(1.5) cal K⁻¹ mol⁻¹ for **1OTs**.⁵ Russell and co-workers reported a slightly lower activation enthalpy value (15.2 kcal mol⁻¹) in their studies on the gold-catalyzed oxidative coupling of arylsilanes and arenes.⁶ Thus, the methoxylation of 3-hexyne catalyzed by **1BF₄** and **1OTs** requires free energies ΔG^\ddagger at 303 K of 20.1(1.3) and 19.5(1) kcal mol⁻¹, respectively. These values are, to the best of our knowledge, the first obtained in gold catalysis as a function of the nature of the counterion, and are in nice agreement with our DFT calculations⁷ that predicted an activation barrier for the nucleophilic attack for BF₄⁻ slightly higher than for OTs⁻ (16.5 vs 15.6 kcal mol⁻¹, respectively).

⁴ Zhdanko, A.; Maier, M. M. *Chem. Eur. J.* **2014**, *20*, 1918-1930

⁵ Values of ΔS^\ddagger between 10 and -10 e.u. are considered difficult to interpret

⁶ Ball, L. T.; Lloyd-Jones, G. C.; Russel, C. A. *J. Am. Chem. Soc.* **2014**, *136*, 254-264

⁷ Ciancaleoni, G.; Belpassi, L.; Zuccaccia, D.; Tarantelli, F.; Belanzoni, P. *ACS Catal.* **2015**, *5*, 803-814

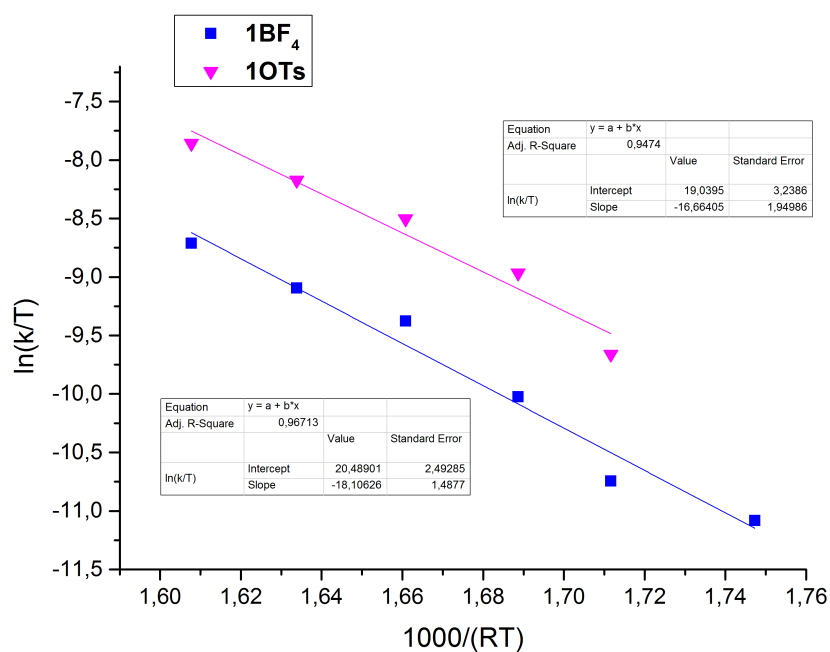


Figure 3. Eyring plot at different temperatures. Reaction conditions: 1OTs (0.5 mol% in $CDCl_3$) [3-hexyne]/[methanol] = $\frac{1}{4}$, at 294, 298, 303, 308 and 313 K. $1BF_4$ (0.5 mol% in $CDCl_3$) [3-hexyne]/[methanol] = $\frac{1}{4}$, at 288, 294, 298, 303, 308 and 313 K. Errors in ΔH and ΔS are expressed as 95% confidence limits.

3. Experimental section

3.1. General procedures and materials

All reagents and solvents were obtained from commercial sources and were used without any further purification. The products were characterized by ^1H NMR spectroscopies. The spectra were recorded with a Bruker AVANCE Ultra ShieldTM 400 spectrometer. Referencing is relative to TMS (^1H).

3.2. Measurement of activation parameters ΔH^\ddagger and ΔS^\ddagger

General procedure for Eyring plot. 3-hexyne (100 μL , 0.88 mmol), TMS (20 μL) and CDCl_3 (400 μL) were added in a screw-cap NMR tube containing 0.5 mol% of catalyst (**1BF₄** and **1OTs**). The NMR tube was placed in the NMR spectrometer where the probe had been set up to the appropriate temperature. The sample was allowed to equilibrate in the spectrometer for ten minutes before acquiring spectra. Then, CH_3OH (143 μL , 3.52 mmol) was added by syringe, it was briefly shaken for a moment and quickly relocated in the spectrometer. The reaction was studied by ^1H NMR, by monitoring the disappearance of 3-hexyne (resonance at 2.14 ppm in CDCl_3). To assure the accuracy of the data, each experiment was replicated. The slope of lines of the [3-hexyne] vs time plot directly give the rate constant value, k_{obs} in $\text{mol} \times \text{L}^{-1} \times \text{h}^{-1}$. The rate constant was calculated using all available data point. The rates are shown in Tables S1-S2. Conversion was calculated from the integral intensities of the corresponding signals (conversion [%] = $(n_{\text{acetal}} + n_{\text{vinylether}} + n_{\text{ketone}}) / (n_{\text{alkyne}}) \times 100$).

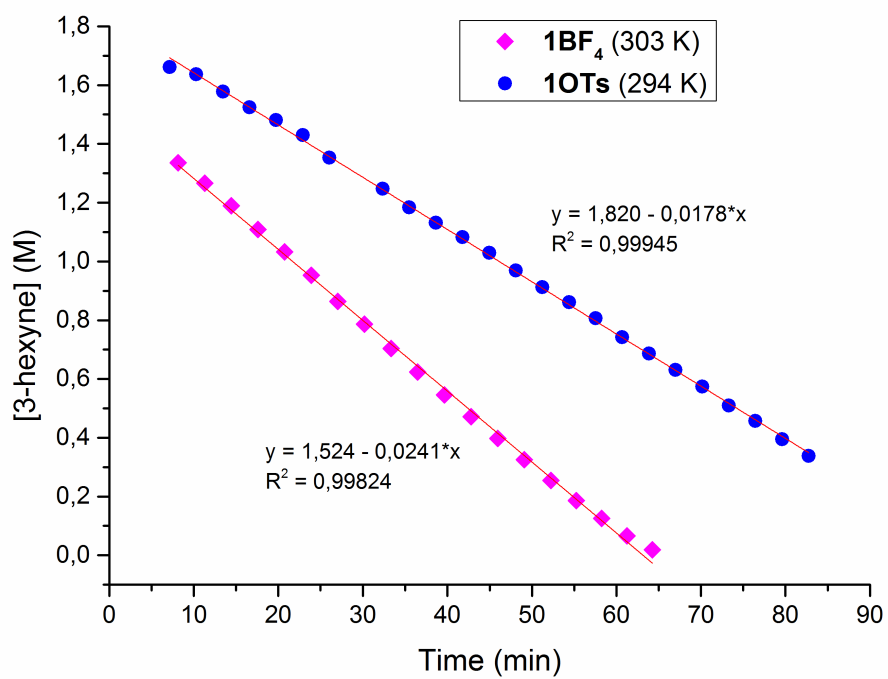


Figure S1. Representative kinetic plot for 1OTs at 294 K and 1BF₄ at 303 K

Table S1. 1OTs

T (K)	k_{obs} ($\text{mol} \times \text{L}^{-1} \times \text{h}^{-1} \times 10^{-2}$) ^a
294	$1.8 \pm 0.14 \times 10^{-3}$
298	$3.8 \pm 0.6 \times 10^{-3}$
303	$6.1 \pm 0.3 \times 10^{-2}$
308	$8.6 \pm 0.7 \times 10^{-2}$
313	12.1 ± 0.01

^aValues represent an average of two kinetics runs

Table S2. 1BF₄

T (K)	k_{obs} ($\text{mol} \times \text{L}^{-1} \times \text{h}^{-1} \times 10^{-2}$) ^a
288	$0.4 \pm 3.2 \times 10^{-5}$
294	$0.6 \pm 0.4 \times 10^{-3}$
298	$1.3 \pm 0.13 \times 10^{-3}$
303	$2.5 \pm 0.3 \times 10^{-3}$
308	$3.4 \pm 0.6 \times 10^{-3}$
313	$5.1 \pm 1.4 \times 10^{-3}$

^aValues represent an average of two kinetics runs

Table S3. Activation parameters^a for 1OTs and 1BF₄

	ΔH^\ddagger (Kcal • mol ⁻¹)	ΔS^\ddagger (cal K ⁻¹ mol ⁻¹)	ΔG^\ddagger (Kcal • mol ⁻¹)
1OTs	16.7 ± 1.9	-9.4 ± 1.5	19.5 ± 1
1BF₄	18.1 ± 1.5	-6.5 ± 0.6	20.1 ± 1.3

^atemperature 303 K

CHAPTER

6

COMPUTATIONAL STUDY OF
COUNTERION EFFECT

This chapter describes a rational understanding of the anion effect from a computational point of view on the basis of our catalytic and kinetic evidences in the alkoxylation reaction (see **Chapter 3** and **4**).

Indeed, an extensive computational work has been carried out by Dr. Leonardo Belpassi, Prof. Paola Belanzoni and Prof. Francesco Tarantelli from Istituto di Scienze e Tecnologie Molecolari del CNR (CNR-ISTM) and University of Perugia.

All the results confirm the general mechanistic picture in which the anion plays an active role in all the steps of the reaction mechanism: pre-equilibrium, nucleophilic attack and protodeauration.

The most important factors seem to be the ability to abstract the proton from the nucleophile, which is proportional to both the anion basicity and its coordinating power.

These anion properties have a great under-evaluated impact on the catalytic performances of gold complexes.

In the following sections the influence of the anion on the catalytic efficiency will be described in detail in all steps of the reaction mechanism of the intermolecular addition of methanol to 2-butyne, used as models for nucleophile and substrate, through a density functional theory (DFT) approach.

Furthermore, a trend between coordinating ability and experimental TOF values will be established and those experimental catalytic results that at first glance appears unexpected (including for instance the poor performance of the complex with PFHp⁻ anion, see **Chapter 3**) will be rationalized; finally, the anion effect will be investigated also in relationship with different nucleophiles.

The chapter is based on the papers:

- Trinchillo, M., Belanzoni, P., Belpassi, L., Biasiolo, L., Busico, V., D'Amora, A., D'amore, L., Del Zotto, A., Tarantelli, F., Tuzi, A., and Zuccaccia, D. *Organometallics*, **2016**, *35*, 641–654;
- Ciancaleoni, G., Belpassi, L., Zuccaccia, D., Tarantelli, F., Belanzoni, P. *ACS Catal.* **2015**, *5*, 803-814;
- Biasiolo, L.; Trinchillo, M.; Belanzoni, P.; Belpassi, L.; Busico, V.; Ciancaleoni, G.; D'Amora, A.; Macchioni, A.; Tarantelli, F.; Zuccaccia, D. *Chem. Eur. J.* **2014**, *20*, 14594-14598

1. Introduction

Despite the large amount of work on the alkoxylation of alkynes, no systematic computational data are available yet about the role of the counterion.

Up to now, the role of the anion has been firmly recognized only in the protodeauration step, acting as a proton shuttle, or forming weak interactions with the substrate in order to explain the enantioselectivity,¹ or modulating the reactivity of cationic intermediates.² A rational understanding of anion effects in gold catalysis is therefore lacking, particularly in the light of new experimental results, described in **Chapter 3** and **4**.

Considering the complete set of gold(I) complexes [(NHC)AuX] (NHC = 1,3-bis(2,6-diisopropylphenyl)-imidazol-2-ylidene and $X^- = OTs^-, OTf^-, BF_4^-, TFA^-, OAc^-, BARF^-, OMs^-, NO_3^-, ClO_4^-, ptm^-, NTf_2^-$ and PFHp⁻) as catalysts in the alkoxylation of 3-hexyne, with different nucleophiles, the trend of the activities does not match with the coordinating ability of the anions. This is a counterintuitive or unexpected result, since weak coordinating anions are commonly chosen as anion in homogeneous gold catalysis in order to enhance the catalyst efficiency, and deserves a detailed investigation on the role of the anion in the reaction mechanism. Since under our catalytic conditions the nucleophilic attack is the rate-determining step, an active role of the anion is expected also within this step.

The mechanism proposed combining theoretical and experimental findings is summarized in Scheme 1.

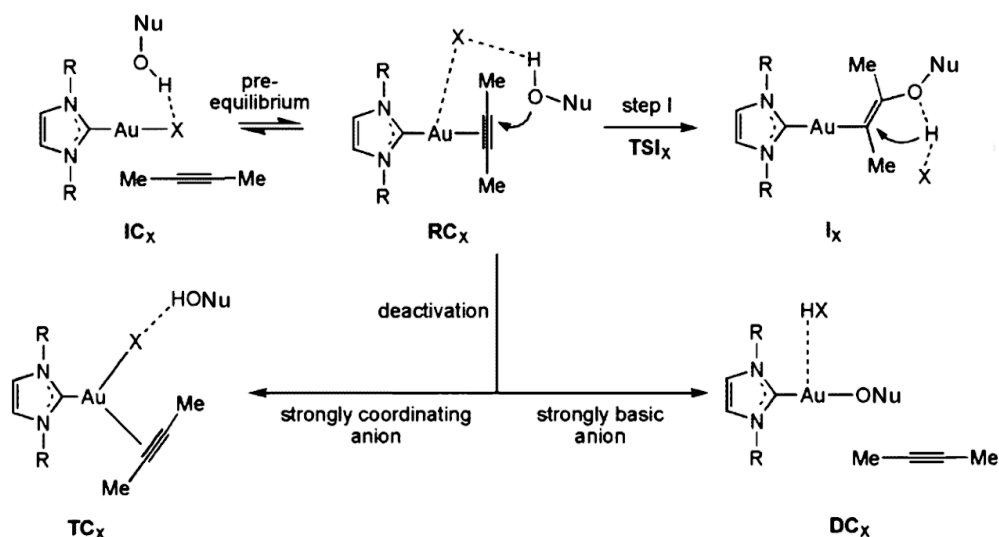
The role of the anion is emphasized in all the steps of the pathways: the pre-equilibrium, the nucleophilic attack (step I) and the proton transfer to the unsaturated carbon atom (protodeauration, step II).

Step I, however, can be disrupted by an anion-induced catalyst poisoning, through two possible deactivation pathways: a strongly coordinating anion will shift the pre-

¹ (a) Bandini, M.; Bottoni, A.; Chiarucci, M.; Cera, G.; Miscione, G. P. *J. Am. Chem. Soc.* **2012**, *134*, 20690–20700. (b) Kim, J. H.; Park, S.-W.; Park, S. R.; Lee, S.; Kang, E. J. *Chem. Asian J.* **2001**, *6*, 1982–1986

² Zhou, T.; Xu, L.; Xia, Y. *Org. Lett.* **2013**, *15*, 6074–6077

equilibrium stronger to the left (ISIP species), eventually forming an intermediate tricoordinated complex, $[(\text{NHC})\text{AuX}(\text{2-butyn})]-(\text{MeOH})$ (TC_x , Scheme 1); alternatively, a strongly basic anion can abstract a proton from the methanol, leading to the formation of the corresponding acid HX and free MeO^- , which deactivates the catalyst through the formation of the catalytically inactive species (deactivated complex, DC_x , Scheme 1). Actually, the presence of $[(\text{NHC})\text{AuOMe}]$ has been experimentally observed when TFA^- was used as anion (see **Chapter 3**).



Scheme 1. Pre-equilibrium, nucleophilic attack and deactivation steps in the reaction mechanism between 2-butyne and an alcohol nucleophile catalyzed by the $[(\text{NHC})\text{AuX}]$ complex

A density functional theory (DFT) description of the first nucleophile molecule addition is reported, since experimental evidence showed that the addition of the second molecule of nucleophile is fast.

In order to elucidate the anion role on the reaction mechanism, the bare $[\text{NHCu}]^+$ complex is included, without any anion. This could be a good model when a polar solvent is used or in the presence of very low coordinating anions, such as $\text{BAR}^{\text{F}-,3}$,

³ In the present work, the $\text{BAR}^{\text{F}-}$ anion will not be considered because of its large size, its extremely low tendency to form ion pairs, and its inability to form hydrogen bonds

which is known to prevent the ion pairing phenomenon, at least at low concentration.⁴

⁴ Zuccaccia, D.; Bellachioma, G.; Cardaci, G.; Ciancaleoni, G.; Zuccaccia, C.; Clot, E.; Macchioni, A. *Organometallics* **2007**, *26*, 3930–3946.

2. Results and discussion

2.1. Pre-equilibrium step: substrate vs anion coordination

The study started searching for the most stable species formed by the catalyst, the anion and the nucleophile. Basicity and coordinating ability of the anion are investigated in the presence of methanol by examining the relative stabilities of the possible ternary adducts in the absence of 2-butyne substrate and, for comparison, the adduct without the anion but including an additional methanol molecule is considered. The inclusion of methanol allows to compare jointly both proton acceptor and coordinating ability of the different anions. To analyze the role of the methanol–anion interaction, the energy difference (in gas phase) has been calculated between methanol-coordinated $[\text{NHCAu}-(\text{OHCH}_3)]\text{X}$ and anion-coordinated $[\text{NHCAu-X}](\text{CH}_3\text{OH})$ adducts. The most stable adduct for each species is depicted in Figure 1.

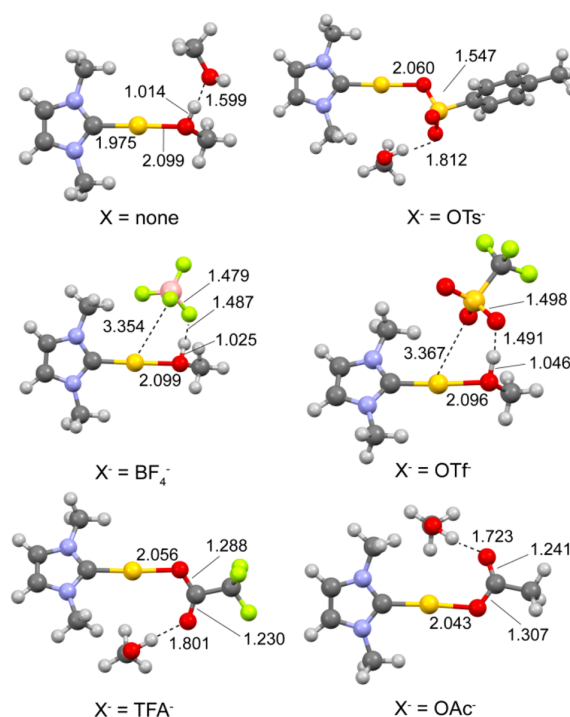


Figure 1. Optimized geometries of the most stable ternary adduct species. Distances are in angstroms

In Table 1, the relative energies of the anion-coordinated $[\text{NHCAu-X}](\text{CH}_3\text{OH})$ and

methanol-coordinated $[\text{NHCAu}(\text{OHCH}_3)]\text{X}$ species are reported, and $\text{H}-\text{OCH}_3$ and $\text{X}-\text{HOCH}_3$ distances are summarized for the CH_3OH -coordinated species.

Indeed, the analysis of the ternary adducts of the $[\text{NHC-Au}]^+$ catalyst with X^- and methanol allows to probe the extent of the anion hydrogen-bonding ability. The distance between the anion and the hydrogen of the gold-coordinated methanol is 1.062 Å for OAc^- , 1.255 Å for TFA^- , 1.425 Å for OTs^- , 1.487 Å for BF_4^- , and 1.491 Å for OTf^- (Table 1 and Figure 1).

Table 1. Relative dissociation energies (kcal/mol) Calculated As the Energy Difference between Methanol- Coordinated $[\text{NHCAu}(\text{OHCH}_3)]\text{X}$ and Anion-Coordinated $[\text{NHCAu-X}](\text{CH}_3\text{OH})$ Species, Methanol $\text{O}\cdots\text{H}$, and Anion-Methanol ($\text{CH}_3\text{OH}\cdots\text{X}$) hydrogen bond Distances (Å) in $[\text{NHCAu}(\text{OHCH}_3)]\text{X}$ Species^a

X^-	ΔE	$\text{CH}_3\text{O}\cdots\text{H}$	$\text{CH}_3\text{OH}\cdots\text{X}$
None (CH_3OH)	-34.4	1.014	1.599
OTs^-	+3.6	1.071	1.425
BF_4^-	-8.3	1.025	1.487
OTf^-	-0.5	1.046	1.491
TFA^-	+5.9	1.177	1.255
OAc^-	+5.7	1.468	1.062

^a Species without anion and with one additional methanol are also shown

The extent of proton transfer from gold-coordinated methanol to the anion correlates with the relative stability of the $[\text{NHCAu}(\text{OHCH}_3)]\text{X}$ with respect to the $[\text{NHCAu-X}](\text{CH}_3\text{OH})$ adducts. Interestingly enough, for BF_4^- anion, the hydrogen bond with gold-coordinated methanol does not tend to abstract the proton rather it causes a B-F bond elongation from 1.404 to 1.479 Å (see Figure 2). For this reason, the distance between the hydrogen and the oxygen of the gold-coordinated methanol is a

more suitable geometrical parameter to quantify the hydrogen-bonding basicity and, then, the nucleophilic activation ability of the different anions: the $\text{CH}_3\text{O}\cdots\text{H}$ distance is 1.468 Å for OAc^- , 1.177 Å for TFA^- , 1.071 Å for OTs^- , 1.046 Å for OTf^- , 1.025 Å for BF_4^- , and 1.014 Å for CH_3OH .

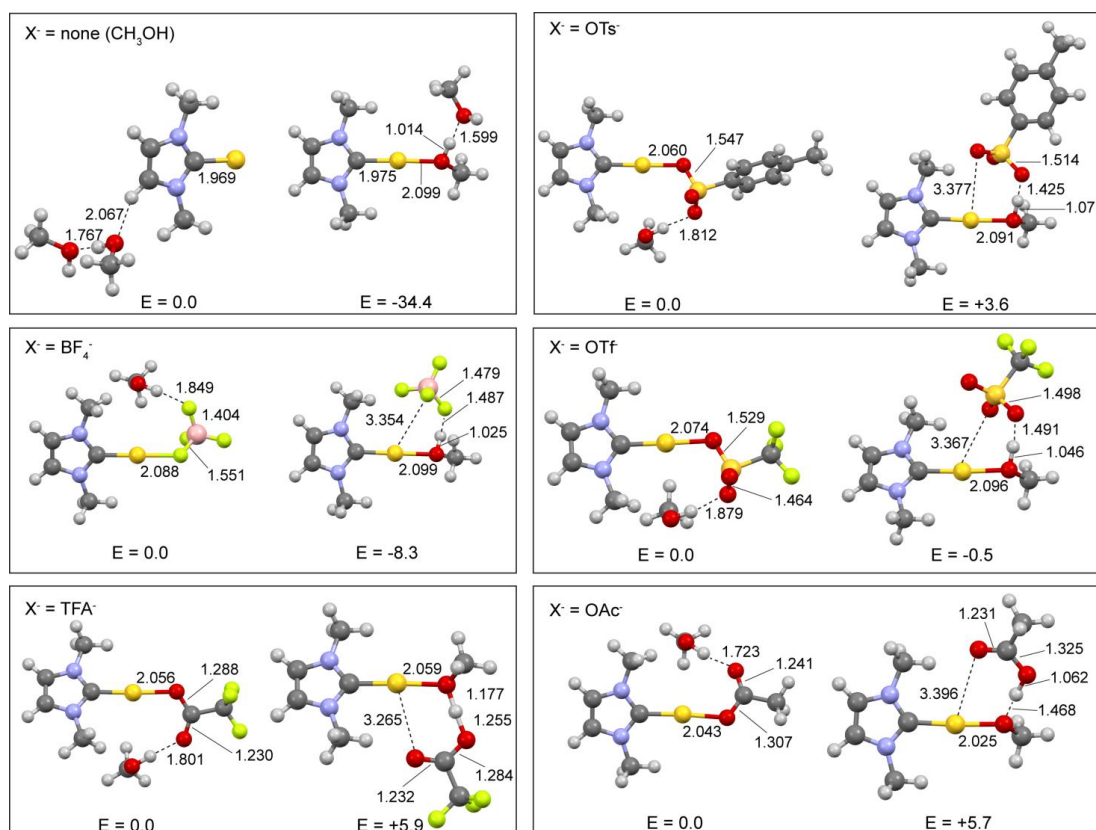


Figure 2. Optimized geometries of the considered ternary adduct species: $[\text{NHCAu-X}](\text{CH}_3\text{OH})$ (left side of each panel), $[\text{NHCAu}-(\text{OHCH}_3)]\text{X}$ (right side of each panel). From top to bottom: $\text{X} = \text{none}$ (CH_3OH), OTs^- , BF_4^- , OTf^- , TFA^- and OAc^- . Distances are in Å, energies in kcal/mol

It can be seen that the $[\text{NHCAu}-(\text{OHCH}_3)]^+(\text{CH}_3\text{OH})$ bond dissociation is calculated to be 34.4 kcal/mol with respect to $[\text{NHCAu}(\text{CH}_3\text{OH})_2]^+$, where the two hydrogen-bonded methanol molecules form an additional hydrogen bond with the backbone of the NHC ligand (Figure 2). In the presence of the anion, calculations predict that gold-anion bond adducts $[\text{NHCAu-X}](\text{CH}_3\text{OH})$ are more stable than gold-methanol bond

adducts $[\text{NHCAu}(\text{OHCH}_3)]\text{X}^-$ for all X^- , except for BF_4^- (-8.3 kcal/mol) and OTf^- (-0.5 kcal/mol). Notable, for OTs^- , ΔE is smaller than that for TFA^- or OAc^- .

Such a trend well correlates with the anion coordination power, identified with the metal–anion dissociation energies in a noncoordinating solvent (dichloroethane) and calculated by Lledoś et al.⁵ for $[\text{PAuX}] \rightarrow [\text{PAu}]^+ + \text{X}^-$ ($\text{P} = \text{PH}_3$ and PPh_3 , $\text{X}^- = \text{TFA}^-$, Cl^- , NO_3^- , OTs^- , OTf^- , and BF_4^-). However, the calculated ΔE values in Table 1 are generally lower than those computed by Lledoś et al., and this is due to the presence of a $\text{CH}_3\text{OH}\cdots\text{X}$ hydrogen bond, which facilitates the decoordination of the anion. If the anion is a strong base, experimental observations showed that the alcoholic proton is completely abstracted from the methanol, with the formation of a methoxide moiety (see **Chapter 3**).

The first step of the catalysis is the ligand substitution, CH_3OH or X^- , by the alkyne. Quaternary adducts formed between the anion X^- , methanol, 2-butyne, and $[\text{NHC-Au}]^+$ were computationally found in which the 2-butyne is coordinated through its triple bond. However, the initial complex (**IC_X**) is represented by the most stable ternary adduct calculated above for each anion plus the 2-butyne substrate in the second coordination sphere (Scheme 1).

Coordination of 2-butyne to the metal center leads to different conformations. Among them, two conformations are of interest for the nucleophilic attack step. In the most stable one, the hydrogen-bonded $[\text{X}(\text{CH}_3\text{OH})]^-$ group is located above the gold. We denote it as structure **NC_X** (non-activating complex), and it is given for all the species (Figures 3 and 4).

⁵ Kovačs, G.; Ujaque, G.; Lledoś, A. *J. Am. Chem. Soc.* **2008**, *130*, 853–864

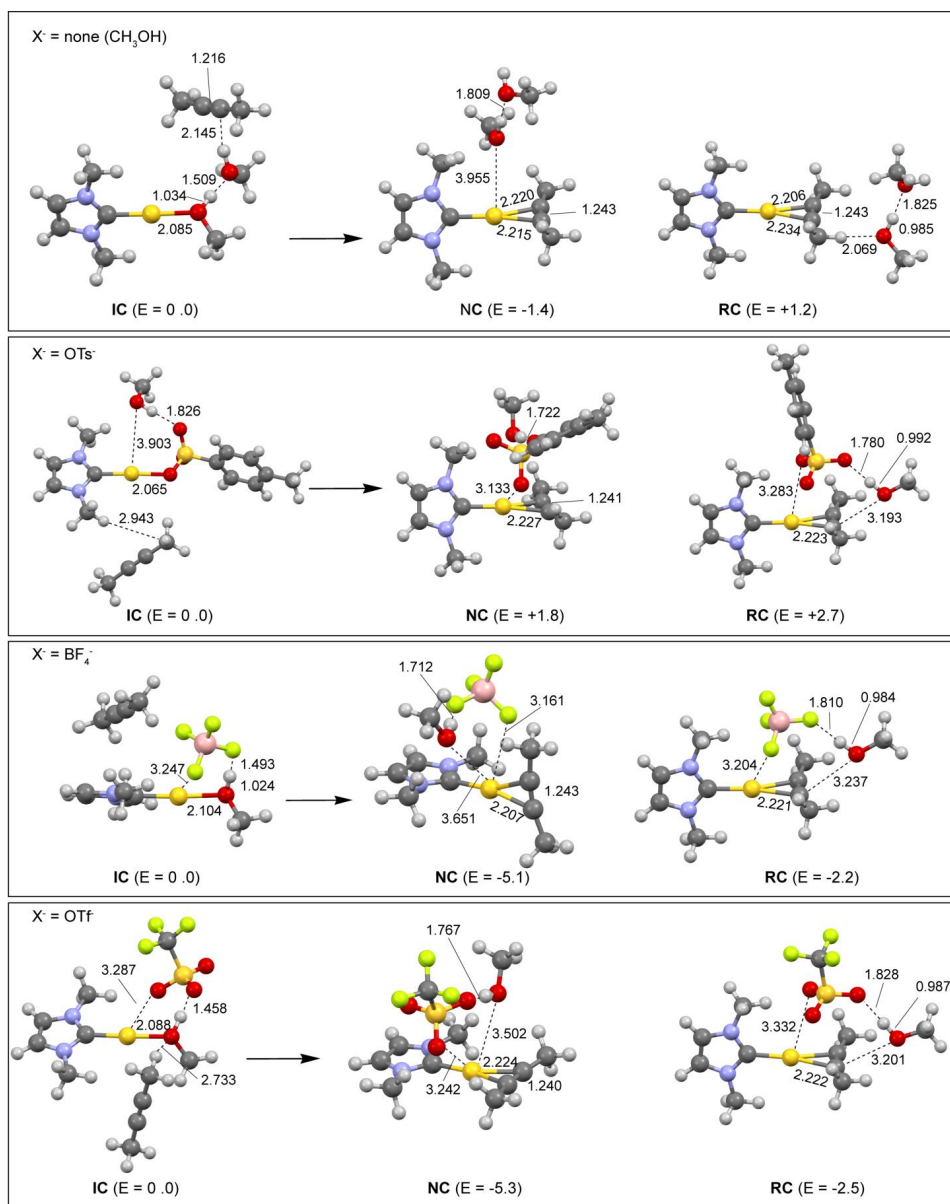


Figure 3. Optimized geometries of the considered quaternary adducts for the cationic species: initial complex IC (left side of each panel), reactants complex for outer-sphere attack (RC, right side of each panel) and reactant complex for inner-sphere attack (NC, center). From top to bottom: $X^- = \text{none (CH}_3\text{OH)}$, OTs^- , BF_4^- and OTf^- . Distances are in Å. Relative stabilities of RC and NC with respect to IC are also reported (kcal/mol)

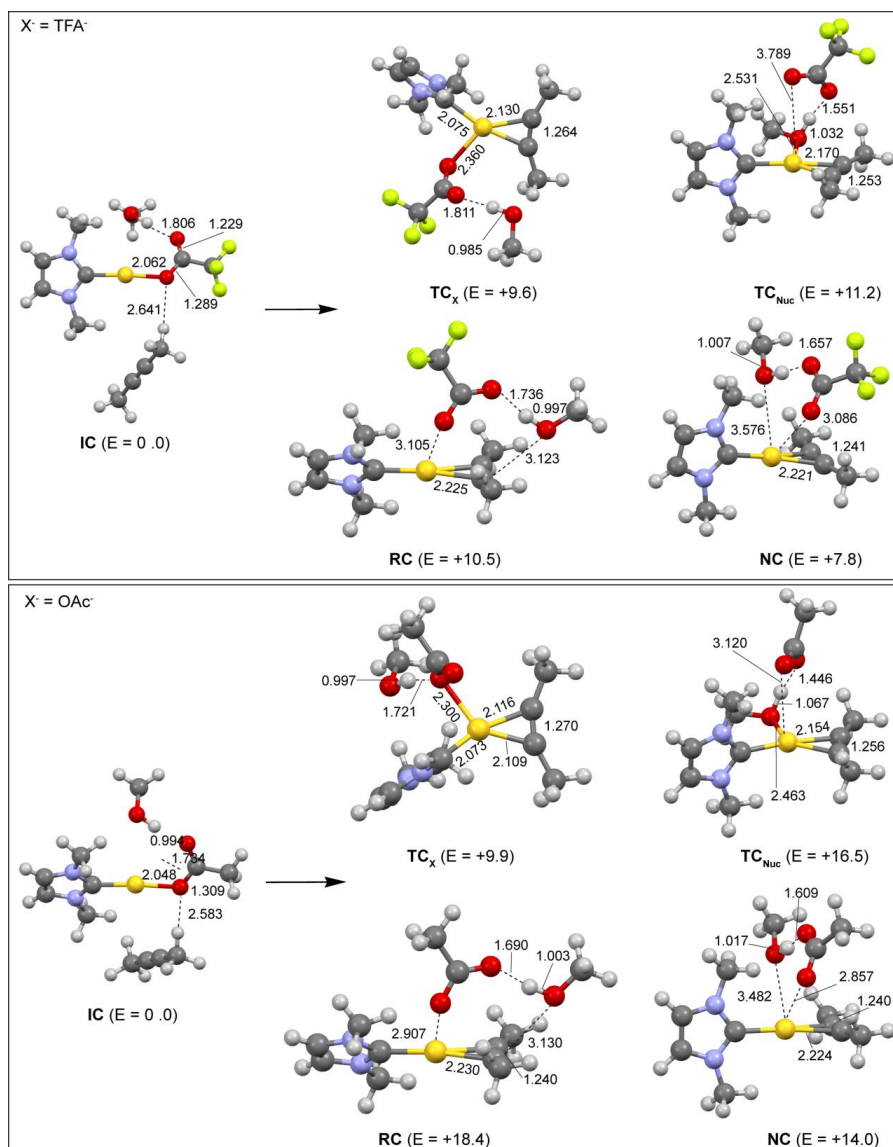


Figure 4. Optimized geometries of the considered quaternary adducts for the neutral species: $[\text{NHCAu-X}](\text{CH}_3\text{OH})(2\text{-butyne})$ initial complex IC (left), $[\text{NHCAu}(2\text{-butyne})][\text{X}(\text{CH}_3\text{OH})]$ reactants complex RC (bottom, middle), tricoordinated complex (TC_X) (top, middle), tricoordinated complex (TC_{Nuc}) (top, right), and non-activating complex NC (bottom, right) for the outer-sphere attack. From top to bottom: X⁻ = TFA⁻ and OAc⁻. Distances are in Å. Relative stabilities of RC, TC_X, TC_{Nuc}, and NC with respect to IC are also reported (kcal/mol)

The **NC_x** conformation corresponds either to the reactant complex for the nucleophilic attack in the syn periplanar (inner- sphere) mechanism, which is unfavorable on the basis of the calculations (it was not possible to locate a transition state for this mechanism on the potential energy surface) and on experimental grounds,⁶ or to a nonactivating complex for the nucleophilic attack in the outer-sphere mechanism.

In the second conformation, the $[X(\text{CH}_3\text{OH})]^-$ group occupies an area around the alkyne but in the opposite site of the Au center and its energy is generally slightly higher than that of **NC_x**. It represents the reactants complex for the nucleophilic attack to the C–C triple bond in the anti periplanar (outer-sphere) mechanism (structure **RC_x** in Scheme 2).

The optimized geometries of the initial complexes **IC_x**, the reactant complexes for the outer-sphere mechanism **RC_x**, and the tri-coordinated **TC_x** complexes are shown in Figure 5 for X = none (CH₃OH), OTs⁻, BF₄⁻, OTf⁻, TFA⁻, and OAc⁻, where the relative stabilities of the **RC_x** and **TC_x**, calculated with respect to the **IC_x**, are also reported.

First we consider the catalyst without the anion. The alkyne catalytic cycle initiates when the 2-butyne passes from the second (**IC_{none}**) to the first coordination sphere. The optimized structures after ligand substitution can be described as linear gold complexes, where the two Au–C bond distances are slightly different in **RC_{none}** (2.206 and 2.234 Å). The consequence of the alkyne coordination is the lengthening of the triple bond (the C–C distance is 1.216 Å in **IC_{none}** and 1.243 Å when coordinated). The (CH₃OH)₂ dimer forms a weak interaction with a hydrogen of the butyne through (CH \cdots O–H = 2.069 Å) in **RC_{none}**. Optimization of a tri-coordinated structure, where both the butyne and one methanol molecule are coordinated to gold, was unsuccessful, always ending up in two-coordinated structures as **NC_{none}** and **RC_{none}**. The former is more stable than the initial complex by 1.4 kcal/mol, whereas the latter is less stable by 1.2 kcal/mol (Figure 3 and Figure 5).

⁶ Zhdanko, A.; Maier, M. E. *ACS Catal.* **2014**, *4*, 2770–2775

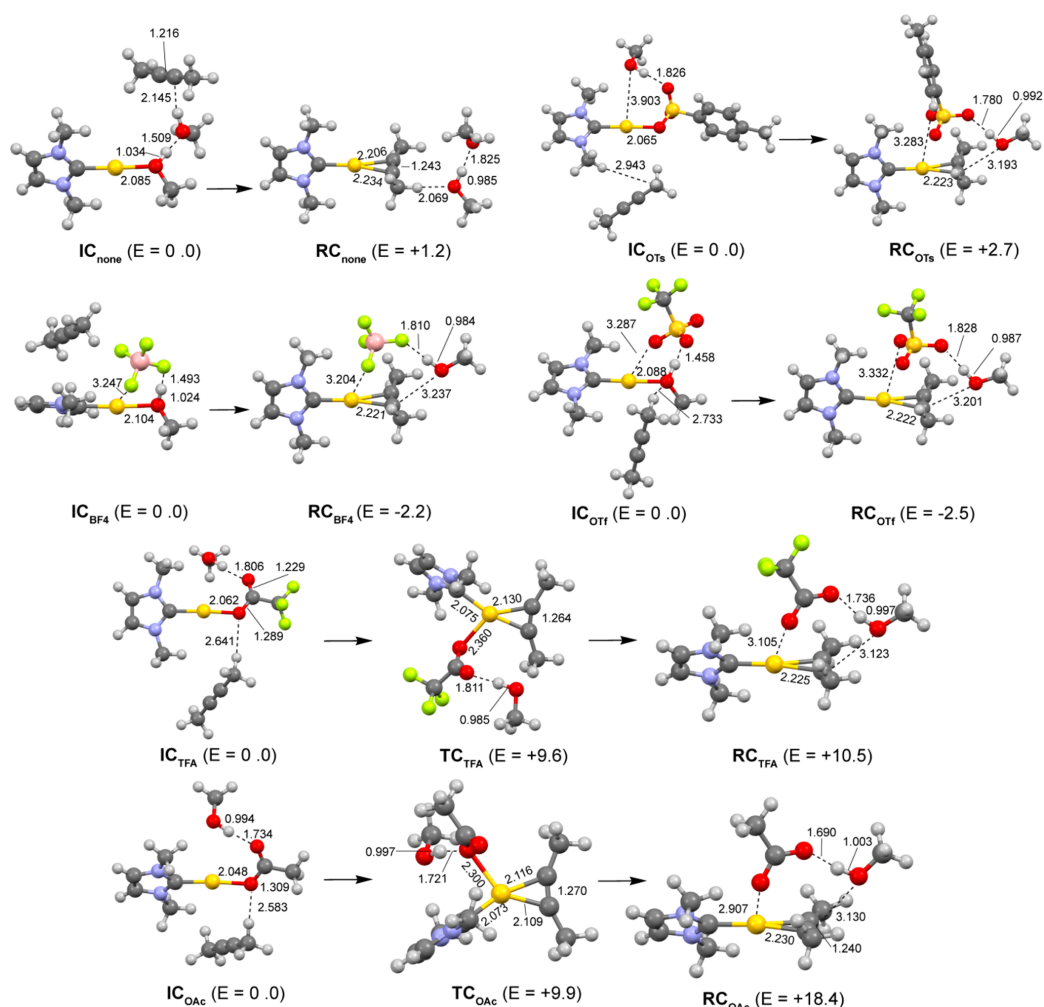


Figure 5. Optimized geometries of the initial complex IC_x , reactants complex for outer-sphere attack RC_x and intermediate tricoordinated complex TC_x for all the considered quaternary adducts. Distances are in Angstroms. Relative stabilities of RC_x and TC_x with respect to IC_x are also reported (kcal/mol)

Considering now the inclusion of the anion X^- , the initial quaternary complex IC_x is the anion-coordinated species with the 2-butyne in the second coordination sphere, $[NHCAu-X](CH_3OH)(2\text{-butyne})$, except for BF_4^- and OTf^- , for which the methanol-coordinated species is more stable and is taken as the initial complex. For BF_4^- and OTs^- IC_x s the 2-butyne is weakly interacting through hydrogen bond with the NHC ligand, whereas for OTf^- , TFA^- , and OAc^- it forms a hydrogen bond with the oxygen

atom of the methanol or the anion coordinated to Au (Figure 5).

After ligand substitution, in the butyne-coordinated complexes the $[(\text{CH}_3\text{OH})\text{X}]^-$ adduct can be found either at the same side of the substrate (RC_x) or between the catalyst and the substrate, weakly or strongly interacting with the Au center through the X^- anion (see NC_x structures in Figures 3 and 4).

In all RC_x complexes at least one basic atom of the anion weakly interacts with the metal center ($\text{Au}\cdots\text{O} = 3.283 \text{ \AA}$ for OTs^- , 3.332 \AA for OTf^- , 3.105 \AA for TFA^- , and 2.907 \AA for OAc^- ; $\text{Au}\cdots\text{F} = 3.204 \text{ \AA}$ for BF_4^- , Figure 5) while forming a hydrogen bond with methanol. The oxygen atom of methanol is at about $3.1\text{--}3.2 \text{ \AA}$ distance from the closest carbon atom of the coordinated butyne.

The search for tri-coordinated species, either having the 2-butyne and the anion (TC_x) (see Scheme 1 and Figure 5) or the 2-butyne and the methanol (TC_{Nuc}) (Figure 4) coordinated to the metal, was successful for TFA^- and OAc^- but not for OTs^- , BF_4^- , and OTf^- , always ending up in two-coordinated structures. Tri-coordinated species TC_x thus represent substitution reaction intermediates for TFA^- and OAc^- , whereas TC_x is a transition state for OTs^- .

In TC_{TFA} , TFA^- forms relatively strong interaction with the gold center through one of its oxygen atoms ($\text{Au}\cdots\text{O} = 2.360 \text{ \AA}$), also strengthening the 2-butyne/gold interaction ($\text{Au}\cdots\text{C} = 2.130$ and 2.127 \AA , compared to 2.22 \AA in the two-coordinated complexes and $\text{C}\text{--}\text{C} = 1.264 \text{ \AA}$ compared to 1.24 \AA in two-coordinated complexes) (Figure 5). The OAc^- anion forms even stronger interaction with the metal in TC_{OAc} , with an $\text{Au}\text{--}\text{O}$ distance of 2.300 \AA , also in this case with a strengthening of the 2-butyne/gold interaction ($\text{Au}\cdots\text{C} = 2.109$ and 2.116 \AA , $\text{C}\text{--}\text{C} = 1.270 \text{ \AA}$) (Figure 5).

Very interestingly, in the two-coordinated RC_{OAc} , the nucleophile locates near the 2-butyne, forming one hydrogen bond between the oxygen atom of the anion and the proton of the methanol ($\text{O}\cdots\text{H} = 1.690 \text{ \AA}$, $\text{CH}_3\text{O}\text{--}\text{H} = 1.003 \text{ \AA}$), thus revealing again a strong proton acceptor behavior of OAc^- .

All the NC_x complexes are slightly more stable than the reactant complexes RC_x for OTs^- , BF_4^- , OTf^- , and TFA^- (in the range $0.9\text{--}2.9 \text{ kcal/mol}$). For TFA^- the tricoordinated

complex \mathbf{TC}_{TFA} is 1.8 kcal/mol less stable than \mathbf{NC}_{TFA} and only 0.9 kcal/mol more stable than \mathbf{RC}_{TFA} . The exception is OAc^- : the tricoordinated complex \mathbf{TC}_{OAc} is calculated to be the most stable structure, 8.5 kcal/mol more stable than \mathbf{RC}_{OAc} .

The formation of the \mathbf{RC}_x adducts from the corresponding initial complexes \mathbf{IC}_x is thermodynamically favored for BF_4^- and OTf^- , with energies of -2.2 and -2.5 kcal/mol, respectively. For OTs^- , TFA^- , and OAc^- the reaction is endothermic by $+2.7$, $+10.5$, and $+18.4$, respectively, but the \mathbf{RC}_x adduct is easily accessible from \mathbf{NC}_x for OTs^- (0.9 kcal/mol) and TFA^- (2.7 kcal/mol) (Table 2). The thermodynamical analysis shows that, at least for OAc^- , the anion substitution by substrate process is not feasible. The \mathbf{RC}_{OAc} is less favorable than \mathbf{IC}_{OAc} by 18.4 kcal/mol, meaning that the $\mathbf{IC}_{\text{OAc}} \rightarrow \mathbf{RC}_{\text{OAc}}$ equilibrium should be shifted toward \mathbf{IC}_{OAc} and the activation barrier for the OAc^- substitution is certainly larger than 18.4 kcal/mol, that looks already quite high.

Thus, the \mathbf{RC}_x formation energy in the presence of methanol is in the order $\text{OAc}^- > \text{TFA}^- > \text{OTs}^- > \text{BF}_4^- > \text{OTf}^-$ (see Table 2). However, this trend is a result of a net balance between the metal coordinating and the proton acceptor abilities of the anion. In the absence of methanol, the \mathbf{NC}_{OTs} formation energy from \mathbf{IC}_{OTs} is $+3.6$ kcal/mol, indicating a somewhat unfavorable alkyne substitution of the coordinated OTs^- , whereas this value lowers to $+1.8$ kcal/mol when one molecule of methanol is introduced, thanks to the hydrogen bond formation between the methanol and the anion. However, whether the OTs^- substitution process is feasible or not could be crucial for explaining the best catalytic efficiency by OTs^- . For this counterion the energy barrier for the reaction $\mathbf{IC}_{\text{OTs}} \rightarrow \mathbf{NC}_{\text{OTs}}$ has been calculated to be 11.5 kcal/mol, and the transition state structure, a tricoordinated species, is shown in Figure 6 ($\mathbf{TS}_{\text{PreeqOTs}}$). This result indicates a feasible anion substitution by alkyne.

Table 2. Relative IC_x and RC_x Energies (kcal/mol), Metal–Anion (M···X) (the Anion Basic Atom Closest to the Metal Is Reported) and Metal–Hydrogen (M···HOCH₃) Bond Distances (Å) in RC^a

X ⁻	ΔE	M···X	X···HOCH ₃
None (CH ₃ OH)	+1.2		1.825
OTs ⁻	+2.7	3.283	1.780
BF ₄ ⁻	-2.2	3.204	1.810
OTf ⁻	-2.5	3.332	1.828
TFA ⁻	+10.5	3.105	1.736
OAc ⁻	+18.4	2.907	1.690

^a Species without anion and with one additional methanol are also shown

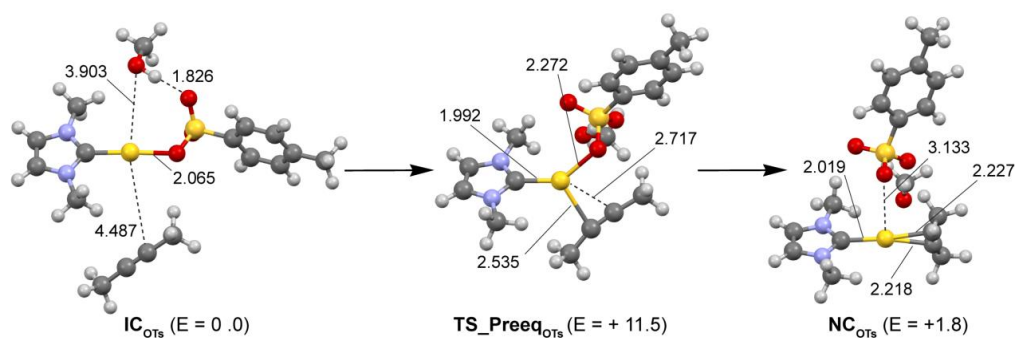


Figure 6. Optimized geometries of the stationary points involved in the pre-equilibrium for OTs⁻ substitution by 2-butyne. Relative stabilities are also reported (kcal/mol). Distances are expressed in Å

This picture is consistent with the experimental results where no catalytic activity was found using OAc^- as anion. The high coordination energy of OAc^- makes the formation of the reactant complex RC_{OAc} highly disfavored. On the other hand, one could be tempted to predict that the most active anion should be OTf^- , since for the latter the RC_{OTf} is the most stable one. Unfortunately, pre-equilibrium alone, mostly driven by the coordinating ability of the anion, cannot explain the experimentally observed trend, according to which the catalytic activity is higher when OTs^- is used.

Considering the complete set of anions employed in the methoxylation of 3-hexyne (see **Chapter 3**), their coordination power trend has been roughly estimated, using again the same approach adopted by Lledòs *et al.*⁵ by evaluating the bond dissociation energy (BDE) for the reaction $[\text{LAuX}] \rightarrow [\text{LAu}]^+ + \text{X}^-$ (L = phosphine and X^- = anion).

The results are reported in Table 3, where experimental TOF values are also shown for easy reference.

Table 3. Calculated (DFT) bond dissociation energy (BDE) and experimental TOF values for the anion series employed in the methoxylation of 3-hexyne

Anion	Bond Dissociation Energy (kcal/mol)	TOF (h^{-1})
BF_4^-	108.3	178
NTf_2^-	114.1	185
ClO_4^-	116.7	140
OTf^-	117.1	196
OTs^-	126.8	309
PFHp^-	128.9	135
OMs^-	130.2	294
NO_3^-	133.3	0
TFA^-	133.9	40
ptm^-	147.8	0
OAc^-	150.0	0

The trend in the BDE values correlates enough with the expected coordinating ability⁷ of the anions which increases in the order: $\text{BF}_4^- < \text{NTf}_2^- < \text{ClO}_4^- < \text{OTf}^- < \text{OTs}^- < \text{PFHp}^- < \text{OMs}^- < \text{NO}_3^- < \text{TFA}^- < \text{ptm}^- < \text{OAc}^-$. The calculated trend is also in agreement with that estimated previously by Lledòs *et al.*⁵ (*i.e.* $\text{BF}_4^- < \text{OTf}^- < \text{OTs}^- < \text{NO}_3^- < \text{TFA}^-$). The graphical plot of the results reported in Table 3 (depicted in Figure 7a) shows a general trend where anions with a medium-low coordination property (BF_4^- , NTf_2^- , ClO_4^- , OTf^-) exhibit a moderate catalytic activity, whereas highly coordinating anions (NO_3^- , TFA^- , ptm^- , OAc^-) perform poorly for the alkoxylation. On the other hand, the best performances are achieved with the anions of intermediate coordinating ability property (OTs^- and OMs^-).

Note that also the NO_3^- and TFA^- anions present intermediate coordination ability but their catalytic performances are very scarce.

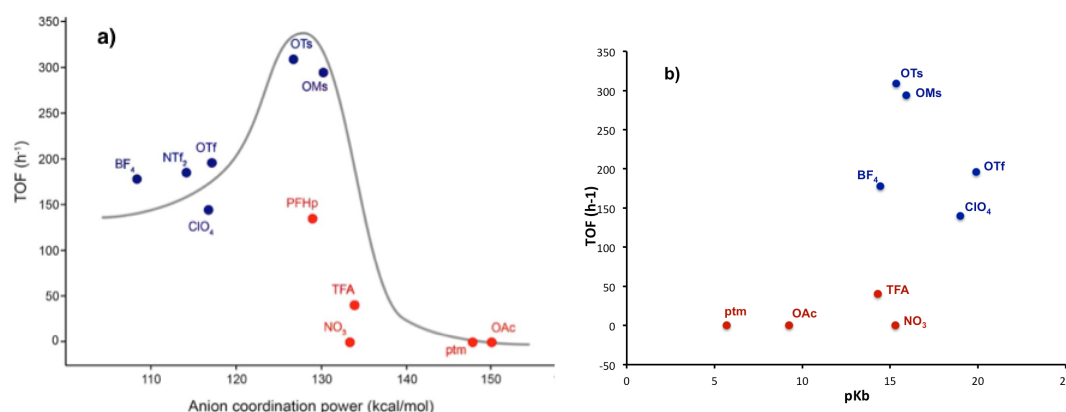


Figure 7. Blue colour: “more spherical” tridentate anions; red colour: “planar” bidentate anions. a) Plot of the calculated anion’s coordination power (BDE values) versus TOF values calculated for the corresponding [(NHC)-Au-X] complexes. b) Plot of the anion’s basicity (pKb values, taken from literature data)⁸ versus TOF values calculated for the corresponding [(NHC)-Au-X] complexes

⁷ Macchioni, A. *Chem. Rev.* **2005**, *105*, 1917-2722

⁸ Only values of pKb detected in water where considered: (a) for OMs^- , Guthrie Can, J. P. *J. Chem.* **1978**, *56*, 2342. (b) for OTs^- , Serjeant, E.P.; Dempsey, B. IUPAC Chemical Data Series No 23, Oxford, New York: Pergamon Press **1979**. (c) for TFA^- , Henne, A. L.; Fox, C. J. *J. Am. Chem. Soc.* **1951**, *73*, 2323-2325. (d) for BF_4^- , Sudakova, T. N.; Krasnoshchekov, V. V. *Zh Neorg. Khim.* **1978**, *23*, 1506-1508 and Bessiere, J. *Bull. Soc. Chem. Fr.* **1969**, *9*, 3356-3364. (e) for ptm^- , Higginson, W. C. E. *Pro. Royal Soc.* **1949**, *197*, 141-159

Anion coordinating ability and hydrogen-bond basicity are expected to be related in gold catalysis however a dedicated study is absent in literature. So it may be interesting to analyze the catalytic performances also in terms of the anion basicity (pK_b data taken from literature⁸ and calculated in aqueous, Figure 7b). It comes out that a certain correlation between anion coordination ability (evaluated as BDE) and its basicity exists. The anions with no catalytic activity are indeed those with a more basic/coordinative character (ptm⁻, OAc⁻) while anions with a moderate activity present also the weakest basicity or coordinative power (OTf⁻, ClO₄⁻). The performances of the anions with an intermediate coordination ability or basicity are more difficult to rationalize simply in terms of basic/coordinative power. In this case, the catalytic performances appear related to their geometry: those having a "more spherical" shape (as OTs⁻ and OMs⁻) are the most active and those with a "planar" geometry (TFA⁻, NO₃⁻) show a poor catalytic activity.

Concerning PFHp⁻ anion, in spite of its intermediate coordination power, being predicted between the two outperforming anions (OTs⁻ and OMs⁻), it shows an undeniable lower TOF value than one may expect.

The most stable structure for the initial complex **IC_{PFHp}** is the anion-coordinated species (Figure 8), which has been taken as the zero reference energy. When 2-butyne enters the first coordination sphere in **TS_{preeq_{PFHp}}** it coordinates with the metal center forming two bonds (Au...C = 2.453 and 2.612 Å), while the PFHp⁻ anion interacts with Au with one oxygen atom (Au...O = 2.281 Å). The activation barrier for the pre-equilibrium step is 12.9 kcal/mol. **TS_{preeq_{PFHp}}** leads to the catalytically inactive tricoordinated complex (**TC_{PFHp}**) where the 2-butyne/gold distances decrease (Au...C = 2.151 and 2.165 Å) whereas the distance between gold and the oxygen atom of the anion increases to 2.485 Å. The active species **RC_{PFHp}** is 4.0 kcal/mol less stable than **TC_{PFHp}** and 9.1 kcal/mol less stable than **IC_{PFHp}**. Very interestingly, this peculiar tricoordinated species has been found for highly coordinating anions such as TFA⁻ and OAc⁻, but not for OTs⁻¹⁸ despite its coordinating ability is close to that of PFHp⁻.

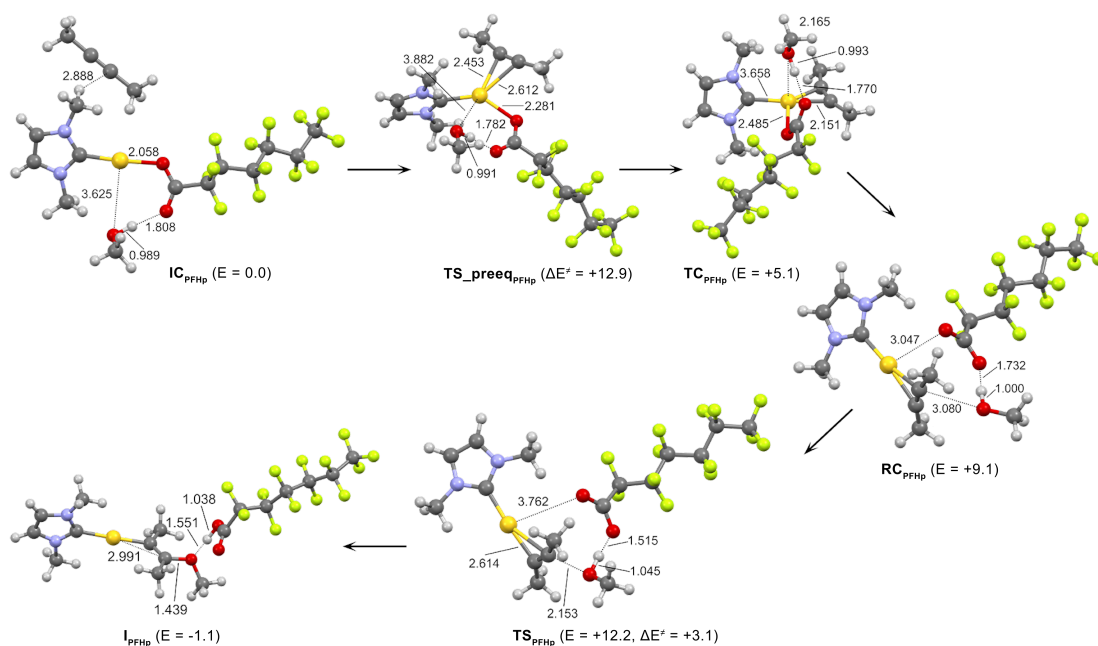


Figure 8. Initial complex IC_{PFHp} , tricoordinated complex TC_{PFHp} , reactant complex RC_{PFHp} , intermediate IP_{PFHp} , transition state $TS_{preeq_{PFHp}}$ for the pre-equilibrium step and transition state TS_{PFHp} for the methanol nucleophile attack to 2-butyne in the presence of the $PFHp^-$ anion. Energies values (kcal/mol) refer to IC_{PFHp} , taken as zero. Bond lengths are in Å

It is remarkable that these tri-coordinated species TC_X represent substitution reaction intermediates for TFA^- , OAc^- and $PFHp^-$, whereas TC_X is a transition state for OTs^- . In addition, the formation of the RC_X adducts from the corresponding initial complex IC_X is thermodynamically unfavored for OTs^- , $PFHp^-$, TFA^- , and OAc^- by +2.7, +9.1, +10.5, and +18.4 kcal/mol, respectively. So, in the pre-equilibrium step $PFHp^-$ closely resembles TFA^- , which is not surprising in the light of their similar geometrical structures. The coordinating capability of the anions has been rationalized in literature also in terms of their relative geometry.⁹ As a matter of fact, the more “spherical” symmetry of OTs^- ($-SO_3^-$ group presents a tetrahedral structure and is a tridentate ligand towards Au) with respect to $PFHp^-$, TFA^- , and OAc^- ($-CO_2^-$ group being planar and bidentate ligand towards Au) correlates with its lower attitude to form tri-coordinated species with respect to the corresponding structures computed for with

⁹ Jia, M.; Bandini, M. *ACS Catal.* **2015**, *5*, 1638-1652, and reference therein

PFHp⁻, TFA⁻, and OAc⁻ (**TC**_{OTs} and **RC**_{OTs} structures are destabilized and stabilized, respectively). Whereas the **IC** geometrical structure is similar for OTs⁻, and PFHp⁻, TFA⁻, and OAc⁻, the **RC** geometry is very different, showing the OTs⁻ as a good leaving group in the substitution reaction by substrate and the PFHp⁻, TFA⁻, and OAc⁻ anions as bad leaving groups. Interestingly enough, from this analysis we have seen that the coordination ability of the anion to gold may not solely correlate with its ability as leaving group in the substitution reaction by substrate but also its geometry (more “spherical” tridentate or bidentate character) contributes to it.¹⁰

Looking at **TS**_{PFHp}, an incipient abstraction of the methanol proton by PFHp⁻ can be observed (CH₃O–H = 1.045 Å, CH₃OH···O(PFHp⁻) = 1.515 Å) while it is completely abstracted in the intermediate **I**_{PFHp} (CH₃O···H = 1.551 Å and H–O(PFHp⁻) = 1.038 Å). In the next section the addition of methanol to 2-butyne will be investigated in detail.

¹⁰ Antoniotti, S.; Dalla, V.; Dunak, E. *Angew. Chem. Int. Ed.* **2010**, *49*, 7860-7888

2.2. Nucleophilic attack (Step I) and protodeauration (Step II)

The cationic butyne-coordinated species, $[\text{NHCAu}-(2\text{-butyne})]^+(\text{CH}_3\text{OH})_2$ $\text{RC}_{\text{none-MeOH}}$, has been analyzed in the absence of the anion. The inclusion of a second methanol molecule is needed to activate the first methanol molecule (nucleophile), which otherwise would be not sufficiently nucleophilic to attack the substrate. All the attempts to locate a transition state for the nucleophilic attack without the anion and only one molecule of methanol failed.

The activation barrier corresponding to the transition state structure involved in the outer-sphere nucleophilic attack amounts to 12.0 kcal/mol (Figure 9). The transition state ($\text{TSI}_{\text{none-MeOH}}$) evolves with the formation of the intermediate $\text{I}_{\text{none-MeOH}}$, which is less stable than $\text{RC}_{\text{none-MeOH}}$ by 8.9 kcal/mol (3.1 kcal/mol more stable than the transition state leading to it, Figure 9). In $\text{TSI}_{\text{none-MeOH}}$, the bond between the gold center and the carbon atom on which the nucleophile attacks (C1) is elongated (2.770 Å), while that between the gold and the other carbon of the triple bond (C2) becomes shortened (2.100 Å).

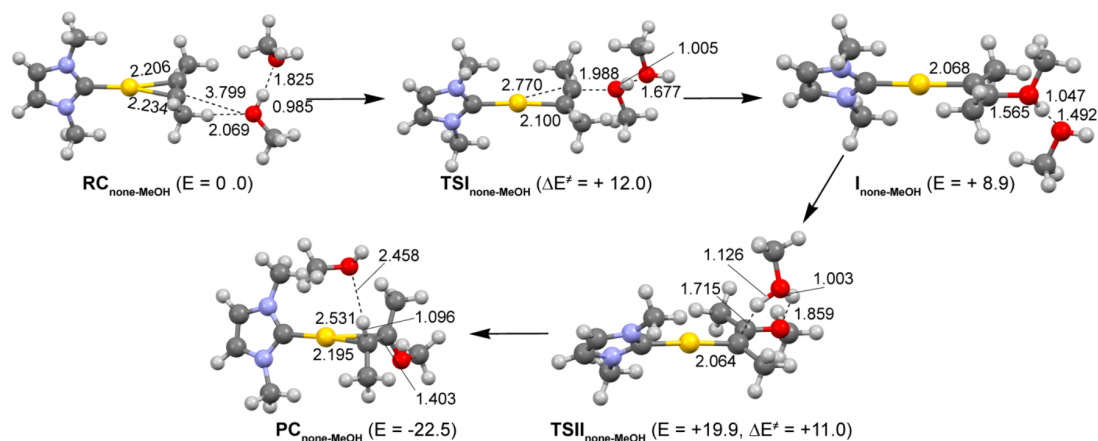


Figure 9. Reactant complex $\text{RC}_{\text{none-MeOH}}$, intermediate $\text{I}_{\text{none-MeOH}}$, product complex $\text{PC}_{\text{none-MeOH}}$, transition state $\text{TSI}_{\text{none-MeOH}}$ for the methanol nucleophilic attack (step I), and transition state $\text{TSII}_{\text{none-MeOH}}$ for the proton migration (step II) for the addition of methanol to 2-butyne reaction in the absence of the anion. Energies values (kcal/mol) refer to $\text{RC}_{\text{none-MeOH}}$ taken as zero. Bond lengths are in angstroms

Simultaneously, the C1–C2 bond length increases (1.283 Å) and the distance between C1 and the oxygen atom of the nucleophile is 1.988 Å. The intermediate $I_{\text{none-MeOH}}$ structure is very similar to that of the transition state, with a much reduced C1...O distance (1.565 Å). The second methanol molecule assisting the nucleophilic attack is not sufficiently strong to abstract the proton from the coordinated nucleophile: the O–H bond length in coordinated methanol is 1.047 Å, and the hydrogen of the coordinated methanol is at a distance of 1.492 Å from the O atom of the assisting methanol molecule.

The methanol addition is completed by the migration of the proton bound to the oxygen atom of the nucleophile in the intermediate complex $I_{\text{none-MeOH}}$ to C2 (protodeauration), through the transition state $TSII_{\text{none-MeOH}}$. In the latter, the second molecule of methanol acts simultaneously as a proton acceptor (with respect to the coordinated methanol, O...H1 = 1.003 Å), and a proton donor (with respect to C2, O...H2 = 1.126 Å). The calculated activation barrier for this step is 11.0 kcal/mol, and the product is highly stabilized with respect to the intermediate species (–31.4 kcal/mol). $TSII_{\text{none-MeOH}}$ evolves to the final product complex ($PC_{\text{none-MeOH}}$, Figure 9), in which the organic moiety is η^2 -coordinated to the gold via its remaining unsaturated double bond in an asymmetric fashion (Au...C2 = 2.195, Au...C1 = 2.531 Å). The ΔE for the overall reaction of methanol addition to 2-butyne is calculated to be exothermic by –22.5 kcal/mol. From the whole reaction energy profile, it is evident that the hydrogen atom migration is subjected to only a slightly lower energy barrier than the initial nucleophile attack step (11.0 vs 12.0 kcal/mol, Figure 9), but it is important to note that the absolute energy of $TSII_{\text{none-MeOH}}$ is higher than that of $TSI_{\text{none-MeOH}}$ (19.9 vs. 12.0 kcal/mol with respect to the $RC_{\text{none-MeOH}}$, respectively).

Next, we consider only three out of the five different anions X^- , namely OTs^- , BF_4^- , and OAc^- , as representative for the activity observed experimentally, in order to emphasize the critical role of the anion. In particular, OTs^- and BF_4^- have been chosen because the former shows a higher catalytic activity than the latter, in spite of its higher coordinating ability, while OAc^- has been chosen for its catalyst deactivator

behavior. The concerted nucleophilic attack to butyne and hydrogen abstraction from nucleophile by the anion (i.e., nucleophile activation) has been investigated with the aid of two-dimensional plots of the energy. For BF_4^- , two additional two-dimensional energy plots have been constructed for concerted nucleophilic attack/protodeauration mechanism and for protodeauration step with an additional methanol molecule.

Let us focus on OTs^- first.

The transition state for the nucleophilic attack step gives an activation barrier of 15.6 kcal/mol and the formation of the intermediate (I_{OTs}) is exothermic by 1.5 kcal/mol (Figure 10).

In the TSI_{OTs} the attack of methanol at C1 causes gold to change its coordination, forming an almost direct bond with the other carbon atom that lies at 2.101 Å from it. The C1–C2 bond length increases (1.275 Å), and the distance between C1 and the oxygen atom of the nucleophile is 2.084 Å, with the anion facilitating the attack in two ways: it acts as a template, keeping the reactive methanol molecule in the right position for the addition, and, simultaneously, it “activates” the nucleophile through an hydrogen bond ($\text{CH}_3\text{O}-\text{H} = 1.033$ Å, $\text{CH}_3\text{OH}\cdots\text{O}(\text{OTs}^-) = 1.538$ Å).

In the intermediate complex I_{OTs} the $\text{H}-\text{O}(\text{OTs})$ distance is 1.035 Å and the $\text{CH}_3\text{O}\cdots\text{H}$ is 1.565 Å, therefore the hydrogen of methanol has been completely abstracted by OTs^- , and this causes a larger stabilization of the intermediate I_{OTs} (–1.5 kcal/mol) with respect to the corresponding species formed with the additional methanol molecule, in the absence of the anion (+8.9 kcal/mol).

For the protodeauration, the fact that anions can assist and facilitate proton transfers by lowering the energy barriers is well-known in literature.^{5,11} In the transition state TSII_{OTs} the proton is found between the OTs^- oxygen ($\text{H}\cdots\text{O} = 1.252$ Å) and C2 ($\text{H}\cdots\text{C2} = 1.418$ Å), therefore the proton transfer takes place in one step. In the product complex PC_{OTs} , the hydrogen is bound to C2 in the trans position with respect to the

¹¹ Krauter, C. M.; Hashmi, A. S. K.; Pernpointner, M. *ChemCatChem*. **2010**, *2*, 1226–1230

methoxy and the product is η^2 -coordinated to the gold via its remaining unsaturated double bond ($\text{Au}\cdots\text{C2} = 2.209$, $\text{Au}\cdots\text{C1} = 2.430$ Å), with the OTs^- weakly interacting with the gold center.

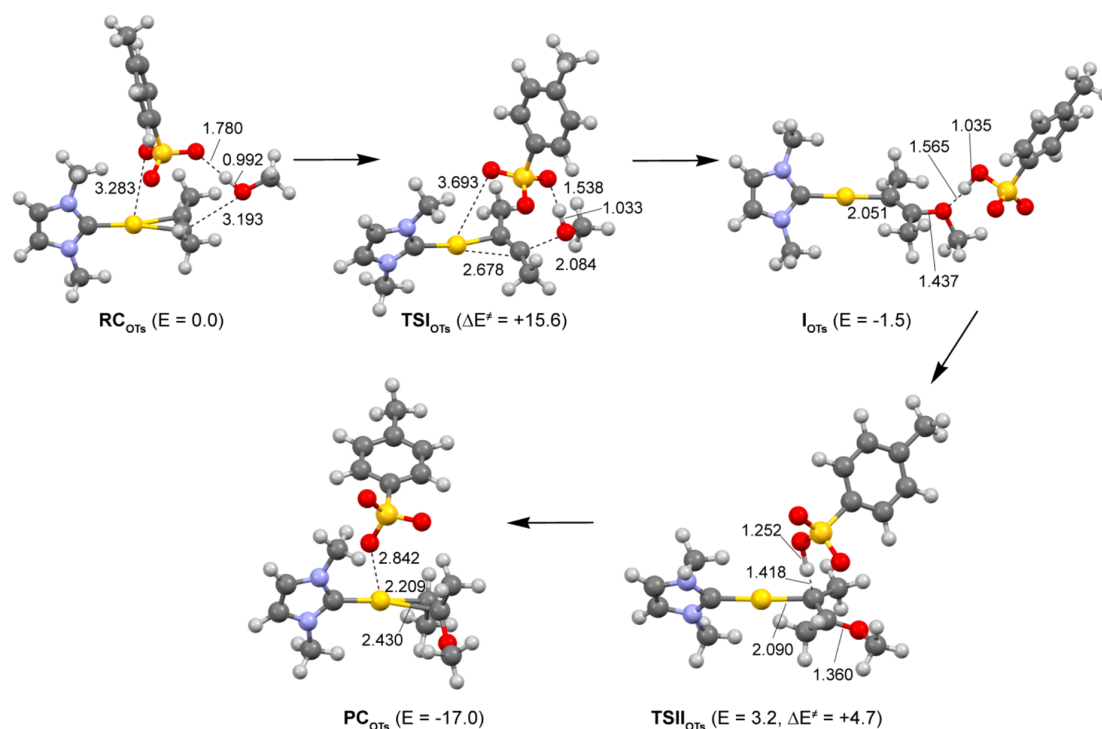


Figure 10. Reactants complex RC_{OTs} , intermediate I_{OTs} , product complex PC_{OTs} , transition state TSI_{OTs} for the methanol nucleophilic attack (step I), and transition state TSII_{OTs} for the proton migration (step II) for the addition of methanol to butyne reaction in the presence of the OTs^- anion. Energies values (kcal/mol) refer to RC_{OTs} taken as zero. Bond lengths are in angstroms

The calculated energy barrier for the hydrogen transfer to the carbon is only 4.7 kcal/mol. The product complex PC_{OTs} is stabilized with respect to the intermediate I_{OTs} by 15.5 kcal/mol, and the ΔE for the overall reaction of methanol addition to 2-butyne is -17.0 kcal/mol (Figure 10).

To check the effect of an additional nucleophile molecule mediating the proton transfer on the activation barriers, the nucleophilic attack and protodeauration steps have been recalculated for OTs^- with the inclusion of a second methanol molecule. The reactants complex $\text{RC}_{\text{OTs-MeOH}}$, intermediate $\text{I}_{\text{OTs-MeOH}}$, product complex $\text{PC}_{\text{OTs-MeOH}}$,

transition state $\text{TSI}_{\text{OTs-MeOH}}$, and transition state $\text{TSII}_{\text{OTs-MeOH}}$ structures and energies referred to $\text{RC}_{\text{OTs-MeOH}}$ taken as zero are provided in Figure 11. Indeed, the activation barrier of the step I is greatly lowered to 7.3 kcal/mol (compared to 15.6 kcal/mol including only one methanol molecule), whereas the activation barrier for step II is not affected (4.7 kcal/mol, the same value as in the case with only one methanol molecule).

We move now to BF_4^- anion assisted nucleophilic attack of methanol to butyne.

Also in this case the formation of the O–C1 bond (nucleophilic attack to butyne) and the H–F bond formation (hydrogen abstraction from nucleophile by anion) is a concerted process, although in the intermediate I_{BF_4} the optimal H...F distance is at about 1.25 Å and the hydrogen abstraction is not complete. A transition state calculation shows that the activation energy required for TSI_{BF_4} is 16.5 kcal/mol and the formed intermediate I_{BF_4} is 9.9 kcal/mol above the reactants complex RC_{BF_4} (Figure 12). In TSI_{BF_4} the distance between the oxygen atom of methanol and C1 is 1.994 Å, and, simultaneously, gold changes its coordination, forming an almost direct bond with C2 that lies 2.092 Å from it, and the C1–C2 bond distance increases to 1.282 Å. An incipient abstraction of hydrogen of methanol by BF_4^- can also be observed ($\text{CH}_3\text{O-H} = 1.014$ Å, $\text{CH}_3\text{OH}\cdots\text{FBF}_3^- = 1.550$ Å), but less pronounced than that by OTs^- . Similarly to OTs^- , the characteristic template structure of RC_{BF_4} with the anion in a bridging position between Au and methanol is retained in TSI_{BF_4} .

In the intermediate structure I_{BF_4} the methanol nucleophile hydrogen atom has not been completely abstracted by the BF_4^- anion. However, quite interestingly, the H–F distance is 1.278 Å and the B–F bond length elongates to 1.556 Å.

Compared to the intermediate species with the anion, BF_4^- , although less coordinating, is a less effective hydrogen acceptor from methanol than OTs^- , and the activation barrier for the nucleophilic attack is slightly higher (16.5 vs 15.6 kcal/mol), in agreement with the experiment (see **Chapter 5**).

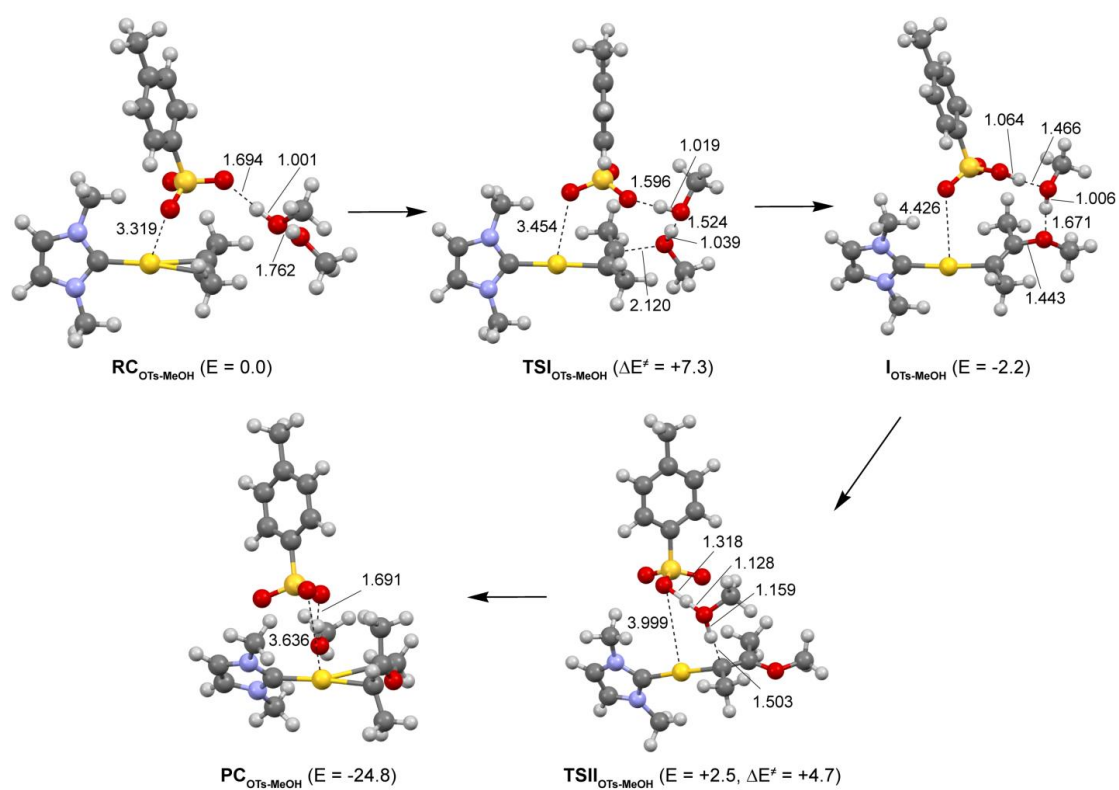


Figure 11. Reactants complex RC_{OTs-MeOH}, intermediate I_{OTs-MeOH}, product complex PC_{OTs-MeOH}, transition state TSI_{OTs-MeOH} for the methanol nucleophilic attack (step I) and transition state TSI_{OTs-MeOH} for the proton migration (step II) for the addition of methanol to 2-butyne reaction in the presence of the OTs⁻ anion with an additional methanol molecule. Energy values (given in kcal/mol) refer to RC_{OTs-MeOH} taken as zero. Bond lengths are in Å

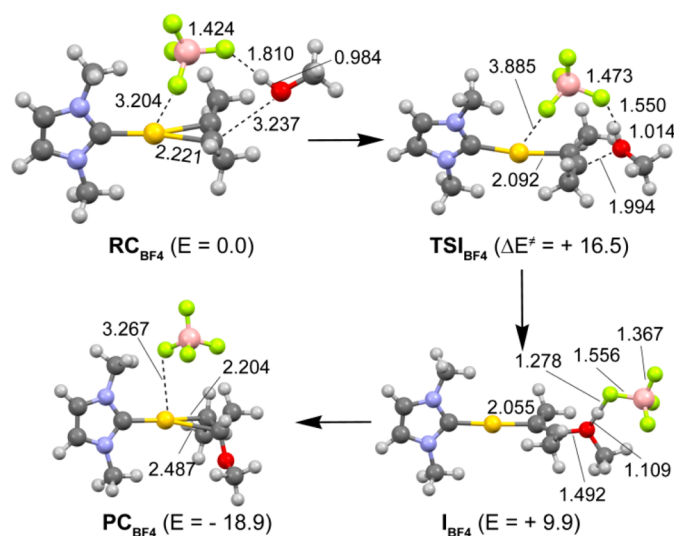


Figure 12. Reactant complex RC_{BF_4} , intermediate I_{BF_4} , product complex PC_{BF_4} , and transition state TSI_{BF_4} for the methanol nucleophilic attack (step I) for the addition of methanol to 2-butyne reaction in the presence of BF_4^- . Energy values (kcal/mol) refer to RC_{BF_4} taken as zero. Bond lengths are in angstroms

For the proton transfer step, in an attempt to find a transition state structure by approaching the methanol proton to C1, a very high energy structure, characterized by a four-membered COHC-ring, has been found.

An estimate of the energy barrier for this process would lead to a very high value, higher than 40 kcal/mol (at BP86 level). This barrier would be too high, thus this pathway can be ruled out and two alternative pathways, one considering a concerted nucleophilic attack to butyne and proton migration to the second carbon atom and one including a second methanol molecule mediating the proton transfer, have been considered.

Due to the calculated very high activation energy (larger than 40 kcal/mol at BP86 level), also the concerted nucleophilic attack/proton migration process can be ruled out too.

On the other hand, inclusion of a second methanol molecule has indeed a beneficial effect on the whole step. The activation barrier of the step I drops to 14.8 kcal/mol and the endothermicity to 6.4 kcal/mol (Figure 13).

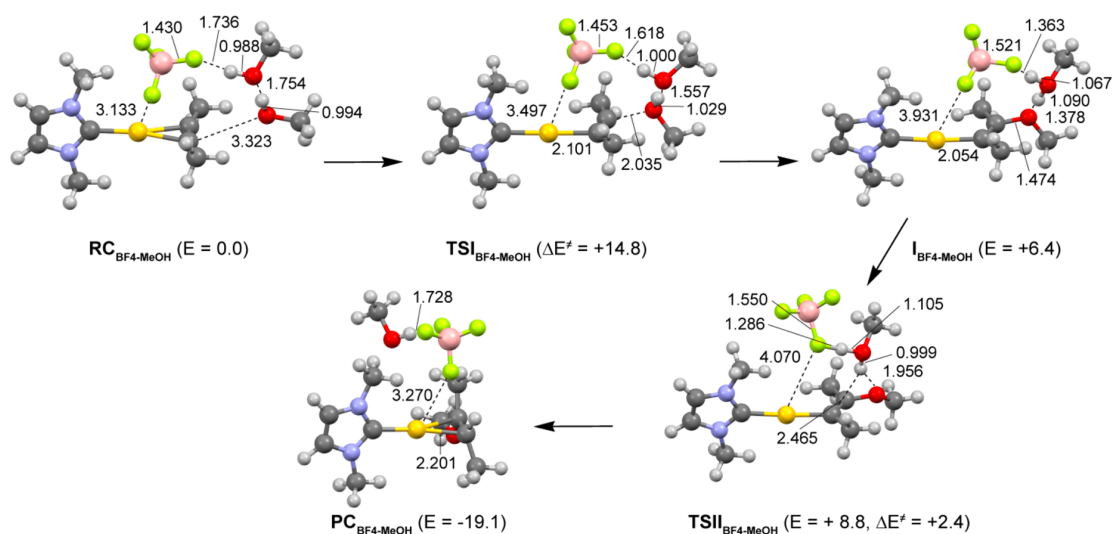


Figure 13. Reactant complex $\text{RC}_{\text{BF}_4\text{-MeOH}}$, intermediate $\text{I}_{\text{BF}_4\text{-MeOH}}$, product complex $\text{PC}_{\text{BF}_4\text{-MeOH}}$, transition state $\text{TSI}_{\text{BF}_4\text{-MeOH}}$ for the methanol nucleophilic attack (step I), and transition state $\text{TSII}_{\text{BF}_4\text{-MeOH}}$ for the proton migration (step II) for the addition of methanol to 2-butyne reaction in the presence of the BF_4^- anion with an additional methanol molecule. Energy values (kcal/mol) refer to $\text{RC}_{\text{BF}_4\text{-MeOH}}$ taken as zero. Bond lengths are in angstroms

In $\text{RC}_{\text{BF}_4\text{-MeOH}}$, BF_4^- and the additional CH_3OH molecules bridge the Au center and the attacking methanol, building up a chain. The anion distance from Au decreases to 3.133 Å and the anion $\cdots\text{HOCH}_3$ distance is 1.736 Å. Compared to TSI_{BF_4} for the process with only one methanol molecule, the $\text{TSI}_{\text{BF}_4\text{-MeOH}}$ including two methanol molecules shows that the nucleophilicity of the attacking methanol molecule is enhanced by the $\text{BF}_4^- \cdots \text{HOCH}_3$ chain, acting as a better proton acceptor than the single BF_4^- : the distance between the oxygen atom of the nucleophile and C1 is 2.035 Å, and an incipient abstraction of hydrogen of methanol nucleophile by additional CH_3OH is observed ($\text{CH}_3\text{O-H} = 1.029$ Å), as well as of hydrogen of additional methanol by BF_4^- ($\text{CH}_3\text{O-H} = 1.000$ Å).

In the intermediate structure $\text{I}_{\text{BF}_4\text{-MeOH}}$, the methanol nucleophile hydrogen atom has been almost completely abstracted by the additional CH_3OH ($\text{CH}_3\text{O-H} = 1.378$ Å), which acts both as a proton acceptor and a proton donor ($\text{CH}_3\text{O-H} = 1.090$ Å with the proton from nucleophile, $\text{CH}_3\text{O-H} = 1.067$ Å with the proton interacting with BF_4^-).

As also noticed in literature, the solvent molecules play a central role in the overall reaction mechanism, since the participation of other molecules (like the additional methanol molecule) can lead to significantly lower reaction barriers and to a much more efficient proton transfer than in the strictly molecular case.¹²

In the intermediate product **I**_{BF₄-MeOH}, the methanol-coordinated hydrogen has been almost completely transferred to the additional methanol (H–O = 1.090 Å) which is forming an HB with the anion. In the transition state **TSII**_{BF₄-MeOH} the migrating proton is far from the methanol nucleophile oxygen (1.956 Å), bound to the additional methanol molecule (O–H = 0.999 Å) and at a distance of 2.465 Å from the unsaturated carbon atom, while BF₄[−] is accepting the second proton from the additional methanol (F–H = 1.286 Å, O–H = 1.105 Å).

The actual proton transfer takes place in one step, where the additional methanol plays a crucial role. In the product complex **PC**_{BF₄-MeOH}, the hydrogen is bound to carbon in the trans position with respect to methoxy and the product is coordinated to gold via its remaining unsaturated double bond in an asymmetric fashion (Au–C = 2.201, 2.474 Å), with the BF₄[−] weakly interacting with the gold center.

The calculated energy barrier for the hydrogen transfer to the carbon is only 2.4 kcal/mol. This barrier is very low, thus showing that the proton transfer is greatly facilitated by the additional CH₃OH–BF₄[−] proton shuttle chain.

The product complex **PC**_{BF₄-MeOH} is stabilized with respect to intermediate **I**_{BF₄-MeOH} by 25.5 kcal/mol, and the ΔE for the overall reaction of methanol addition to 2-butyne is −19.1 kcal/mol. Ultimately, with the inclusion of a second methanol molecule, the activation barrier for the nucleophilic attack is much higher in case of BF₄[−] (14.8 kcal/mol) in comparison with OTs[−] (7.3 kcal/mol).

In Figure 8, all the energy profiles for OTs[−], BF₄[−], including both one and two nucleophile molecules, and for the species without the counterion are summarized.

¹² a) Schelwies, M.; Dempwolff, A. L.; Rominger, F.; Helmchen, G. *Angew. Chem., Int. Ed.* **2007**, *46*, 5598–5601. b) Zhang, Z.; Widenhoefer, R. A. *Org. Lett.* **2008**, *10*, 2079–2081. c) Weber, D.; Jones, T. D.; Adduci, L.; Gagné, M. R. *Angew. Chem., Int. Ed.* **2012**, *51*, 2452–2456. d) Kovačs, G.; Lledoś, A.; Ujaque, G. *Organometallics* **2010**, *29*, 3252–3260

From this figure it can be easily seen that inclusion of two methanol molecules is crucial to see the effect of each counterion on each step of the profile. In addition, the reaction mechanism with OTs^- and BF_4^- with two methanol molecules can be directly compared to that with the catalyst without the anion. We conclude that the anion greatly facilitates the proton migration step (activation energy 2.4 kcal/mol for BF_4^- and 4.7 kcal/mol for OTs^- vs 11.0 kcal/mol without the anion, respectively), making the nucleophilic attack the rate-determining step. The nucleophilic attack is, in turn, greatly facilitated by a stronger proton acceptor anion.

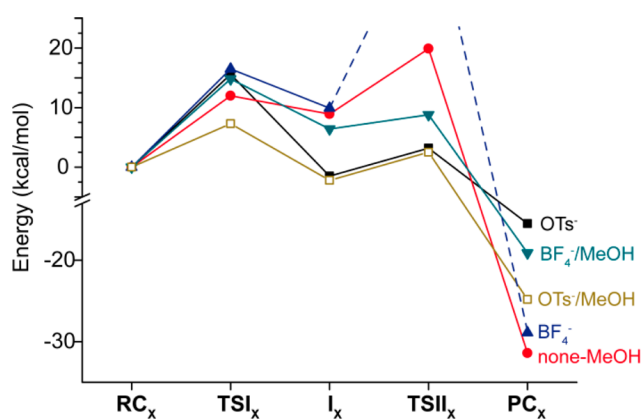


Figure 14. Energy profiles for the nucleophilic attack (step I) and protodeauration (step II) for OTs^- , BF_4^- , including one (OTs^- , BF_4^-) and two (OTs^-/MeOH , $\text{BF}_4^-/\text{MeOH}$) methanol molecules, and without the anion (none-MeOH)

2.3. Catalyst deactivation pathways

In order to analyze the catalyst deactivation pathways competing with the first nucleophilic attack step, we investigate a hypothetical OAc^- assisted nucleophilic attack of methanol to 2-butyne, with the aid of the two-dimensional plot of the energy, which is provided (Figure 15).

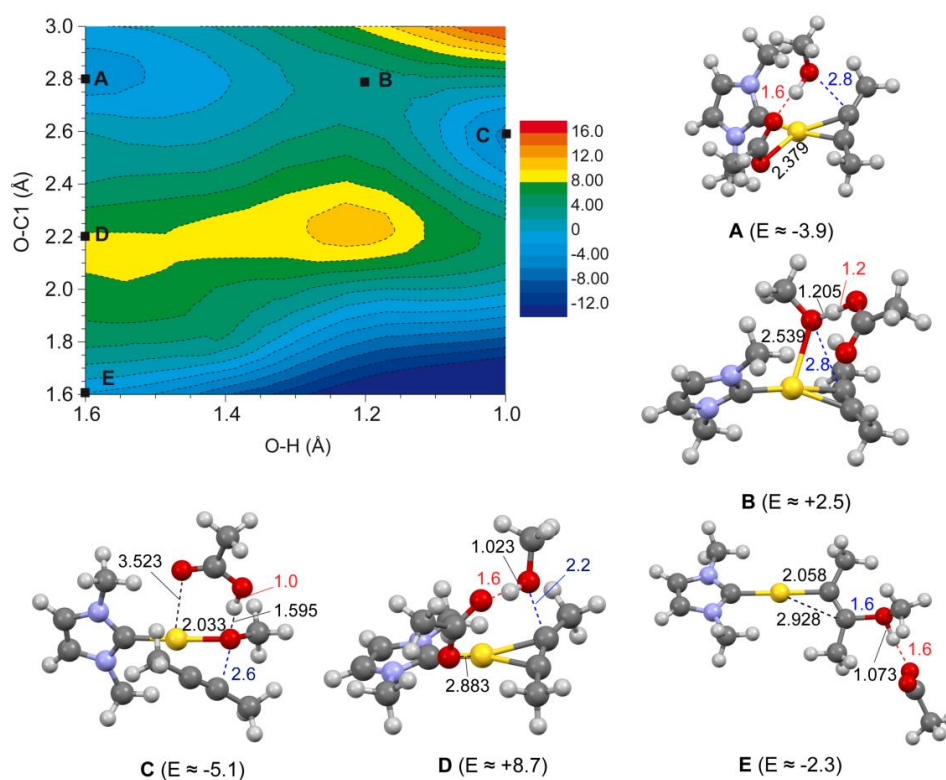


Figure 15. C-O bond formation/ OAc^- proton abstraction pathways: two-dimensional contour plot of the energy as a function of the distance between C1 and the oxygen of methanol O (O-C1), and of the distance between the oxygen atom of acetate O and the hydrogen of methanol H (O-H). The A-E structures, evidenced in the plot, are also shown. Energies are reported with respect to RC_{OAc} in kcal/mol at BP86 level, distances in Å

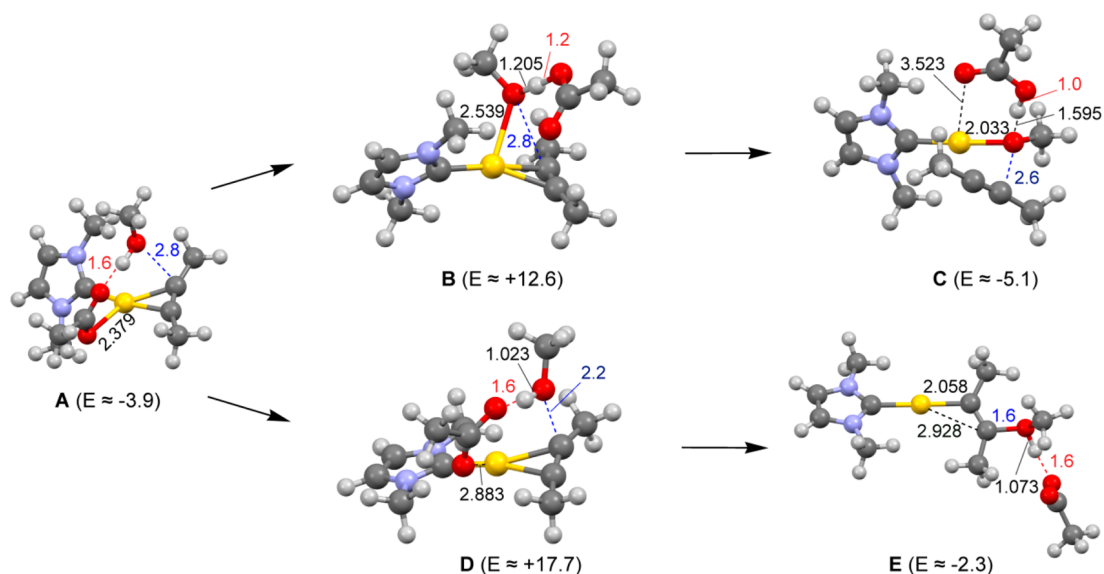


Figure 16. Optimized geometries at five key points in the two-dimensional contour plot for the C–O bond formation and OAc^- proton abstraction pathways: low-energy structure (structure A); estimated transition state for proton abstraction (structure B); estimated product complex from proton abstraction path (structure C); estimated transition state for C–O bond formation (structure D); estimated product complex from C–O bond formation path (structure E). The fixed parameters are shown in red and blue. Estimated energy values at the DFT/BP86 level are in kilocalories per mole; distances are in angstroms (see text)

The plot gives an interesting view of the catalyst inactivating process in the nucleophilic attack step and five key point structures are shown in Figure 16. A starting low energy point is represented by structure A (-3.9 kcal/mol with respect to RC_{OAc}) that is somewhat similar to TC_{OAc} , the most stable structure where both the butyne and the anion are coordinated to gold (compare Figures 5 and 16). A transition state can be reached easily by shortening the O–H distance to 1.2 Å, which represents the transition state for hydrogen abstraction from methanol. The geometry optimization with O–C1 fixed at 2.8 Å and O–H at 1.2 Å gives the structure shown in Figure 16, denoted as B. As we can see from Figure 15, the hydrogen abstraction by OAc^- takes place before the nucleophilic attack starts, since the O–C1 distance is still very large. Moreover, the hydrogen abstraction is able to induce the anion decooordination from gold. Then the system proceeds to a low-energy region (at about O–C1 = 2.5 Å and O–H = 1.0 Å). The geometry optimization with O–C1 fixed at

2.6 Å and O–H at 1.0 Å gives the structure C (Figure 16), which shows that the 2-butyne has been released and CH_3O^- methoxy species formed is coordinated to Au, with the protonated HOAc forming an hydrogen bond with the methoxy group. This path clearly indicates a strong basicity of OAc^- , which would be able to deprotonate the nucleophile so that it could displace the substrate and attack directly the metal center, thus inactivating the catalyst. An estimate of the energy barrier for this deactivating path can be done from the energy of structure B with respect to the energy of RC_{OAc} , i.e. about 2.5 kcal/mol at DFT/BP86 level, which indicates that if RC_x could be easily reached this would be a facile process. However, the whole deprotonation path would start from IC_x , which for OAc^- is 18.5 kcal/mol more stable than RC_{OAc} at DFT/BP86 level, meaning that B would be 21.0 kcal/mol higher in energy than IC_{OAc} . Therefore, this deactivation pathway leading to the formation of the catalytically inactive species DC_x from RC_x can be ruled out for OAc^- , but not for TFA^- . In principle, TFA^- has a relatively strong proton acceptor capacity and, at the same time, the RC_{TFA} is accessible. Interestingly enough, the 2-butyne is located in the second coordination sphere both in IC_{OAc} and in structure C. Thus, alternatively, the DC_{OAc} (or the DC_{TFA}) species could be generated in the pre-equilibrium step, before the substrate coordination to the catalyst takes place. In order to investigate this point, we considered the two ternary adducts depicted in Figure 2 for both OAc^- and TFA^- , and a transition state structure for the anion substitution by nucleophile has been calculated (see Figures 17 and 18). Indeed, the process leading to the methoxy inactivated species is feasible, with an activation energy barrier of 16.9 kcal/mol for OAc^- and 14.8 kcal/mol for TFA^- . This result is in agreement with the experimental observation that the reaction of the gold catalyst in the presence of OAc^- with methanol and in the absence of substrate is very slow (10% of acetic acid in 24 h), whereas in the presence of TFA^- it is faster (complete formation of TFAH after 3 h).

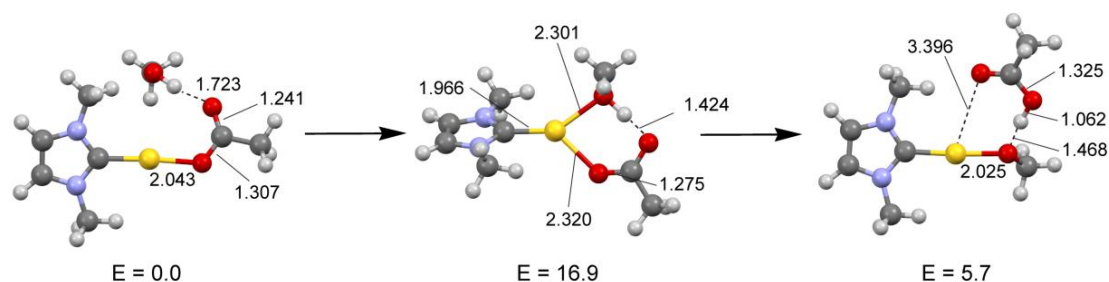


Figure 17. Optimized geometries of the stationary points involved in the ligand exchange between methanol and OAc^- . Relative stabilities are also reported (kcal/mol). Distances are expressed in Å

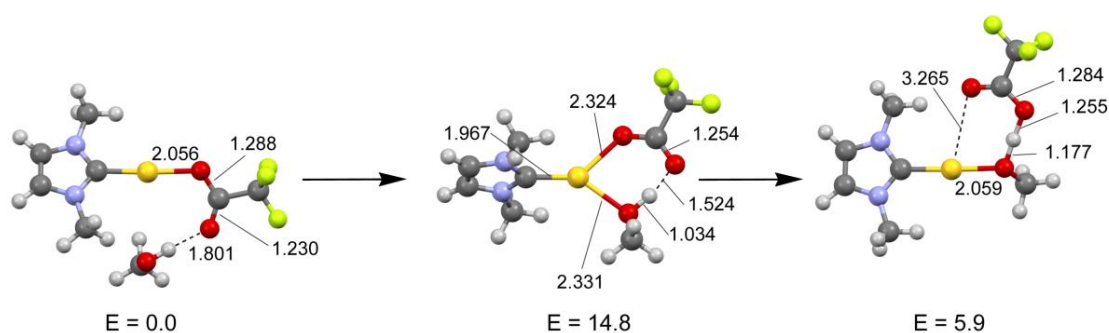


Figure 18. Optimized geometries of the stationary points involved in the in the ligand exchange between methanol and TFA^- . Relative stabilities are also reported (kcal/mol). Distances are expressed in Å

The geometry optimization with O–C1 fixed at 2.2 Å and O–H at 1.6 Å gives the structure D shown in Figure 16. Then, the system precedes to the vinyl ether intermediate product I (bottom, right corner in the plot) by only shortening the O–H distance (i.e., the hydrogen abstraction step follows the nucleophilic attack step). The geometry optimization with O–C1 fixed at 1.6 Å and O–H at 1.6 Å gives the structure E, depicted in Figure 16, which indeed is close to the I structure.

However, this process requires an even higher activation barrier (estimated value from the energy of structure D with respect to the energy of RC_{OAc} of about 8.7 kcal/mol (at DFT/BP86 level) than that of the hydrogen abstraction from methanol. D would be 27.2 kcal/mol higher in energy than IC_{OAc} . We conclude that the strong coordinating ability of OAc^- is more responsible than the strong proton acceptor capacity for the lack of catalytic activity of the gold catalyst in the presence of the

OAc⁻ anion. The strong coordinating power is related to the inability of acetate to form stable template character reactants complex **RC_{OAc}**. Since OAc⁻ requires a relatively high energy to hold the reactive methanol molecule in the right position for an outer-sphere addition, a concerted nucleophilic attack to butyne/nucleophile activation by anion cannot take place. On the other hand, the TFA⁻ strong proton acceptor character and less strong coordinating ability than OAc⁻ lead to the inactivation of the catalyst through the methoxy nucleophilic attack to gold and concomitant release of the substrate, as experimentally observed (see **Chapter 3**).

In **Chapter 3**, we have seen that during the methoxylation reaction the formation of methoxide and H-PFHp was not appreciable. The formation of the deactivated complex **DC_{PFHp}** has an activation barrier of 13.9 kcal/mol and the formation of **DC_{PFHp}** from **IC_{PFHp}** is endothermic by +4.9 kcal/mol (Figure 19), thus indicating the deactivation path through free methoxy catalyst poisoning as an alternative but less plausible competitive process in the pre-equilibrium step for PFHp⁻. The unexpected low activation barrier calculated for the nucleophilic attack of methanol to 2-butyne in presence of the PFHp⁻ anion related to the intermediate activity in the series of investigated anion should then not surprise: the reaction rate progressively decreases over the time, probably due to a tricoordinate (**TC_{PFHp}**) deactivation path. Recently, a tricoordinated species performed by TFA⁻ anion has been invoked in driving the reactivity of [{2,4-(tBu)₂C₆H₃O}₃P-Au-TFA] with 2,3-dimethyl-1*h* indole and N-tosyl-N-phenyl-allen-1-amine.¹³

¹³ Rocchigiani, L.; Jia, M.; Bandini, M.; Macchioni, A. *ACS Catal.* **2015**, *5*, 3911–3915

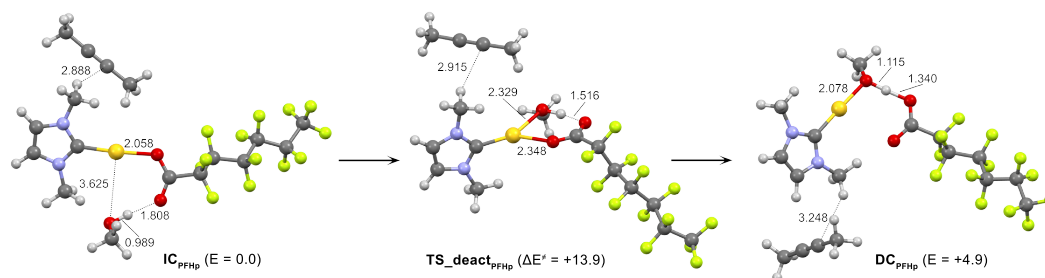


Figure 19. Initial complex IC_{PFHp} , deactivated complex DC_{PFHp} , transition state $TS_{deact_{PFHp}}$ for the deactivation pathway of the methanol nucleophile attack to butyne in the presence of the $PFHp^-$ anion. Energies values (kcal/mol) refer to IC_{EtOH} , taken as zero. Bond lengths are in angstroms

We conclude that a general trend between coordinating ability and experimental TOF values for the alkyne alkoxylation reaction may be established, provided that the geometry of the anion is taken into account:

i) for "more spherical" tridentate anions¹⁴ such as BF_4^- , ClO_4^- , NTf_2^- , OTf^- , OTs^- , and OMs^- ($-SO_3^-$ group presents a tetrahedral structure), the catalytic performance increases from low to intermediate coordinating ability; ii) for anions bearing "planar" anchoring, such as $PFHp^-$, NO_3^- , TFA^- , OAc^- and ptm^- the catalyst deactivation processes are important, either by preventing the alkyne coordination (NO_3^- , OAc^- and ptm^-) forming tricoordinate species ($PFHp^-$), or by forming free alkoxide (TFA^-), during the reaction, which determine a progressive decreasing of the reaction rate over the time.

¹⁴ Appelhans, L. N.; Zuccaccia, D.; Kovacevic, A.; Chianese, A. R.; Miecznikowski, J. R.; Macchioni, A.; Clot, E.; Eisenstein, O.; Crabtree, R. H. *J. Am. Chem. Soc.* **2005**, *127*, 16299-16311

2.4. Anion effect in relationship with different nucleophiles

In the following, we move to analyze the anion effect in relationship with different nucleophiles. In particular we start with the study of the activation of the nucleophile in the rate determining step for three different molecules: namely EtOH, and TFE, in combination with the OTs⁻ anion, as representative for their different activity observed experimentally (similar to methanol and no catalytic activity, respectively), and triethylene glycol monomethyl ether (Gly-OMe) in the absence of the anion, because of its unchanging activity in combination with different anions (see Chapter 4).

First, we focus on the activation of EtOH and TFE nucleophiles by hydrogen-bond acceptor ability of OTs⁻ anion. Starting from EtOH, the calculated initial complex **IC_{EtOH}**, reactant complex **RC_{EtOH}**, intermediate **I_{EtOH}**, transition state **TS_{preeq}_{EtOH}** for the preequilibrium step and transition state **TS_{EtOH}** for the ethanol nucleophile attack to butyne in the presence of the OTs⁻ anion are shown in Figure 20.

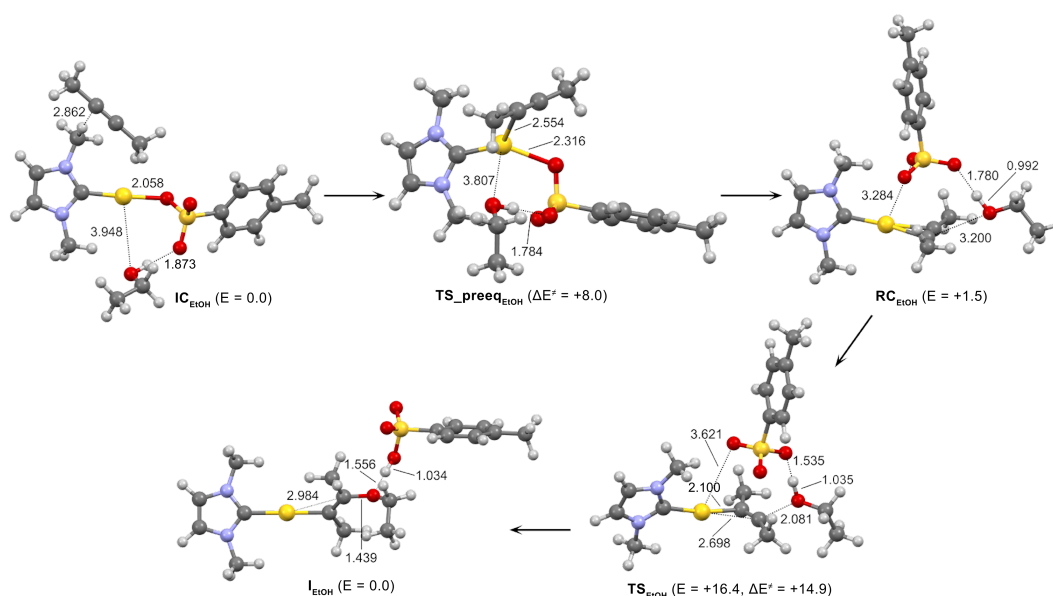


Figure 20. Initial complex **IC_{EtOH}**, reactant complex **RC_{EtOH}**, intermediate **I_{EtOH}**, transition state **TS_{preeq}_{EtOH}** for the preequilibrium step and transition state **TS_{EtOH}** for the ethanol nucleophile attack to 2-butyne in the presence of the OTs⁻ anion. Energies values (kcal/mol) refer to **IC_{EtOH}**, taken as zero. Bond lengths are in Å

The most stable species formed by the catalyst, the anion and the nucleophile has been calculated to be the anion-coordinated initial complex ($\mathbf{IC}_{\text{EtOH}}$), and has been taken as the zero reference energy. In the initial complex $\mathbf{IC}_{\text{EtOH}}$ the 2-butyne is in the second coordination sphere, weakly interacting with the NHC ligand. After anion substitution by 2-butyne, in the reactant complex ($\mathbf{RC}_{\text{EtOH}}$) the anion acts as a template and holds the nucleophile in the right position for an outer sphere addition. In the $\mathbf{RC}_{\text{EtOH}}$ complex one of the basic atom of the anion weakly interacts with the metal center ($\text{Au}\cdots\text{O} = 3.284 \text{ \AA}$), while forming a hydrogen bond with the nucleophile. The $\text{O}(\text{OTs}^-)\cdots\text{H}(\text{OEt})$ distance is 1.780 \AA . The formation of the $\mathbf{RC}_{\text{EtOH}}$ from the initial complexes $\mathbf{IC}_{\text{EtOH}}$ is thermodynamically unfavored: the reaction is endothermic by $+1.5 \text{ kcal/mol}$ with an activation barrier of 8.0 kcal/mol . This pre-equilibrium step can be eventually disrupted by an anion-induced catalyst poisoning through two possible deactivation pathways (Scheme 1). From previous studies using methanol, it is known that only one of them could be active for OTs^- , which has enough basicity to abstract a proton from the nucleophile leading to the formation of the corresponding acid HX and free alkoxide. The latter deactivates the catalyst through the formation of the catalytically inactive species (deactivated complex \mathbf{DC}_x), whereas the formation of the tri-coordinated complexes (\mathbf{TC}_x) has been ruled out and has been calculated only for strong coordinating anions such as OAc^- and TFA^- . The formation of the $\mathbf{DC}_{\text{EtOH}}$ complex from $\mathbf{IC}_{\text{EtOH}}$ is calculated to be endothermic by $+2.4 \text{ kcal/mol}$ with an activation barrier of 9.6 kcal/mol . For the nucleophilic attack step of EtOH to the butyne-coordinated species $\mathbf{RC}_{\text{EtOH}}$, the transition state gives an activation barrier of 14.9 kcal/mol . In the $\mathbf{TS}_{\text{EtOH}}$ the attack of ethanol at C1 causes a rearrangement in the coordination of the Au atom, forming an almost direct bond with the C2 carbon atom that lies at 2.100 \AA from it, while that between C1 and the gold is elongated (2.698 \AA). On the whole, the characteristic template structure of $\mathbf{RC}_{\text{EtOH}}$ with the anion in a bridging position between Au and ethanol is retained in $\mathbf{TS}_{\text{EtOH}}$. The distance between C1 and the oxygen atom of the ethanol is 2.081 \AA and the distance between oxygen of OTs^- and the metal center is 3.621 \AA . An incipient abstraction of hydrogen of the

-OH groups of ethanol by OTs^- can be observed ($\text{CH}_3\text{CH}_2\text{O}-\text{H} = 1.035 \text{ \AA}$, $\text{CH}_3\text{CH}_2\text{OH}\cdots\text{O}(\text{OTs}^-) = 1.535 \text{ \AA}$). In the intermediate complex I_{EtOH} the $\text{H}-\text{O}(\text{OTs})$ distance is 1.034 \AA and the $\text{CH}_3\text{CH}_2\text{O}\cdots\text{H}$ is 1.556 \AA , therefore the hydrogen of ethanol has been completely abstracted by OTs^- . The overall activation barrier from IC_{EtOH} to I_{EtOH} is 16.4 kcal/mol . For the same reaction involving methanol, similar geometries of the initial complex, reactants complex, intermediate and transition states have been calculated and comparable potential energy profiles have been found. For the nucleophilic attack step of MeOH to RC_{MeOH} the activation barrier amounts to 15.6 kcal/mol (vs. 14.9 kcal/mol for EtOH), and the overall activation barrier from IC_{MeOH} to I_{MeOH} is 18.3 kcal/mol (vs. 16.4 kcal/mol for EtOH). These DFT results are in line with TOF obtained for the two alcohols (see **Chapter 4**). Next we move to the TFE case that, in spite of the structural similarity with EtOH, is not able to react with 3-hexyne to give the product (see **Chapter 4**). Here, the electron withdrawing $-\text{CF}_3$ group may: i) induce a stronger acidity to the $-\text{OH}$ group so that the proton can be easily removed in the presence of an anion and the resulting methoxy leads to catalyst deactivation; ii) reduce the nucleophilic ability of the $-\text{OH}$ group in such a way that is not able to attach the triple bond of the substrate. The calculated initial complex IC_{TFE} , reactant complex RC_{TFE} , intermediate I_{TFE} , transition state $\text{TS}_{\text{preeqTFE}}$ for the pre-equilibrium step and TS_{TFE} for the TFE nucleophile attack to butyne in the presence of the OTs^- anion are shown in Figure 21.

Similarly to EtOH, the most stable species has been calculated to be the anion-coordinated initial complex (IC_{TFE}), which has been taken as the zero reference energy, with the 2-butyne in the second coordination sphere weakly interacting with the NHC ligand. In the reactant complex (RC_{TFE}) the anion acts as a template and holds the TFE nucleophile in the right position for an outer sphere attack. In RC_{TFE} one of the basic atoms of the anion weakly interacts with the metal center ($\text{Au}\cdots\text{O} = 3.284 \text{ \AA}$), while forming an HB with the nucleophile. The $\text{O}(\text{OTs}^-)\cdots\text{H}(\text{OTFE})$ distance is 1.679 \AA , shorter than that in RC_{EtOH} , due to the presence of the electron withdrawing CF_3 group which leads to a stronger interaction between the alcoholic proton and the

basic oxygen atom of the anion. The reaction of \mathbf{RC}_{TFE} formation from the initial complexes \mathbf{IC}_{TFE} is endothermic by +2.4 kcal/mol, with an activation barrier of 9.1 kcal/mol.

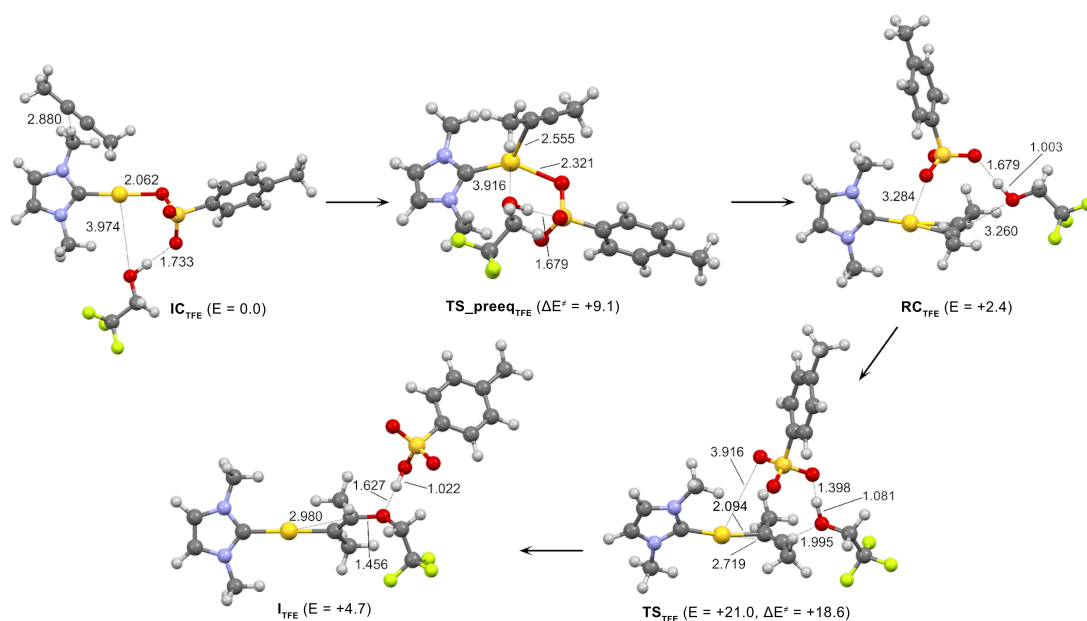


Figure 21. Initial complex \mathbf{IC}_{TFE} , reactant complex \mathbf{RC}_{TFE} , intermediate \mathbf{I}_{TFE} , transition state $\mathbf{TS}_{\text{preeq}_{\text{TFE}}}$ for the preequilibrium step and transition state \mathbf{TS}_{TFE} for the trifluoroethanol nucleophile attack to butyne in the presence of the OTs^- anion. Energies values (kcal/mol) refer to \mathbf{IC}_{TFE} , taken as zero. Bond lengths are in Å

The formation of the catalytically inactive \mathbf{DC}_{TFE} complex from the \mathbf{IC}_{TFE} is calculated to be also endothermic by +6.9 kcal/mol, with an activation barrier of 13.2 kcal/mol (see Supporting Information). So this deactivation path (throughout the formation of alkoxyde) is even less accessible here than what was found above for EtOH (we recall that the $\mathbf{DC}_{\text{EtOH}}$ energy of formation from $\mathbf{IC}_{\text{EtOH}}$ is 2.4 kcal/mol and the activation energy is 9.6 kcal/mol). In the \mathbf{TS}_{TFE} for the nucleophilic attack of TFE to the butyne-coordinated species \mathbf{RC}_{TFE} the bond between the gold center and the carbon atom on which the nucleophile attacks (C1) is elongated (2.719 Å) while that between gold and C2 is 2.094 Å. The distance between oxygen of OTs^- and the metal center is 3.916 Å, larger than that calculated for EtOH, and the incipient abstraction of the TFE

hydrogen by OTs^- is more pronounced ($\text{CF}_3\text{CH}_2\text{O}-\text{H} = 1.081 \text{ \AA}$, $\text{CF}_3\text{CH}_2\text{OH}\cdots\text{O}(\text{OTs}^-) = 1.398 \text{ \AA}$) in this case due to the presence of the CF_3 group leading to a more acidic proton. This larger “acid-like” character of OTs^- , apparently indicating a larger activation of the TFE by hydrogen bond acceptor property of the anion, results however in a higher activation barrier (18.6 kcal/mol) with respect to EtOH (14.9 kcal/mol) for the nucleophilic attack, showing an intrinsically poor nucleophilic character of TFE. The transition state TS_{TFE} evolves with the formation of the intermediate complex I_{TFE} where the hydrogen of trifluoroethanol has been completely abstracted by OTs^- ($\text{CF}_3\text{CH}_2\text{O}\cdots\text{H} = 1.627 \text{ \AA}$ and $\text{H}-\text{O}(\text{OTs}) = 1.022 \text{ \AA}$). The overall activation barrier from IC_{TFE} to I_{TFE} is 21.0 kcal/mol. From these results we conclude that i) in the pre-equilibrium step for both EtOH and TFE nucleophiles the **RC** formation is favored over the **DC** formation, thus precluding a catalyst poisoning through alkoxy-deactivated species; ii) in the nucleophilic attack step for both EtOH and TFE the OTs^- anion acts as a hydrogen-bond acceptor, enhancing the nucleophilicity of the attacking ethanol and trifluoroethanol, nevertheless the latter remaining scarcely nucleophilic. These findings suggest that a too low nucleophilic power rather than a catalyst poisoning is the reason why TFE is not experimentally active when both **1OTs** and **1BAR^F** are employed as catalyst.

Finally, we studied the nucleophilic attack of triethylene glycol monomethyl ether (Gly-OMe) to 2-butyne via auto-activation through $\text{OH}\cdots\text{O}$ hydrogen bond in order to rationalize its observed similar reaction time in combination with different anions. Gly-OMe can be found in many different rotational conformers, and three possible stable conformations are conceivable with the alcoholic hydrogen forming an internal hydrogen bond with the oxygen atom of one of the two ethylene glycol groups (1-O and 2-O) or with the oxygen of the ether group (3-O, Scheme 4, Experimental Section). Only these three conformations have been considered in the calculations and the one with the smaller activation barrier is reported here. The study started from the reactant complex $\text{RC}_{\text{Gly-OMe}}$ since no anion is taken into account in order to verify that the addition to butyne may take place via an auto-activation. In the $\text{RC}_{\text{Gly-}}$

OMe complex (Figure 22) the Gly-OMe is held in a suitable position for the outer sphere nucleophilic attack through formation of a HB between the oxygen atom of the ether group and one hydrogen of the butyne ($\text{H}_{\text{butyne}} \cdots \text{3-O(OMe)} = 2.328 \text{ \AA}$) while the distance between the Gly-OMe oxygen which performs the nucleophilic attack and the C1 carbon of the butyne is 3.420 \AA . The alcoholic hydrogen in Gly-OMe forms in turn an internal hydrogen bond with the ethylene glycol oxygen atom (2-O) that lies at 2.157 \AA from it. This latter distance becomes shorter in $\text{TS}_{\text{Gly-OMe}}$ ($\text{OH} \cdots \text{2-O}$ (ethylene glycol) = 1.940 \AA) with $\text{O-H} = 1.002 \text{ \AA}$ which is only slightly elongated with respect to that in the $\text{RC}_{\text{Gly-OMe}}$ complex (0.984 \AA). A peculiar feature of the $\text{TS}_{\text{Gly-OMe}}$ structure is the almost co-planar approach of the oxygen atom of the nucleophile towards the substrate C1 carbon (dihedral angle $\text{Au-C2-C1-O} = 174.5^\circ$), at a variance with the substantial out-of-plane approach found in the TS structures for the MeOH, EtOH, and TFE nucleophilic attack to 2-butyne mediated by the OTs^- anion (dihedral angle $\text{Au-C2-C1-O} = 155.1^\circ, 154.0^\circ, \text{ and } 153.8^\circ$, respectively), a constraint due to the anion template effect. The calculated activation barrier is 10.4 kcal/mol , indicating an efficient auto-activation of the nucleophile, which may be then ascribed not only to the possibility of forming internal hydrogen bond, but also to the possibility of allowing a co-planar nucleophilic attack, which seems to stabilize the transition state. $\text{TS}_{\text{Gly-OMe}}$ evolves with the formation of the intermediate $\text{I}_{\text{Gly-OMe}}$ which is less stable than $\text{RC}_{\text{Gly-OMe}}$ by 1.5 kcal/mol .

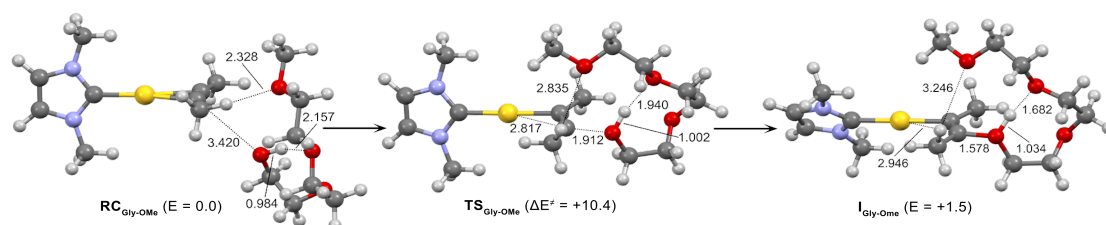


Figure 22. Reactant complex $\text{RC}_{\text{Gly-OMe}}$, intermediate $\text{I}_{\text{Gly-OMe}}$ and transition state $\text{TS}_{\text{Gly-OMe}}$ for the triethylene glycol monomethyl ether nucleophile attack to 2-butyne without the anion. Energies values (kcal/mol) refer to $\text{RC}_{\text{Gly-OMe}}$, taken as zero. Bond lengths are in \AA

The intermediate structure is very similar to that of the transition state, with much reduced C1...O (1.578 Å) and OH...2-O(ethylene glycol) (1.682 Å) distances, and an elongated O-H bond (1.034 Å). The results clearly show that Gly-OMe as nucleophile is auto-activating for the alkyne attack via both internal hydrogen bond formation and structural flexibility that releases steric constraints and allows a co-planar substrate attack. Here the activation of OH via the hydrogen bond acceptor ability of the anions is not needed, in agreement with the Gly-OMe experimentally observed activity, which remains almost constant independently of the used anion (see **Chapter 4**).

CHAPTER

7

**GOLD(I) N-HETEROCYCLIC CARBENE COMPLEXES
AS ANTICANCER AGENTS:
THE OTHER SIDE OF THE COIN**



rijksuniversiteit
 groningen

Visiting Ph.D. student (Erasmus+ Project) at the Department of Pharmacokinetics, Toxicology and Targeting at the Research Institute of Pharmacy

University of Groningen (Netherlands)

October 2015 – February 2016 (four months)

In this chapter another important application of gold(I) complexes is explored, in addition to their prominent success in the field of homogeneous catalysis: their use as anticancer agents.

A preliminary *in vitro* screening of several N-heterocyclic carbene gold(I) complexes showed promising antiproliferative activities. In particular, two different types of compounds have been investigated:

- [(NHC)AuX] complexes (**1X**), where NHC is 1,3-bis(2,6-di-isopropylphenyl)imidazol-2-ylidene (**L1**), and X is OTs⁻ (*p*-toluenesulfonate), NO₃⁻ (nitrate), NTf₂⁻ (bis(trifluoromethylsulfonyl)imide), OTf (trifluoromethanesulfonate), and 2,2,3,3,4,4,5,5,6,6,7,7,7-tridecafluoroheptanoate (PFHp⁻);
- (magi)AuX (**7X**) and [(magi)AuR]BF₄ (**[7R]BF₄**) complexes, where magi is 1-

methyl-3-(2,3,4,6-tetra-*O*-acetyl- β -D-glucopyranosyl)imidazolylidene, **L7**, X is chloride and 2-mercaptopyrimidine, and R is PPh₃ and magi.

The compounds have been tested in different human cancer cells and the intriguing results may represent the starting point for new possibilities of these organometallic gold(I) complexes for biological applications.

1. Introduction

Metal complexes play important roles in several biological processes, being involved in cellular functions. For example, they are essential to maintain the human body homeostasis and they are involved in the structure of several enzymes, the “metalloenzymes”.

Coordination chemistry can help to describe the interactions of metal ions in cells, but it is also a useful tool to develop new metal-based drugs for medicinal applications.

The roots of the medicinal chemistry can be traced back to the XXth century, when the arsenic based compound was used for the treatment of syphilis; afterward, others metal-based compounds were used as treatments for several diseases, such as stomach ulcers (bismuth),¹ diabetes (vanadium),² rheumatoid arthritis (gold)³ and cancer (platinum).⁴ Furthermore, metal complexes can be also used for diagnosis purposes in medicine, for example as contrast agent in Magnetic Resonance Imaging (MRI) (gadolinium-, manganese- or iron-based complexes)⁵ or as radio-pharmaceuticals (^{99m}technetium, ⁶⁸galium or ¹⁸⁶rhenium).^{6,7}

A cartoon-picture of the current use of metal-based and inorganic compounds in the clinic is depicted in Figure 1.⁸

¹ Sun, H. Z.; Zhang, L.; Szeto, K. Y. *Met. Ions Biol. Syst.* **2004**, *41*, 333–378

² Thompson, K. H.; Orvig, C. *J. Chem. Soc. Dalton Trans.* **2000**, 2885–2892

³ Ward, J. R.; Williams, H. J.; Egger, M. J.; Reading, J. C.; Boyce, E.; Altz-Smith, M.; Samuelson Jr., C. O.; Willkens, R. F.; Solsky, M. A.; Hayes, S. P.; Blocka, K. L. Weinstein, A.; Meenan, R. F.; Guttadauria, M.; Kaplan, S. B.; Klippel, J. *Arthritis & Rheumatism*, **1983**, *26*, 1303-1315

⁴ Rosenberg, B.; Vancamp, L.; Krigas, T. *Nature* **1965**, *205*, 698–699

⁵ Hermann, P.; Kotek, J.; Kubicek, V.; Lukes, I. *Dalton Trans.* **2008**, 3027–3047; Terreno, E.; Castelli, D. D.; Viale, A.; Aime, S. *Chem. Rev.* **2010**, *110*, 3019–3042

⁶ Correia, J. D. G.; Paulo, A.; Raposinho, P. D.; Santos, I. *Dalton Trans.* **2011**, *40*, 6144–6167

⁷ Thorp-Greenwood, F. L.; Coogan, M. P. *Dalton Trans.* **2011**, *40*, 6129-6145

⁸ Thompson, K. H.; Orvig, C. *Science* **2003**, *300*, 936-939

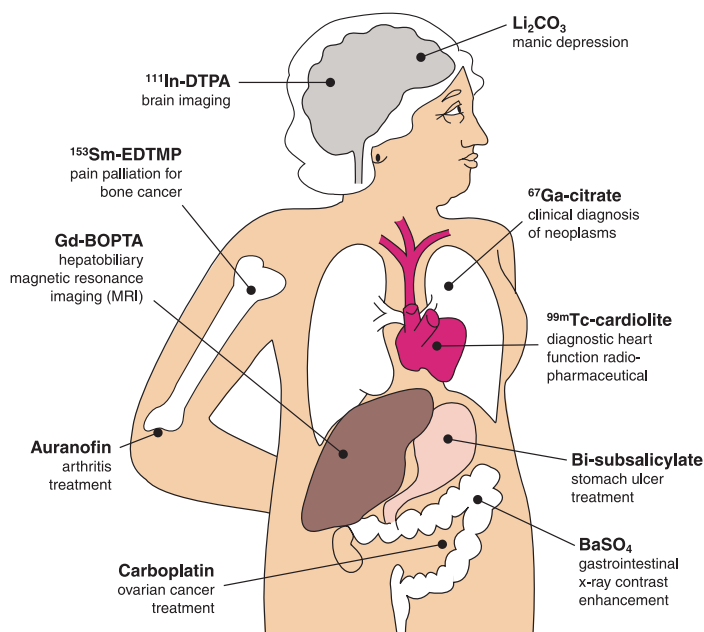


Figure 1. Overview of metal-based drugs and their applications. Reproduced from ref. 8

Among the metal-based compounds, platinum(II) complexes are important drugs for cancer chemotherapy. The *cis*-diamminodichloridoplatinum(II), cisplatin, discovered by Rosenberg,⁶ is one of the worldwide approved anticancer drugs, together with Carboplatin and Oxaliplatin, whereas other three have been approved at least in one country: Nedaplatin in Japan, Lobaplatin in China and Heptaplatin in the Republic of Korea (Figure 2).⁹

⁹ Wheate, N. J.; Walker, S.; Craig, G. E.; Oun R. *Dalton Trans.* **2010**, 39, 8113-8127

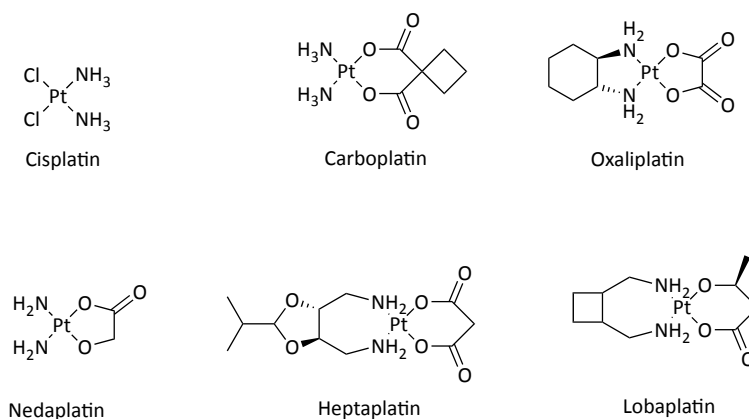


Figure 2. Platinum compounds marketed in at least one country

Cisplatin is currently used to treat several types of cancers, including testicular, ovarian, bladder, melanoma, non-small cell lung cancer (NSCLC), small cell lung cancer (SCLC), lymphomas and myelomas.¹⁰ However, in spite their great clinical success, the severe side effects, including nephrotoxicity, emetogenesis and neurotoxicity, limit its uses. Although some side effects can be reduced through the combination with other drugs, the nephrotoxicity remains a major concern.

Concerning its cytotoxic mode of action, cisplatin is activated in the cell through the sequential replacement of *cis*-chloride ligands with water molecules, due to the lower chloride intracellular concentration (3-20 mM), as compared to ≈100 mM in the extracellular fluid.¹¹

The cellular target of cisplatin is nuclear DNA: the activated platinum complex can interact with DNA *via* the reaction with the nucleophilic centers on the purine bases of DNA (guanine and adenine), in particular through the coordination of the *cis*-[Pt(NH₃)₂] fragment to the N⁷ atom of guanosine and adenosine residues, by displacing the aqua ligands. The two labile coordination sites on the platinum center permit the cross-linking of adjacent guanine bases or, to a smaller extent, the

¹⁰ Bosl, G. J., Bajorin, D. F. & Sheinfeld, J. *Cancer of the Testis* (eds DeVita, V. T. J., Hellman, S. & Rosenberg, S. A., Lippincott Williams & Wilkins, Philadelphia, **2001**); Watson, M.; Barrett, A.; Spence, R.; Twelves, C. *Oncology*, Oxford University Press, Oxford, 2nd edn, **2006**

¹¹ Pil, P.; Lippard, S.J. Cisplatin and related drugs. In: Joseph, R.B., editor. *Encyclopedia of Cancer*. New York: Academic Press; **2002** 525-543

platinum center can coordinate to guanine bases from different DNA strands forming interstrand cross-links.

A significant distortion in DNA double helix results from the major intrastrand cross-link,¹² bending it significantly toward the major groove and modifying the binding site of proteins. This bending inhibits the transcription, inducing apoptotic cell death: during the transcription, RNA polymerases stall at the platinum cross-link and recruit the transcription-coupled repair machinery. If this cellular machinery is unable to repair the lesion, then the cell evokes a programmed cell death pathway.¹³

A cartoon-picture of the most relevant Cisplatin-DNA adducts is depicted in Figure 3.¹⁴

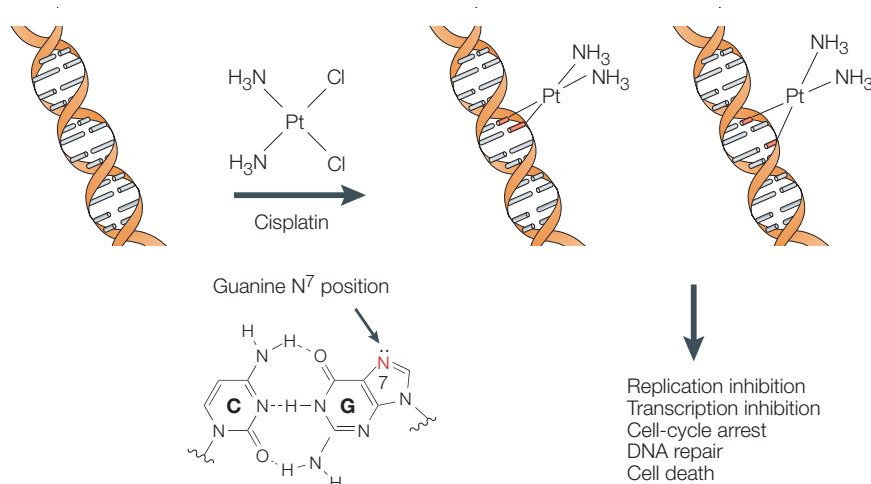


Figure 3. Mechanism of cisplatin interaction with DNA. Reproduced from ref. 14

As mentioned above, treatment with platinum compounds presents important drawbacks: besides the dose-limiting side effects, another serious limitation is the development of drug resistance by some types of cancer. For this reason, a large number of alternative metal complexes have been investigated for their cytotoxic properties, including ruthenium, iron and gold compounds.^{15,16,17,18,19} Particularly, gold

¹² Takahara PM, Rosenzweig AC, Frederick CA, Lippard SJ. *Nature* **1995**, *377*, 649–652

¹³ Johnstone TC, Park GY, and Lippard, SJ *Anticancer Res.* **2014**, *34*, 471–476

¹⁴ Wang, D.; Lippard, S. J. *Nat. Rev. Drug Discov.* **2005**, *4*, 307–320

¹⁵ Nobili, S.; Mini, E.; Landini, I.; Gabbiani, C.; Casini, A.; Messori, L. *Med. Res. Rev.* **2010**, *30*, 550-580

¹⁶ Nagy, E. M.; Ronconi, L.; Nardon, C.; Fregona, D. *Mini-Rev. Med. Chem.* **2012**, *12*, 1216- 1229

complexes have appeared in the last few decades as potential anticancer agents. The first representative member of this family is Auranofin ((2,3,4,6-tetra-O-acetyl-1-(thio-κS)-β-D-glucopyranosato)(triethylphosphane)gold(I)) (Fig. 4), which was developed during the 1970s and early 1980s as an orally administered compound for rheumatoid arthritis treatment and approved for clinical use in 1985.^{20,21}

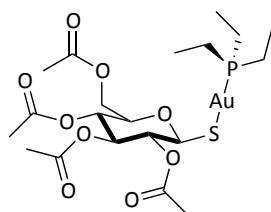


Figure 4. Auranofin

The biochemical pathways, associated to rheumatoid arthritis, are also relevant to cancer development, therefore gold complexes have been intensively investigated as new anticancer drugs.

Indeed, auranofin itself was shown in the mid 1980s to inhibit the growth of cultured tumour cells in vitro, as well as having limited in vivo antitumour activity in one mouse tumour model.²²

Mechanistic studies showed that interactions of gold complexes with DNA are not as tight as those found for platinum(II) drugs, which suggests the occurrence of different pathways of cytotoxicity.²³ Indeed, it has been showed that several gold compounds induce apoptosis via targeting mitochondria, but also through the interaction with

¹⁷ Gianferrara, T.; Bratsos, I.; Alessio, E. *Dalton Trans.* **2009**, 37, 7588-7598

¹⁸ Vessieres, A.; Top, S.; Beck, W.; Hillard, E.; Jaouen, G. *Dalton Trans.* **2006**, 529-541

¹⁹ Reedijk, J. *Eur. J. Inorg. Chem.* **2009**, 1303-1312

²⁰ B. M. Sutton, E. McGusty, D. T. Walz and M. J. DiMartino, *J. Med. Chem.*, **1972**, 15, 1095-1098

²¹ B. M. Sutton, *Gold Bull.*, **1986**, 19, 15-16

²² Berners-Price, S. J., Filipovska, A. *Metallomics*, **2011**, 3, 863-873

²³ a) A. de Almeida, B. L. Oliveira, J. D. G. Correia, G. Soveral, A. Casini, *Coord. Chem. Rev.* **2013**, 257, 2689-2704; b) L. Ronconi, D. Fregona, *Dalton Trans.* **2009**, 10670-10680; c) A. Casini, C. Hartinger, C. Gabbiani, E. Mini, P. J. Dyson, B. K. Keppler, L. Messori, *J. Inorg. Biochem.* **2008**, 102, 564-575.

different proteins/enzymes.²⁴ These interactions deserve more attention, since they play important roles in metal complex uptake and biodistribution processes and in determining their overall toxicity profile.

Several proteins were proposed to represent effective targets for cytotoxic gold compounds, such as thioredoxin reductase, cathepsins, protein tyrosine phosphatase, proteasome, iodothyronine deiodinase and zinc finger protein poly(adenosine diphosphate(ADP)-ribose) polymerases (PARPs).^{26,25}

The intracellular mechanism of Auranofin has been extensively studied: it displayed a different mode of action than the traditional platinum anticancer drugs, targeting DNA, and it induces apoptosis *via* a mitochondria-related pathway.²⁶

Auranofin was shown to be a highly potent and selective inhibitor of the thioredoxin reductases, seleno-enzymes essential in the so-called thioredoxin system, with an IC₅₀ on the nanomolar range,²⁷ leading to altered mitochondrial functions and to initiation of the apoptotic process.

The thioredoxin system is constituted by thioredoxin (Trx), thioredoxin reductase (TrxR) and NADPH, and it is present both in mitochondria and in cytosol.

The thioredoxin system, together with the glutathione one, is crucially involved in the regulation of the intracellular redox metabolism. In fact, among the several functions displayed by mitochondria, such as the control of cellular calcium fluxes,²⁸ induction

²⁴ Bindoli, A., Rigobello, M. P., Scutari, G., Gabbiani, C., Casini, A., Messori, L. *Coord. Chem. Rev.* **2009**, *253*, 1692.

²⁵ M. J. McKeage, L. Maharaj and S. J. Berners-Price, *Coord. Chem. Rev.*, **2002**, *232*, 127; P. J. Barnard and S. J. Berners-Price, *Coord. Chem. Rev.*, **2007**, *251*, 1889; K. P. Bhabak, B. J. Bhuyan and G. Mugesh, *Dalton Trans.*, **2011**, 2099; X. Zhang, M. Frezza, V. Milacic, L. Ronconi, Y. H. Fan, C. F. Bi, D. Fregona and Q. P. Dou, *J. Cell. Biochem.*, **2010**, *109*, 162; A. Casini, G. Kelter, C. Gabbiani, M. A. Cinellu, G. Minghetti, D. Fregona, H. H. Fiebig and L. Messori, *JBIC, J. Biol. Inorg. Chem.*, **2009**, *14*, 1139; M. V. Baker, P. J. Barnard, S. J. Berners-Price, S. K. Brayshaw, J. L. Hickey, B. W. Skelton and A. H. White, *Dalton Trans.*, **2006**, 3708; F. Mendes, M. Groessl, A. A. Nazarov, Y. O. Tsybin, G. Sava, I. Santos, P. J. Dyson and A. Casini, *J. Med. Chem.*, **2011**, *54*, 2196.

²⁶ Simon, T. M.; Kunishima, D. H.; Vibert, G. J.; Lorbe, A. *Cancer* **1979**, *44*, 1965-1975

²⁷ Scutari, G.; Bindoli, A. *J. Inorg. Biochem.* **2004**, *98*, 1634-1641; Rigobello, M. P.; Messori, L.; Marcon, G.; Cinellu, M. A.; Bragadin, M.; Folda, A.;

²⁸ P.S. Brookes, Y. Yoon, J.L. Robotham, M.W. Anders, S.-S. Sheu, *Am. J. Physiol. Cell. Ph.* **2004**, *287*, C817; T.E.Gunter, D.I.Yule, K.K.Gunter, R.A.Eliseev, J.D.Salter, *FEBS Lett.* **2004**, *567*, 96

of apoptosis mediated by the release of proapoptotic factors,²⁹ and their major metabolic role of producing energy, there is the production of reactive oxygen species (ROS)³⁰. In particular, some components of respiratory chain undergo autoxidation, originating superoxide anion, which rapidly dismutates to hydrogen peroxide. H₂O₂ is largely removed by glutathione and thioredoxin systems, leading to the equilibrium between formation and removal of hydrogen peroxide. The glutathione and thioredoxin systems are depicted in Figure 5.³¹

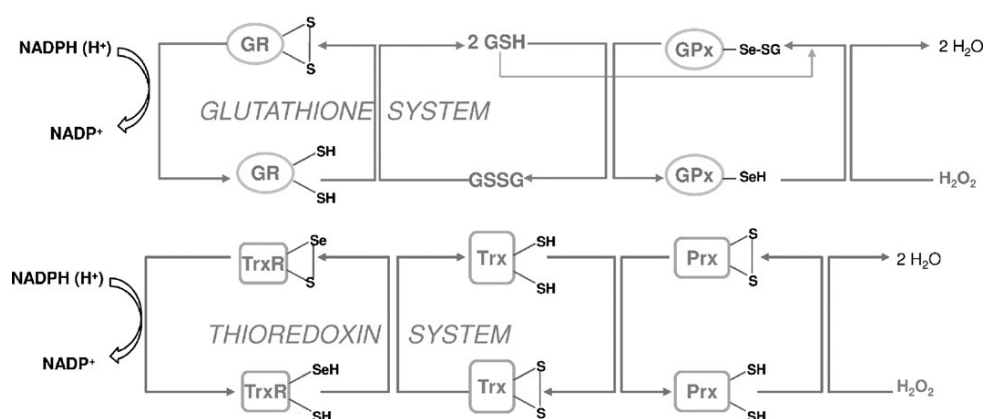


Figure 5. Glutathione and thioredoxin pathways, mediating the reduction of hydrogen peroxide.³² Reproduced from ref. 31

²⁹ G. Kroemer, L. Galluzzi, C. Brenner, *Physiol. Rev.* **2007**, 87, 99

³⁰ E. Cadenas, K.J.A. Davies, *Free Radic. Biol. Med.* **2000**, 29, 222; H.J. Forman, J.A. Kennedy, *Biochem. Biophys. Res. Commun.* **1974**, 60, 1044; G. Loschen, A. Azzi, C. Richter, L. Flohé, *FEBS Lett.* **1974**, 42, 68; G. Loschen, L. Flohé, B. Chance, *FEBS Lett.* **1971**, 18, 261; S. Raha, B.H. Robinson, *Trends Biochem. Sci.* **2000**, 25, 502

³¹ Bindoli, A.; Rigobello, M. P.; Scutari, G.; Gabbiani, C.; Casini, A.; Messori, L. *Coord. Chem. Rev.* **2009**, 253, 1692-1707

³² Mitochondrial respiratory substrates and the cytosolic pentose phosphate cycle reduce NADP⁺ to NADPH that, in turn, feeds reducing equivalents to both thioredoxin and glutathione systems. In mitochondria, electrons are transferred from NADH to NADP⁺ by the membrane-bound transhydrogenase. The thiol/disulfide redox systems finally transfer electrons to hydrogen peroxide that is reduced to water. Inhibition of either pathways markedly increases hydrogen peroxide concentration in the cell. Thioredoxin reductase and glutathione peroxidase are selenoenzymes. *Abbreviations:* GR(SH)₂, reduced glutathione reductase; GR(SS), oxidized glutathione reductase; GSH, reduced glutathione; GSSG, oxidized glutathione; GPx-SeH, reduced glutathione peroxidase; GPx-SeSG, oxidized glutathione peroxidase; TrxR(SH)₂, reduced thioredoxin reductase; TrxR(SS), oxidized thioredoxin reductase; Trx(SH)₂, reduced thioredoxin; Trx(SS), oxidized thioredoxin; Prx(SH)₂, reduced peroxiredoxin; Prx(SS), oxidized peroxiredoxin.

After inhibition of thioredoxin or glutathione systems, devoted to hydrogen peroxide reduction, a decreased consumption of ROS occurs.

The oxidized thioredoxin, Trx(SS), is reduced by thioredoxin reductase to Trx(SH)₂, supplying electrons to other enzymes, such as ribonucleotide reductase,³³ methionine sulfoxide reductase,³⁴ and peroxinoredoxin,³⁵ which regulates the level of cellular hydrogen peroxide. Furthermore, the reduced cytosolic thioredoxin-1 (TrxR1) is able to bind to ASK1, the apoptosis signal-regulating kinase 1, which is a member of the mitogen-activated protein kinase kinase kinase (MAP3K) family, inhibiting its activity and acting as a negative effector of apoptosis. The inhibition is interrupted when Trx-1 is oxidized and dissociates from ASK1.³⁶

Gold compounds have been found to be potent inhibitors of thioredoxin reductases, which are overexpressed in cancer cells. Increased expression of TrxR is linked to proliferant tumor cell growth, suppressed apoptosis, and resistance to conventional chemotherapy,³⁷ whereas its inhibition can induce cell death.³⁸

TrxR is a selenoenzyme, containing a very accessible selenocysteine on its flexible C-terminal domain, and several indications suggest that a direct coordination bond between gold and the selenocysteine could be responsible of the enzyme inhibition.³⁹ This view is corroborated by the established “soft Lewis acid” nature of gold compounds, especially those in the oxidation state +1, manifesting high affinity for “soft” donors, such as selenolate groups.

The inhibition of mitochondrial thioredoxin reductase, TrxR2, by gold complexes prevents the reduction of Trx(SS) to Trx(SH)₂ (Figure 6)³¹ and leads to the accumulation of hydrogen peroxide in mitochondria. In presence of large amount of

³³ T.C. Laurent, E.C. Moore, P. Reichard, *J. Biol. Chem.* **1964**, 239, 3436

³⁴ R.L. Levine, J. Moskovitz, E.R. Stadtman, *IUBMB Life* **2000**, 50, 301

³⁵ B. Hofmann, H.J. Hecht, L. Flohé, *Biol. Chem.* **2002**, 383, 347; S.G. Rhee, H.Y. Chae, K. Kim, *Free Radic. Biol. Med.* **2005**, 38, 1543

³⁶ M.Saitoh, H.Nishitoh, M.Fujii, K.Takeda, K.Tobiome, Y.Sawada, M.Kawabata, K. Miyazono, H. Ichijo, *EMBO J.* **1998**, 17, 2596

³⁷ A. Burke-Gaffney, M. E. J. Callister and H. Nakamura, *Trends Pharmacol. Sci.*, **2005**, 26, 398.

³⁸ M. P. Rigobello, A. Folda, M. C. Baldoin, G. Scutari and A. Bindoli, *Free Radical Res.*, **2005**, 39, 687.

³⁹ Y. Omata, M. Folan, M. Shaw, R.L. Messer, P.E. Lockwood, D. Hobbs, S. Bouillaguet, H. Sano, J.B. Lewis, J.C. Wataha, *Toxicol. in Vitro* **2006**, 20, 882–890

H_2O_2 , thioredoxin is oxidized by peroxinredoxin (Prx3) irreversibly, and Trx(SS), together with hydrogen peroxide, act on several different intramitochondrial targets, leading to an increased permeability of the mitochondrial membranes and the release of proapoptotic factors. These factors activate caspase-3 and caspase-9, which lead to cell death.

On the other hand, as the hydrogen peroxide can freely cross the mitochondrial membranes, a large concentration of H_2O_2 is found in cytosol, where it causes the oxidation of Trx1, because, similarly to the mitochondrial Trx2, it can not be reduced back by the inhibited thioredoxin reductase, TrxR1. Trx(SS)1 stimulates the MAPKinases pathways, leading to cell death.

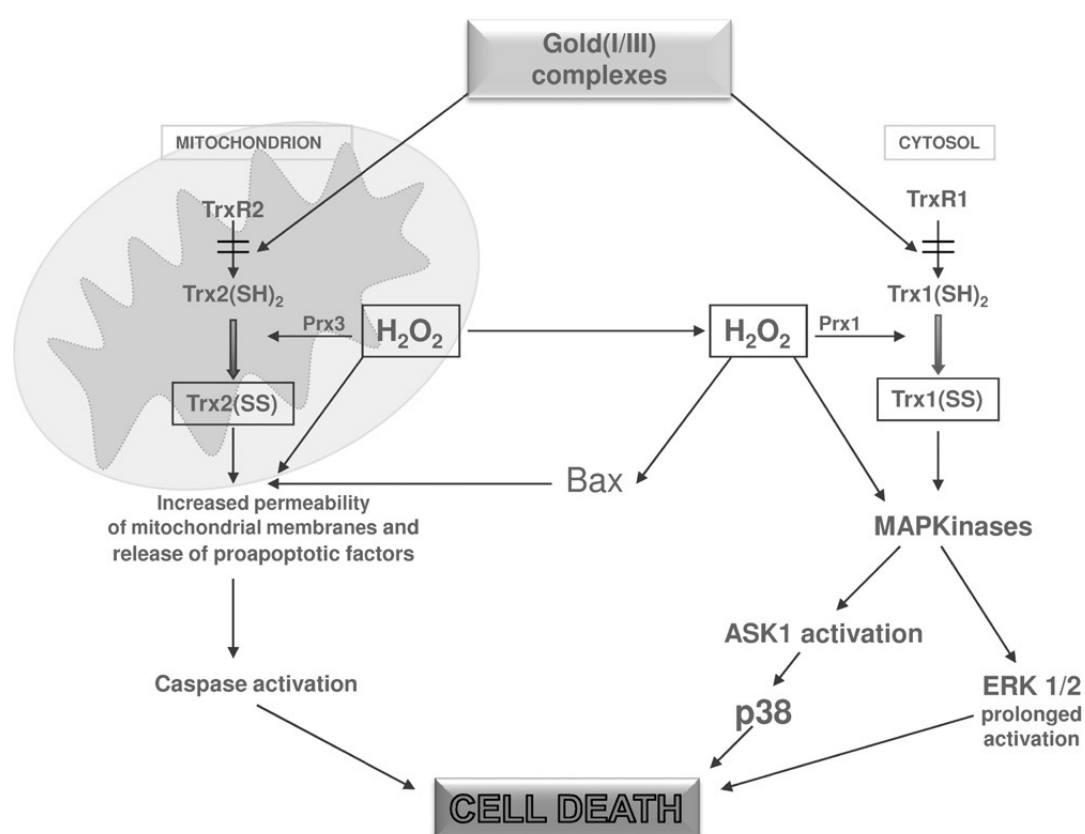


Figure 6. Model depicting the mechanism of action of cell death induction by gold(I/III) compounds. Reproduced from ref. 31

Gold compounds are highly specific inhibitors of mitochondrial thioredoxin reductase,

whereas a few other metal ions (*e.g.* cadmium(II) ions, etc) are significantly less effective.

Concerning Auranofin, its intracellular mechanism has been extensively studied. It has been identified as one of the most potent and selective inhibitors of the mitochondrial protein thioredoxin reductase (TrxR).⁴⁰

Beyond TrxR, auranofin has been resulted to be inhibitor of sulphur-containing enzyme glutathione-S-transferase, which is probably involved in the mechanism of resistance to Cisplatin.⁴¹

Within this frame, auranofin displayed promising attributes as chemotherapy drug able to overcome the resistance and selectivity problems presented by conventional chemotherapy; in fact three clinical trials, studying the use of auranofin in cancer treatment, are currently active.

Several Auranofin analogues, where the sugar and the phosphine ligand were varied, have been investigated and from the structure-activity relationships the great importance of the phosphine ligand for the toxicity resulted.

In the reaction between gold compounds (Auranofin, [Et₃P-Au-Cl]) and cysteine or methylselenocysteine, the same products [Et₃P-Au-cysteine]⁺ and [Et₃P-Au-methylselenocysteine]⁺ were formed, as shown by mass spectrometry, suggesting that the Auranofin's properties can be enhanced by replacing thio-β-D-glucose tetraacetate moiety.⁴²

A series of gold phosphine complexes with general formula [R₃P-Au-Cl] (R = alkyl or aryl) showed a positive correlation between the size of the R substituents and cellular uptake and toxicity.⁴³

Several targets have been investigated, including TrxR, but also other proteins/enzymes relevant to cancer: [Ph₃P-Au-Cl] has been shown to efficiently

⁴⁰ (a) S. Gromer, L. D. Arscott, C. H. Williams, R. H. Schirmer and K. Becker, *J. Biol. Chem.*, 1998, 273, 20096; (b) S. Urig, K. Fritz-Wolf, R. Re' au, C. Herold-Mende, K. Tó th, E. Davioud-Charvet and K. Becker, *Angew. Chem., Int. Ed.*, **2006**, 45, 1881.

⁴¹ De Luca, A.; Hartinger, C. G.; Dyson, P. J.; Lo Bello, M.; Casini, A. *J. Inorg. Biochem.* **2013**, 119, 38-42

⁴² Shoeib, T.; Atkinson, D. W.; Sharp, B. L. *Inorg. Chim. Acta* **2010**, 363, 184-192

⁴³ Scheffler, H.; You, Y.; Ott, I. *Polyhedron* **2010**, 29, 66-69

inhibit *in vitro* cathepsin B, an enzyme belonging to the cysteine protease family implicated in inflammatory mechanisms.⁴⁴ Other highly efficient inhibitors of TrxR and GR, were gold(I)-phosphole chloride (GoPI) (Figure 7) and its thiosugar analogue (GoPI-sugar), the latter being more stable under physiological conditions, with cytotoxic activities in the low micromolar range against glioblastoma or breast cancer cells *in vitro*.^{45, 46}

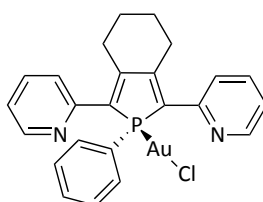


Figure 7. Gold(I)-phosphole chloride (GoPI)

Following the successful application of auranofin and gold phosphine complexes as antitumor agents, a variety of organometallic cationic mononuclear gold(I) bis-carbene complexes (Figure 8, **8a-d**) were synthesized by Berners-Price *et al.* and investigated as chemotherapeutic drugs.^{47, 48, 49} Suitable modification of R substituents allows to adjust the lipophilic character of the complexes, a critical factor for targeting cancer cells. Their strong antimetabolic effects can be ascribed to their cationic and lipophilic character.

⁴⁴ Gunatilleke, S. S.; Barrios, A. M. *J. Inorg. Biochem.* **2008**, *102*, 555-563

⁴⁵ Deponte, M.; Urig, S.; Arscott, L. D.; Fritz-Wolf, K.; Réau, R.; Herold-Mende, C.; Konkarevic, S.; Meyer, M.; Daviout-Charvet, E.; Ballou, D. P.; Williams, C. H.; Becker, K. *J. Biol. Chem.* **2005**, *280*, 20628-206

⁴⁶ Viry, E.; Battaglia, E.; Deborde, V.; Müller, T.; Réau, R.; Daviout-Charvet, E.; Bagrel D. *ChemMedChem* **2008**, *3*, 1667-167

⁴⁷ Baker, M. V.; Barnard, P. J.; Berners-Price, S. J.; Brayshaw, S. K.; Hickley, J. L.; Skelton, B. W.; White, A. H. *Dalton Trans.* **2006**, 3708-3715

⁴⁸ Barnard, P. J.; Baker, M. V.; Berners-Price, S. J.; Day, D. A. *J. Inorg. Biochem.* **2004**, *98*, 1642-1647

⁴⁹ Hickey, J. L.; Ruhayel, R. A.; Barnard, P. J.; Baker, M. V.; Berners-Price, S. J.; Filipovska, A. *J. Am. Chem. Soc.* **2008**, *130*, 12570-12571

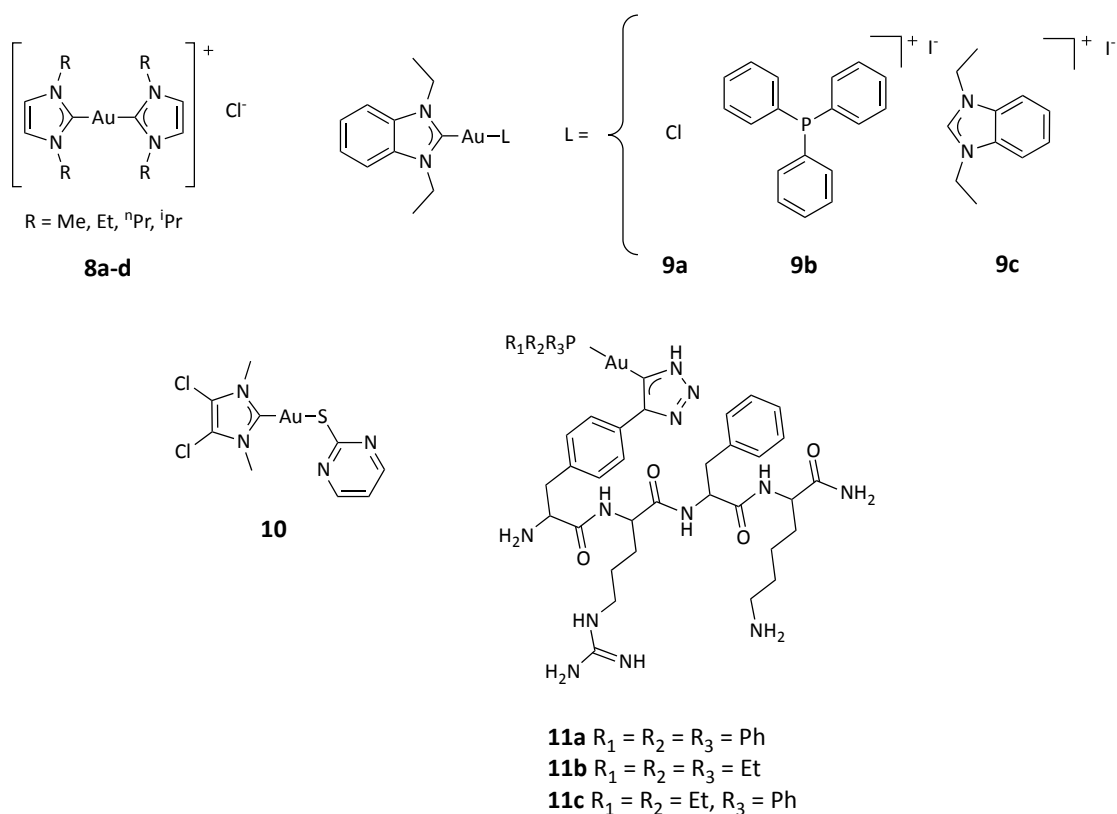


Figure 8. Gold(I)-NHC complexes

The presence of an ancillary ligand, in addition to the NHC, can influence the biological activity of the complex, as demonstrated by Rubbiani *et al.*,⁵⁰ who synthesized three 1,3-benzimidazol-2-ylidene gold(I) complexes (Figure 8, **9a-c**) with different ligands, Cl, NHC and PPh₃, showing differences in bond dissociation energies (BDEs), as revealed by DFT calculations, with an order of stability Cl < PPh₃ < NHC. This order reflects the TrxR inhibition one: the chlorido complex resulted strong and selective, as well as the triphenylphosphine derivative, whereas the cationic bis-carbene species exhibited the lowest TrxR inhibition. The complexes are able to firmly bind the Selenocysteine and block the selenolate group. It was observed through tandem MS experiments, a direct coordination to gold(I) of the selenolate group of Selenocysteine, in a linear synthetic dodecapeptide, exactly reproducing the C-terminal portion of the

⁵⁰ Pratesi, A., Gabbiani, C., Michelucci, E., Ginanneschi, M., Papini, A. M., Rubbiani, R., Ott, I., Messori, L., *J. Inorg. Biochem.*, **2014**, *136*, 161-169

human TrxR.

Furthermore, marked and selective inhibition of both cytosolic and mitochondrial isoforms of the TrxR enzyme, especially in cancer cells, has been reported with NHC-Au-L, with NHC = 1,3-substituted imidazole-2-ylidene and benzimidazol-2-ylidene ligands and L = Cl or 2-mercapto-pyrimidine (Figure 8, **10**).⁵¹

It is worth mentioning that a direct correlation between TrxR inhibition and NHC gold(I) complexes cytotoxicity can not be always asserted,⁵² thus other mechanisms might be involved. Recently, some studies demonstrated that another enzyme could be a target for this class of compounds,⁵³ the Poly(ADP-ribose) polymerase 1 (PARP-1), which is involved in the DNA repair mechanism⁵⁴ and is suspected to be implicated into resistance to Cisplatin.⁵⁵ In addition, some N-heterocyclic carbene gold(I) complexes showed to be good inhibitors of cysteine dependent protein tyrosine phosphatases (PTPs),⁵⁶ an enzyme family, which plays important roles in several cellular processes and signal pathways, considered as targets for cancer and autoimmune disorders.

The high degree of structural diversity is the main feature that makes NHC gold(I) compounds very attractive in drug design, as in case of the recently reported peptide-Au-NHC compounds⁵⁷ (Figure 8, **11a-c**), resulting as powerful inhibitors of TrxR, inducing ROS formation and apoptosis, and triggering antimitochondrial effects.

Furthermore, among the new strategies currently implemented in cancer chemotherapy, a new potential target of NHC gold(I) complexes is found in the G-quadruplex structure of DNA. G-quadruplexes are peculiar nucleic acid architectures

⁵¹ Shuh, E.; Pfluger, C.; Citta, A.; Folda, A.; Rigobello, M. P.; Bindoli, A.; Casini, A.; Mohr, F. *J. Med. Chem.* **2012**, *55*, 5518-5528

⁵² Rubbiani, R.; Shuh, E.; Meyer, A.; Lemke, J.; Wimberg, J.; Metzler-Nolte, N.; Meyer, F.; Mohr, F.; Ott, I. *MedChemComm* **2013**, *4*, 942-948

⁵³ Rubbiani, R.; Salassa, L.; de Almeida, A.; Casini, A.; Ott, I. *ChemMedChem* **2014**, *9*, 1205-1210

⁵⁴ Jeggo, P. A. *Curr. Biol.* **1998**, *8*, 49-51

⁵⁵ Bouchard, V.J.; Rouleau, M.; Poirier, G. G. *Exp. Hematol.* **2003**, *31*, 446-454

⁵⁶ Krishnamurthy, D.; Karver, M. R.; Fiorillo, E.; Orru, V.; Stanford, S. M.; Bottini, N.; Barrios, A. M. *J. Med. Chem.* **2008**, *51*, 4790-4795

⁵⁷ Köster, S. D.; Alborzina, H.; Can, S.; Kitanovic, I.; Wöfl, S.; Rubbiani, R.; Ott, I.; Riesterer, P.; Prokop, A.; Merz, K.; Metzler-Nolte, N. *Chem. Sci.* **2012**, *3*, 2062-2072

adopted by guanine-rich DNA and RNA sequences: four guanine bases can associate through Hoogsteen hydrogen-bonding arrangement,⁵⁸ to form a square planar structure, called a guanine tetrad, and two or more guanine tetrads can stack on top of each other to form a G-quadruplex, which is further stabilized by the presence of a cation (usually K^+), sitting in a central channel between each pair of tetrads (Figure 9).⁵⁹ the stabilization by selective small molecules of G-quadruplex, the so-called G-quadruplex ligands,⁶⁰ are suspected to be involved in the control of key cellular events, such as telomere homeostasis and chromosomal stability, as well as regulation of oncogene expression.

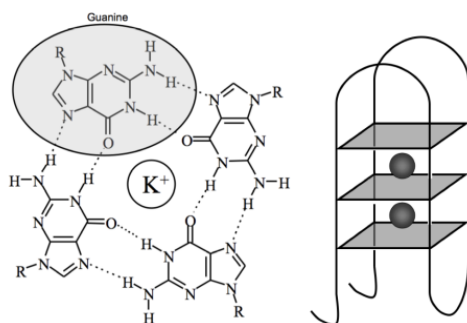


Figure 9. Scheme of a guanine quartet stabilized by the presence of a potassium cation (left) and an example of a G-quadruplex DNA structure in which planes represent quartets (right). Spheres represent K^+ ions

⁵⁸ Collie, G. W.; Parkinson, G. N *Chem. Soc. Rev.* **2011**, *40*, 5867-5892

⁵⁹ Campbell, Nancy H.; Neidle, Stephen "Chapter 4. G-Quadruplexes and Metal Ions". In Astrid Sigel, Helmut Sigel and Roland K. O. Sigel. *Interplay between Metal Ions and Nucleic Acids. Metal Ions in Life Sciences*, Springer, 2012, *10*, 119–1134

⁶⁰ Monchaud, D.; Teulade-Fichou, M. P. *Org. Biomol. Chem.* **2008**, *6*, 627-636

A number of G-quadruplex stabilizing small molecules have been synthesized, but they often lack selectivity when incubated with duplex DNA.⁶¹ Among them, metal compounds possess interesting properties, but only few studies are focusing on gold complexes,^{62, 63, 64} and, most importantly, gold(III) complexes are investigated so far.

Within this frame, recently, the bis-carbene species $[\text{Au}(\text{caffeine-2-ylidene})_2]\text{BF}_4$ has been proved to be an efficient and selective quadruplex-interacting agent.⁶⁵

In organometallic gold complexes the presence of a direct carbon-gold bond greatly stabilizes the gold oxidation state and guarantees more controlled chemical speciation in biological systems. Indeed, the risk associated to the biological applications of gold compounds is the remarkable oxidizing character of gold(III)/gold(I) centers and the tendency to reduce to gold(I)/gold(0), which leads to an extensive and unselective cell damage, as well as to a possible inactivation of the compounds in the aqueous environment.⁶⁶

In general, both organometallic gold(I) and gold(III) compounds have increased stability compared to the classical gold-based coordination complexes, allowing the possibility to modulate the redox properties and ligand exchange reactions to achieve selective activation in diseased cells.⁶⁶

In addition, as mentioned above, Au(I)-NHC compounds present the possibility to modulate their lipophilic character, a critical factor for targeting malignant cells, through the appropriate modification in the ligand structure, but also by the derivatization possibilities associated to the presence of a ancillary ligand coordinated to gold (e.g. phosphines, thiols, as well as a second NHC ligand).

Recently, also the relevance of the anion in a metallodrug has been studied, considering a series of four Ag(I) compounds, bearing norharmane (9H-Pyrido[3,4-

⁶¹ Le, T. V. T.; Han, S.; Chae, J.; Park, H. J. *Curr. Pharm. Des.* **2012**, *18*, 1948-1972

⁶² Stefan, L.; Bertrand, B.; Richard, P.; Le Gendre, P.; Denat, F.; Picquet, M.; Monchaud, D. *ChemBioChem* **2012**, *13*, 1905

⁶³ Suntharalingam, K.; Gupta, D.; Miguel, P. J. S.; Lippert, B.; Vilar, R. *Chemistry - Eur. J.* **2010**, *16*, 3613

⁶⁴ Sun, R. W. Y.; Li, C. K. L.; Ma, D. L.; Yan, J. J.; Lok, C. N.; Leung, C. H.; Zhu, N.; Che, C. M. *Chemistry - Eur. J.* **2010**, *16*, 3097

⁶⁵ Bertrand, B., Stefan, L., Pirrotta, M., Monchaud, D., Bodio, E., Richard, P., Le Gendre, P., Warmerdam, E., H. de Jager, M., Groothuis, G. M. M., Picquet, M., Casini, A., *Inorg. Chem.* **2014**, *53*, 2296-2303

b]indole; Hnor) as ligand and different anions, such as ClO_4^- , NO_3^- , BF_4^- , PF_6^- .⁶⁶ Their *in vitro* antiproliferative effects were evaluated on the human lung cancer cell line A549 and human ovarian cancer A2780 cells and all the compounds appeared to be moderately toxic in both cell line, but, interestingly, the complex with ClO_4^- showed the highest activity in the considered series, similar to cisplatin. It suggested that the anion plays an important role in determining the cytotoxicity, although the mechanism of antiproliferative activity is not well established.

In view of these considerations, it has been investigated the anion effect also from the biological point of view, studying the *in vitro* antiproliferative activities of some of $[(\text{NHC})\text{AuX}]$, previously used as catalysts (see **Chapter 2, 3, 4**).

In addition, in order to enhance the anticancer properties of carbene gold(I) compounds, another class of complexes was developed, a glucopyranoside-incorporated N-heterocyclic carbene gold(I) complexes, as showed in Figure 10. Indeed, saccharide-incorporated ligands confer to their complexes highly water solubility, which is of great toxicological importance, because it is one of the major factors influencing the availability and absorption of metal compounds in biological systems.

Carbohydrates are the most abundant biological molecules on earth and fill numerous roles in organism,⁶⁷ but they also play a major role in signalling and recognition processes.⁶⁸ Therefore, they represent the building blocks for the synthesis of biologically active compounds.⁶⁹

Furthermore, suitable functionalization through the OH groups allows finely tune the lipophilicity in order to improve the cellular uptake.

The relevance of interactions between saccharides for cell recognition makes this type

⁶⁶ R. Ahmad Khan et al. *Journal of Inorganic Biochemistry*, **2014**, *140*, 1–5

⁶⁷ (a) Lindhorst, T.K., *Chem. Unserer Zeit* **2000**, *34*, 38; (b) Nelson, D.L., Cox, M.M., *Lehninger Principles of Biochemistry*, Palgrave Macmillan, **2004**

⁶⁸ Osborn, H.; Khan, T. *Oligosaccharides, Their Synthesis and Biological Roles*; Oxford University Press: Oxford, U.K., **2000**, 7

⁶⁹ Liu, X.Y., Stocker, B.L., Seeberger, P.H. *J. Am. Chem. Soc.* **2006**, *128*, 3638, and references cited there

of compounds suitable for anticancer drug delivery.⁷⁰

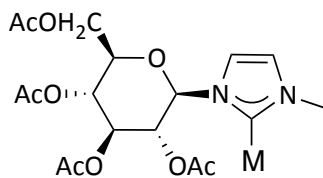


Figure 10. Sugar incorporated N-heterocyclic carbene ligand, L7

⁷⁰ Nishioka, T., Shibata, T., Kinoshita, I., *Organometallics*, **2007**, *26*, 1126-1128

2. Results and discussion

In vitro cell viability assays

The antiproliferative properties of the complexes **1OTs**, **1NO₃**, **1NTf₂**, **1OTf**, and **1PFHp** (Figure 11), with cisplatin used as comparison, were assessed by monitoring their ability to inhibit cell growth using the classical MTT (3-(4,5-dimethylthiazol-2-yl)-2,5-diphenyltetrazolium bromide) assay in colorectal and lung cancer cell lines (HCT p53 +/- and A549). The IC₅₀ values of the NHC-based gold(I) compounds are presented in Table 1.

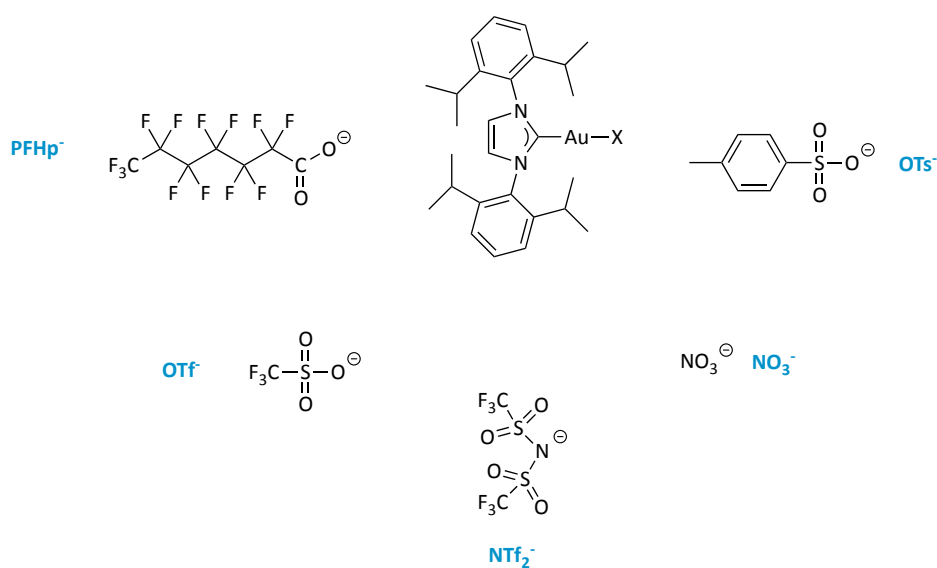


Figure 11. [(NHC)AuX] complexes

Table 1. Effect of gold compounds on cell viability (IC₅₀ values) in human colorectal carcinoma cells (HCT) and human lung cancer cells (A549) after 72h incubation at 37 °C^a

Compound	IC ₅₀ (μM) ^b ± SE ^c	
	HCT p53 +/+	A549
1OTs	10.4 ± 1.9	29.5 ± 5.7
1PFHp	39.5 ± 0.096	73.3 ± 5.6
1NTf₂	47.9 ± 5.9	51.1 ± 24.7
1OTf	38.8 ± 3.8	57.7 ± 2.9
1NO3	9.5 ± 1.8	29.0 ± 9.1
Cisplatin	10.6 ± 1.3	8.0 ± 0.5

^a Solutions of the gold complexes were prepared by diluting a freshly prepared stock solution (10⁻² M in DMSO) of the corresponding compounds in cell culture medium. The stability of the complexes in DMSO was checked: after 20 h at room temperature no degradation and no ligand replacement by DMSO was observed. Cisplatin stock solutions were prepared in MilliQ water; ^bIC₅₀ is the inhibitory concentration of a drug needed to inhibit a given biological process by half; ^c Values are the mean of at least three experiments ± SE.

Several conclusions can be drawn in light of the results displayed in Table 1:

- All the compounds appear to be moderately toxic in both cell lines (IC_{50} values lying in the microM range), and more active against HCT p53+/+ cells compared to A549 cells, which can be explained by the well-known resistance properties of human lung cancer cells to platinum chemotherapy.

- As in catalysis, we observed an anion effect: OTs⁻ anion showed the highest activity for both cell lines, together with NO₃⁻, with IC_{50} values similar to cisplatin in HCT p53 +/+ cell line, whereas in A549 cell line the IC_{50} values are slightly higher.

Moreover, the moderate antiproliferative activity of **1OTs** and **1NO₃** prompted us to broaden their investigation against other cell lines, namely the HCT p53 -/- cell line (which differs from the wild type p53 +/+ for the inactivated p53 gene) and MCF7, human breast adenocarcinoma cell line.

As reported in Figure 11 and Table 2, gold(I) complexes show different behavior in each cell line, which leads to conclude that a certain cell line selectivity takes place. Furthermore, they interestingly appear to be more active on HCT p53 -/- and MCF7 cells than cisplatin.

Table 2. Effect of gold compounds on cell viability (IC_{50} values) in human colorectal carcinoma cells (HCT) and human breast adenocarcinoma cells (MCF7) after 72h incubation

Compound	IC_{50} (μ M) \pm SE ^a	
	HCT p53-/-	MCF7
1OTs	12.9 \pm 1.5	14.6 \pm 1.2
1NO₃	12.1 \pm 2.2	6.81 \pm 4.0
Cisplatin	22.1 \pm 1.9	21.4 \pm 1.4

^a Values are the mean of at least three experiments \pm SE.

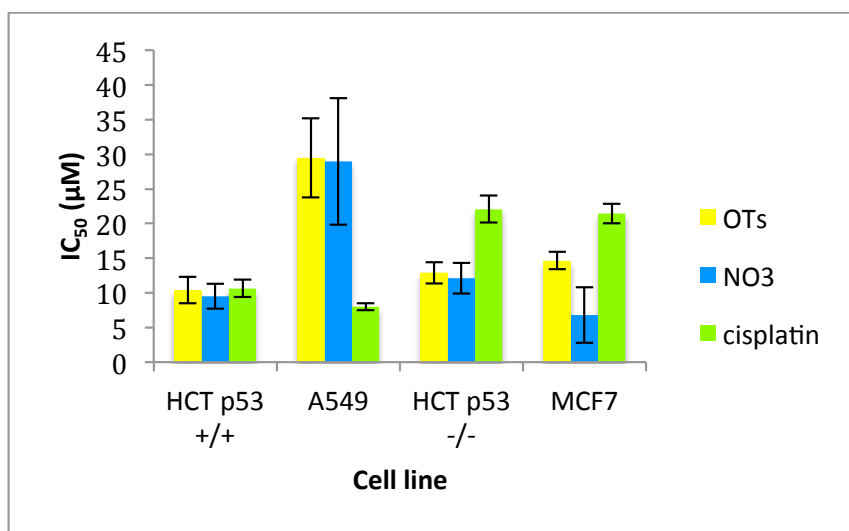


Figure 11. Effect of 1OTs and 1NO₃ on cell viability in HCT, A549 and MCF7 cell lines

In addition, four gold(I) complexes, bearing **L7** ligand, 1-methyl-3-(2,3,4,6-tetra-*O*-acetyl- β -D-glucopyranosyl)imidazolylidene, have been synthesized, as depicted in Figure 12: in the typical linear coordination geometry of gold(I), in all the compounds gold(I) center is bonded to the same ligand, on one side, whereas on the opposite side to another ligand, which can be, in turn, chloride, a second **L7**, triphenylphosphine or 2-mercaptopyrimidine. All these complexes were synthesized for the very first time, as reported in **Chapter 2**.

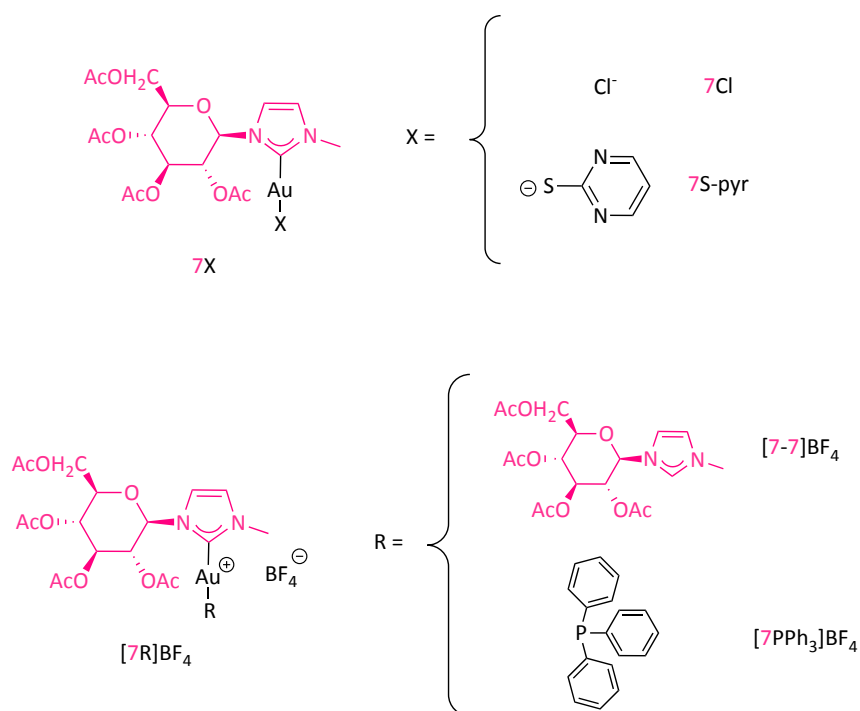


Figure 12: Sugar incorporated N-heterocyclic carbene gold(I) complexes

Thus, the antiproliferative properties of these complexes were investigated in a preliminary *in vitro* screening on human lung cancer A549 cell line.

From the results (Table 3), **[7-PPh₃]BF₄**, showed a very interesting antiproliferative activity, with IC₅₀ value lower than cisplatin; on the other hand, the remaining complexes show no activity at all.

Table 3. Effect of [7PPh₃]BF₄ complex on cell viability (IC₅₀ values) in human lung cancer cells (A549) after 72h incubation

Compound	A549
Cisplatin	8 ± 0.5
7Cl	105
[7-7]BF₄	185
7S-pyr	104
[7PPh₃]BF₄	4.9 ± 0.3

In general, the very low cytotoxicity can be explained considering a possible low cellular uptake of neutral species **7Cl** and **7S-pyr**; in these cases the lipophilic/hydrophilic character of the metal complexes does not allow them to penetrate the cellular wall. Conversely, the uptake is governed also by the charge, as well as the hydrophobicity of a substance, thus the cationic species could use different uptake routes.

Surprisingly, only the complex bearing the phosphine led to a very interesting antiproliferative activity, even higher than cisplatin in the cisplatin-resistant A549 cell line. Unfortunately, the bis-carbene complex **[7-7]BF₄** showed the highest IC₅₀ value, and probably the reason lies in the enhanced complex stability given by the presence of two gold-carbon bonds, which do not permit the metal center to bind the intracellular targets.

Table 4. Effect of [7PPh₃]BF₄ on cell viability (IC₅₀ values) in different cell lines after 72h incubation

Compound	IC ₅₀ (μM) ± SE				
	A549	MCF7	HCT +/+	HCT -/-	A375
Cisplatin	8 ± 0.5	21.4 ± 1.4	10.6 ± 1.3	22.1 ± 1.9	3.7 ± 0.9
[7PPh₃]BF₄	4.9 ± 0.3	3.8 ± 1.2	4.1 ± 1.3	0.42 ± 0.2	2.8 ± 0.2

Furthermore, **[7PPh₃]BF₄** has been screened for its cytotoxic properties also against a large panel of cancer cells, including MCF7, HCT116, and A375 (epidermoid carcinoma) cell lines, confirming its very promising antiproliferative activity, which in all cases leads to IC₅₀ values lower than cisplatin, (Table 4). It should be noted that part of the observed anticancer effect may be also partly due to the presence of the phosphine ligand, which has known cytotoxic properties when released intracellularly upon ligand exchange reactions. Further studies should investigate the selectivity of this compound for cancerous cells, with respect to non-tumorigenic ones, in order to avoid the occurrence of possible side effects *in vivo*.

3. Experimental section

Cell culture and inhibition of cell growth

The human lung cancer cell line A549 (purchased at the ATCC), human colon cancer cell lines HCT116 (p53 wt and p53 K.O., kindly provided by Dr. Götz Hartleben, RUG), human breast cancer cell lines MCF7 (Leibniz-Institut DSMZ - Deutsche Sammlung von Mikroorganismen und Zellkulturen GmbH), and human skin cancer cell lines A375 (kindly provided by Prof. Sylvestre Bonnet, Leiden University) were cultured respectively in DMEM (Dulbecco's Modified Eagle Medium) (from Invitrogen), at 37 °C in a humidified atmosphere of 95% of air and 5% CO₂ (Heraeus, Germany).

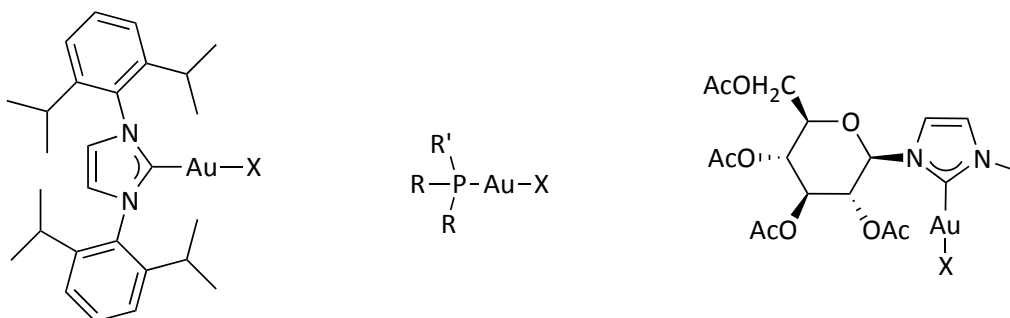
For evaluation of growth inhibition, cells were seeded in 96-well plates (Costar, Integra Biosciences, Cambridge, MA) at a concentration of 10000 cells/well and grown for 24 h in complete medium. Solutions of the compounds were prepared by diluting a freshly prepared stock solution (10⁻² M in DMSO) of the corresponding compound in aqueous media (DMEM). Afterwards, the intermediate dilutions of the compounds were added to the wells (200 µL) to obtain a final concentration ranging from 0 to 100 µM, and the cells were incubated for 72 h. Following 72 h drug exposure, 3-(4,5-dimethylthiazol-2-yl)-2,5-diphenyltetrazolium bromide (MTT) was added to the cells at a final concentration of 0.5 mg ml⁻¹ incubated for 2 h, then the culture medium was removed and the violet formazan (artificial chromogenic precipitate of the reduction of tetrazolium salts by dehydrogenases and reductases) was dissolved in DMSO. The optical density of each well (96-well plates) was quantified three times in triplicates at 550 nm using a multi-well plate reader, and the percentage of surviving cells was calculated from the ratio of absorbance of treated to untreated cells. The IC₅₀ value was calculated as the concentration reducing the proliferation of the cells by 50% and it is presented as a mean (± SE) of at least three independent experiments.

CHAPTER

8

GENERAL CONCLUSIONS

Within this study new series of cationic gold(I) [L-Au-X] complexes were readily prepared in excellent yields and fully characterized.



The class of [(NHC)-Au-X] catalysts has been used in the alkoxylation of alkynes varying the counteranion (up to twelve), which exhibits different coordinating power and basicity. Through catalytic studies and theoretical calculations, it may be concluded that anions containing the $-\text{SO}_3$ fragment are the best choice. In the presence of these anions (NTf_2^- , OTf^- , OTs^- and OMs^-) the pre-equilibrium is shifted towards the OSIP and their characteristic basicity promotes the nucleophilic attack. On the other hand, anions having a strong coordination ability (NO_3^- , OAc^- and ptm^-) slow down the reaction rate (the $\text{ISIP} \rightleftharpoons \text{OSIP}$ equilibrium being shifted towards ISIP),

while too basic anions (TFA^-) inhibits the catalysis owing to the formation of the inactive metal alkoxide. Less coordinating and less basic anions ($\text{BAr}^{\text{F}-}$, BF_4^- , ClO_4^-), instead, do not promote efficiently the nucleophilic attack. As regards the PFHp^- anion, its coordination power is expected to be intermediate between the outperforming OTs^- and OMs^- anions. Notwithstanding this, the efficiency of complex $[(\text{NHC})\text{-Au-PFHp}]$ in the methoxylation of 3-hexyne, as judged by the low TOF value, was unexpectedly poor. DFT calculations and NMR experiments seem to suggest that the reason lies in the formation of a tricoordinated intermediate species which makes the anion a bad leaving group and thus less available for the nucleophile activation. A general trend between coordinating ability and catalytic performances in the alkoxylation of alkynes may be established when the geometry of the anion is taken into account: anions with more spherical anchoring group (such as OTs^- and OMs^-) tend to destabilize the unreactive tricoordinated species which, in turn, may be formed by anions bearing a 'planar' anchoring group, as in the case of PFHp^- .

Another important conclusion that may be inferred from this work is that the effect of the anion can be very marked and, especially, it is linked to the nature of the nucleophile. When the alcohol is a poor nucleophile and does not present specific functional groups (able to activate $-\text{OH}$ during the attack), we observe a large difference of reactivity depending on the employed anion. In the case of benzyl alcohol the reactivity increases (about 20 times) on going from $\text{BAr}^{\text{F}-}$ to OTs^- . The use of methanol has led to a flattening of the differences between the anions (compare $\text{BAr}^{\text{F}-}$ with OTs^-), due to the formation of hydrogen bonding with a second alcohol molecule that improves the nucleophilicity of the attacking methanol.

On the other hand, the use of suitably functionalized alcohols that contribute to the polarization of the $-\text{OH}$ bond through intramolecular interactions (this is the case of Gly-OMe) flatten the effect of the anion (thus complexes with $\text{BAr}^{\text{F}-}$ and OTs^- show analogous catalytic performances). Alcohols with too low nucleophilic power (as TFE) are not active when both **1OTs** and **1BAr^F** are employed as catalyst.

Moreover, the activation parameters of the process have been determined, and these values are in agreement with those obtained theoretically and clearly indicate the crucial role of the counterion in the rate determining step of the reaction (the alcohol attack).

This study highlights the crucial role of the anion X^- in the catalysis promoted by L-Au-X derivatives and, in particular, how this effect depends on both its intrinsic properties (basicity, coordinating power and even geometry) and its correlation with the nucleophile.

Additionally, further insights have been achieved from a regioselective point of view in the alkoxylation reaction of symmetrically and unsymmetrically substituted internal alkynes.

Furthermore, this study demonstrates that the improvement of the performances of [L-Au-X] species in catalysis can be realized through the suitable choice of the ligand, which is strongly depending on the nature of the anion, and *vice versa*.

Contrary to the NHC ligand, whose best combination is with the OTs⁻ anion, in case of complexes bearing phosphanes, a different behavior has been outlined: combining five P-ligands with two counterions, OTs⁻ and OTf⁻, triflate anion resulted to be the best choice (except for PAR^F ligand, probably due to the catalyst deactivation).

A possible explanation can be found in the higher affinity of the counterion (especially OTs⁻) for the gold fragment when the ancillary ligand L is a phosphane with respect to NHC: a higher gold affinity inhibits the reaction, when the rate determining step is the nucleophilic attack, because of the shift of the ISIP–OSIP equilibrium in favor of ISIP.

The relevance of the counterion in catalysis has been further corroborated, by studying the role of ion pairs in solution, using solvents with increasing permittivity.

The choice of the solvent is influential to realize the right distance of the anion from the active site, allowing the formation of the OSIP species and the “template” effect of the anion for the activation of the nucleophile.

This complicated and intriguing scenario suggests even more that detailed experimental and theoretical studies are necessary in order to reach the best catalytic performances of L-Au-X species applied to a given organic transformation.

While N-heterocyclic carbenes (NHC) are ubiquitous ligands in catalysis for organic and industrial synthesis, their potential to form transition metal complexes for medicinal applications has still to be exploited.

Within this frame, a novel class of N-heterocyclic carbene gold(I) complexes, bearing a sugar moiety for suitable functionalization, has been synthesized and, although more biological studies should be undertaken to further investigate the mechanism of action of this new series of compounds, preliminary *in vitro* antiproliferative assays have revealed the promising cytotoxic properties of the compounds in cancer cells. Overall, we are confident that these results will allow new possibilities of fine-tuning of the chemico-physical properties of organometallic Au(I)-NHC scaffolds for biological applications.

APPENDIX**A****ACRONYM AND ABBREVIATION LIST**

1. Units

Å	Ångström
°C	Celsius Degree
cal	calorie
eV	Electronvolt
g	Gram
h	Hour
Hz	Hertz
K	Kelvin degree
kcal	kilocalorie
Kg	Kilogram
L	Liter
M	Molar
MHz	Megahertz
min	Minute
mL	Milliliter
mM	Millimolar

mmol	Millimole
mol	Mole
m/z	Mass unit on elementary charge
nm	nanometer
ppm	Part per million
t	Tonne
Z	Nuclear charge
ϵ_r	Dielectric constant
μL	microliter
μM	micromolar
€	Euro

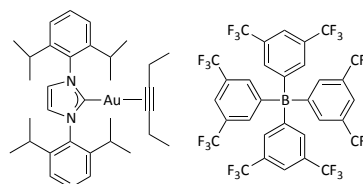
2. Chemical groups and compounds

Ar	aryl
BAr^{F}	tetrakis(3,5-bis(trifluoromethyl)phenyl)borate
BF_4	tetrafluoroborate
Bn	benzyl
BnOH	benzyl alcohol
Bu	butyl
DMSO	dimethyl sulfoxide
Et	ethyl
Gly-OMe	triethylene glycol monomethyl ether
Hnor	9H-Pyrido[3,4-b]indole
JohnPhos	2(di- <i>tert</i> -butylphosphino)biphenyl
magi	1-methyl-3-(2,3,4,6-tetra- <i>O</i> -acetyl- β -D-glucopyranosyl)imidazolylidene
Me	methyl

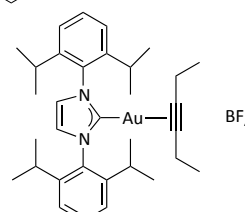
MsOH	methanesulfonic acid
MTT	3-(4,5-dimethylthiazol-2-yl)-2,5-diphenyltetrazolium bromide
NHC	1,3-bis(diisopropylphenyl)imidazol-2-ylidene
NTf ₂	bis(trifluoromethylsulfonyl)imide
OAc	acetate
OEt	ethoxyde
OMe	methoxyde
OMs	methanesulfonate
OTf	trifluoromethanosulfonate
OTs	<i>p</i> -toluensulfonate
PAr ^F	tris(3,5-bis(trifluoromethyl)phenyl)phosphine
P(^t Bu) ₃	<i>t</i> -butyl phosphine,
PC	propylene carbonate
PFHp	2,2,3,3,4,4,5,5,6,6,7,7,7-tridecafluoroheptanoate
Ph	phenyl
phos	phosphite
PPh ₃	triphenyl phosphine
ⁱ Pr	isopropyl
ⁿ Pr	normal propyl
ptm	phtalimide
S-pyr	2-mercaptopyrimidine
TFA	trifluoroacetate
TFAH	trifluoroacetic acid
TFE	2,2,2-trifluoroethanol
THT	tetrahydrothiophene
TMS	tetramethylsilane
<i>p</i> TsOH	<i>p</i> -toluensulfonic acid

2,6-DMP	2,6-dimethoxyphenol
^1H	hydrogen-1 isotope
^{13}C	carbon-13 isotope
^{19}F	florine-19 isotope
^{31}P	phosphorous-31 isotope

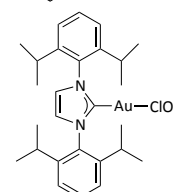
1BAr^F Gold, [1,3-bis[2,6-bis(1-methylethyl)phenyl]-1,3-dihydro-2*H*-imidazol-2-ylidene] tetrakis(3,5-bis(trifluoromethyl)phenyl)borate



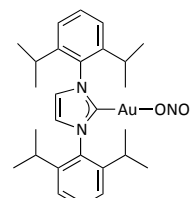
1BF₄ Gold, [1,3-bis[2,6-bis(1-methylethyl)phenyl]-1,3-dihydro-2*H*-imidazol-2-ylidene] tetrafluoroborate



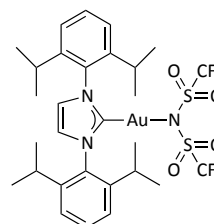
1ClO₄ Gold, [1,3-bis[2,6-bis(1-methylethyl)phenyl]-1,3-dihydro-2*H*-imidazol-2-ylidene] perchlorate



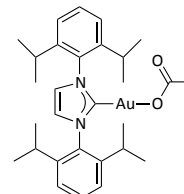
1NO₃ Gold, [1,3-bis[2,6-bis(1-methylethyl)phenyl]-1,3-dihydro-2*H*-imidazol-2-ylidene] nitrate

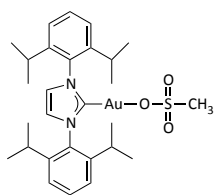
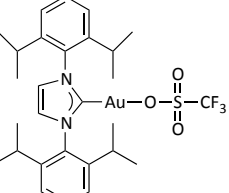
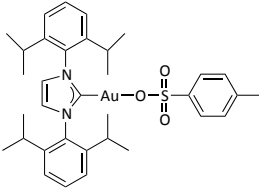
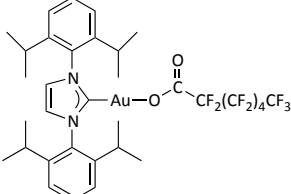
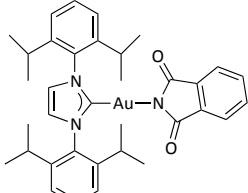
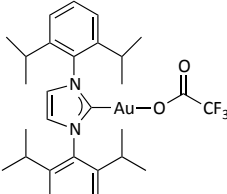
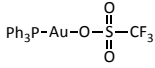
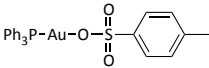
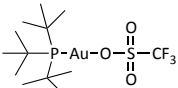


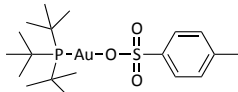
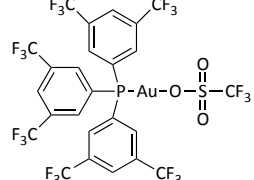
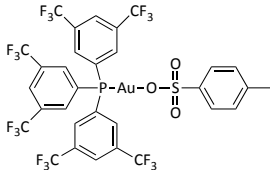
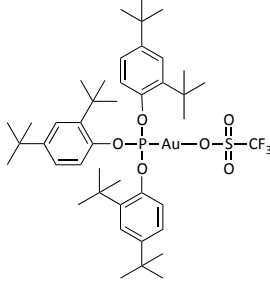
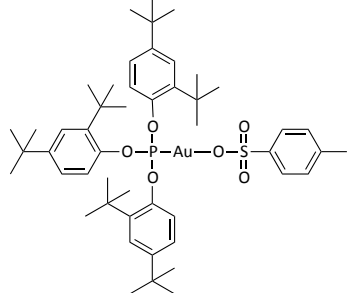
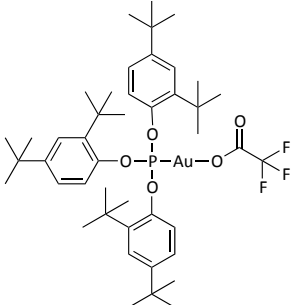
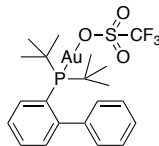
1NTf₂ Gold, [1,3-bis[2,6-bis(1-methylethyl)phenyl]-1,3-dihydro-2*H*-imidazol-2-ylidene] bis(trifluoromethylsulfonyl)imide



1OAc Gold, [1,3-bis[2,6-bis(1-methylethyl)phenyl]-1,3-dihydro-2*H*-imidazol-2-ylidene] acetate



1OMs	Gold, [1,3-bis[2,6-bis(1-methylethyl)phenyl]-1,3-dihydro-2 <i>H</i> -imidazol-2-ylidene] methanesulfonate	
1OTf	Gold, [1,3-bis[2,6-bis(1-methylethyl)phenyl]-1,3-dihydro-2 <i>H</i> -imidazol-2-ylidene] trifluoromethanesulfonate	
1OTs	Gold, [1,3-bis[2,6-bis(1-methylethyl)phenyl]-1,3-dihydro-2 <i>H</i> -imidazol-2-ylidene] <i>p</i> -toluensulfonate	
1PFHp	Gold, [1,3-bis[2,6-bis(1-methylethyl)phenyl]-1,3-dihydro-2 <i>H</i> -imidazol-2-ylidene] 2,2,3,3,4,4,5,5,6,6,7,7,7-tridecafluoroheptanoate	
1ptm	Gold, [1,3-bis[2,6-bis(1-methylethyl)phenyl]-1,3-dihydro-2 <i>H</i> -imidazol-2-ylidene] phthalimide	
1TFA	Gold, [1,3-bis[2,6-bis(1-methylethyl)phenyl]-1,3-dihydro-2 <i>H</i> -imidazol-2-ylidene] trifluoroacetate	
1X	(NHC)AuX	
2OTf	Gold, triphenylphosphine trifluoromethanesulfonate	
2OTs	Gold, triphenylphosphine <i>p</i> -toluensulfonate	
3OTf	Gold, <i>t</i> -butyl phosphine trifluoromethanesulfonate	

3OTs	Gold, <i>t</i> -butyl phosphine <i>p</i> -toluenesulfonate	
4OTf	Gold, tris(3,5-bis(trifluoromethyl)phenyl)phosphine trifluoromethanesulfonate	
4OTs	Gold, tris(3,5-bis(trifluoromethyl)phenyl)phosphine <i>p</i> -toluenesulfonate	
5OTf	Gold, tris(2,4-di- <i>tert</i> -butylphenyl)phosphite trifluoromethanesulfonate	
5OTs	Gold, tris(2,4-di- <i>tert</i> -butylphenyl)phosphite <i>p</i> -toluenesulfonate	
5TFA	Gold, tris(2,4-di- <i>tert</i> -butylphenyl)phosphite trifluoroacetate	
6OTf	Gold, 2(di- <i>tert</i> -butylphosphino)biphenyl trifluoromethanesulfonate	

60Ts	Gold, 2(di- <i>tert</i> -butylphosphino)biphenyl <i>p</i> -toluensulfonate	
[7-7]BF₄	Bis(1-methyl-3-(2,3,4,6-tetra- <i>O</i> -acetyl-β-D-glucopyranosyl)imidazol-2-yl)gold(I) tetrafluoroborate	
7Cl	1-methyl-3-(2,3,4,6-tetra- <i>O</i> -acetyl-β-D-glucopyranosyl)imidazol-2-yl)gold(I)chloride	
[7PPh₃]BF₄	1-methyl-3-(2,3,4,6-tetra- <i>O</i> -acetyl-β-D-glucopyranosyl)imidazol-2-yl)(triphenylphosphine)gold(I) tetrafluoroborate	
[7R]BF₄	[(magi)AuR]BF ₄	
7S-pyr	1-methyl-3-(2,3,4,6-tetra- <i>O</i> -acetyl-β-D-glucopyranosyl)imidazol-2-yl)gold(I)-pyrimidine-2-thiolate	
7X	(magi)AuX	

3. Other acronyms and abbreviations

AB [‡]	Activated complex
ADP	adenosine diphosphate
ASK1	apoptosis signal-regulating kinase 1
BDE	bond dissociation energy
CD	Charge displacement
DC	Deactivated complex
DCD	Dewar-Chat-Duncanson
DCM	Dichloromethane
DFT	Density functional theory
DMEM	Dulbecco's Modified Eagle Medium
DNA	Deoxyribonucleic acid
E	<i>Entgegen</i> (E/Z notation for isomerism)
E _a	Activation energy
eq	Equivalent
GoPI	gold(I)-phosphole chloride
GR	Glutathione reductase
<i>h</i>	Planck constant
HOMO	Highest unoccupied molecular orbital
I	Intermediate
IC	Initial complex
IC ₅₀	Cell viability
IR	Infrared
ISIP	Inner sphere ion pair
<i>k</i>	Rate constant
<i>k_B</i>	Boltzmann constant
KIE	Kinetic isotopic effect

k_{obs}	Observed rate constant
L	Ligand
LUMO	Lowest unoccupied molecular orbital
<i>m</i> -	<i>meta</i> -
MAP3K	mitogen-activated protein kinase kinase kinase
MRI	Magnetic Resonance Imaging
MS	Molecular sieves
<i>n</i> -	<i>normal</i> -
n_{acetal}	mol of acetal
n_{alkyne}	mol of alkyne
NC	Nonactivating complex
n_{catalyst}	mol of catalyst
n_{ketone}	mol of ketone
NMR	Nuclear magnetic resonance
n_{product}	mol of product
NSCLC	non-small cell lung cancer
$n_{\text{vinylether}}$	mol of vinylether
<i>o</i> -	<i>ortho</i> -
OSIP	Outer sphere ion pair
<i>p</i> -	<i>para</i> -
PARP	poly(adenosine diphosphate(ADP)-ribose) polymerases
PC	Product complex
Prx3	peroxinredoxin
PTP	protein tyrosine phosphatase
q	Partition function
R	Alkyl group

RC	Reactant complex
RNA	Ribonucleic acid
ROH	Generic alcohol
ROS	reactive oxygen species
r.t.	Room temperature
S	Substrate
S2	diphenylacetylene
S3	1-phenyl-1-propyne
S2a	(<i>E,Z</i>)- 1-(1-methoxyethene-1,2-diyl)dibenzene
S3a	(2,2- dimethoxypropyl)benzene
S3b	(1,1- dimethoxypropyl)benzene
SCLC	small cell lung cancer
SE	Standard error
<i>T</i>	Temperature
TC	Tricoordinated complex
TOF	Turnover frequencies
Trx	thioredoxin
TrxR	thioredoxin reductase
TrxR1	reduced cytosolic thioredoxin-1
TrxR2	mitochondrial thioredoxin reductase
Trx(SH) ₂	Reduced thioredoxin
Trx(SS)	Oxidized thioredoxin
TS	Transition state
<i>Z</i>	<i>Zusammen</i> (<i>E/Z</i> notation for isomerism)
<i>v</i>	Reaction rate
v/v	Volume to volume
X	Counterion

δ	Chemical shift
ΔG^\ddagger	Gibbs energy of activation
ΔH^\ddagger	Enthalpy of activation
ΔS^\ddagger	Entropy of activation
θ	Tolman's cone angle
κ	Transmission coefficient
ν	Vibration frequency

APPENDIX

B

LIST OF PUBLICATIONS

- Biasiolo, L.; Trinchillo, M.; Belanzoni, P.; Belpassi, L.; Busico, V.; Ciancaleoni, G.; D'Amora, A.; Macchioni, A.; Tarantelli, F.; Zuccaccia, D. *Chem. - Eur. J.* **2014**, *20*, 14594–14598;
- Marina Trinchillo, Paola Belanzoni, Leonardo Belpassi, Luca Biasiolo, Vincenzo Busico, Angela D'Amora, Lorenzo D'Amore, Alessandro Del Zotto, Francesco Tarantelli, Angela Tuzi, and Daniele Zuccaccia *Organometallics*, **2016**, *35*, 641–654